MARIANA BENITES

Geochemistry and formation of ferromanganese crusts and associated mineral deposits in the Rio Grande Rise, Southwest Atlantic Ocean

São Paulo
2023

MARIANA BENITES

Geochemistry and formation of ferromanganese crusts and associated mineral deposits in the Rio Grande Rise, Southwest Atlantic Ocean

A thesis submitted to the Instituto Oceanográfico of the Universidade de São Paulo in partial fulfillment for the degree of Doctor of Science, Oceanography, with emphasis in Geological Oceanography.

Advisor: Prof. Dr. Luigi Jovane
Co-advisor: Prof. Dr. Christian Millo

São Paulo

2023

BENITES, Mariana. **Geochemistry and formation of ferromanganese crusts and associated mineral deposits in the Rio Grande Rise, Southwest Atlantic Ocean**. Thesis (Doctorate) submitted to the Instituto Oceanográfico of the Universidade de São Paulo in partial fulfillment for the degree of Doctor of Science, Oceanography, with emphasis in Geological Oceanography.

Approved in: ___/___/_____

Examining Committee

Prof. Dr. _____ Institution_____

President Signature_____

Prof. Dr. _____ Institution_____

Grade_____ Signature_____

Prof. Dr. _____ Institution_____

Grade_____ Signature_____

Prof. Dr. _____ Institution_____

Grade_____ Signature_____

ACKNOWLEDGEMENTS

To Luigi for trusting me with the task of taking care of important goals of the 'Marine E-tech' project with my Ph.D. thesis research, and allowing me to conduct my research with freedom and autonomy.

To Christian for being always willing to help with his geochemistry expertise, being receptive to discussing anything, and giving a different perspective. His work ethic and positive attitude are things I much appreciated.

To Jim for being an incredible mentor since the very beginning and nurturing me not only with all the expertise he accumulated over decades, but also enthusiasm, courage, confidence, and friendship. He was tireless at advising me either in person or remotely and making sure that each of the chapters presented here was at a high level, regardless of retirement. If it wasn't for him, this thesis wouldn't even have a first outline. He also generously introduced me to the community of deep-sea minerals researchers and genuinely believed in my capacity to belong there.

To Javier for embracing the idea to explore new samples from the South Atlantic Ocean, making all efforts to make my way to the IGME in Madrid possible, and successful at generating high-quality data, giving the enthusiast I needed to push my Ph.D. thesis a bit further.

To the Pacific Coastal and Marine Science Center, U. S. Geological Survey, for receiving me to develop part of my research. I owe the Marine Mineral Lab team (Kira, Amy, Denise, Sam, and Liz) the assistance with lab work and discussions. I thank especially Kira Mizell for supporting with samples collection and processing during cruise RGR1 and at the OSU repository, not to mention her immense contribution to the first three chapters of this thesis with her sharp sense.

To the Geological Survey of Spain (IGME-CSIC) for receiving me to develop part of my thesis research. I am thankful for the Marine Geology Resources and Extreme Environments Research Group for sharing their knowledge with me. I owe the IGME Lab staff at Trés Cantos for assistance with all the lab work (Jesús, Ana, Mayte, Eva, Begonia).

To the Oceanographic Institute (IO-USP), for the opportunity to take the course and to the CORE team at IO-USP for support even with a completely different scientific subject such as mine and making the tribulations of graduate school feel more fun and enjoyable.

To the National Council for Scientific and Technological Development (CNPQ) for granting funding for this thesis. To The São Paulo Research Foundation (FAPESP) for granting

a doctoral scholarship and financial support for carrying out this research through grant 2018/05114-8 and Research Internships Abroad (BEPE) grants 2019/15587-3 and 2020/13258-0.

Finally, I have a deep gratitude for my mother, my partner, and my friends for encouraging me throughout my PhD, for listening patiently and bolstering me when I needed it most.

RESUMO

BENITES, Mariana. **Geochemistry and formation of ferromanganese crusts and associated mineral deposits in the Rio Grande Rise, Southwest Atlantic Ocean**. 2023. 212 f. Tese (Doutorado) – Instituto Oceanográfico, Universidade de São Paulo, São Paulo, 2023.

A crescente demanda por metais críticos e estratégicos tem chamado a atenção para os depósitos minerais do fundo profundo. As elevações oceânicas são importantes áreas-alvo para depósitos de crosta de ferromanganês (FeMn), ricas em Co, Te, Mo, Bi, Pt, W, Zr, Nb, Y e os elementos terras raras (ETR). A Elevação de Rio Grande (ERG) é uma das mais extensas elevações oceânicas do Oceano Atlântico Sul, mas seus depósitos minerais foram pouco investigados até recentemente. Esta tese de doutorado investiga a gênese e evolução de crostas de FeMn desde o cume (600 m) até profundidades abissais (> 5000 m) provenientes de diversos locais na ERG, mas também minerais associados, como fosforitas e ironstones. Para isso, foram aplicadas diversas técnicas analíticas mineralógicas, químicas e isotópicas. As crostas de FeMn da ERG diferem significativamente se vêm do cume ou de águas profundas. As crostas de FeMn do cume apresentam estruturas duais com a maior parte de seu volume composta por crosta velha fosfatizada coberta por uma fina crosta jovem não fosfatizada. Como resultado, as crostas de FeMn do cume carregam uma assinatura diagenética com enriquecimentos de P, Ni, Li e Y e baixos conteúdos de Co, ETR, Mo e Zr. Por outro lado, as crostas de águas profundas (> 2000 m) são totalmente hidrogenéticas e ricas em As, Be, Co, Cu, Mo, Sb, Se, Ti, Th, Tl, U, Zn e ETR. As crostas de FeMn começaram a se formar na ERG provavelmente por volta de 47 Ma e a fosfatização ocorreu ao longo do Mioceno, refletindo importantes mudanças climáticas, como o Ótimo Climático do Mioceno, quando ocorreu uma maior produtividade biológica de superfície. Crostas acima de 1500 m foram fosfatizadas devido à proximidade com a zona de mínimo de oxigênio, um grande reservatório para P. Os principais controles sobre as variações observadas na composição química das crostas com a profundidade da água são a oxigenação e conteúdo de nutrientes das massas de água e paleoprodutividade. Em relação aos ironstones, é proposta uma hipótese para sua origem envolvendo bactérias oxidadoras de Fe e um fluido geotérmico de baixa temperatura. Esta tese contribui para preencher a lacuna de conhecimento de base para futuras atividades de mineração na ERG e entender como condições oceanográficas contemporâneas e passadas controlam a composição de crostas para melhor direcionar a busca por depósitos com características específicas.

Palavras-chave: Elevações Oceânicas. Mineração em águas profundas. Crostas Ferromanganesíferas. Fosfatização. Elevação de Rio Grande.

ABSTRACT

BENITES, Mariana. **Geochemistry and formation of ferromanganese crusts and associated mineral deposits in the Rio Grande Rise, Southwest Atlantic Ocean**. 2023. 212 f. Thesis (Doctorate) – Instituto Oceanográfico, Universidade de São Paulo, São Paulo, 2023.

The increasing demand for critical and strategic metals has driven attention to deep-sea mineral deposits as an alternative supply for high-technology industries. Oceanic elevations are important target areas for ferromanganese (FeMn) crust deposits, which are extremely enriched in rare metals including Co, Te, Mo, Bi, Pt, W, Zr, Nb, Y, and rare earth elements (REE). The Rio Grande Rise (RGR) is one of the most extensive oceanic elevations in the South Atlantic Ocean, but its seafloor mineral deposits were poorly investigated until recently. This thesis investigates the genesis and evolution of FeMn crusts from the summit (600 m) to abyssal water depths (> 5000 m) in a wide range of locations in the RGR, but also investigates associated minerals such as phosphorites and ironstones. For this, a suite of mineralogical, chemical, and isotopic analytical techniques were applied. FeMn crusts from RGR differ significantly, whether they come from the summit or from deep water. FeMn crusts from the summit present dual structures, with most of their volume comprising old phosphatized crusts covered by thin young non-phosphatized crusts. As a result, FeMn crusts from the summit bear a diagenetic signature with P, Ni, Li, and Y enrichment and Co, REE, Mo, and Zr depletion. On the other hand, deep-water FeMn crusts (> 2000 m) are entirely hydrogenetic and enriched in As, Be, Co, Cu, Mo, Sb, Se, Ti, Th, Tl, U, Zn, and REE. FeMn crusts most likely started to form in the RGR about 47 Ma. Phosphatization occurred throughout the Miocene, reflecting important climatic shifts such as the Middle Miocene Climatic Optimum, when enhanced surface biological productivity occurred. Especially the crusts shallower than 1500 m were phosphatized, due to proximity to the oxygen minimum zone, a large reservoir for P. The major controls on the observed variations of chemical composition of crusts with water depth are water masses oxygenation, nutrients and paleoproductivity. Regarding the ironstones, a hypothesis for their origin involving Fe oxidizing bacterial mats and a low-temperature geothermal fluid is proposed. This thesis contributed to filling the knowledge gap on baseline information for future mining activities in the RGR and to understanding the controls of modern and past oceanographic conditions on FeMn crust composition, to better target specific crust characteristics.

Key-words: Oceanic Elevations. Deep-sea Mining. Ferromanganese Crusts. Phosphatization. Rio Grande Rise.

SUMMARY

1 THESIS INTRODUCTION

The increasing societal demand for critical and strategic metals and the shortage of such resources on land calls for the seek of marine resources to supply high-technology industries. This context could place deep-sea mining as an inevitable reality in the near future. Oceanic elevations, for instance, host seafloor mineral deposits such as ferromanganese crusts, phosphorites, and hydrothermal deposits (iron oxides, manganese oxides, and sulfides) (Hein et al., 2010). Ferromanganese crusts (herein FeMn crusts) precipitate from seawater and are found from 400 to 7000 m (Koschinsky and Hein, 2017). Phosphorites formed under suboxic conditions at the top of most seamounts in the Cenozoic, which also accompanied the phosphatization of old FeMn crusts (Koschinsky and Hein, 2017). Hydrothermal deposits are found on active hot spot volcanoes and arc seamounts.

FeMn crusts are the main target for deep-sea mining at oceanic elevations, due to extreme enrichment in rare and critic metals such as Co, Te, Mo, Bi, Pt, W, Zr, Nb, Y, and rare earth elements (REE). This occurs because FeMn crusts form by slow precipitation of Fe and Mn oxyhydroxides from seawater at rates of 1-10 mm/Myr and have very high porosity and specific surface area, all contributing to sorption of metals from seawater (Hein et al., 2013). For instance, Co, Bi, Pt, Tl, and W are enriched by factors of about 100 relative to the Earth's crust, whereas Te is enriched by a factor of 10^4 (Hein et al., 2010).

The Rio Grande Rise (RGR) is one of the largest oceanic elevations in the South Atlantic Ocean and the presence of FeMn crust deposits is known at least since 2009. In 2015, the state-owned Companhia de Pesquisa de Recursos Minerais (CPRM) signed a 15-year contract with the International Seabed Authority (ISA) for FeMn crust exploration along the summit of RGR. However, detailed studies on the formation of these deposits were not available until the beginning of this Ph.D. Thesis in 2018. Besides, the majority of studies of seamount mineral deposits in the Atlantic Ocean are concentrated in the Northeast Atlantic, whereas studies in the South Atlantic Ocean are scarce.

This thesis address the formation of FeMn crusts and associated mineral deposits in the RGR, one of the most prominent exploration target areas in the South Atlantic Ocean. Chapter 1 deals with the origin of FeMn crusts from the RGR for the first time. The study area comprised three small sectors at the summit of RGR along the Cruzeiro do Sul Rift, considered the most prominent target areas to FeMn crusts. Chapter 1 presents the mineralogical, geochemical, and isotopic characteristics of FeMn crusts from the summit of RGR, which are strongly phosphatized, investigating the content of critical metals and the history of crust

formation and phosphatization. Chapter 2 dwells into the investigation of the mechanisms of phosphatization of FeMn crusts and other rock types, and the dating of phosphatization events within the paleoceanographic framework of the RGR and the South Atlantic Ocean. Chapter 3 investigates enigmatic iron formation found in association with the FeMn crusts and phosphorites, using chemical analyses, microscopy, and geochronological tools to unravel their genesis. Finally, Chapter 4 presents a new suite of FeMn crust samples from deep-water (1505 – 5060 m) covering a wide area in the RGR to evaluate the vertical extent of phosphatization and the environmental and regional controls on the chemical composition of crusts. Deep-water crusts are compared to summit crusts. This chapter presents the first work dealing with crusts from shallow (600 m) to abyssal (5060 m) water depths in the South Atlantic Ocean.

This thesis contributes to filling the knowledge gap on baseline information needed for potential future mining activities in the RGR and the need to understand the influence of modern and past oceanographic conditions on FeMn crust composition, to establish criteria to target specific crust characteristics.

References

Hein, J.R., Conrad, T.A., Staudigel, H., 2010. Seamount minerals deposits: a source of rare metals for high-technology industries. Oceanography 23, 184–189.

Hein, J.R., Mizell, K., Koschinsky, A., Conrad, T.A., 2013. Deep-ocean mineral deposits as a source of critical metals for high- and green-technology applications: Comparison with land-based resources. Ore Geol. Rev. 51, 1–14. https://doi.org/10.1016/j.oregeorev.2012.12.001

Koschinsky, A., Hein, J.R., 2017. Marine Ferromanganese Encrustations: Archives of Changing Oceans. Elements 13, 177–182. https://doi.org/10.2113/gselements.13.3.177

2 GENESIS AND EVOLUTION OF FERROMANGANESE CRUSTS FROM THE SUMMIT OF RIO GRANDE RISE (CHAPTER I)

Manuscript published on the Journal Minerals

Mariana Benites[1], James R. Hein[2], Kira Mizell[2], Terrence Blackburn[3], Luigi Jovane[1]

[1]Institute of Oceanography, University of São Paulo, Praça do Oceanográfico 191, 05508-120 São Paulo, SP, Brazil

[2]U.S. Geological Survey, PCMSC, 2885 Mission St., Santa Cruz, CA 95060, USA

[3]Department of Earth Sciences, University of California, Santa Cruz, 1156 High Street EMS A108, Santa Cruz, CA 95064, USA

Abstract

The Rio Grande Rise (RGR) is a large elevation in the Atlantic Ocean and known to host potential mineral resources of ferromanganese crusts (Fe–Mn), but no investigation into their general characteristics have been made in detail. Here, we investigate the chemical and mineralogical composition, growth rates and ages of initiation, and phosphatization of relatively shallow-water (650–825 m) Fe–Mn crusts dredged from the summit of RGR by using computed tomography, X-ray diffraction, $^{87}Sr/^{86}Sr$ ratios, U–Th isotopes, and various analytical techniques to determine their chemical composition. Fe–Mn crusts from RGR have two distinct generations. The older one has an estimated age of initiation around 48–55 Ma and was extensively affected by post-depositional processes under suboxic conditions resulting in phosphatization during the Miocene (from 20 to 6.8 Ma). As a result, the older generation shows characteristics of diagenetic Fe–Mn deposits, such as low Fe/Mn ratios (mean 0.52), high Mn, Ni, and Li contents and the presence of a 10 Å phyllomanganate, combined with the highest P content among crusts (up to 7.7 wt %). The younger generation is typical of hydrogenetic crusts formed under oxic conditions, with a mean Fe/Mn ratio of 0.75 and mean Co content of 0.66 wt %, and has the highest mean contents of Bi, Nb, Ni, Te, Rh, Ru, and Pt among crusts formed elsewhere. The regeneration of nutrients from local biological productivity in the water column is the main source of metals to crusts, providing mainly metals that regenerate rapidly in the water column and are made available at relatively shallow water depths (Ni, As, V, and Cd), at the expense of metals of slower regeneration (Si and Cu). Additionally, important contributions of nutrients may derive from various water masses, especially the South Atlantic Mode Water and Antarctic Intermediate Water (AAIW). Bulk Fe–Mn crusts from the summit of RGR plateau are generally depleted in metals considered of greatest economic interest in crusts like

Co, REE, Mo, Te, and Zr, but are the most enriched in the critical metals Ni and Li compared to other crusts. Further investigations are warranted on Fe–Mn crusts from deeper-water depths along the RGR plateau and surrounding areas, which would less likely be affected by phosphatization.

Keywords: ferromanganese crusts; phosphatization; Rio Grande Rise; critical metals

2.1 Introduction

Ferromanganese (Fe–Mn) crusts are ubiquitous chemical sedimentary rocks occurring on oceanic elevations (ridges, seamounts, and guyots) formed by the precipitation of Fe oxyhydroxide and Mn oxide directly from seawater onto a hard surface [1]. This process is called hydrogenesis and is remarkably slow, resulting in crust growth rates typically on the order of 1–5 mm/Myr [2]. During formation, crusts take up and concentrate critical metals from seawater (e.g., Co, Ni, Cu, Te, Pt, Zr, Nb, W, Bi, La, Ce, Nd, Eu, and Tb) in substantial concentrations relative to their ocean-water concentrations. Economic deposits of many of these critical elements, such as metals crucial for high-tech and green-tech applications, that may undergo sporadic shortages [3], and may be rare on the continents [4,5,6]. In particular, Co, Te, Bi, and many heavy rare earth elements (REE) plus yttrium (HREY) are more enriched in Fe–Mn crusts compared to most land-based mineral deposits. For these reasons, interest in mining Fe–Mn deposits from the ocean floor has intensified.

Since Fe–Mn crusts form by chemical precipitation at slow rates, the study of crust layers provides valuable information about the evolution of the past ocean [2]. However, large areas of Fe–Mn crust deposits in the global ocean remain unexplored, and the Rio Grande Rise (RGR) in the Southwest Atlantic Ocean is one of those areas.

Fe–Mn crust deposits have been moderately well studied in the so-called prime crust zone (PCZ) in the Northwest Pacific Ocean (defined by [7]), where crusts have the highest metal contents and tonnages [1] due to their growth on the oldest seamounts in the global ocean. Crust deposits from elsewhere are typically described in comparison to PCZ crusts. The Atlantic Ocean is a much younger ocean basin with fewer volcanic edifices for crust growth; however, Fe–Mn crust from seamounts in the NE Atlantic around the Madeira, Canary, and Azores islands have been moderately well-studied. These NE Atlantic deposits show characteristics similar to those of hydrogenetic crusts adjacent to continental margins as they have lower contents of Mn-phase elements, Mn, Co, Ni, Zn, and Cu and higher terrigenous input as exemplified by relatively higher Fe, Pb, Al, Si, and Th contents than open-ocean crusts

[8,9,10,11]. In the Canary Island Seamount Province, crusts can be thick (maximum 250 mm) and may be as old as 76 Ma [11]. On Tropic seamount, crusts ages average 10 Ma and growth rates are higher than for PCZ crusts, and phosphatization of Tropic Seamount crusts is not as pronounced as in crusts from the PCZ [8]. Here, we use “Ma” for millions of years ago and “Myr” for a time interval of millions of years.

Typical black to dark-grey hydrogenetic Fe–Mn crusts were found on São Paulo Ridge at 2871 m depth, which is close to RGR; those crusts started growing 30 Ma with growth rates of 0.5–3 mm/Myr and show no evidence of growth hiatuses or influence of phosphatization [12]. In addition, one pebble coated by Fe–Mn lamina of hydrogenetic origin was studied [13]. Comparison of RGR crusts with the distant NE Atlantic Fe–Mn crusts in addition to the nearby São Paulo Ridge provides valuable information regarding the varying oceanographic conditions throughout the Atlantic Ocean and also provides insight into which regions should be prioritized for economic exploration.

Knowledge about the environment of RGR is scarce and even baseline information needed for potential future mining activities is not available [14], especially concerning the extent of mineral deposits, the main sediment and rock types, small-scale morphology, and ecosystems. Here, we explore mineralogical, geochemical, and isotopic characteristics of Fe–Mn crusts from the summit area of RGR. We evaluate their content of critical metals and controls on metal enrichments. We also investigate the history of crust formation and phosphatization of the crusts.

2.2 Study Area

RGR is located about 1000 km east of the Brazilian coast and 2000 km west of the Mid Atlantic Ridge (MAR) and is composed of the Western Rio Grande Rise (WRGR) and the Eastern Rio Grande Rise (ERGR; Figure 1). RGR is one of the largest oceanic elevations in the South Atlantic Ocean, rising to up to 500 m water depth, and is surrounded by abyssal plains 4000 m-deep. These high elevations separate the Brazil Basin (BB) to the north and the Argentine Basin (AB) to the south. The Vema Channel isolates the WRGR from the continental shelf. An NW–SE trending 10 to 20 km-wide and 1000 m-deep valley cuts through the center of the entire RGR, which may correspond to an accommodation zone resulting from extension in the region [15]. The central valley provides an extremely steep slope up to the rim of RGR plateau, which is an area where Fe–Mn crusts are likely to form due to lower sedimentation on the slope as well as exposed rock surfaces [14].

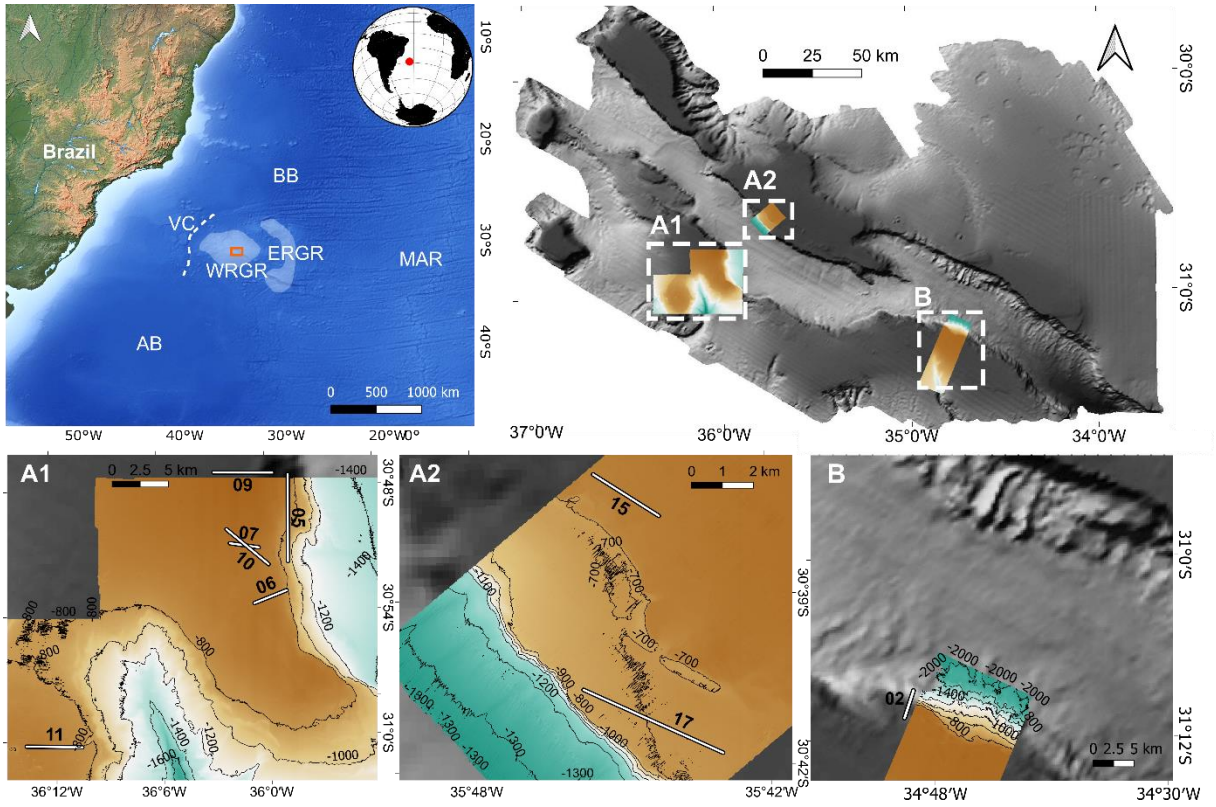

Figure 1. (Upper left) Location map with main morphological features comprising the southwest Atlantic Ocean. AB = Argentine Basin; BB = Brazilian Basin; MAR = Mid-Atlantic Ridge; WRGR = Western Rio Grande Rise; ERGR = Eastern Rio Grande Rise; VC = Vema Channel. The orange square corresponds to the map in the upper right, which shows the surveyed areas A1, A2, and B. (Lower right to left) location of dredges (white lines) in each surveyed area.

Although the formation of RGR is not fully understood, some agreement exists among studies that RGR and Walvis Ridge in the southeast Atlantic formed together as a single ridge on the MAR during the Coniacian/Santonian (85 Myr; [16]). The two ridges then separated and drifted apart due to seafloor spreading. After cooling and thermal subsidence of the oceanic crust, the rise received pelagic sediments [17], until another volcanic event affected the RGR about 46 Myr ago during the Eocene [16]. This volcanic activity uplifted RGR and created several volcanic islands and seamounts. On the islands, volcanism generated pyroclastic debris that was deposited across the platform by turbidity currents. Once the volcanic activity ceased, thermal subsidence again took place and the islands were eroded and leveled by waves and currents as they subsided, creating the flat-topped edifice (guyot) characteristic of RGR's highest elevations of today. Since then, accumulation of pelagic sediment composed mainly by nannofossils and planktonic foraminifera with a small amount of terrigenous components has been the dominant sedimentation processes along RGR [18].

The Ce anomaly of carbonate sediments suggests that anoxic ocean-water conditions prevailed on RGR until the Maastrichtian (70 Myr), followed by increasing oxygenation during the early Eocene (70–55 Myr), when it reached redox conditions similar to modern conditions

[19], and possibly the conditions that allowed the Fe and Mn (oxyhydr)oxides to accumulate. This shift is associated with the RGR-Walvis Ridge subsidence and extensional creation of the north-south deep-water passage, which improved deep-water circulation [20].

Currents around RGR are strong (up to 50 cm·s−1) but variable due to tidal effects [21]. The horizontal current velocity at the seabed is enhanced along the shallower areas of the RGR main plateau [14], which may promote Fe–Mn crust erosion.

2.3 Samples and methods

2.3.1 Samples

Twenty-two Fe–Mn crusts were used in this work, dredged during a multidisciplinary expedition (RGR1) to the summit of WRGR on board the research vessel Alpha Crucis (Instituto Oceanográfico, Universidade de São Paulo, Brazil), from 30 January to 20 February 2018 (Figure 1; [22]). The dredge location and water depth (Table 1) were taken as averages between dredge on-bottom and off-bottom positions. The rock samples were rinsed with fresh water on board ship during cutting.

Table 1. List of samples and locations[1]

Sample ID[2]	Latitude			Longitude			Depth (m)	Area
RGR1_D02_022	31	9.351	S	34	49.804	W	825.5	B
RGR1_D02_030	31	9.351	S	34	49.804	W	825.5	B
RGR1_D02_039	31	9.351	S	34	49.804	W	825.5	B
RGR1_D05_011	30	53.367	S	35	58.854	W	739	A1
RGR1_D05_016	30	53.367	S	35	58.854	W	739	A1
RGR1_D06_003	30	53.634	S	35	59.933	W	716.5	A1
RGR1_D06_013	30	53.634	S	35	59.933	W	716.5	A1
RGR1_D07_002	30	51.136	S	36	1.319	W	684	A1
RGR1_D07_003	30	51.136	S	36	1.319	W	684	A1
RGR1_D07_005	30	51.136	S	36	1.319	W	684	A1
RGR1_D07_009	30	51.136	S	36	1.319	W	684	A1
RGR1_D07_020	30	51.136	S	36	1.319	W	684	A1
RGR1_D09_001	30	47.638	S	36	1.398	W	650.5	A1
RGR1_D09_002	30	47.638	S	36	1.398	W	650.5	A1
RGR1_D09_003	30	47.638	S	36	1.398	W	650.5	A1
RGR1_D10_002	30	51.205	S	36	1.146	W	686.5	A1
RGR1_D10_003	30	51.205	S	36	1.146	W	686.5	A1
RGR1_D11_003	31	0.5395	S	36	12.495	W	751	A1
RGR1_D11_004	31	0.5395	S	36	12.495	W	751	A1
RGR1_D15_017	30	37.518	S	35	45.712	W	648	A1
RGR1_D17_016	30	41.499	S	35	44.508	W	697	A2
RGR1_D17_017	30	41.499	S	35	44.508	W	697	A2

[1]Latitude, longitude, and water depths are mean values for dredge on-bottom and off-bottom positions.

[2]The dredge number (Dxx) is followed by the rock number in that dredge haul.

Fe–Mn crusts collected from the slopes into the central valley (dredge D02 in area B; Table 1) are typical black crusts (Figure 2a), while Fe–Mn crusts collected from the top of the plateau (dredges D05, D06, D07, D09, D10, D11, D15, and D17 in areas A1 and A2) were black with a whitish haze through most of the crust thickness (Figure 2). The whitish haze indicates that the Fe–Mn crust was phosphatized, as confirmed by X-ray diffraction and chemical composition (see the Results section for details). Some of the plateau phosphatized crusts have an overlying 1–10 mm-thick black non-phosphatized layer. Additionally, crusts from the plateau show off-white to pinkish phosphorite lenses of variable sizes. The main substrate rocks for the crusts are basalt (Figure 2a), sandstone (Figure 2e), carbonates (Figure 2f), and ironstone (Figure 2c), however, most commonly the crusts collected were detached from their substrate. The Fe–Mn crusts on the plateau in area A2 were strongly eroded, as indicated by their polished surface, ultimately resulting in only remnants of a Fe–Mn crust on the basalt surfaces (Figure 2h). Brown ironstone material is frequently observed as vertical flame-like structures within Fe–Mn crusts (Figure 2b), as wavy laminations serving as a substrate for Fe–Mn crusts (Figure 2e), or as laminae between the Fe–Mn crust layers (Figure 2c,f).

The mineralogy, chemical, and Sr isotopes composition measurements were performed in bulk Fe–Mn crusts, Fe–Mn crust layers (specified by the sample ID followed by "L" plus the depth interval in millimeters, e.g., "RGR1_D02_022 L0-10"), phosphorite lenses (specified by the ID of the layer in which they are contained plus "lens", e.g., "RGR1_D07_002 L8-33 lens"), and substrate.

2.3.2 Methods

2.3.2.1 Computed Tomography (CT)

A three-dimensional CT scan of sample RGR1_D07_002 was made using an Xradia Versa XRM-510 scanner from Zeiss, at the Technological Characterization Laboratory from Escola Politécnica, Universidade de São Paulo, in Brazil. A slab of sample RGR1_D07_002 was scanned for 3 hours using a 160 kV and 10 W X-ray source under a 36 × objective. The number of views was 1000 at 8 s per view and the detector resolution was 1024 pixels × 1024 pixels, each pixel having a 54-µm size.

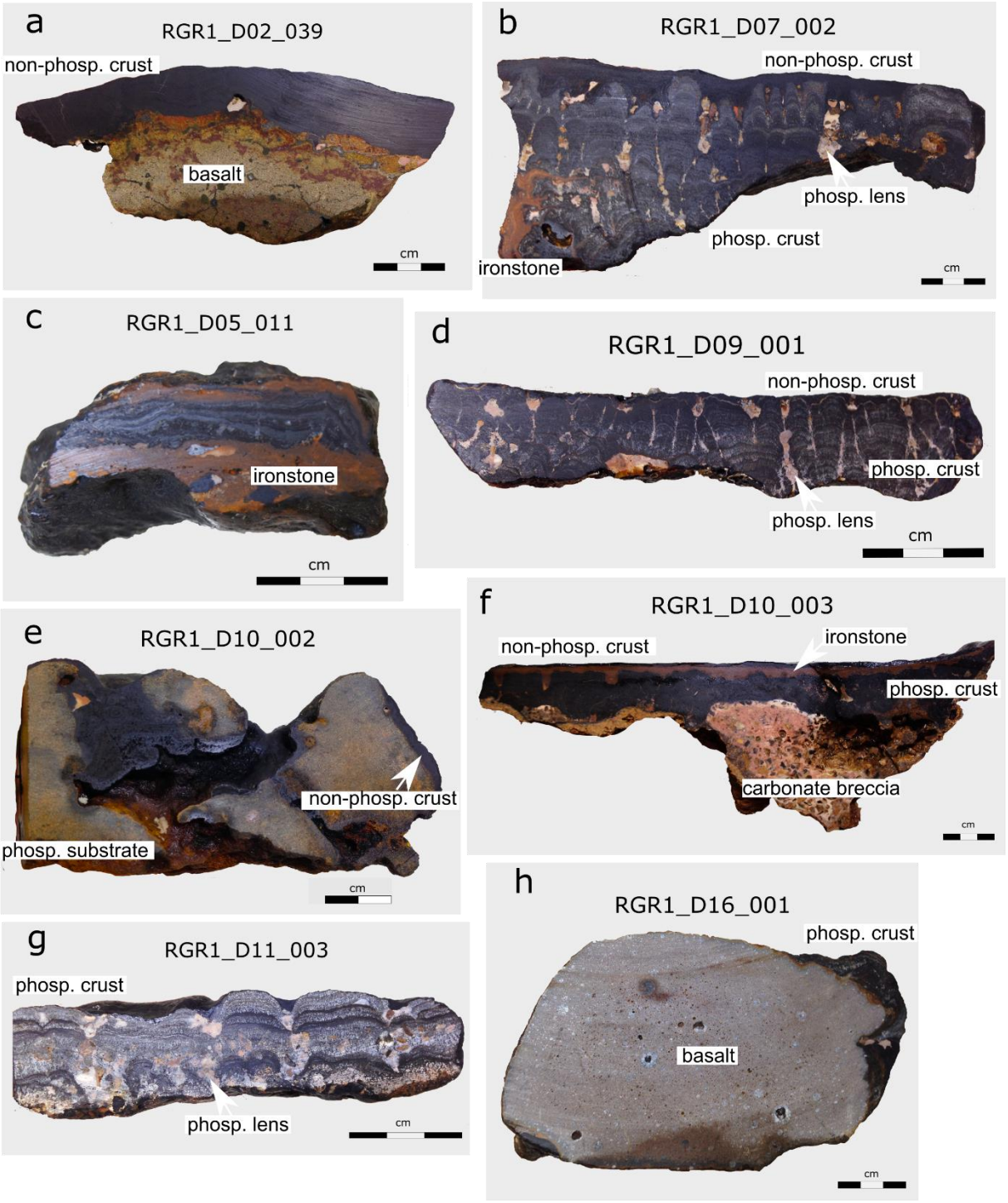

Figure 2. Examples of Fe–Mn crusts from the RGR. Non-phosp. crust = non-phosphatized Fe–Mn crust; phosp. crust = phosphatized Fe–Mn crust; phosp. lens = phosphorite lenses. (a) A typical non-phosphatized crust on altered basalt; (b) phosphatized Fe–Mn crust (white haze) and pink phosphorite lenses between Fe–Mn crust columns; a thin black non-phosphatized crust overlies the phosphatized crust (white haze); ironstone material is present (lower left); no substrate rock was collected; (c) Fe–Mn crust between two ironstone layers; (d) thin non-phosphatized Fe–Mn layer capping phosphatized Fe–Mn crust and phosphorite lenses; (e) anomalous diagenetic non-phosphatized Fe–Mn crust (see results section for details) above a sandstone; (f) phosphatized Fe–Mn crust on carbonate-clast breccia; a thin non-phosphatized Fe–Mn layer is at the top; an ironstone layer is present; (g) pervasively phosphatized Fe–Mn crust with more pronounced white haze and phosphorite lens; and (h) eroded phosphatized Fe–Mn crust on basalt.

2.3.2.2 Mineralogy

The mineralogy of 42 subsamples from the 22 Fe–Mn crusts was analyzed by X-ray diffraction (XRD) using a Phillips diffractometer with Cukα radiation and carbon monochromator at the United States Geological Survey (USGS) in Santa Cruz, California, USA. The powder from different subsamples was drilled using a Dremel and crushed in an agate mortar. XRD scans were from 4 to 70° 2θ. Three subsamples of the Fe–Mn crusts were heated to 300 °C for 24 hours to check if the 10 Å peak corresponds to a phyllomanganate or a tectomanganate. The percentages of minerals in the samples were determined semiquantitatively based on the intensity of the peaks and weighting factors relative to quartz [23,24]. Mineral compositions were divided into three semiquantitative categories based on the estimated percentages: major (>25%), moderate (5–25%), and minor (<5%).

2.3.2.3 Scanning Electron Microscopy (SEM)

Four polished thin sections of samples RGR1_D02_039, RGR1_D05_011, RGR1_D09_001, and RGR1_D09_002 were carbon-coated and observed using a Leo 440i from Leo Electron Microscopy Ltd. at the Laboratory of Scanning Electron Microscopy (LabMEV), Instituto de Geociências, Universidade de São Paulo. The observations were performed under a high vacuum with an electron high tension (EHT) of 20 keV, work distance of 25 mm and an ion probe current of 1–2 nA. Backscatter electron (BSE) and secondary electron (SE) micrographs were created. Chemical element maps were carried using energy dispersive spectroscopy (EDS) with a Si (Li) solid-state detector with INCA 300 software from Oxford Microanalysis.

2.3.2.4 Purification of Carbonate Fluorapatite (CFA)

Chemical procedures for leaching were carried out to eliminate the Fe and Mn (oxyhydr)oxide phases, carbonates, and organic matter to obtain purified CFA aliquots for Sr isotope and chemical composition analyses. The procedures used were based on those from [25]. Step 1: 15 Fe–Mn crust layers and bulk had their Fe and Mn (oxyhydr)oxides were eliminated using a reductant made of Na-citrate, Na-bicarbonate, and Na-dithionite (pH 8) and the solution was filtered to collect the solid filtrate. Step 2: The residual powder from step 1 and powder samples from three phosphorite lenses had the carbonate removed by using a 0.5 M triammonium citrate solution (8.1 ± 0.1) and filtered to collect the solid filtrate [26]. Step 3: The organic matter was oxidized from the residual powder of step 2 by washing with a 30%

H2O2 solution and centrifuging to pellet the CFA residue. At each step, the residue was analyzed by XRD to confirm the elimination of the mineral phase targeted.

2.3.2.5 Chemical Composition

Five different analytical techniques were used for element and compounds analyses of the Fe–Mn crusts, which were done at SGS Mineral Services, Canada. Fourteen Fe–Mn crusts were analyzed including 7 bulk crusts and 16 layers measurements, totalizing 23 samples. Al, Ca, Fe, K, Mg, Mn, Na, P, Si, and Ti were determined from borate fused discs using X-ray fluorescence (XRF); loss on ignition (LOI) was measured at 1000 °C; Ce, Co, Dy, Er, Eu, Gd, Ho, La, Lu, Mo, Nb, Nd, Ni, Pr, Sm, Tb, Tm, U, V, W, Y, Yb, and Zr were determined by ICP-MS using lithium metaborate fused discs; Ag, As, Ba, Be, Bi, Cd, Cr, Cu, Hf, Li, Pb, Rb, S, Sb, Sc, Sr, Te, Th, Tl, and Zn were determined from four-acid digested aliquots by ICP-MS; CO2 was determined by coulometry; Se was determined by hydride generation and graphite furnace atomic absorption spectroscopy (AAS); and Cl and F were determined by an ion-specific electrode. A subgroup of the samples was analyzed for platinum group metals (PGM: Ir, Pd, Pt, Rh, and Ru) and Au by Ni-sulfide fire assay and ICP-MS by Intertrek Genalysis Perth, Australia, which included four bulk crusts and 10 crust layers.

Precision was better than 5% for all elements, except for Eu (5.5%), Lu (5.9%), Be (6.9%), Pt (18%), and Cr (33%). Accuracy was better than 5% for most elements; 5% to 10% for Gd, Er, Tb, Sm, Tl, Hf, Th, Pb, Rb, and Sc; 10% to 25% for Bi, Ag, and Ti; and could not be determined for Cl, Co, F, Mo, Nb, Ni, P, V, W, and Zr because they did not have certified values of the standards. However, Co, Cu, Mo, Ni, P, V, Te, and W were also run by four acid digestion ICP-MS with accuracy better than 14%, excepting Te and W. No certified value of the standard material was available for Nb, Os, and Zr.

REE plus Y (REY) plots were made using concentrations normalized to shale (Post Archean Australian Shale, PAAS) concentrations using values from [27]. The Ce anomaly was calculated using the equation $Ce_{sn}^{*} = 2*Ce_{sn}/(La_{sn} + Pr_{sn})$, where sn = shale normalized values. A correlation matrix was calculated for Pearson coefficients using the software R Studio. Q-mode factor analysis was performed using Matlab after [28].

2.3.2.6 Age of Initiation and Growth-Rate Estimates of Fe–Mn Crusts Based on the Co-Chronometer

The Co-chronometer empirical Equations of [29] and [30] were used to estimate the growth rates of Fe–Mn crusts, and from that to estimate the initiation age of crust growth at

RGR. For this, the Co, Fe, and Mn contents (wt %) of bulk crusts and layers were used in the following Equations:

$GR = 0.68/Co_n^{1.67}$, where $Co_n = Co * 50/(Fe + Mn)$ [29].

$GR = 1.28/(Co - 0.24)$ [30].

The equation of Puteanus and Halbach (1988) was not applied to the phosphatized layers since their Co content is < 0.24%, which is the threshold required to use that equation. The Co-chronometer method assumes that the incorporation of Co by Fe–Mn crusts is constant over time and space. However, postdepositional processes, especially phosphatization, may alter the Co content of Fe–Mn crusts making results from these equations questionable. In this regard, we compared results from the Equation of [29] calculated by two different approaches: (1) using growth rates estimated for the phosphatized layers; and (2) using growth rates extrapolated from the non-phosphatized layers of the same sample when a non-phosphatized layer was present. We compared the results from the two approaches with the age of phosphatization determined by Sr isotopes to check if the Co-chronometer ages were realistic, i.e., ages of initiation of crust growth should be older than the age of phosphatization events.

2.3.2.7 U and Th isotopes

The uppermost non-phosphatized Fe–Mn crust was used for U-Th dating. Four replicates (10–14 mg) were collected from five sublayers of sample RGR1_D07_002 by drill. Each sublayer was drilled using a micro mill system with a drill bit of 0.5 mm diameter and was spaced at 0.3 mm. Isotopic compositions and concentrations of U and Th were determined at The University of Texas at El Paso. For measurements of U and Th isotopic compositions and concentrations, 10–100 mg powdered sample were weighed in a Teflon vial, spiked with a mixed ^{233}U–^{229}Th, and completely dissolved using an HCl-HF acid mixture. Uranium and Th separation and purification were performed by anion-exchange chromatography. The total procedural blanks were 10 pg for U and 30 pg for Th, which were negligible about the amounts of U and Th in the samples. Isotope measurements were performed using a Nu Instruments Nu Plasma MC-ICP-MS. A sample-standard bracketing method was used to correct for instrumental mass bias. U concentrations were calculated using the measured $^{235}U/^{233}U$ isotopic ratios. ($^{234}U/^{238}U$) activity ratios were calculated using the analyzed $^{234}U/^{235}U$ ratios and assuming a constant $^{238}U/^{235}U$ ratio of 137.88, with the following decay constants: $\lambda 238 = 1.551 \times 10^{-10}$ yr^{-1} and $\lambda 234 = 2.826 \times 10^{-6}$ yr^{-1} [31,32]. Duplicate analyses of basalt BCR-2 rock standard (N = 5) yielded a mean ($^{234}U/^{238}U$) activity ratio of 1.004 ± 0.004, a mean U concentration of 1.685 ± 0.003 ppm, a mean ($^{230}Th/^{232}Th$) activity ratio of 0.889 ± 0.031, and a

mean Th concentration of 5.880 ± 0.057 ppm. These values are consistent with previously published values [33]. In order to improve the degree of certainty of the model for the growth rate, a final U–Th analysis of the outermost rind (close of the 0 age) of sample RGR1_D07_002 was conducted at the University of California, Santa Cruz W.M. Keck Isotope Facility (Santa Cruz, CA, USA). A 10 mg sample was digested as described above, spiked with a mixed ^{229}Th–^{236}U tracer. Thorium and uranium isotopic compositions were measured by thermal ionization mass spectrometry (TIMS) in an IsotopX Phoenix x62.

2.3.2.8 Sr Isotopes

Sr was isolated from pure CFA and carbonates samples by Sr-spec column chemistry at the University of California, Santa Cruz W.M. Keck Isotope Facility. The samples were digested in concentrated HNO_3 and the resulting solution was separated from residual solids by centrifuge. Then, the solution was loaded onto the columns containing Sr-SPEC RESIN and the residual solution containing Sr was collected in Teflon vials. ^{87}Sr and ^{86}Sr isotopes were determined by thermal ionization mass spectrometry (TIMS) in an IsotopX Phoenix x62. The 2SD was less than 0.000091. The ^{87}Sr/^{86}Sr ratios of the samples were compared to ^{87}Sr/^{86}Sr ratios for Cenozoic seawater and corresponding numerical ages were obtained using the LOWESS 5 fit curve from [34].

2.4 Results

2.4.1 Mineralogy

Fe–Mn crusts from RGR are composed predominantly of Mn oxides, amorphous FeOOH, minor to major amounts of carbonate fluorapatite (CFA) and calcite, and minor amounts of quartz (Table 2), as determined by the XRD patterns (Supplementary Material Figure S1). CFA is the main phosphate mineral that impregnates Fe–Mn crusts during phosphatization events, and it has white to off-white colors, which accounts for the whitish haze in phosphatized Fe–Mn crusts.

The mineralogical terminologies of marine Mn oxides are not always clear and often divergent, however, the compilation of [35] was used here because it offers a practical guide based on systematic descriptions of crystallographic features based on synchrotron studies. Two types of Mn oxides were observed in the Fe–Mn crusts of RGR. The first has no basal reflection and diagnostic reflections at 2.45 Å and 1.42 Å, which correspond to the disordered phyllomanganate vernadite [36,37], also termed Fe-vernadite by some authors because it corresponds to Vernadite epitaxially intergrown with amorphous FeOOH [35,38,39].

Table 2. Mineralogy of Fe–Mn crusts and associated phosphorite and ironstones from the Rio Grande Rise; semiquantitative categories are major >25%, moderate 5–25%, and minor <5%. CFA = Carbonate fluorapatite; 10 Å = 10 Å phyllomanganate. Interpretation based on the mineralogy.

Sample ID	Subsample	Major	Moderate	Minor	Interpretation
RGR1_D02_022	L0-10	Fe-vernadite	Calcite	-	Non-phosphatized Fe-Mn crust
	L10-15	Fe-vernadite, asbolane	Calcite, CFA	-	Phosphatized Fe-Mn crust
RGR1_D02_030	L0-13	Fe-vernadite	-	Calcite	Non-phosphatized Fe-Mn crust
	L13-20	Fe-vernadite, asbolane, CFA	Calcite	-	Phosphatized Fe-Mn crust
RGR1_D02_039	L0-10	Fe-vernadite	-	Quartz, calcite	Non-phosphatized Fe-Mn crust
	L10-15	Fe-vernadite	-	Calcite, dolomite	Non-phosphatized Fe-Mn crust
RGR1_D05_011	L2-10	Asbolane, pyrolusite	CFA, calcite	Quartz	Hydrothermal Mn layer
	L10-19	Goethite	CFA	Quartz	Ironstone
RGR1_D05_016	L0-1	Fe-vernadite, asbolane, CFA	-	-	Phosphatized Fe-Mn crust
	L0-23	Asbolane, Fe-vernadite, CFA	Calcite	-	Phosphatized Fe-Mn crust
	L23-34	Goethite	CFA	Calcite	Ironstone
RGR1_D06_003	Bulk	Fe-vernadite, asbolane	CFA	Calcite	Phosphatized Fe-Mn crust
RGR1_D06_013	Bulk	Fe-vernadite, asbolane, CFA	Calcite	-	Phosphatized Fe-Mn crust
RGR1_D07_002	L0-6	Fe-vernadite	Calcite	-	Non-phosphatized Fe-Mn crust
	L6-18	Fe-vernadite, asbolane, CFA	Calcite	Minor quartz	Phosphatized Fe-Mn crust
	L18-33	Fe-vernadite, asbolane	CFA	Quartz, calcite	Moderately phosphatized Fe-Mn crust
	L18-33 lens	Calcite, CFA	-	Quartz	CFA-cemented biogenic particles
	L33-55	Fe-vernadite, asbolane, CFA	-	-	Phosphatized Fe-Mn crust
RGR1_D07_003	L0-5	Fe-vernadite	Calcite or Mg-calcite/Mn-calcite	-	Non-phosphatized Fe-Mn crust
	Upper L5-18	Fe-vernadite, asbolane, CFA	-	-	Phosphatized Fe-Mn crust
	Lower L5-18	CFA, Fe-vernadite	Calcite, asbolane	-	Phosphatized Fe-Mn crust
	L5-18 lens	CFA, calcite	-	Quartz	CFA-cemented biogenic particles
RGR1_D07_009	Bulk	Fe-vernadite	-	Calcite	Non-phosphatized Fe-Mn crust
RGR1_D07_020	L0-15	Fe-vernadite, asbolane, CFA	Calcite, Mg-calcite	Quartz	Phosphatized Fe-Mn crust
	L15-33	CFA, Fe-vernadite, asbolane	Calcite	-	Phosphatized Fe-Mn crust
RGR1_D09_001	L0-1	Fe-vernadite, asbolane	CFA	-	Moderately phosphatized Fe-Mn crust
	L1-13	CFA, Fe-vernadite	Calcite, asbolane	-	Phosphatized Fe-Mn crust
	L14-28	CFA, calcite	Fe-vernadite, asbolane	Quartz, plagioclase	Phosphatized Fe-Mn crust

	L14-28 lens	CFA, calcite	-	Quartz	CFA-cemented biogenic particles
RGR1_D09_002	L0-8	Asbolane, Fe-vernadite	-	Calcite	Non-phosphatized Fe-Mn crust
	L8-14	Goethite	-	CFA, calcite	Ironstone
RGR1_D09_003	L1-3	Goethite	-	Calcite	Ironstone
	L1-3 lens	Calcite, Mg-calcite	-	Minor CFA	Carbonate lens
RGR1_D10_002	Edge	Fe-vernadite, asbolane, calcite	-	-	Non-phosphatized Fe-Mn crust
	Center	CFA	Calcite	Quartz	Phosphatized carbonate sand
	L0-2	Fe-vernadite	-	Calcite	Non-phosphatized Fe-Mn crust
	L0-2 edge	CFA	Goethite, Fe-vernadite, calcite	Ramsdellite-like mineral	Phosphatized Fe-Mn crust
RGR1_D10_003	L2-5	Goethite	Calcite		Ironstone
	L5-20	CFA	-	Calcite, pyrolusite	Phosphorite lamina, minor hydrothermal component
	Substrate 1	Calcite	-	CFA, quartz	Phosphorite breccia
	Substrate 2	Calcite	-	CFA, quartz	Phosphorite
RGR1_D11_003	Bulk	CFA	Asbolane, calcite	Goethite, Fe-vernadite	Pervasively phosphatized Fe-Mn crust
RGR1_D11_004	Bulk	Fe-vernadite, asbolane	CFA	Calcite	Moderately phosphatized Fe-Mn crust
RGR1_D15_017	Bulk	Fe-vernadite, asbolane, CFA	Calcite	Quartz	Phosphatized Fe-Mn crust
RGR1_D17_016	L0-20	Goethite	-	Calcite	Ironstone
RGR1_D17_017	Bulk	Calcite	Asbolane, Fe-vernadite, CFA		Biocalcite-rich Fe-Mn crust, moderately phosphatized

The second has basal reflections at 10 Å and 5 Å and possible reflections overlapping with those of Vernadite at 2.45 Å and 1.42 Å peaks, which are together characteristic of 10 Å phyllomanganates, which can be either disordered 10 Å vernadite, or ordered buserite or asbolane, or a mixture of them [35,40,41,42,43]. The reflections at 10 Å and 5 Å could also belong to the tectomanganate todorokite, which has reflections at 9.7 Å and 4.8 Å. However, heating three samples at 300 °C for 24 hours resulted in the collapse of the 10 Å peak (Supplementary Material Figure S2), which occurs typically to the 10 Å phyllomanganates asbolane and buserite and not to todorokite [35,44,45].

Vernadite is the only Mn phase that composes the non-phosphatized Fe–Mn crusts from RGR, except for samples RGR1_09_002 and RGR1_D10_002 that also contain a 10 Å phyllomanganate as a dominant phase. The phosphatized Fe–Mn crusts are composed of both vernadite and one or more 10 Å phyllomanganates. The XRD reflections of sample RGR1_D05_011 indicate the presence of pyrolusite (Supplementary Material Figure S1), which is a Mn mineral typically formed under hydrothermal conditions [46,47]. Although no iron phases were identified in the Fe–Mn crusts by XRD, chemical composition data indicate 9% Fe on average, suggesting that the X-ray amorphous FeOOH is present as a nanometer-structured material. Lenses of biogenic material between the Fe–Mn columns are composed predominantly of calcite and CFA with minor amounts of quartz. The brown ironstone present in many Fe–Mn crust samples is composed of major goethite, minor to major calcite, and minor to moderate amounts of CFA.

2.4.2 Structure of Fe–Mn Crusts and Associated Minerals

Three-dimensional CT revealed the internal structure of the sample RGR1_D07_002 (Figure 3). In the image, bright shades correspond to molecularly denser material, while dark shades correspond to less-dense material. The non-phosphatized Fe–Mn crust was massive and less bright than the phosphatized Fe–Mn crust, indicating that the phosphatized layers had a higher density. The phosphatized Fe–Mn crust had, in general, a columnar structure with columns 10–20 mm wide and up to 10 mm high. Trapped biogenic particles are present between the columns and correspond dominantly to foraminifera tests, as observed by SEM (Figure 4). Ironstone material was present and was denser than the Fe–Mn crust. Its flame-like structures were observed entering and spreading vertically and horizontally between layers of phosphatized Fe–Mn crust.

SEM micrographs revealed that the texture of the non-phosphatized top crust layer was botryoidal and laminated with <10 μm-thick laminae (Figure 4a). The columns of the

phosphatized crust show arcuate growth laminae or even cauliform/botryoidal texture in which the lamina thickness was highly variable from 10 to 500 µm (Figure 4c). Other areas of the phosphatized crust show a mottled texture (Figure 4b). Regardless of the texture, planktonic foraminifer tests were widespread within the crust laminae. Layers with a massive presence of foraminifera tests and Fe–Mn dendrites occurred in some Fe–Mn crust samples (Figure 4d), indicating periods of extreme pelagic sedimentation during crust formation.

From EDS chemical maps, the impregnation of the Fe–Mn crust matrix by CFA was seen by the Ca and P maps (Figure 4e). In general, CFA is present in Mn-rich layers but is not detected in Fe-rich layers. Mn and Fe distributions mostly overlap but there are Fe-rich, Mn-depleted layers, and vice versa, although the latter is less frequently observed.

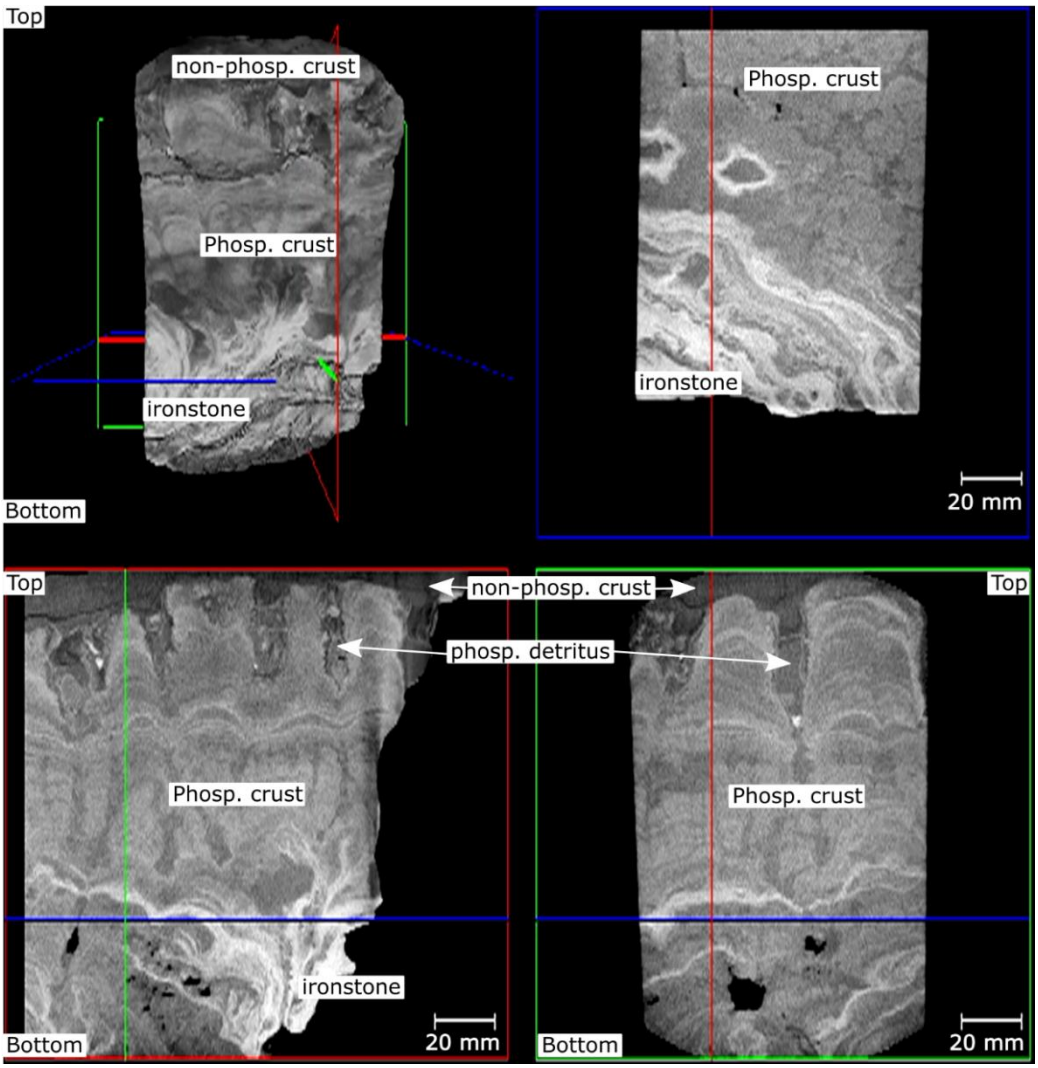

Figure 3. Three-dimension computed tomography image of sample RGR1_D07_002. Non-phosp. crust = non-phosphatized Fe–Mn crust; Phosp. crust = phosphatized Fe–Mn crust; Phosp. Detritus = biogenic particles cemented by CFA between Fe–Mn columns. Red, green, and blue squares and lines correspond to cross-section views of the sample displayed in the top left. Red = x-section; green = y-section; and blue = z-section.

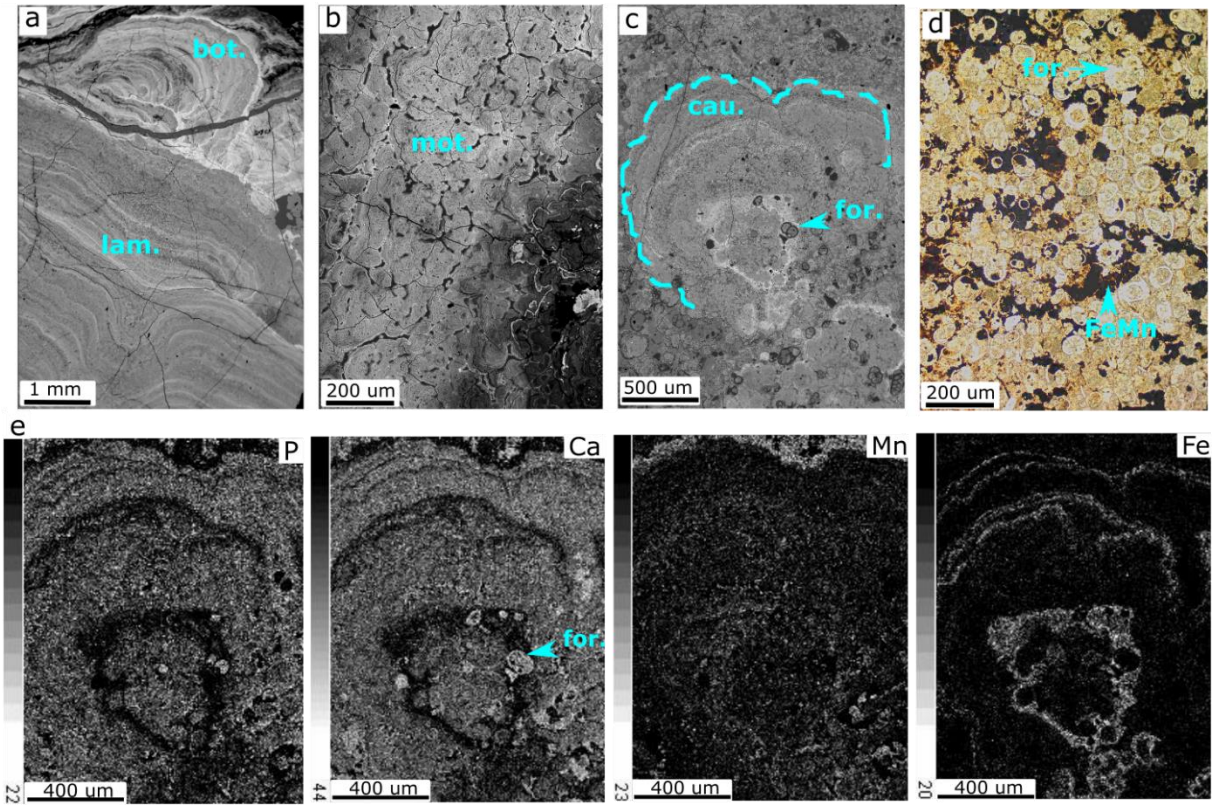

Figure 4. SEM micrographs showing different cross-section textures of Fe–Mn layers observed in crusts from the RGR. (a) Top layer of sample RGR1_D02_030 showing mostly botryoidal texture upper part and laminated texture lower part; (b) top layer of crust RGR1_D09_002 showing micro-botryoids producing a mottled texture; (c) middle layer of RGR1_D09_001 showing an isolated cauliflower structure in a mottled matrix; (d) optical microscope image of a consolidated foraminifera ooze with Fe–Mn oxide dendrites and cement; and (e) EDS mapping of chemical elements P, Ca, Mn, and Fe of the area in "c" showing the influence of phosphatization. Brighter areas indicated higher concentrations of each of the mapped elements. Lam. = laminated; cau. = cauliflower; bot. = botryoidal; for. = foraminifer tests; FeMn = Fe–Mn dendrites.

2.4.3 Chemical Composition

The chemical composition of each sample is provided in Supplementary Material Table S1. The summary statistics of chemical data of Fe–Mn crusts were compiled for four different datasets: Bulk crusts (n = 14), combined bulk crusts and layers (n = 29), non-phosphatized layers (n = 6), and phosphatized layers (n = 16; Supplementary Material Table S2). For the 14 bulk crusts, data for six were calculated by averaging the layer chemical compositions weighed by the thickness of each layer.

2.4.3.1 All Data, Combined Bulk Crusts, and Layers

The chemical composition of bulk Fe–Mn crusts and layers combined (n = 29), expressed as mean wt % (min–max%) was 16.6% Ca (3.93–29.5%), 15.0% Mn (5.06–24.5%), 9.06% Fe (2.21–19.1%), 3.94% P (0.43–7.67%), 2.43% Mg (1.42–5.30%), 1.38% Al (0.60–3.70%), 0.91% F (0.03–1.85%), and 0.61% Si (0.41–1.14%; Supplementary Material Table S2).

An important characteristic of RGR Fe–Mn crusts was the low mean Fe/Mn ratio of 0.56 (0.28–1.10), which contrasts with the mean Fe/Mn ratios for other crust deposits, 0.74–2.67 [5]. The mean Si/Al ratio was 0.54 (0.19–1.22), which is also atypical, showing a strong enrichment of Al relative to Si; these were much lower ratios than typical for volcanic and sedimentary rocks (e.g., 3.37 for basalts; [48]). The mean Ca/P ratio for the crusts was 6.25 (2.97–17.1).

The contents of elements of greatest economic interest were 3073 ppm Co (912–8586 ppm), 400 ppm Cu (117–1557 ppm), 5595 ppm Ni (3000–11015 ppm), 1333 ppm total REY (138–3189 ppm), 731 ppm V (246–1219 ppm), 342 ppm Mo (135–630 ppm), and 117 ppm W (38–305 ppm). The %HREY complement of the total REY (Heavy REY = Eu, Gd, Tb, Dy, Ho, Er, Tm, Yb, Lu, and Y) is on average 33% (11–50%), which is much higher than crusts found elsewhere [10], although total REY contents were low. The highest individual REY concentrations were Ce (34.1–2159, mean 631ppm), Y (40.7–802, mean 222 ppm), La (23.0–371, mean 163 ppm), and Nd (16.1–324, mean 138 ppm). The highest mean platinum group metals (PGM) were 360 ppb Pt (49.3–765 ppb), 34.1 ppb Rh (3.08–94.0 ppb), and 15.8 ppb Ru (1.03–45.7 ppb).

Other elements of high concentrations in the RGR crusts were Li (2.56–330, mean 100 ppm) and especially Te (4.04–106 ppm, mean 38.9 ppm).

The mean bulk Fe–Mn crust element contents had the same trends as for the entire dataset, which shows pervasive phosphatization for most samples, consistent with the mineralogy (Supplementary Material Table S2).

2.4.3.2 Non-Phosphatized Fe–Mn Crust

Seven non-phosphatized Fe–Mn crust layers from RGR were analyzed for chemical composition, but only six of them were used for statistics because sample RGR1_D10_002 was an outlier for some elements, especially Mg, Al, Li, F, and Cu, as described below (Supplementary Material Figure S3). The mean chemical composition of six non-phosphatized Fe–Mn crust layers was higher for Fe, Mn, Na, K, Ti, V, Cl, and Ni compared to the bulk composition, while it was lower for Ca, Si, Al, Mg, S, and F. The non-phosphatized crusts have Fe/Mn ratios between 0.67 and 0.83 (mean 0.75), mean Si/Al is 0.82 (0.45–1.22), and mean Ca/P is 11.3 (7.31–17.12), all of which were higher compared to the bulk crusts.

The contents of elements of greatest economic interest (Co, Cu, Ni, total REY, V, Mo, W, and Nb) were higher in the non-phosphatized crusts than in the bulk crust, except for Cu and W. The %HREY complement of the total REY was on average 13.6% (10.7–15.4%), which was lower than typical crusts from other areas. The mean individual REY concentrations were

higher in non-phosphatized Fe–Mn crusts than in the bulk crusts and phosphatized crust layers. Mean PGM contents were much higher in the non-phosphatized crust than in the bulk crusts, for example, Pt (mean 661 ppb). Other elements of mean high concentrations in the RGR non-phosphatized crusts are Bi (62.7 ppm), Nb (106 ppm), and Te (96.3 ppm); the mean Te content was very high compared to other crusts.

Sample RGR1_D10_002 shows an anomalously high content of Al (3.70%), Mg (5.31%), F (1.16%), Ni (1.10%), Cu (1557 ppm), Li (330 ppm), and Zn (951 ppm) compared to the mean contents for non-phosphatized Fe–Mn crust layers from RGR.

2.4.3.3 Phosphatized Fe–Mn Crusts

The phosphatized Fe–Mn crusts show higher mean contents of Ca, Mg, Si, Al, P, S, F, and CO2 and lower contents of Fe, Mn, Na, K, Ti, and Ni than non-phosphatized crusts (Supplementary Material Table S2). The mean Fe/Mn ratio was 0.52 and varied from 0.28 to 1.10, which was lower than that of the non-phosphatized crusts. The wide variations of Ca, P, and F reflected the degree of phosphatization as was also determined by the mineralogy, ranging from mildly phosphatized to pervasively phosphatized samples. Mean Si/Al was 0.42 (0.22–0.64), which was lower than that of the non-phosphatized crusts and similar to typical volcanic and sedimentary rocks (e.g., 3.37 for basalts; [48]). Ca/P was 4.19 on average (2.97–8.05) and was lower than the mean of 7.31 of non-phosphatized crusts.

The contents of elements that are typical of greatest economic interest were Co 1546 ppm (912–2889 ppm), Cu 362 ppm (118–737 ppm), total REY 793 ppm (138–2396 ppm), V 564 ppm (246–1209 ppm), Mo 241 ppm (135–332 ppm), Nb 22.3 ppm (5.14–56.8 ppm), Te 16.3 ppm (4.04–37.1 ppm), and W 117 ppm (38.2–305 ppm). Co, V, Mo, Nb, Te, and total REY contents in the phosphatized crusts were much lower than in non-phosphatized crusts, whereas W was relatively more enriched.

Other elements in high concentration in the phosphatized RGR crusts were Li (30.9–217, mean 127 ppm), which was much more enriched compared to the non-phosphatized crust, and the %HREY (29.1–50.2%, mean 40.8%), which was also very high compared to the non-phosphatized crusts and similar to the range determined for marine phosphorites by [49]. The highest individual REY concentrations were Ce (34.1–426, mean 195 ppm), Y (40.7–802, mean 237 ppm), La (23.0–370, mean 120 ppm), and Nd (16.1–324, mean 99.8 ppm). Except Y, mean individual REY as well as Pt, Rh, and Ru contents in the phosphatized crusts were much lower than in non-phosphatized crusts.

2.4.4 Correlation between Elements

2.4.4.1 Non-Phosphatized Fe–Mn Crusts

Correlation coefficients for chemical elements in the non-phosphatized Fe–Mn crusts from RGR (n = 7; Supplementary Material Table S3) show no correlation between Fe and Mn at the 95% confidence level (CL), suggesting that the two phases they represent were independent variables. Significant positive correlations at the 99% CL exist between Fe and Na, K, Ba, Bi, Pb, Sb, Sr, Te, U, and all the REY; positive correlations at the 95% CL also existed between Fe and As, Cl, and Zr. Significant negative correlations at the 99% CL occurred between Fe and Al, Mg, Cd, Cu, F, Li, Ni, Zn, and the HREY. In the non-phosphatized crusts, Mn had no significant positive correlation above the 95% CL. Significant negative correlations ($R < -0.85$) existed between Mn and Si (99% CL), Ca (99% CL), and CO2 (95% CL). Silicon was correlated with Ca and CO2 (both 95% CL) suggesting a biogenic phase(s) composed of calcium carbonate and silica. Al, Mg, Cd, Cu, Li, Ni, and Zn were correlated with each other at the 99% CL and each of them was negatively correlated with Fe and show no correlation at the 95% CL with Mn, Ca, CO2, Si, or P. Thus, Al, Mg, Cd, Cu, Li, Ni, and Zn were not strongly or solely associated with any mineral group of phase, suggesting the existence of a residual biogenic phase. Pt was significantly correlated with Fe, Ti, and P (at the 99% CL), while Rh was correlated with Bi, Cd, Pb (99% CL), and Nb (95% CL). Ru was correlated with Bi and some HREY (Y, Er, Ho, Tm, Yb, and Lu) at the 99% CL, and to Ti at the 95% CL.

2.4.4.2 Phosphatized Fe–Mn Crusts

The phosphatized Fe–Mn crust layers show a correlation between Fe and Mn at the 99% CL (Supplementary Material Table S4). Iron correlates positively with As, Ba, Co, Cr, Sb, and V at the 99% CL, and negatively with Ca, P, S, and F. Manganese correlates with V, Be, Co, Ni Tl, and Zn at the 99% CL, and at the 95% CL with Mg, As, Ba, Cl, Mo, Pb, and Sb. Negative correlations existed between Mn and Ca and CO2 (99% CL) and between Mn and P and S (95% CL). The correlation between Si and CO2 was significant at the 99% CL but Si and Ca did not correlate at the 95% CL, and Si had a negative correlation with P and F (95% CL), indicating that Si was not related to the CFA phase. Si shows a correlation with elements Al, Ti, Cu, Mo, and Nb at the 95% CL. Positive correlations between P and Ca, F, S, Sr, U, and the HREY occurred at the 99% CL, reflecting the CFA phase.

2.4.5 Factor Analysis

Q-mode factor analysis of the chemical composition of non-phosphatized and phosphatized Fe–Mn crusts from RGR resulted in a different number of factors that were interpreted to represent different mineral phases and their hosted elements (Table 3). Three factors explained 93.5% of the variance of the chemical data of the non-phosphatized crust. Factor 1 was interpreted to represent a mixture of Fe and Mn (oxyhydr)oxide phases (43.1% of variance) including elements typically associated to the Fe-oxyhydroxide phase (Nb, Zr, As, Pb, Ti, and Bi) and to Mn-oxide (Ba), and those partitioned between both phases (Te and V; [1]). Factor 2 represents a residual biogenic phase (17.7% of the variance) and includes elements with a nutrient-type distribution in ocean water (P, Ni, Cu, Zn, and Cd), associated with organic matter (Ca, Mg, Fe, and F), or are biointermediate elements (Mo; [50]). Factor 3 (33.2% of the variance) represents a mixture of biocarbonates (Rb, Th, Ba, and Sr) and biosilica (Si).

For the phosphatized crusts, four factors explained 93.2% of the variance of the chemical composition and they correspond to (Factor 1) a residual biogenic phase; (Factor 2) the CFA phase (Ca, P, F, Sr, and HREY); (Factor 3) Fe and Mn phases; and (Factor 4) a biocarbonate phase that is most likely calcite based on XRD and perhaps biosilica.

Table 3. Q-mode rotated factor scores for the chemical composition of non-phosphatized and phosphatized crusts from RGR (bold are elements that indicate the major phase(s)).

Non-phosphatized crust						Phosphatized Fe-Mn crust							
Factor 1		**Factor 2**		**Factor 3**		**Factor 1**		**Factor 2**		**Factor 3**		**Factor 4**	
43.10%		*17.20%*		*33.20%*		*41.3%*		*33.90%*		*12.30%*		*5.00%*	
Nb	0.219	**F**	0.31	**Si**	0.327	Mo	0.287	**P**	0.402	Cr	0.377	Rb	0.401
Fe	0.187	**P**	0.272	**CO**	0.298	Al	0.272	**F**	0.385	Ba	0.326	**CO**	0.384
Mn	0.295	*Ni*	0.271	**Ca**	0.291	Nb	0.238	Na	0.353	Sb	0.323	**Ca**	0.329
Zr	0.272	*Mg*	0.27	Th	0.261	*Mg*	0.233	S	0.345	V	0.317	K	0.239
U	0.271	*Li*	0.27	Rb	0.241	Zr	0.228	**Ca**	0.334	**Mn**	0.311	**Si**	0.224
As	0.245	*W*	0.27	Sc	0.224	Ti	0.222	Sr	0.293	**Fe**	0.297	Cr	0.194
Pb	0.218	*Al*	0.269	Cr	0.215	Li	0.219	U	0.273	As	0.268	Hf	0.153
Ti	0.216	*Cu*	0.268	LR	0.2	*Cu*	0.212	Zn	0.174	Zn	0.254	Cu	0.145
V	0.215	*Zn*	0.266	RE	0.196	*Ni*	0.206	HR	0.145	Co	0.222		
Te	0.203	Rb	0.263	Co	0.186	LR	0.205	Sc	0.133	Tl	0.166		
Bi	0.203	*Cd*	0.262	Sb	0.181	RE	0.205			K	0.162		
Sn	0.199	Mo	0.24	Tl	0.168	Te	0.199			Be	0.157		
HR	0.198	**CO**	0.158	Be	0.165	Th	0.194						
K	0.196	**Ca**	0.143	Ba	0.158	W	0.186						
Ba	0.193	Si	0.141	Sr	0.156	Pb	0.172						
Sr	0.192			W	0.144	Rb	0.162						
Na	0.173			K	0.142	Bi	0.161					Ni	-0.135
P	0.155			Cl	0.141	Tl	0.154					RE	-0.176
Sb	0.154			Na	0.139	Be	0.146					LR	-0.176
				Fe	0.133	HR	0.143					U	-0.18
Ca	-0.113					*Cd*	0.134					Zr	-0.192
CO	-0.132			Ni	-0.137	Hf	0.132					HR	-0.208

Si	-0.132	**Mn**	-0.137	Si	0.131	Zn	-0.215

CO = CO_2
LR = total light rare earth elements (%)
HR = total heavy rare Earth elements (%)

2.4.6 Sr Isotopic Composition and Age Dates of Diagenetic CFA

The CFA from phosphatized Fe–Mn crusts yielded 87Sr/86Sr ratios between 0.708408 and 0.708957, which, when compared to the Cenozoic 87Sr/86Sr seawater curve calibrated ages, corresponds to ages that vary from 20.2 Ma to 6.8 Ma (Supplementary Material Table S5). Phosphatization affected nearly the entire thickness of the Fe–Mn crusts collected from the RGR plateau and phosphatization of the crusts ended about 6.8 Ma. Most of the ages fell into two groups, i.e. two main episodes of phosphatization: one between 20.2 and 16.0 Ma and one between 9.9 and 6.8 Ma, with one sample at 12 Ma. In crusts RGR1_D07_002 and RGR1_D11_003, different ages were observed for different phosphatized stratigraphic layers, resulting in more recently formed layers yielding younger ages of phosphatization. For crust RGR1_D07_002, five different layers yielded ages that could be grouped into three main episodes of phosphatization: about 20.2–18.5 Myr, 15.6 Myr, and about 9.9–9.6 Myr (Figure 5). For crust RGR1_D11_003, two episodes were recognized, at 17.5 Ma and 12.5 Ma. Each age is a mean age for the stratigraphic interval sampled.

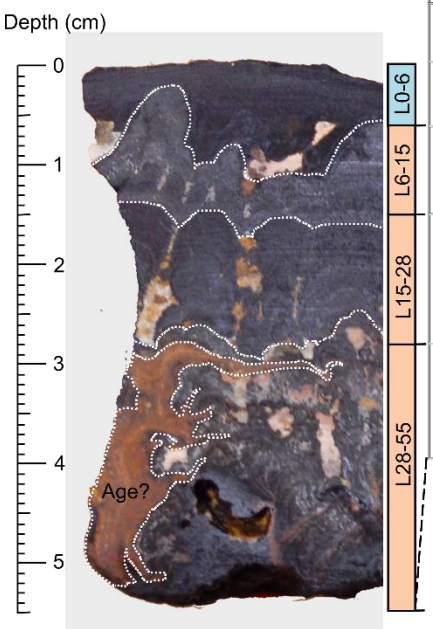

Estimated ages (Ma)						
Co-chronometer*	U-Th**			Age of phosphat. (Ma)	Major mineralogy	Texture
5.2	12.0	6.0	2.4	-	Vernadite	Massive. Little accumulation of foram. tests.
13.0	30.0	15.0	6.0	9.6-9.9	Vernadite, 10Å phyllomanganate, and CFA	Botryoidal to columnar. High accumulation of foram. tests.
24.3	56.0	28.0	11.2	15.8-18.5	Vernadite, 10Å phyllomanganate, calcite, and CFA	Botryoidal to columnar. High accumulation of foram. tests.
47.8	110.0	55.0	22.0	20.2	Vernadite, 10Å phyllomanganate, and CFA	Mottled and chaotic. High accumulation of foram. tests.

*Growth rate of 1.15 mm/Myr estimated using the equation of Manheim and Lane-Bostwick (1989)
**The three columns correspond to growth rates of 0.5, 1 and 2.5 mm/Myr, respectively.

Second generation of Fe-Mn crust
First generation of Fe-Mn crust

Figure 5. Stratigraphic sequence of crust RGR1_D07_002 showing estimated ages of initiation, age of phosphatization, major mineralogy, and texture of Fe–Mn layers. Layer L0-6 is the non-phosphatized second generation of the Fe–Mn crust, while layers L6-15, L15-28, and L28-55 are the phosphatized first generation of

the Fe–Mn crust. Possible ages of initiation of growth on Fe–Mn layers are based on different growth rates determined by using the Co-chronometer Equation of [29] and U-Th isotopes.

2.4.7 Estimated Co-Chronometer Growth Rates and Ages of Initiation

Estimated Co-chronometer growth rates and ages of initiation of crust growth derived from the Equations of [29] and [30] for the non-phosphatized layers differed significantly (Table 4). Growth rates derived from the first Equation were between 0.57 and 1.39 mm/Myr, while the second equation resulted in much higher growth rates between 2.07 and 4.31 mm/Myr. These rates using the two different Equations result in the oldest ages of initiation of the thickest non-phosphatized crust (RGR1_02_039) of 23.15 Ma and 6.39 Ma, respectively. The youngest ages for the initiation of crust growth were for sample RGR1_D10_003 L0-2, which were 1.44 and 0.46 Ma respectively for each equation. Growth rates resulting from the [29] Equation also differed between non-phosphatized and phosphatized layers, with phosphatized layers having higher rates, between 1.48 and 4.38 mm/Myr.

The only method that consistently yielded estimated ages of initiation of growth for phosphatized crusts layers that are older than the age of phosphatization of those layers was the extrapolation of the growth rate of a non-phosphatized layer derived from the Equation of [29]. The only exception is sample RGR1_D10_003 L5-20, which contains a layer of ironstone material of unknown age in between the phosphatized and non-phosphatized crust generations, which means that an unknown time gap must be accounted for and that the age of 12.3 Ma will be older than indicated. Based on these data, the oldest estimated age of initiation of crust growth was about 47.8 Ma for the thickest crust sample RGR1_D07_002, which included the estimate for the phosphatized portion (Figure 5).

Table 4. Estimated growth rates (mm/Myr) and ages of initiation (Ma) of Fe–Mn crust formation from Rio Grande Rise based on the Co-chronometer Equations of [29] and [30]; samples shaded in brown correspond to phosphatized layers.

		Manheim and Lane-Bostwick[1]		Manheim and Lane-Bostwick[2]		Halbach and Puteanus[2]		Age of phosphatization
Sample ID	mm	GR	Age	GR	Age	GR	Age	
RGR1_D02_030_L0-13	13	0.88	14.7	0.88	14.7	2.89	4.49	--
RGR1_D02_030_L13-20	7	2.7	17.29	0.88	22.62	2.89	6.91	16.2
RGR1_D02_039_L0-10	10	0.57	17.41	0.57	17.41	2.07	4.83	--
RGR1_D02_039_L10-15	5	0.87	23.15	0.87	23.15	3.2	6.39	--
RGR1_D05_011_L2-10	8	4.38	1.83	--	--	--	--	--
RGR1_D05_016_L0-19	19	2.83	6.72	--	--	--	--	9.9
RGR1_D06_003_B0-8	8	3.62	2.21	--	--	--	--	--
RGR1_D07_002_L0-6	6	1.15	5.23	1.15	5.23	3.96	1.52	--

RGR1_D07_002_L6-18	12	3.13	9.06	1.15	15.68	3.96	4.55	9.9
RGR1_D07_002_L18-33	15	3.65	13.17	1.15	28.75	3.96	8.34	15.6-18.5
RGR1_D07_002_L33-55	22	4.04	18.61	1.15	47.91	3.96	13.9	20.2
RGR1_D07_003_L0-5	5	0.92	5.42	0.92	5.42	2.9	1.72	
RGR1_D07_003_L5-20	15	2.72	10.95	0.92	21.69	2.9	6.89	16
RGR1_D09_001_L0-1	1	2.16	0.46	2.16	--	--	--	--
RGR1_D09_001_L1-13	12	2.3	5.67	2.16	--	--	--	16.1
RGR1_D09_001_L14-28	14	3.01	10.33	2.16	--	--	--	16.8
RGR1_D09_002_B0-10	10	1.86	5.37	--	--	--	--	--
RGR1_D10_002_L0-2	2	1.2	1.66	--	--	--	--	--
RGR1_D10_003-L0-2	2	1.39	1.44	1.39	1.44	4.31	0.46	--
RGR1_D10_003-L5-20	15	2.74	6.93	1.39	12.26	4.31	3.95	20
RGR1_D11_003-B0-20	20	1.48	13.48	--	--	--	--	--
RGR1_D15_017-B0-13	13	2.19	5.95	--	--	--	--	8.5
RGR1_D17_017-B0-14	14	2.26	6.2	--	--	--	--	6.8

[1]Growth rates calculated for the non-phosphatized and phosphatized layers.

[2]Growth rates calculated for the non-phosphatized layer were extrapolated for the phosphatized layers of the same crust sample.

2.4.8 Growth Rate and Age of Initiation by U and Th Isotopes

The accretion rate of hydrogenetic Fe–Mn crusts can be estimated using U–Th geochronology following analytical and modeling procedures outlined by [51]. During crust formation, oxides incorporate an excess abundance of ^{230}Th derived from the ^{234}U decay dissolved in ocean water. This initial excess ^{230}Th decays with time to a ^{230}Th abundance that is controlled by the U content of the oxide. To simplify the model estimation of accretion rates, [51] calculated the "excess" ^{230}Th from accretion alone, not sourced from in situ ^{234}U decay and defined as $^{230}Th_{excess}$ (Supplementary Material Table S6). As the ferromanganese crusts grow, this $^{230}Th_{excess}$ decays to zero. Figure 6 presents the $^{230}Th_{excess}$ relative to ^{232}Th (which is stable on the timescales considered here) as a function of depth within-sample RGR1_D07_002. As predicted, the ($^{230}Th_{excess}/^{232}Th$) decreases with depth reflecting decay of the initial excess ^{230}Th. Note that brackets denote activity ratios. Estimates of the rate of crust accretion can be made using Equation (1) from [51]. The observed ($^{230}Th_{excess}/^{232}Th$) ratios from sample RGR1_D07_002 were consistent with modeled accretion rates of 1 mm/Myr and lie between a range of 0.5–2.5 mm/Myr (Figure 6), which is consistent with the growth rate derived from the Co-chronometer using the equation of Manheim and Lane-Bostwick (1988) and in good agreement with the 0.5–3.0 mm/Myr rates of non-phosphatized Fe–Mn crusts from the São Paulo Plateau determined by the $^{187}Os/^{188}Os$ method [12]. It is important to use more than one method for determining crust growth rates and ages more accurately, as described by [52].

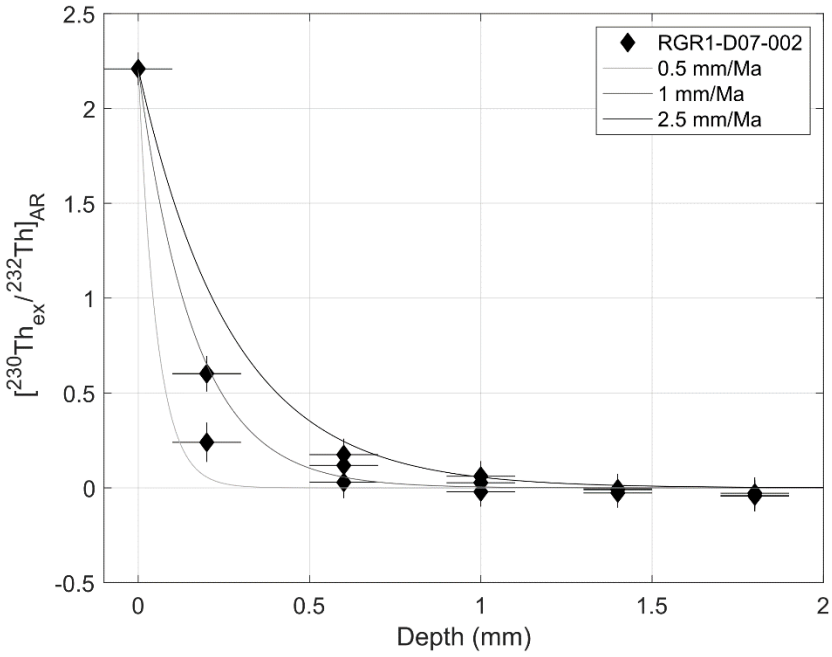

Figure 6. Observed $^{230}Th_{excess}/^{232}Th$ ratios with depth in sample RGR1_D07_002 and modeled accretion rates of 0.5, 1, and 2.5 mm/Myr.

If the faster estimated growth rate of 2.5 mm/Myr was extrapolated to the rest of the sample RGR1_D07_002, some phosphatized Fe–Mn layers yield ages of initiation younger than the age of phosphatization (Figure 5), which is not possible. On the other hand, if the slower estimated growth rate of 0.5 mm/Myr was used, the age of crust initiation (110 Ma) was older than the age of RGR itself, which is also unrealistic. However, when the estimated growth rate of 1 mm/Myr was extrapolated to the thickest (9 mm) non-phosphatized layer of RGR1_D07_002, the resulting estimated age of 9 Ma was consistent with the age of phosphatization of the underlying layer (9.6 Ma), and the entire sample would have an estimated age of about 55 Ma for initiation of crust growth, roughly comparable with the estimated Co-chronometer age of 48 Ma.

2.5 Discussion

2.5.1 Two Generations of Fe–Mn Crusts on Rio Grande Rise

Apart from the Fe–Mn crust samples from the central valley slope (dredge D02), typical structures, textures, and mineralogy of Fe–Mn crusts from RGR revealed two different crust generations (Figure 5). The first generation comprised of the major portion of the crusts and was capped by a thin 1–10 mm-thick second generation. The first generation was marked by CFA impregnation and accumulation of biogenic material, while the second crust generation grew after the phosphatization events and when biogenic particle accumulation decreased. In some samples, the first generation was the only one present and the lack of the second

generation suggests that it was eroded by the strong currents that impacted the RGR plateau. Eroded botryoids of the top surface of the second generation in some samples corroborated this erosional process. Bottom currents of more than 0.2 m/s may be capable of eroding Fe–Mn crust surfaces [53]. The prevalence of columnar and mottled texture is related to a higher amount of biogenic particle input that constrains or interrupts the formation of laminations [54].

Although thick Fe–Mn crusts from many northwest and central Pacific seamounts also present two crust generations with an older phosphatized crust and a younger non-phosphatized crust [54,55,56,57], the phosphatization of the first crust generation of RGR is more pervasive and intense. The phosphatized older crust generations from the Pacific seamounts have P contents of up to 5.5% [54,58,59]. The phosphatized crust generation from RGR has a mean P content of 5.3% and ranges up to 7.7%. The CFA content of the first generation from Pacific crusts may be up to 30% but generally, makes-up less than 10% of the crystalline phases [54], while the RGR phosphatized crust generation contains generally 25% CFA but, is as high as 50% in sample RGR1_D11_003.

In the Pacific, the influence of phosphatization was found to be strong above 2500 m water depth and decreases with depth as only minor phosphatization is found in crusts from 2800 to 4000 m depth [55]. The crusts in RGR are at 600–800 m water depths today and may have been even shallower at the time the first generation was impregnated with CFA before thermal subsidence of RGR and the oceanic crust [17,60]. The very shallow water depth may be an important key in the formation of strongly phosphatized crusts on RGR and elsewhere. Shallower crusts may be more phosphatized because they experience higher phosphate concentrations during phosphatization than deeper crusts, and they may contain higher amounts of carbonate debris that can be easily replaced by CFA since they are closer to primary productivity and associated biogenic particle flux. Similar mixed Fe–Mn phosphorite pavements occur along the Blake Plateau in the northwest Atlantic Ocean [61] at comparable depths (500–800 m).

The fact that the crust samples from dredge D02 from the slope at about 825 m are not as phosphatized as the ones from the top of the plateau at 650–750 m indicates that local oceanographic variables, for example, the water depth and circulation, play a role in controlling the degree of phosphatization. The mineralogy of crust sample RGR1_D02_039 (15 mm-thick) from the slope shows that CFA was absent and P content was not higher than 0.48%.

The formation of 10 Å phyllomanganate in a Fe–Mn crust may occur due to the less-oxidizing conditions associated with phosphatization [56]. All the phosphatized generations of

the crusts from the RGR plateau had a 10 Å phyllomanganate phase, while only two out of 10 non-phosphatized crusts layers contained this phase.

5.2.2 Chemical Composition of RGR Crusts Compared to Other Crusts

5.2.2.1 Recent Hydrogenetic Crust Formation

The recent non-phosphatized Fe–Mn crusts (<10 mm-thick) from the summit of RGR are typical hydrogenetic crusts and differ significantly from the bulk crusts. They mostly resemble crusts from the PCZ concerning Fe, Mn, Co, and total REY contents (Figure 7; Supplementary Material Table S7). However, they are remarkably enriched in Mg, Ca, S, As, Bi, Nb, Ni, Pb, Te, V, Ce, Rh, Ru, and Pt compared in general to Fe–Mn crusts from the Atlantic, Indian, and South Pacific Oceans, the PCZ, and the California margin. Nevertheless, the RGR crusts are the most depleted in Si, K, and Cu. The Ca and Mg enrichments are due to the high flux of planktonic foraminifera and nannoplankton tests. All of the elements mentioned can be related to biological productivity, through flux and dissolution of fine-grained carbonate and silica tests and frustules and release of sorbed metals, organic matter flux, and organic matter sorption of metals and release during oxidation. For example, Nb and V occur in foraminifera tests [62] for which the most delicate tests and fragments, as well as aragonite tests (i.e., Pteropods), would dissolve even at the relatively shallow-water depths of crusts in this study.

Figure 7. Comparison between the chemical composition of bulk, non-phosphatized Fe–Mn crusts, and phosphatized crusts from the RGR summit and Fe–Mn deposits formed elsewhere, compiled by [10] from [1]. Peru Basin nodules correspond to the diagenetic end-member.

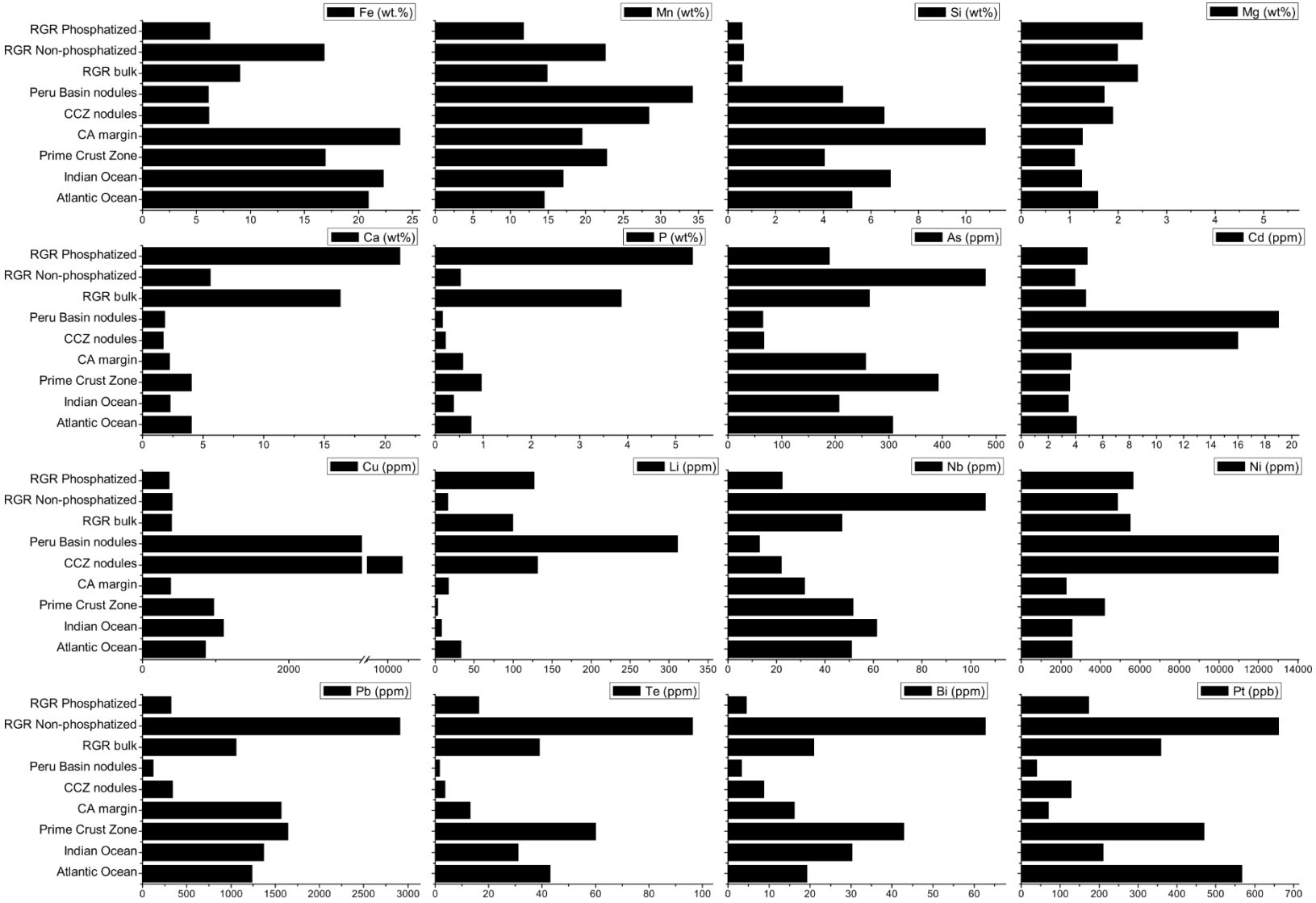

Many of the metals above have a nutrient-like distribution and are involved in biogeochemical processes in the water column. Ni is a nutrient-type metal that regenerates more rapidly than Si and Cu in the water column and, therefore, is made available in its dissolved form at shallower depth compared to the other two. This is especially evident by the increasing Cu content of crusts with an increasing water depth of crust formation [63]. Arsenic is another metal that has a nutrient-like vertical distribution in the ocean and its species and distribution are strongly controlled by biological processes in the water column [64]. Arsenate (As5+) is taken up by phytoplankton at the surface to produce organic compounds and is regenerated at the base of the euphotic zone, having a low concentration in surface waters and maximum concentration in the subsurface with a peak at about 1000 m water depth [65]. Rhodium has a nutrient-type distribution and is enriched in pelagic sediments and marine phosphorites [66]. Dissolved V has a surface minimum concentration, associated with binding to organic particulate matter, which is rapidly remineralized, like phosphate [67]. In contrast, Si, Cr, and Cu are regenerated in deeper waters [68] as also are Zr and Hf [69]. Thus, the water depth of the RGR summit relative to the depth of regeneration of sinking particles seems to play a key role in the chemical composition of the crusts.

Other metals most enriched in the recent non-phosphatized crust had a scavenging-type behavior in the ocean-water column, i.e., their concentration was high at the surface and decreased with water depth. Their distribution was most similar to that of Mn. Ce, Bi, Pb, and Te have a scavenging-type distribution in the water column [70,71,72,73], and are regenerated at rather shallow depths 400 m. The concentration of Te decreases with depth in the Angola Basin (South Atlantic; [71]). These scavenged metals should be available for sorption on crusts at the water depths of the RGR crusts.

The vertical distribution of Pt contrasts in different oceans [74,75], however many stations across the southwestern Atlantic Ocean showed that a peak in Pt concentration at 800 m water depth occurs within the Antarctic Intermediate Water close to the location of RGR [76]. The content of most of the PGM in Fe–Mn crusts is inversely correlated with water depth [77], which may explain the high contents of Pt as well as Rh and Ru in RGR summit non-phosphatized crusts. Generally, Pt, Rh, and Ru are derived from the seawater, although Ru can also derive from detrital material [54].

Past studies on northeast Atlantic and Arctic Ocean Fe–Mn crusts found a strong terrigenous component (i.e., enrichments in Fe, Pb, Al, and Si and a mean Fe/Mn ratio of >1.30) in those crusts compared to Pacific Ocean crusts due to input by aeolian and fluvial transport [9,11,78,79]. In contrast, the lowest Si content and Si/Al ratios occur in RGR summit crusts

compared to crusts from elsewhere (Figure 7), indicating only minor terrigenous input. In that regard, the hydrogenetic crusts from the RGR summit are more similar to open-ocean Pacific seamount crusts [5].

In summary, dissolved Mn contents are controlled mainly by oxygen concentration in ocean water and are higher in crusts from shallower less-oxygenated waters [54,63,80]. The crusts from the RGR summit are a good example of shallow-water type, Mn-rich crusts from the Atlantic Ocean. An important source of metals to the younger generation, non-phosphatized crusts is related to biological productivity. However, more than that, the rate of regeneration of metals carried by biogenic particles (both labile and refractory) plays a key role in the RGR crust chemical composition. Ultimately, the rate of remineralization dictates the availability of the dissolved form of metals related to biological productivity and the degradation of those products, which are then available for sorption by crust oxide minerals. Secondly, the depth of RGR crusts also enables them to receive dissolved metals from aeolian sources, which because of scavenging in surface waters would not be as available to crusts formed in deeper waters. Therefore, younger generation RGR crust formation is a result of an optimal depth of availability of metals in ocean water from scavenging distribution (Bi, Pb, and Te) and nutrient-type distribution with rapid regeneration (As, Ni, and V).

2.5.2.2 Influence of Phosphatization on the Chemical Composition of RGR Crusts

Several processes are known to have altered the mineralogy and chemical composition of hydrogenetic Fe–Mn crusts in the Pacific and Indian Oceans during phosphatization. For example, the replacement of carbonate, replacement of Fe oxyhydroxides preferentially over Mn oxides, alteration of the Mn oxide, and precipitation of CFA in pore spaces have been observed [55,81,82]. Here, we show that these secondary processes also acted in changing the chemical composition and mineralogy of originally hydrogenetic RGR summit Fe–Mn crusts.

The decrease of the Fe/Mn ratio from non-phosphatized crusts (mean 0.7) to phosphatized crusts (mean 0.5) for RGR summit crusts was consistent with the preferential replacement of the Fe oxyhydroxides preferentially over Mn oxides during phosphatization. The Si/Al ratios decreased from 0.7 to 0.4, which might have resulted from the preferential replacement of Si-rich phases over Al-rich phases, Si adsorbed onto Fe oxyhydroxides, or bio-silica [6].

The phosphatized generation of RGR crusts had lower contents of most elements compared to the non-phosphatized generation (Figure 8). All of these metals are hosted by the

Fe oxyhydroxide or both the Fe and Mn phases (e.g., Te) in the non-phosphatized crust and their decrease in the phosphatized crusts are consistent with a loss of part of the Fe phase [55].

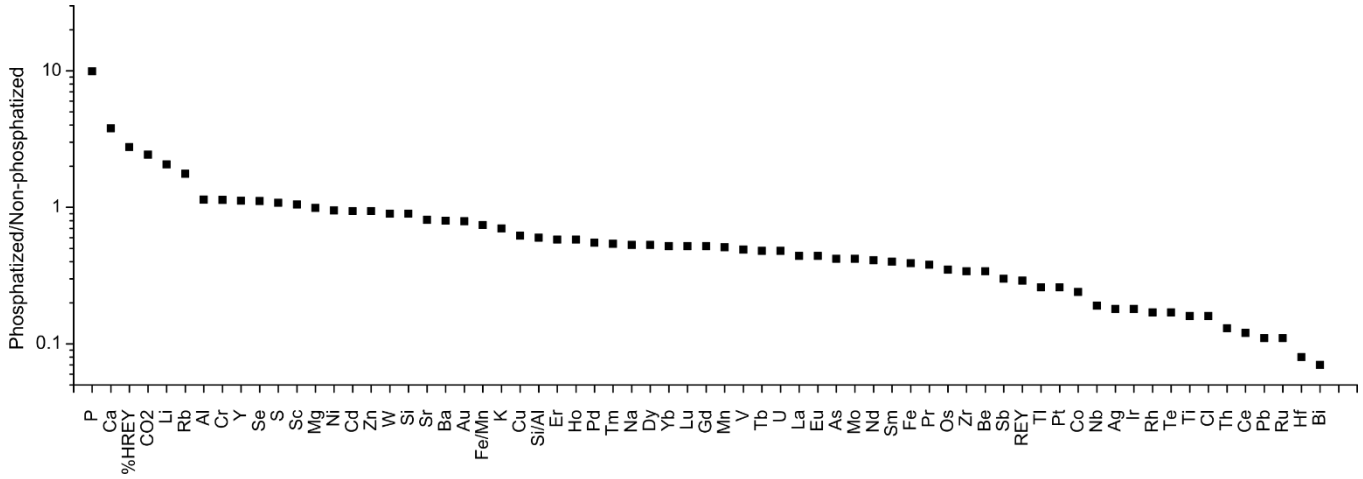

Figure 8. Element enrichment for mean phosphatized (n = 16) and mean non-phosphatized (n = 6) generations of crusts from the Rio Grande Rise. Elements above the line are enriched in the phosphatized generation, while elements below the line are enriched in the non-phosphatized generation.

Elements not associated with the CFA should have contents reduced because of dilution by diagenetic CFA formation. However, the enrichment in Ni and Zn, elements that are typically associated with the Mn phase and not the CFA, means that these elements increased over the dilution process, although the content of their predominant host, Mn, did not. This may be due to the diagenetic alteration of the vernadite to the 10 Å phyllomanganate during the formation of CFA under suboxic conditions, promoting the acquisition of more Ni^{2+} and Zn^{2+} [6,83]. Ni, together with Cu and Zn, become enriched in crusts that have been phosphatized [6,11] because these cations are accommodated in the structure of 10 Å manganates [84]. Cu and Zn do not accompany the remarkable enrichment of Ni in crusts from RGR, and their content is equal to or even lower than in crusts from elsewhere. This difference may be explained by the different rates of remineralization with water depth for Ni, Cu, and Zn, as discussed previously. The Ni vertical distribution most resembles that of the nutrients NO_3 and PO_4, which regenerate more rapidly, while the vertical distribution of Zn and Cu most resembles that of Si, which regenerates more slowly in the water column [85,86,87].

The same similarity with NO_3 and PO_4 distribution occurs with Cd [86,88,89]. Cd and its isotopes are a proxy for biological productivity [90,91]. The enrichment in Cd contents in the phosphatized RGR crusts suggests a high input of biological material. Additionally, Cd enrichment in phosphatized crusts from the Ninetyeast Ridge in the Indian Ocean was suggested to reflect the replacement of Cd_{2+} for Ca_{2+} in the CFA due to their similar ionic radius [49].

Aluminum enrichment is unexpected since it usually shows a strong depletion in phosphatized crusts [55]. The aluminum content of seamount phosphorites increases with

increasing biogenic silica [49] since Al is a component of silica frustules of diatoms in variable amounts [92]. In this case, we would expect an enrichment of Si in the phosphatized crust of equal magnitude as Al, which is not found because the Si phases likely underwent replacement preferentially over Al phases during phosphatization [55]. Besides, there is only a weak correlation between Al and Si. A high Al content decoupled from terrigenous particle flux can be associated with the removal of Al from ocean water by settling biogenic particles [93]. The correlations between Al and elements that have nutrient-type distribution in the water column, Cd, Cu, and Ni support this hypothesis.

As for Li, its enrichment of manganese nodules has been associated with a source from diagenetic reactions in the sediment and the presence of 10 Å manganates as a host for the Li (e.g., [1,94]). The 10 Å manganates can incorporate high amounts of Li into their structure, while δ-MnO2 can only adsorb small amounts of Li. Further, it has been suggested that Li can be inherited from planktonic tests and adsorbed onto CFA [49]. In that regard, the high Li enrichment in the phosphatized RGR crusts can also be due to the high accumulation of foraminifera tests during crust growth and incorporation of Li from diagenetic reactions during phosphatization, which occurs in a suboxic environment.

Sulfate (SO_4) substitutes for phosphate (PO_4) in the apatite structure [95,96], which is consistent with the correlation between S and P at the 99% CL (Supplementary Material Table S4). Substitution might also be the reason for HREY enrichments. Yttrium (Y^{3+}) and the REE^{3+} replace Ca^{2+} in the CFA structure [49,96], which is consistent with the positive correlation between the REY (excepting Ce) and P, especially for Y. [49] found that the %HREY of the total REY complement from seamount phosphorites is higher than in associated Fe–Mn crusts, due to different mechanisms of REE incorporation. While REE are sorbed by the Fe–Mn oxyhydroxides, they predominantly replace Ca in the CFA structure, and this process is favored for the HREE [49,96]. Additionally, a strong complexation exists between REE and carbonate in ocean water, which increases with the increasing atomic number of the REE and which can be inherited by the CFA. However, the idea that phosphatized crusts are more enriched in REY compared to non-phosphatized crusts because of the presence of CFA [49,54] is not true for phosphatized crusts from the RGR. This might be due to the shallower water depth of crust formation at RGR since dissolved REY concentrations in ocean water tend to increase with increasing water depth [97,98]. Besides, the lower REY can be due to younger ages of the RGR CFA, since aging phosphorites allow for enrichment in REY over time [49].

In summary, the chemical composition of Fe–Mn crusts from the summit of RGR was affected during phosphatization due to the precipitation of CFA, loss of part of the Fe phase,

alteration of part of the Mn phase, and incorporation of metals from biological productivity, with some of them probably hosted by a diagenetic 10 Å phyllomanganate.

2.5.2.3 Bulk Crusts

As a result of the remarkable degree of phosphatization, bulk Fe–Mn crusts from the summit of RGR have quite different chemical composition compared to crusts from elsewhere. They contain the lowest Fe contents and Fe/Mn ratios and the highest Ca and P contents (Figure 7; Supplementary Material Table S7). Ca and P are enriched in RGR crusts four and five times, respectively, over crusts from the Atlantic Ocean, four times compared to PCZ crusts, and seven times over California margin crusts. RGR crusts are the most enriched in Ni and Li, in which the concentrations are just somewhat less than that of mixed-type CCZ manganese nodules and diagenetic end-members Peru Basin manganese nodules (Figure 7). Bulk RGR crusts are remarkably enriched in Li, 36 times over PCZ crusts, six times over crusts from the California margin, and three times over Atlantic Ocean crusts (Figure 7; Supplementary Material Figure S4). HREE are most enriched in RGR Fe–Mn crusts (average 50 ppm; Figure 7). The %HREY complement of the total REY complement was three times higher in the RGR crusts compared to PCZ crusts and four times over California margin and Atlantic Ocean crusts. Total REY and individual REE concentrations were depleted in crusts from RGR compared to crusts from elsewhere, except Y.

RGR summit bulk crust Ca and P contents of 16.6% and 3.94% respectively are higher than those of phosphatized crusts from other regions, for example, the Ninetyeast Ridge in the Indian Ocean, 3.38% Ca and 0.82% P [6] and the Tricorn Seamount, Pacific Ocean, 11.0% Ca and 3.7% P [8], which also have an older phosphatized crust generation. Those differences are likely in part because crusts from RGR formed at shallower water depths (700–800 m) compared to crusts from Tricorn seamount and Ninetyeast Ridge, 1100 and 2000 m, respectively. There are also likely differences in primary productivity in these three areas.

In general, the chemical composition of bulk RGR crusts was controlled by high biological productivity for most of the history of crust growth, and also to the growth of RGR crusts at relatively shallow water depths so that nutrient-type elements with rapid regeneration were readily available. Additionally, the strong phosphatization and formation of diagenetic CFA under suboxic conditions in the crusts were a major control of RGR crust composition as there has been a loss of most of the non-phosphatized crust generation to current erosion for RGR summit crusts.

2.5.2.4 Anomalous Diagenetic-type Fe–Mn Crust

The anomalous Li-Ni-rich sample RGR1_D10_002 (Figure 2e) had Li and Ni contents (330 ppm and 1.10 wt %, respectively) as high as the diagenetic Mn nodule end-member from the Peru Basin, which has a mean of 310 ppm Li and 1.30 wt % Ni [35]. Additionally, like the Peru Basin nodules, this sample contains 10 Å manganate, which is a diagenetic phase and accommodates large amounts of divalent cations like Ni, Cu, and Zn [1]. In this anomalous sample, a fractionation between Ni and Cu occurs. This is a unique feature of the diagenetic Peru Basin nodules, which had an Mn/Fe ratio of 5.56 and characterized the diagenetic end-member nodules (Figure 7). However, the Mn/Fe ratio of sample RGR1_D10_002 was 2.3, and its large Cesn anomaly of 3.79 (Figure 9) suggests that this sample formed under oxic conditions. Crusts and nodules formed under oxic conditions but influenced by diagenetic reactions were studied from Shatsky Rise, NW Pacific, where Cu–Ni–Li-rich crusts with an Mn/Fe of 2.0 formed under redox conditions not low enough to form 10 Å manganate [99]. Shatsky Rise crusts have Ni and Li contents lower than in RGR crust RGR1_D10_002. With the somewhat higher Mn/Fe ratio of RGR sample RGR1_D10_002 in, redox conditions were low enough to have a 10Å manganate form, accommodating more Ni^{2+} and Li^{+} cations, but not Cu^{2+}, compared to Shatsky Rise crusts. The fractionation between Ni and Cu can be explained by the rate of regeneration in the water column discussed above, especially evident at RGR since crust RGR1_D10_002 was collected from 680 m water depth, whereas the Shatsky Rise crusts formed at 4000 m. However, this does not fully explain the Ni and Li enrichments and formation of 10 Å manganate in one sample and not in the other non-phosphatized crusts. The water depth is also the reason for Li enrichment in crusts from Shatsky Rise because Li was derived from carbonate dissolution since the highest contents of Li were found in crusts that formed close to the CCD. Lithium is present in foraminifera tests [100], and foraminifera are the dominant component of sediments along RGR. The substrate for sample RGR1_D10_002 is a lithified foraminiferal sand. Although the RGR summit is much shallower than the CCD, the more delicate carbonate tests may have been dissolved in the water column or microenvironments in the sediment and then the released elements incorporated into the 10 Å manganate.

Different from the other samples, the non-phosphatized crust RGR1_D10_002 grew completely around the substrate rock and the studied side may not correspond to the top exposed directly to ocean water but rather to the crust on one of the sides or the bottom of the encrusted rock. Crusts that likewise grow on the sides and bottom of a sample may reflect different redox conditions thereby producing different growth rates; this process has been found, for example, to increase Co contents in Pacific seamount crusts that grew on the sides of thick crusts [54].

This environmental control may decrease or increase redox-sensitive metals in different parts of the crusts. Another different aspect from the other samples is that the substrate rock is a phosphatized foraminifera sandstone and, therefore, experienced diagenesis under suboxic conditions. Although the formation of the non-phosphatized crust requires that the substrate had already been phosphatized before crust formation, it may have influenced the crust formation in microenvironments. For example, the substrate phosphorite is impregnated with Mn oxides showing potential exchange with the crust (Figure 2e). The formation of this anomalous sample may be a combination of processes mentioned in addition to the position of the crust relative to the substrate and the seabed, as well as diagenetic reactions within the substrate. No other sample from dredge D10, or other dredges relatively close to D10, are similar to RGR1_D10_002, so it seems that this unique sample is the specific result of local characteristics of the depositional environment.

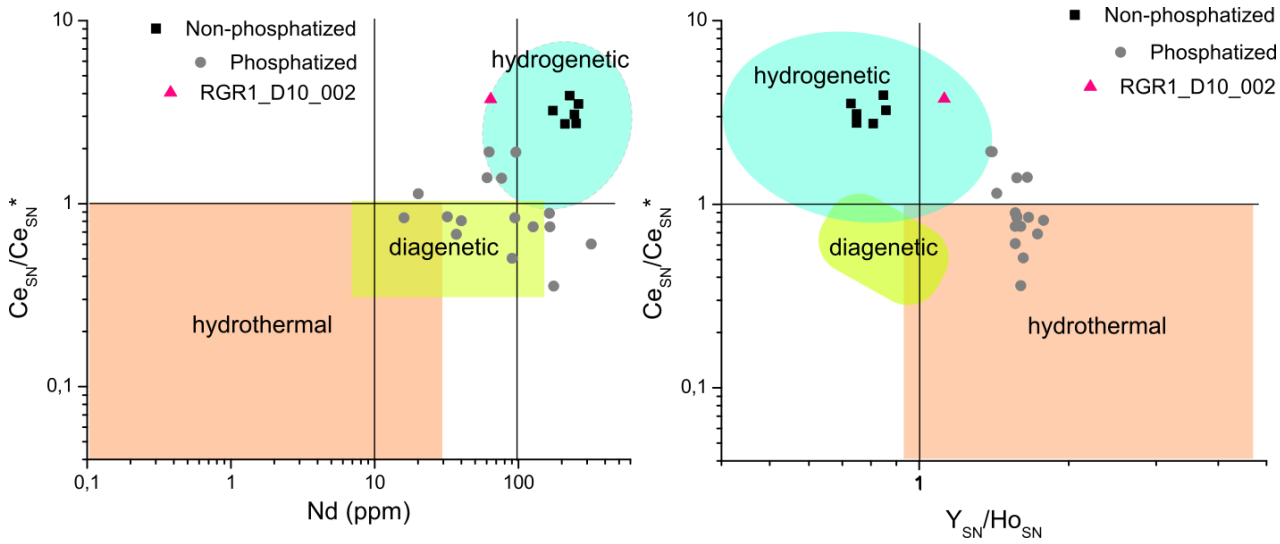

Figure 9. Discrimination diagrams of Ce_{SN}/Ce_{SN}* ratio vs. Nd concentration (left) and Ce_{SN}/Ce_{SN}* ratio vs. Y_{SN}/Ho_{SN} (right) from [101] for non-phosphatized, phosphatized, and anomalous non-phosphatized sample RGR1_D10_002 Fe–Mn crusts from the Rio Grande Rise.

2.5.3 REY Patterns and the Genesis of RGR Crusts

REY_{sn} patterns are commonly used to distinguish the origin of different types of marine precipitates; hydrogenetic, diagenetic, hydrothermal, and mixed origins will show different REY_{sn} configurations [101]. The REY_{sn} patterns of RGR Fe–Mn crusts are distinct for the non-phosphatized and phosphatized generations and reflect the fundamental formation and post-depositional processes. The REY_{sn} curves for the RGR non-phosphatized crusts are typical for hydrogenetic Fe–Mn crusts [101], with an overall flat pattern with strong positive Cesn anomalies and negative Y_{sn} anomalies (Figure 10). On the other hand, the REYsn patterns of the phosphatized crusts from RGR show an increasing trend from Pr to Y, and a slight

decreasing trend to Lu, and with large positive Y_{sn} anomalies, small positive Gd_{sn} anomalies, and variable but mostly negative Ce_{sn} anomalies (Figure 10).

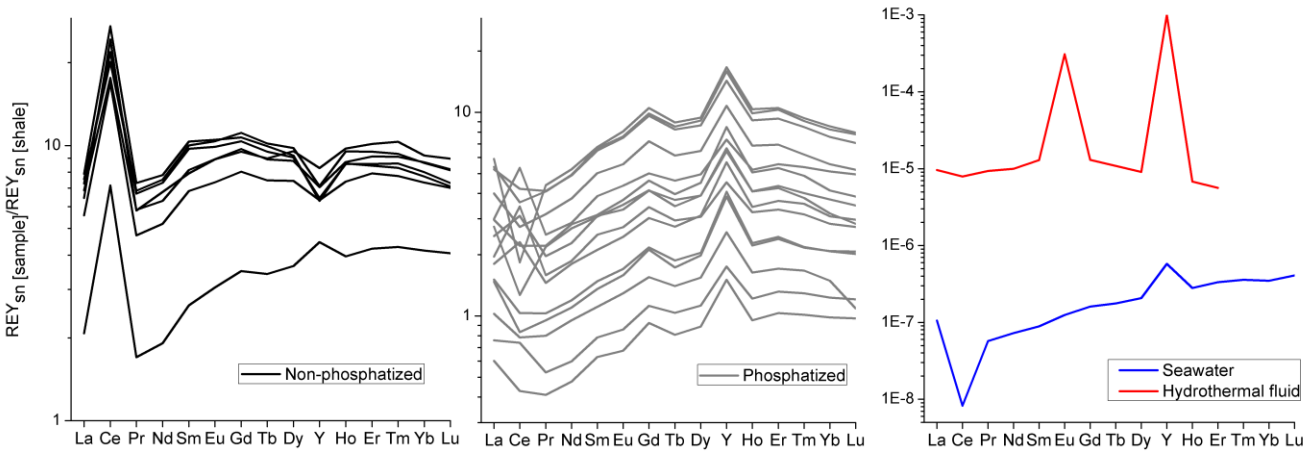

Figure 10. Post Archean Australian Shale (PAAS)-normalized rare earth elements plus yttrium plots for bulk and layers of RGR non-phosphatized (left), phosphatized Fe–Mn crusts (middle), and of hydrothermal fluid from mid-ocean ridges (red; from [104], and seawater at 800 m water depth from offshore Japan (blue; from [73]).

The positive Ce_{sn} anomaly in hydrogenetic crusts is due to the oxidative scavenging of Ce from seawater by the Fe–Mn (oxyhydr)oxides, and its intensity is related to the time of exposure of the Fe–Mn (oxyhydr)oxides to seawater (the growth rate; [47,101,102]). Therefore, the large positive Ce_{sn} anomaly in RGR non-phosphatized crusts reflects slow growth rates of about 1 mm/Myr as determined here by U-series dating. The negative Ce_{sn} anomalies characterize crusts with abundant CFA [103] and it is a feature of seamount phosphorites that reflect the negative Ce anomaly in ocean water and the suboxic conditions under which phosphatization occurred [49,102]. This is accompanied by a mean Ce concentration that increases from 303 ppm in the phosphatized crusts to 1287 ppm for the non-phosphatized crusts. This way, the variable Ce_{sn} anomaly of the phosphatized crusts from RGR reflects the different degrees of phosphatization. Variable Ce_{sn} anomalies are also characteristic of phosphatized crusts from the Ninetyeast Ridge in the Indian Ocean [6].

The negative Y_{sn} anomaly in hydrogenetic crusts strongly contrasts with that of seawater and is due to the preferential scavenging of Y and its geochemical twin Ho by the hydrogenetic (oxyhydr)oxides, since Y generates surface-complexes of lower stability [101,102]. This does not happen to CFA or carbonates, which tend to reflect the typical REYsn pattern of seawater with a positive Y_{sn} anomaly (Figure 10; [49,102]). Additionally, the overall depletion of individual REY_{sn} in the phosphatized crust from RGR, except for Y_{sn}, increases the fractionation with adjacent REY elements and makes a more accentuated Y anomaly. This

is especially clear from the high mean Y/Ho ratios (43), close to that of seawater [6,102], and low mean Y/Ho ratios of non-phosphatized layers (23).

A hydrothermal influence is suspected to have occurred during RGR crusts formation due to the presence of the ironstone layers [105,106], pyrolusite occurrence in one sample [46], high Li and Ni contents [107], the presence of 10 Å manganates [78], and the low Fe/Mn ratios. However, all of those characteristics described above can have alternative explanations as discussed earlier in this paper. Besides, the absence of a positive Eu_{sn} anomaly and lack of evidence of volcanic activity in the RGR for the past 46 Myr does not favor a hydrothermal contribution to the crusts from RGR, although it cannot be excluded for the older parts of thick crusts. A high (Fe + Mn)/Ti ratios (in the 100 s) has been attributed to the influence of hydrothermal fluids in Fe–Mn crust formation on some Atlantic Ocean seamounts [78]. Sample RGR1_D05_011, which contains pyrolusite and ironstone layers, has a (Fe + Mn)/Ti ratio of 588. Thus, the influence of hydrothermal input to some Fe–Mn crusts cannot be excluded.

The REY genetic discrimination diagram (Figure 9) shows that the non-phosphatized layers of RGR Fe–Mn crusts plot in the hydrogenetic area as expected, except RGR1_D10_002, the outlier sample described above. The diagram was not designed for phosphatized samples [101]. The hydrogenetic origin of the Fe–Mn crusts from RGR is also evident from the 10*(Cu + Ni + Co) vs. 100*(Zr + Y + Ce) vs. (Fe + Mn)/4 ternary diagram proposed by [108] (Figure 11), in which the phosphatized crusts and the anomalous non-phosphatized sample RGR1_D10_002 predominantly plot along a mixing line between the hydrogenetic and diagenetic fields. This is in agreement with the post-depositional alteration of Fe–Mn crust during phosphatization. Perhaps a mixing with a hydrothermal component exists in a few samples.

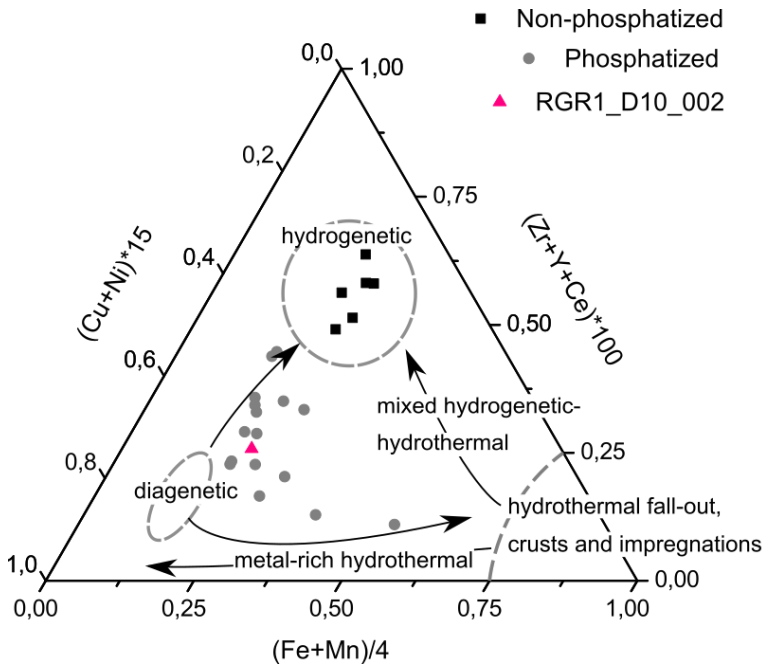

Figure 11. Discrimination diagram based on the content of major (Fe and Mn), trace (Cu and Ni), and high field strength and rare earth elements (Zr, Y, and Ce) from [108]. Non-phosphatized Fe–Mn crusts from RGR fall within the hydrogenetic field, while phosphatized Fe–Mn crusts and the anomalous non-phosphatized RGR1_D10_002 tend to the diagenetic field.

2.5.4 History of Phosphatization of Fe–Mn Crusts on the Summit of RGR

The first phosphatization episode that affected Fe–Mn crusts from the summit of RGR as determined by CFA extracted from the crusts occurred from about 20 to 15 Ma (Figure 12). This is consistent with a large global phosphatization episode at the Oligocene-Early Miocene boundary (between 27 and 21 Ma) that affected seamounts distributed globally [81,109]. This major event was associated with global change in the ocean system, probably a transition from warm water and sluggish circulation to the establishment of cold water and thermohaline overturning circulation [110]. Ultimately, this resulted in the cycling of nutrients and especially phosphorus through increased upwelling [55]. A study based on planktonic foraminifera accumulation rates in an Oligocene-Early Miocene section of a sediment core from RGR shows an increased sedimentation rate and paleoproductivity between 23.9 and 22.9 Ma, with the highest rates at the Oligocene-Miocene boundary (23.3 Ma), followed by an immediate decrease of both sedimentation rates and paleoproductivity [111]. An enrichment of biogenic silica input to sediments also occurred during the late Oligocene and Early Miocene [112]. This first RGR phosphatization age range also coincides with a minor event at 15 Ma identified for Pacific seamounts, where it is separated from the late Oligocene-Early Miocene episode by an interval of no phosphatization [81]. Equatorial East Atlantic reef limestones were phosphatized in the Early Miocene with ages between 23 and 16 Ma [113], suggesting that in the Atlantic,

other regional processes acted to extend this episode of phosphatization. For example, the near continental-margin location of the bank studied by [113] was more subject to consistent upwelling, typical of continental margins like offshore Peru and California.

Younger crust phosphatization events occurred along the RGR summit from 10 to 6.8 Ma (Figure 12), with no parallel in Pacific seamount rocks, but possibly coincides with phosphorites in the equatorial eastern Atlantic dated as 6 Ma [113].

Organic carbon maxima in sediments from Deep Sea Drilling Project (DSDP) Site 516 in the RGR [18] coincide well with ages determined by magnetobiostratigraphy of 19.09 Ma and 15.5 Ma [114]. These organic carbon peaks reflect enhanced biological productivity in surface waters that exported high amounts of P to the RGR seabed that likely facilitated the phosphatization.

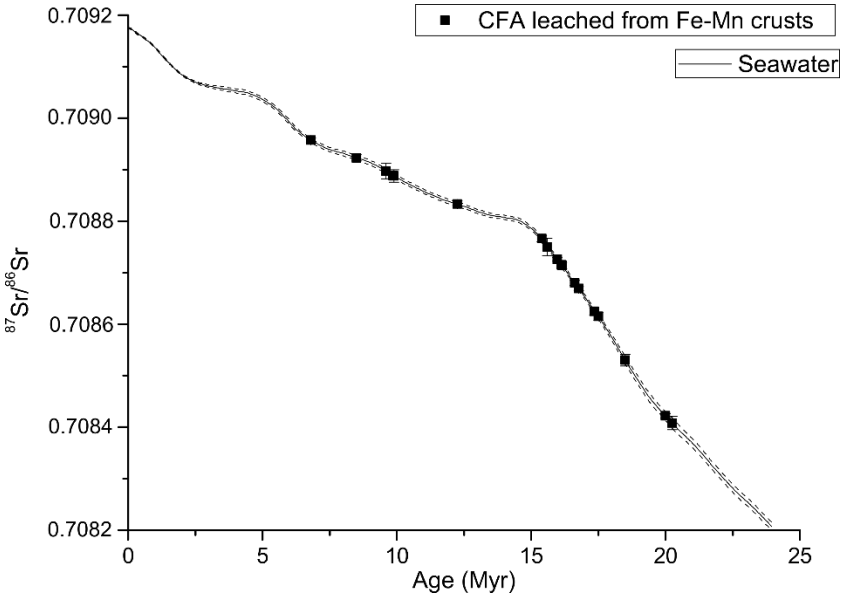

Figure 12. $^{86}Sr/^{87}Sr$ isotopic ratio of seawater (gray line) and CFA leached from phosphatized Fe–Mn crusts from the Rio Grande Rise.

2.5.5 The Role of Surface Biological Productivity in RGR Fe–Mn Crust Formation

The biorelated elements (Ni, Zn, As, and Cd) that are particularly enriched in RGR crusts make them unique in the global ocean and suggest an important source of metals from biological productivity to Fe–Mn crusts forming along the RGR summit in well-oxygenated waters in the recent past (post 6 Ma). Modern oceanographic conditions at RGR suggest that both local primary productivity and advection of nutrients by water masses play important roles in supplying nutrient-type metals (Ni, Zn, As, and Cd) to recent Fe–Mn precipitation, but these conditions cannot be extrapolated to tens of millions year of Fe–Mn crust formation. Nevertheless, periods of enhanced biological productivity occurred in the past above RGR

producing suboxic conditions and supplying the phosphate to seawater that facilitated phosphatization.

Fe–Mn crusts from the RGR summit today are forming above the OMZ, bathed by the oxygenated Antarctic Intermediate Water (AAIW) and below the less oxygenated South Atlantic Mode Water (SAMW; Figure 13). The SAMW forms by sinking of nitrate-rich Si-depleted surface water at high latitude in the Southern Ocean and flows to low latitudes, and is considered the main transport path of nutrients from the Southern Ocean to upwelling zones of the Pacific Ocean [115,116]. Similarly, the AAIW forms close to Antarctica by the sinking of oxygen and nutrient-rich (especially phosphate) surface water of the Southern Ocean to depths right below the SAMW [115], and is suggested to feed temporary biological productivity at lower latitudes [117]. Recent GEOTRACES data from the southwest Atlantic show the injection of oxygenated and nutrient-rich water from the AAIW at about 700–800 m at 30° S, where the Fe–Mn crusts from RGR are located. Furthermore, there is evidence that both the SAMW and the AAIW inject nutrients and trace elements like PO4, Cd, and Zn [76,117,118] into the RGR water column between 600 m and 1200 m depths.

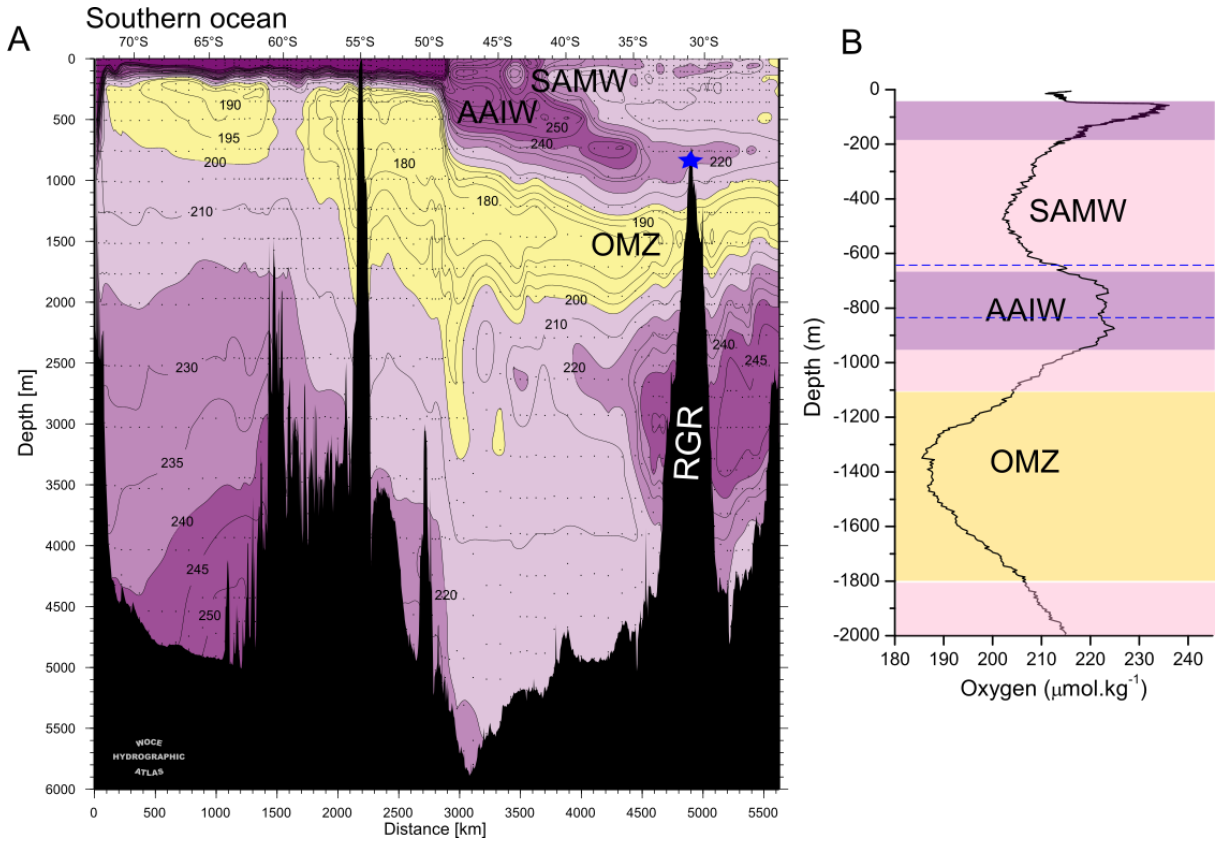

Figure 13. (A) Dissolved oxygen profile in the South Atlantic between 70° S and 20° S showing the South Atlantic Mode Water (SAMW), the Antarctic Intermediate Water (AAIW), the oxygen minimum zone (OMZ), and Rio Grande Rise (RGR) and (B) the dissolved oxygen profile at an oceanographic station at Rio Grande Rise during cruise RGR1, modified from [22]. Blue star and blue dashed lines correspond to the location and depth range of RGR crusts.

Knowledge of the export and remineralization of organic matter in the water column, an important source of dissolved metals to crusts, is scarce for waters over RGR [14]. The RGR is considered to be below the oligotrophic surface waters of the South Atlantic Subtropical regime, with relatively low primary productivity and phytoplankton biomass [119]. However, the global map of annual net primary production shows that the RGR is actually under the surface water of intermediate primary productivity, higher than in the Pacific PCZ but lower than the Northeast Atlantic, and much lower than in the central-east equatorial Pacific for example [120].

No investigation has been done on the possible influence of RGR itself to modify the vertical water column on a local scale. It is known that submarine topography shallower than 1000 m can change the water-mass structure and fertilize the euphotic zone with nutrients from underlying waters, driving enhanced primary production around the rise, or trapping and accumulating organic matter driven by secondary circulation around seamounts (e.g., [121]). It may be that instead of the global water masses providing the unique oceanographic conditions for the Fe–Mn crusts c at RGR, the interaction of water masses with RGR is creating a niche biological and geological environment ideal for Fe–Mn crust formation with unique locality-specific compositions.

2.5.6 Resource Considerations

Cobalt, Mn, Te, Mo, Bi, Pt, W, Zr, Nb, and Y are the critical metals of most economic interest in Fe–Mn crusts [5]. Bulk Fe–Mn crusts from the top of the RGR plateau studied here are depleted in those metals due to phosphatization. They are, instead, the most enriched Fe–Mn crusts in Ni and Li, which are critical metals of economic interest for example in manganese nodules from the Clarion-Clipperton Zone and Peru Basin.

The younger crust generation shows that, when not affected by phosphatization, the Fe–Mn precipitates of RGR have among the highest concentrations of Bi, Nb, Ni, Te, Rh, Ru, and Pt among crusts from other regions. Therefore, crusts from depths deeper than 800 m, which would less likely be affected by phosphatization, maybe more interesting from a resource point of view. Thus, further exploration is warranted to study Fe–Mn crusts from deeper water along RGR and at all depths on the summit and flanks of the seamounts that surround RGR.

The high P and F contents and CFA of RGR plateau crusts indicate that the crusts and substrate rocks in some areas might be considered as potential phosphate ores. This plateau-type phosphorite is being considered for mining offshore New Zealand on Chatham Rise and also occurs in abundance offshore of Southeast USA on Blake Plateau [49].

2.6 Summary and Conclusions

(1) Two generations of layers characterized RGR crusts: an older phosphatized generation and a younger, non-phosphatized generation. They were chemically, mineralogically, and texturally distinct, similar to crusts elsewhere in the global ocean.

(2) The younger generation was typical of hydrogenetic crusts, while the older crust generation had characteristics of diagenetic Fe–Mn deposits, such as low Fe/Mn ratios, high Mn, Ni, and Li contents and presence of 10 Å manganates, all of which were likely related to the processes of phosphatization.

(3) Phosphatization affected the crust by replacing carbonates, altering the Mn-phase and partially replacing Fe oxyhydroxides. Many metals of nutrient-type distribution in the water column were likely enhanced during phosphatization.

(4) Biological productivity was an important source of metals (Ni, Cd, As, V, and Li), but more importantly, was the rate at which the metals were regenerated from sinking particles in the water column.

(5) Fe–Mn crusts most likely grew at an estimated rate of about 1 mm/Myr and may have started to form at about 48–55 Ma along the summit of Rio Grande Rise, which is younger compared to the oldest crust formation in the Pacific and Northeast Atlantic Oceans.

(6) Several episodes of phosphatization strongly affected the crusts during the Miocene, from 20 to 6.8 Ma, starting near the end of a major phosphatization event that affected many seamounts around the globe. Phosphatization was promoted by enhanced primary productivity at the shallow-water depth of formation of the crusts, between 650 and 800 m.

(7) The Co-chronometer equations could be used to estimate the growth rates and ages of initiation of crust growth of the strongly phosphatized layers only if the growth rates are extrapolated from the non-phosphatized layers. Those estimated growth rates were supported by accretion rates estimated by U-series dating and constrained by Sr-isotope ages of phosphatization of the crusts. Neither method detected growth hiatuses in the crusts. Given the potential for strong currents over RGR, there might be missing stratigraphic sections in the crusts.

(8) Bulk RGR crusts were depleted in critical metals typically considered of economic interest like Co, REE, Mo, and Zr, but they were the most enriched in Ni and Li, and also had high contents of the critical metals W, Rh, and Y. RGR could also be considered to host a potential phosphorite deposit like that being considered for mining on Chatham Rise offshore of New Zealand.

References

1. Hein, J.R.; Koschinsky, A. Deep-Ocean Ferromanganese Crusts and Nodules. In Treatise on Geochemistry; Scott, S., Ed.; Elsevier: Amsterdam, Netherlands, 2014; pp. 273–291 ISBN 9780080983004.
2. Koschinsky, A.; Hein, J.R. Marine Ferromanganese Encrustations: Archives of Changing Oceans. Elements 2017, 13, 177–182.
3. Graedel, T.E.; Harper, E.M.; Nassar, N.T.; Nuss, P.; Reck, B.K.; Turner, B.L. Criticality of metals and metalloids. Proc. Natl. Acad. Sci. U. S. A. 2015, 112, 4257–4262.
4. Clark, M.; Heydon, R.; Hein, J.; Smith, S.; Smith, C.; Petersen, S.; Baker, E.; Beaudoin, Y. Cobalt-rich Ferromanganese Crusts, A physical, biological, environmental, and technical review. Deep Sea Miner. 2013, 1C, 1–52.
5. Hein, J.R.; Mizell, K.; Koschinsky, A.; Conrad, T.A. Deep-ocean mineral deposits as a source of critical metals for high- and green-technology applications: Comparison with land-based resources. Ore Geol. Rev. 2013, 51, 1–14.
6. Hein, J.; Conrad, T.; Mizell, K.; Banakar, V.K.; Frey, F.A.; Sager, W.W. Controls on ferromanganese crust composition and reconnaissance resource potential, Ninetyeast Ridge, Indian Ocean. Deep. Res. Part I 2016, 110, 1–19.
7. Hein, J.R.; Conrad, T.A.; Dunham, R.E. Seamount Characteristics and mine-site model applied to exploration- and mining-lease-block selection for cobalt-rich ferromanganese crusts. Mar. Georesources Geotechnol. 2009, 27, 160–176.
8. Koschinsky, A.; Van Gerven, M.; Halbach, P. First investigations of massive ferromanganese crusts in the ne atlantic in comparison with hydrogenetic pacific occurrences. Mar. Georesources Geotechnol. 1995, 13, 375–391.
9. Muiños, S.B.; Hein, J.R.; Frank, M.; Monteiro, J.H.; Gaspar, L.; Conrad, T.; Pereira, H.G.; Abrantes, F. Deep-sea Fe-Mn Crusts from the Northeast Atlantic Ocean: Composition and Resource Considerations. Mar. Georesources Geotechnol. 2013, 31, 40–70.
10. Conrad, T.; Hein, J.R.; Paytan, A.; Clague, D.A. Formation of Fe-Mn crusts within a continental margin environment. Ore Geol. Rev. 2017.
11. Marino, E.; González, F.J.; Somoza, L.; Lunar, R.; Ortega, L.; Vázquez, J.T.; Reyes, J.; Bellido, E. Strategic and rare elements in Cretaceous-Cenozoic cobalt-rich ferromanganese crusts from seamounts in the Canary Island Seamount Province (northeastern tropical Atlantic). Ore Geol. Rev. 2017, 87, 41–61.
12. Goto, K.T.; Nozaki, T.; Toyofuku, T.; Augustin, A.H.; Shimoda, G.; Chang, Q.; Kimura, J.I.; Kameo, K.; Kitazato, H.; Suzuki, K. Paleoceanographic conditions on the São Paulo

Ridge, SW Atlantic Ocean, for the past 30 million years inferred from Os and Pb isotopes of a hydrogenous ferromanganese crust. Deep. Res. Part II Top. Stud. Oceanogr. 2017, 146, 82–92.

13. Benites, M.; Millo, C.; Hein, J.; Nath, B.N.; Murton, B.; Galante, D.; Jovane, L. Integrated Geochemical and Morphological Data Provide Insights into the Genesis of Ferromanganese Nodules. Minerals 2018, 8, 1–16.
14. Montserrat, F.; Guilhon, M.; Vinicius, P.; Corrêa, F.; Menezes, N.; Negrão, C.; Marone, P.; Santos, M.D.L.; Moura, D.; Jovane, L.; et al. Deep-sea mining on the Rio Grande Rise (Southwestern Atlantic): A review on environmental baseline, ecosystem services and potential impacts. Deep. Res. Part I 2019, 145, 31–58.
15. Mohriak, W.U.; Nobrega, M.; Odegard, M.E.; Gomes, B.S.; Dickson, W.G. Geological and geophysical interpretation of the Rio Grande Rise, south-eastern Brazilian margin: extensional tectonics and rifting of continental and oceanic crusts. Pet. Geosci. 2010, 16, 231–245.
16. Ussami, N.; Chaves, C.A.M.; Marques, L.S.; Ernesto, M. Origin of the Rio Grande Rise–Walvis Ridge reviewed integrating palaeogeographic reconstruction, isotope geochemistry and flexural modelling. Geol. Soc. London, Spec. Publ. 2013, 369, 129–146.
17. Camboa, L.A.P.; Rabinowitz, P.D. The evolution of the Rio Grande Rise in the southwest Atlantic Ocean. Mar. Geol. 1984, 58, 35–58.
18. Emelyanov, E.M.; Trimonis, E.S. Geochemical investigation of sediments from the Brazil Basin and the Rio Grande Rise; Santos, Brazil, 1983;
19. Hu, X.; Wang, Y.L.; Schmitt, R. a. Geochemistry of sediments on the Rio Grande Rise and the redox evolution of the South Atlantic Ocean. Geochim. Cosmochim. Acta 1988, 52, 201–207.
20. Liu, Y.G.; Schmitt, R.A. Chemical profiles in sediments and basalt samples from Deep Sea Drilling Project Leg 74, hole 525A, Walvis Ridge; 1984;
21. Harlamov, V.; Lisniowski, M.; Frazão, E.; Pessoa, J.; Aguiar, R.; Lopes, V.; Nobrega, M.; Lisboa, M.; Simões, H.; Cavalcanti, J.; et al. Preliminary results onmid-depth circulation features on Rio Grande Rise. In Proceedings of the Acoustics in Underwater Geosciences Symposium (Rio Acoustics); IEEE: Rio de Janeiro, 2015.
22. Jovane, L.; Hein, J.R.; Yeo, I.A.; Benites, M.; Bergo, N.M.; Corrêa, P.V.F.; Couto, D.M.; Guimarães, A.D.; Howarth, S.A.; Miguel, H.R.; et al. Multidisciplinary Scientific Cruise to the Rio Grande Rise. Front. Mar. Sci. 2019, 6, 1–7.

23. Cook, H.E.; Johnson, P.D.; Matti, J.C.; Zemmels, I. Methods of sample preparation and X-ray data analysis (X-ray mineralogy laboratory, Deep Sea Drilling Project, University of California Riverside); 1975;
24. Hein, J.R.; Schwab, W.C.; Davis, A.S. Cobalt- and platinum-rich ferromanganese crusts and associated substrate rocks from the Marshall Islands. Mar. Geol. 1988, 78, 255–283.
25. Ruttenberg, K.C. Development of a sequential extraction method for different forms of phosphorus in marine sediments. Limnol. Oceanogr. 1992, 37, 1460–1482.
26. Silverman, S.; Fuyat, R.; Weiser, J. Quantitative determination of calcite associated with carbonate-bearing apatites. Am. Mineral. 1952, 37, 211–222.
27. McLennan, S.M. Rare earth elements in sedimentary rocks; influence ofprovenance and sedimentary processes. Rev. Mineral. 1989, 21, 169–200.
28. Pisias, N.G.; Murray, R.W.; Scudder, R.P. Multivariate statistical analysis and partitioning of sedimentary geochemical data sets: General principles and specific MATLAB scripts. Geochemistry, Geophys. Geosystems 2013, 14, 4015–4020.
29. Manheim, F.T.; Lane-Bostwick, C.M. Cobalt in ferromanganese crusts as a monitor of hydrothermal discharge on the Pacific sea floor. Nature 1988, 335, 59–62.
30. Puteanus, D.; Halbach, P. Correlation of Co concentration and growth rate--A method for age determination of ferromanganese crusts. Chem. Geol. 1988, 69, 73–85.
31. Akovali, Y.A. Nuclear data sheets for A=234. Nucl. Data Sheets 1994, 71, 181–259.
32. Cheng, H.; Edwards, R.L.; Hoff, J.; Gallup, C.D.; Richards, D.A.; Asmerom, Y. The half-lives of uranium-234 and thorium-230. Chem. Geol. 2000, 169, 17–33.
33. Matthews, K.A.; Murrell, M.T.; Goldstein, S.J.; Nunn, A.J.; Norman, D.E. Uranium and Thorium Concentration and Isotopic Composition in Five Glass (BHVO-2G, BCR-2G, NKT-1G, T1-G, ATHO-G) and Two Powder (BHVO-2, BCR-2) Reference Materials. Geostand. Geoanalytical Res. 2011, 35, 227–234.
34. McArthur, J.; Howarth, R.J.; Shields, G.A. Strontium isotope stratigraphy. In The Geologic Time Scale 2012; Gradstein, F., Ogg, J.G., Schmitz, M.D., Ogg, G.M., Eds.; Elsevier: Oxford, UK, 2012; pp. 127–144 ISBN 978 0 44 459425 9.
35. Kuhn, T.; Wegorzewski, A.; Rühlemann, C.; Vink, A. Composition, formation, and occurrence of polymetallic nodules. In Deep-Sea Mining; Sharma, R., Ed.; Springer International Publishing: Basel, Switzerland, 2017; pp. 23–63 ISBN 9783319525570.
36. Chukhrov, F. V. On Vernadite. Int. Geol. Rev. 1980, 22, 58–74.
37. Lee, S.; Xu, H.; Xu, W.; Sun, X. The structure and crystal chemistry of vernadite in ferromanganese crusts research papers. Acta Crystallogr. 2019, B75, 591–598.

38. Bodeï, S.; Manceau, A.; Geoffroy, N.; Baronnet, A.; Buatier, M. Formation of todorokite from vernadite in Ni-rich hemipelagic sediments. Geochim. Cosmochim. Acta 2007, 71, 5698–5716.
39. Varentsov, I.M.; Drits, V.A.; Gorshkov, A.I.; Sivtsov, A. V; Sakharov, B.A. Mn-Fe oxyhydroxide crusts from Krylov Seamount (Eastern Atlantic): Mineralogy, geochemistry and genesis. Mar. Geol. 1991, 96, 53–70.
40. Manceau, A.; Lanson, M.; Takahashi, Y. Mineralogy and crystal chemistry of Mn, Fe, Co, Ni, and Cu in a deep-sea Pacific polymetallic nodule. Am. Mineral. 2014, 99, 2068–2083.
41. Manceau, A.; Gorshkov, A.I.; Drits, V.A. Structural chemistry of Mn, Fe, Co, and Ni in manganese hydrous oxides: Part II. Information from EXAFS spectroscopy and electron and X-ray diffraction. Am. Mineral. 1992, 77, 1144–1157.
42. Bilinski, H.; Giovanoli, R.; Usui, A.; Hanžel, D. Characterization of Mn oxides in cemented streambed crusts from Pinal Creek, Arizona U.S.A., and in hot-spring deposits from Yuno-Taki Falls, Hokkaido, Japan. Am. Mineral. 2002, 87, 580–591.
43. Vereshchagin, O.S.; Perova, E.N.; Brusnitsyn, A.I.; Ershova, V.B.; Khudoley, A.K.; Shilovskikh, V. V.; Molchanova, E. V. Ferro-manganese nodules from the Kara Sea: Mineralogy, geochemistry and genesis. Ore Geol. Rev. 2019, 106, 192–204.
44. Novikov, G. V.; Bogdanova, O.Y. Transformations of ore minerals in genetically different oceanic ferromanganese rocks. Lithol. Miner. Resour. 2007, 42, 303–317.
45. Wegorzewski, A. V.; Kuhn, T.; Dohrmann, R.; Wirth, R.; Grangeon, S. Mineralogical characterization of individual growth structures of Mn-nodules with different Ni+Cu content from the central Pacific Ocean. Am. Mineral. 2015, 100, 2497–2508.
46. Usui, A.; Yuasa, M.; Yokota, S.; Nohara, M.; Nishimura, A.; Murakami, F. Submarine hydrothermal manganese deposits from the Ogasawara (Bonin) arc, off the Japan islands. Mar. Geol. 1986, 73, 311–322.
47. Hein, J.R.; Koschinsky, A.; Halbach, P.; Manheim, F.T.; Bau, M.; Kang, J.; Lubick, N. Iron and manganese oxide mineralization in the Pacific. Manganese Miner. Geochemistry Mineral. Terr. Mar. Depos. 1997, 119, 123–138.
48. Dasgupta, R.; Jackson, M.G.; Lee, C.T.A. Major element chemistry of ocean island basalts - Conditions of mantle melting and heterogeneity of mantle source. Earth Planet. Sci. Lett. 2010, 289, 377–392.
49. Hein, J.; Koschinsky, A.; Mikesell, M.; Mizell, K.; Glenn, C.; Wood, R. Marine Phosphorites as Potential Resources for Heavy Rare Earth Elements and Yttrium. Minerals 2016, 6, 88.

50. Bruland, K.W.; Middag, R.; Lohan, M.C. Controls of Trace Metals in Seawater. In Treatise on Geochemistry: Second Edition; Mottl, M.J., Elderfield, H., Eds.; Elsevier Ltd.: Philadelphia, PA, USA, 2013; Vol. 8, pp. 19–51 ISBN 9780080983004.
51. Claude, C.; Suhr, G.; Hofmann, A.W.; Koschinsky, A. U-Th chronology and paleoceanographic record in a Fe-Mn crust from the NE Atlantic over the last 700 ka. Geochim. Cosmochim. Acta 2005, 69, 4845–4854.
52. Josso, P.; Parkinson, I.; Horstwood, M.; Lusty, P.; Chenery, S.; Murton, B. Improving confidence in ferromanganese crust age models: A composite geochemical approach. Chem. Geol. 2019, 513, 108–119.
53. Yeo, I.A.; Howarth, S.A.; Spearman, J.; Cooper, A.; Crossouard, N.; Taylor, J.; Turnbull, M.; Murton, B.J. Distribution of and hydrographic controls on ferromanganese crusts: Tropic Seamount, Atlantic. Ore Geol. Rev. 2019, 114, 103131.
54. Hein, J.R.; Koschinsky, A.; Bau, M.; Manheim, F.T.; Kang, J.; Roberts, L. Cobalt-rich ferromanganese crusts in the Pacific. In Handbook of Marine Mineral Deposits; Cronan, D.S., Ed.; CRC Marine Science Series. CRC Press: Boca Raton, Florida, 2000; pp. 239–279 ISBN 084938429X.
55. Koschinsky, A.; Stascheit, I.A.; Bau, M.; Halbach, P. Effects of phosphatization on the geochemical and mineralogical composition of marine ferromanganese crusts. Geochim. Cosmochim. Acta 1997, 6, 4079–4094.
56. Nishi, K.; Usui, A.; Nakasato, Y.; Yasuda, H. Formation age of the dual structure and environmental change recorded in hydrogenetic ferromanganese crusts from Northwest and Central Pacific seamounts. Ore Geol. Rev. 2017, 87, 62–70.
57. Usui, A.; Nishi, K.; Sato, H.; Nakasato, Y.; Thornton, B.; Kashiwabara, T.; Tokumaru, A.; Sakaguchi, A.; Yamaoka, K.; Kato, S.; et al. Continuous growth of hydrogenetic ferromanganese crusts since 17 Myr ago on Takuyo-Daigo Seamount, NW Pacific, at water depths of 800–5500 m. Ore Geol. Rev. 2017, 87, 71–87.
58. De Carlo, E.H. Paleoceanographic implications of rare earth element variability within a FeMn crust from the central Pacific Ocean. Mar. Geol. 1991, 98, 449–467.
59. McMurtry, G.M.; VonderHaar, D.L.; Eisenhauer, A.; Mahoney, J.J.; Yeh, H.W. Cenozoic accumulation history of a Pacific ferromanganese crust. Earth Planet. Sci. Lett. 1994, 125, 105–118.
60. Barker, P.F. Tectonic evolution and subsidence history of the Rio Grande Rise. Initial reports DSDP, Leg 72, Santos, Brazil 1983, 953–976.

61. Manheim, F.T.; Pratt, R.M.; McFarlin, P.F. Composition and Origin of Phosphorite Deposits of the Blake Plateau. In Marine Phosphorites—Geochemistry, Occurrence, Genesis; Bentor, Y.K., Ed.; SEPM Society for Sedimentary Geology, 1980; Vol. 29, pp. 117–137 ISBN 9781565761599.
62. Lea, D.W. Trace elements in foraminiferal calcite. In Modern Foraminifera; Gupta, B.K.S., Ed.; Springer: Dordrecht, 1999; pp. 259–277.
63. Mizell, K.; Hein, J.R.; Lam, P.J.; Koppers, A.A.P.; Staudigel, H. Geographic and oceanographic influences on ferromanganese crust composition along a Pacific Ocean meridional transect, 14N to 14S. Geochemistry, Geophys. Geosystems 2019.
64. Cutter, G.A.; Cutter, L.S.; Featherstone, A.M.; Lohrenz, S.E. Antimony and arsenic biogeochemistry in the western Atlantic Ocean. Deep. Res. Part II Top. Stud. Oceanogr. 2001, 48, 2895–2915.
65. Andreae, M.O. Arsenic speciation in seawater and interstitial waters: the influence of biological-chemical interactions on the chemistry of a trace element. Limnol. Oceanogr. 1979, 24, 440–452.
66. Bertine, K.K.; Koide, M.; Goldberg, E.D. Aspects of rhodium marine chemistry. Mar. Chem. 1993, 42, 199–210.
67. Collier, R.W. Particulate and dissolved vanadium in the North Pacific Ocean. Nature 1984, 309, 441–444.
68. Heggie, D.; Kahn, D.; Fischer, K. Trace metals in metalliferous sediments, MANOP Site M: interfacial pore water profiles. Earth Planet. Sci. Lett. 1986, 80, 106–116.
69. Sohrin, Y.; Fujishima, Y.; Ueda, K.; Akiyama, S.; Mori, K.; Hasegawa, H.; Matsui, M. Dissolved niobium and tantalum in the North Pacific. Geophys. Res. Lett. 1998, 25, 999–1002.
70. Flegal, A.R.; Patterson, C.C. Vertical concentration profiles of lead in the Central Pacific at 15°N and 20°S. Earth Planet. Sci. Lett. 1983, 64, 19–32.
71. Lee, D.S.; Edmond, J.M. Tellurium species in seawater. Nature 1985, 313, 782–785.
72. Dong Soo Lee; Edmond, J.M.; Bruland, K.W. Bismuth in the Atlantic and North Pacific: a natural analogue to plutonium and lead? Earth Planet. Sci. Lett. 1986, 76, 254–262.
73. Alibo, D.S.; Nozaki, Y. Rare earth elements in seawater: Particle association, shale-normalization, and Ce oxidation. Geochim. Cosmochim. Acta 1999, 63, 363–372.
74. Jacinto, G.S.; Van Den Berg, C.M.G. Different behaviour of platinum in the Indian and Pacific Oceans. Nature 1989, 338, 332–334.

75. Colodner, D.C.; Boyle, E.A.; Edmond, J.M. Determination of Rhenium and Platinum in natural waters and sediments, and Iridium in sediments by flow injection isotope dilution inductively coupled plasma mass spectrometry. Anal. Chem. 1993, 65, 1419–1425.
76. López-Sánchez, D.E.; Cobelo-García, A.; Rijkenberg, M.J.A.; Gerringa, L.J.A.; de Baar, H.J.W. New insights on the dissolved platinum behavior in the Atlantic Ocean. Chem. Geol. 2019, 511, 204–211.
77. Banakar, V.K.; Hein, J.R.; Rajani, R.P.; Chodankar, a. R. Platinum group elements and gold in ferromanganese crusts from Afanasiy-Nikitin seamount, equatorial Indian Ocean: Sources and fractionation. J. Earth Syst. Sci. 2007, 116, 3–13.
78. Baturin, G.N.; Dubinchuk, V.T. Mineralogy and Chemistry of Ferromanganese Crusts from the Atlantic Ocean. Geochemistry Int. 2011, 49, 578–593.
79. Konstantinova, N.; Cherkashov, G.; Hein, J.R.; Mirão, J.; Dias, L.; Madureira, P.; Kuznetsov, V.; Maksimov, F. Composition and characteristics of the ferromanganese crusts from the western Arctic Ocean. Ore Geol. Rev. 2017, 87, 88–99.
80. Glasby, G.P.; Mountain, B.; Vineesh, T.C.; Banakar, V.; Rajani, R.; Ren, X. Role of hydrology in the formation of Co-rich Mn crusts from the equatorial N pacific, equatorial S Indian ocean and the NE Atlantic ocean. Resour. Geol. 2010, 60, 165–177.
81. Hein, J.; Gunn, H.; Sliter, V.; Benninger, M. Two major Cenozoic episodes of phosphogenesis recorded in Equatorial Pacific seamounts deposits. Paleoceanography 1993, 8, 293–311.
82. Benninger, L.M.; Hein, J.R. Diagenetic evolution of seamount phosphorite. Mar. Authigenes. From Glob. to Microb. 2000, 245–256.
83. Koschinsky, A.; Halbach, P.; Hein, J.R.; Mangini, A. Ferromanganese crusts as indicators for paleoceanographic events in the NE Atlantic. Geol. Rundschau 1996, 85, 567–576.
84. Burns, V.M.; Burns, R.G. Post-depositional metal enrichment processes inside manganese nodules from the north equatorial Pacific. Earth Planet. Sci. Lett. 1978, 39, 341–348.
85. Sclater, F.; Boyle, E.A.; Edmond, J.M. On the marine geochemistry of nickel. Earth Planet. Sci. Lett. 1976, 31, 119–128.
86. Bruland, K.W. Oceanographic distributions of cadmium, zinc, nickel, and copper in the North Pacific. Earth Planet. Sci. Lett. 1980, 47, 176–198.
87. Lohan, M.C.; Statham, P.J.; Crawford, D.W. Total dissolved zinc in the upper water column of the subarctic North East Pacific. Deep. Res. Part II Top. Stud. Oceanogr. 2002, 49, 5793–5808.

88. Boyle, E.A.; Sclater, F.; Edmond, J.M. On the marine geochemistry of cadmium. Nature 1976, 263, 42–44.
89. George, E.; Stirling, C.H.; Gault-Ringold, M.; Ellwood, M.J.; Middag, R. Marine biogeochemical cycling of cadmium and cadmium isotopes in the extreme nutrient-depleted subtropical gyre of the South West Pacific Ocean. Earth Planet. Sci. Lett. 2019, 514, 84–95.
90. Dean, W.E.; Zheng, Y.; Ortiz, J.D.; van Geen, A. Sediment Cd and Mo accumulation in the oxygen-minimum zone off western Baja California linked to global climate over the past 52 kyr. Paleoceanography 2006, 21, 1–13.
91. Horner, T.J.; Schonbachler, M.; Rehkamper, M.; Nielsen, S.G.; Williams, H.; Halliday, A.N.; Xue, Z.; Hein, J.R. Ferromanganese crusts as archives of deep water Cd isotope compositions. Geochemistry, Geophys. Geosystems 2010, 11, 1–10.
92. Calvert, S.E. Deposition and diagenesis of silica in marine sediments. In Pelagic sediments: on land and under the sea; Hsu, K.J., Jenkyns, H.C., Eds.; International Association of Sedimentologists Series: Oxford, UK, 1974; Vol. 1, pp. 273–299 ISBN 0632001674.
93. Murray, R.W.; Leinen, M.; Isern, A.R. Biogenic flux of Al to sediment in the Central Equatorial Pacific Ocean: evidence for increased productivity during glacial periods. Paleoceanography 1993, 8, 651–670.
94. Jiang, X.; Lin, X.; Yao, D.; Zhai, S.; Guo, W. Geochemistry of lithium in marine ferromanganese oxide deposits. Deep. Res. Part I Oceanogr. Res. Pap. 2007, 54, 85–98.
95. Manheim, F.T.; Gulbrandsen, R.A. Marine phosphorites. In Marine Minerals; Burns, R.G., Ed.; Mineralogical Society of America: Washington, 1979; pp. 151–173.
96. Jiang, X.-D.; Sun, X.-M.; Chou, Y.-M.; Hein, J.R.; He, G.-W.; Fu, Y.; Li, D.; Liao, J.-L.; Ren, J.-B. Mineralogy and geochemistry of carbonate fluorapatite in seamount Fe Mn crusts from the Pacific Ocean. Mar. Geol. 2020, 423, 106135.
97. De Baar, H.J.W.; Bacon, M.P.; Brewer, P.G.; Bruland, K.W. Rare earth elements in the Pacific and Atlantic Oceans. Geochim. Cosmochim. Acta 1985, 49, 1943–1959.
98. Zhang, J.; Nozaki, Y. Rare earth elements and yttrium in seawater: ICP-MS determinations in the East Caroline, Coral Sea, and South Fiji basins of the western South Pacific Ocean. Geochim. Cosmochim. Acta 1996, 60, 4631–4644.
99. Hein, J.R.; Conrad, T.A.; Frank, M.; Christl, M.; Sager, W.W. Copper-nickel-rich, amalgamated ferromanganese crust-nodule deposits from Shatsky Rise, NW Pacific. Geochemistry, Geophys. Geosystems 2012, 13, 1–23.

100. Delaney, M.L.; Boyle, E.A. Lithium in foraminiferal shells: implications for high-temperature hydrothermal circulation fluxes and oceanic crustal generation rates. Earth Planet. Sci. Lett. 1986, 80, 91–105.
101. Bau, M.; Schmidt, K.; Koschinsky, A.; Hein, J.; Kuhn, T.; Usui, A. Discriminating between different genetic types of marine ferro-manganese crusts and nodules based on rare earth elements and yttrium. Chem. Geol. 2014, 381, 1–9.
102. Bau, M.; Koschinsky, A.; Dulski, P.; Hein, J.R. Comparison of the partitioning behaviours of yttrium, rare earth elements, and titanium between hydrogenetic marine ferromanganese crusts and seawater. Geochim. Cosmochim. Acta 1996, 60, 1709–1725.
103. Baturin, G.N.; Yushina, I.G. Rare earth elements in phosphate-ferromanganese crusts on Pacific seamounts. Lithol. Miner. Resour. 2007, 42, 101–117.
104. Klinkhammer, G.P.; Elderfield, H.; Edmond, J.M.; Mitra, A. Geochemical implications of rare earth element patterns in hydrothermal fluids from mid-ocean ridges. Geochim. Cosmochim. Acta 1994, 58, 5105–5113.
105. Alt, J.C. Hydrothermal oxide and nontronite deposits on seamounts in the eastern Pacific. Mar. Geol. 1988, 81, 227–239.
106. Hein, J.R.; Hsueh-Wen, Y.; Gunn, S.H.; Gibbs, A.E.; Chung-ho, W. Composition and origin of hydrothermal ironstones from central Pacific seamounts. Geochim. Cosmochim. Acta 1994, 58, 179–189.
107. Hein, J.R.; Conrad, T.A.; Staudigel, H. Seamount minerals deposits: a source of rare metals for high-technology industries. Oceanography 2010, 23, 184–189.
108. Josso, P.; Pelleter, E.; Pourret, O.; Fouquet, Y.; Etoubleau, J.; Cheron, S.; Bollinger, C. A New Discrimination Scheme for Oceanic Ferromanganese Deposits using High Field Strength and Rare Earth Elements. Ore Geol. Rev. 2017, 87, 3–15.
109. Hyeong, K.; Kim, J.; Yoo, C.M.; Moon, J.W.; Seo, I. Cenozoic history of phosphogenesis recorded in the ferromanganese crusts of central and western Pacific seamounts: Implications for deepwater circulation and phosphorus budgets. Palaeogeogr. Palaeoclimatol. Palaeoecol. 2013, 392, 293–301.
110. Keigwin, L.D.; Corliss, B.H. Stable isotopes in late middle Eocene to Oligocene foraminifera. Geol. Soc. Am. Bull. 1986, 97, 335–345.
111. Florindo, F.; Gennari, R.; Persico, D.; Turco, E.; Villa, G.; Lurcock, P.C.; Roberts, A.P.; Winkler, A.; Carter, L.; Pekar, S.F. New magnetobiostratigraphic chronology and paleoceanographic changes across the Oligocene-Miocene boundary at DSDP Site 516 (Rio Grande Rise, SW Atlantic). Paleoceanography 2015, 30, 659–681.

112. Levitan, M.A.; Strizhov, V.P.; Schevtchenko, A.Y. Cherts from Rio Grande Rise sediments, Deep Sea Drilling Project leg 72, hole 516F; 2007; Vol. 2;.
113. Jones, E.J.W.; Boudagher-Fadel, M.K.; Thirlwall, M.F. An investigation of seamount phosphorites in the eastern Equatorial Atlantic. Mar. Geol. 2002, 183, 143–162.
114. Berggren, W.A.; Aubry, M.P.; Hamilton, N. Neogene magnetobiostratigraphy of Deep Sea Drilling Project Site 516 (Rio Grande Rise, South Atlantic); 1983; Vol. 516;.
115. Sarmiento, J.L.; Gruber, N.; Brzezinski, M.A.; Dunne, J.P. High-latitude controls of thermocline nutrients and low latitude biological productivity. Nature 2004, 427, 56–60.
116. Ayers, J.M.; Strutton, P.G. Nutrient variability in Subantarctic Mode Waters forced by the Southern Annular Mode and ENSO. Geophys. Res. Lett. 2013, 40, 3419–3423.
117. Poggemann, D.W.; Hathorne, E.C.; Nürnberg, D.; Frank, M.; Bruhn, I.; Reißig, S.; Bahr, A. Rapid deglacial injection of nutrients into the tropical Atlantic via Antarctic Intermediate Water. Earth Planet. Sci. Lett. 2017, 463, 118–126.
118. Middag, R.; de Baar, H.J.W.; Bruland, K.W. The relationships between dissolved zinc and major nutrients phosphate and silicate along the GEOTRACES GA02 transect in the West Atlantic Ocean. Global Biogeochem. Cycles 2019, 33, 63–84.
119. Perez, J.A.A.; Alves, E.S.; Clark, M.R.; Bergstad, O.A.; Gebruk, A.; Cardoso, I.A.; Rogacheva, A. Patterns of life on the Southern Mid-Atlantic Ridge: compiling what is known and adressing future research. Oceanography 2012, 25, 16–31.
120. Behrenfeld, M.J.; Falkowski, P.G. Photosynthetic rates derived from satellite-based chlorophyll concentration. Limnol. Oceanogr. 1997, 42, 1–20.
121. Vilas, J.C.; Arístegui, J.; Kiriakoulakis, K.; Wolff, G.A.; Espino, M.; Polo, I.; Montero, M.F.; Mendonça, A. Seamounts and organic matter — Is there an effect ? The case of Sedlo and Seine Seamounts: Part 1. Distributions of dissolved and particulate organic matter. Deep. Res. Part II 2009, 56, 2618–2630.

2.7 Supplementary Materials

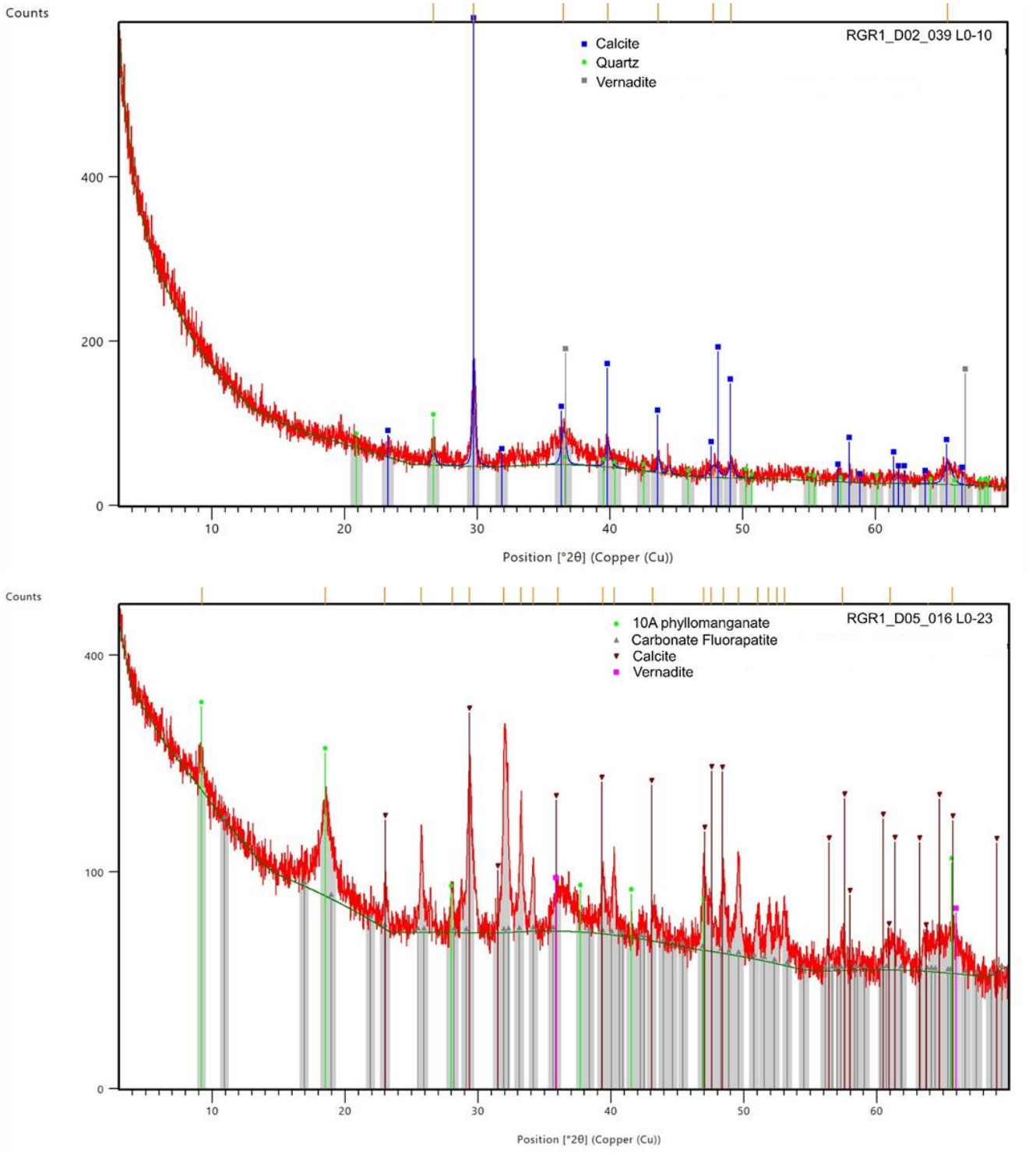

Figure S1: X-ray diffraction patterns of representative crusts: a non-phosphatized Fe–Mn crust (RGR1_D02_039 L0-10) and phosphatized crusts (RGR1_D05_016 L0-23). The Mn phase MnO2 corresponds to vernadite with reflections only at 2.45 Å (37°) and 1.42 Å.

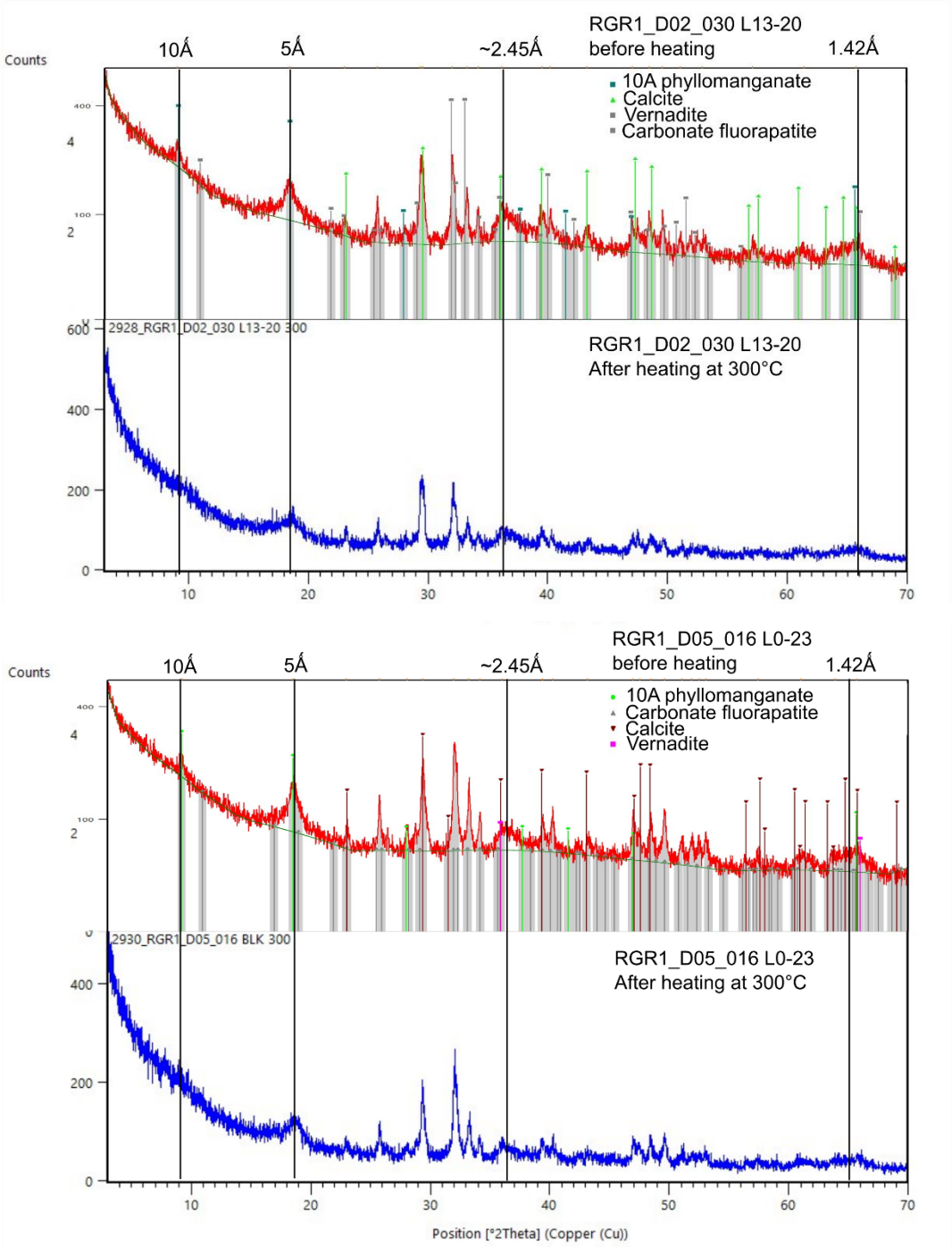

Figure S2: XRD patterns of phosphatized Fe–Mn crusts RGR1_D02_030 L13-20, RGR1_D05_011 L2-10, and RGR1_D05_016 L0-23 before and after heating the sample at 300 °C for 24 h. The collapse of the 10 Å peak after heating is observed in all three samples.

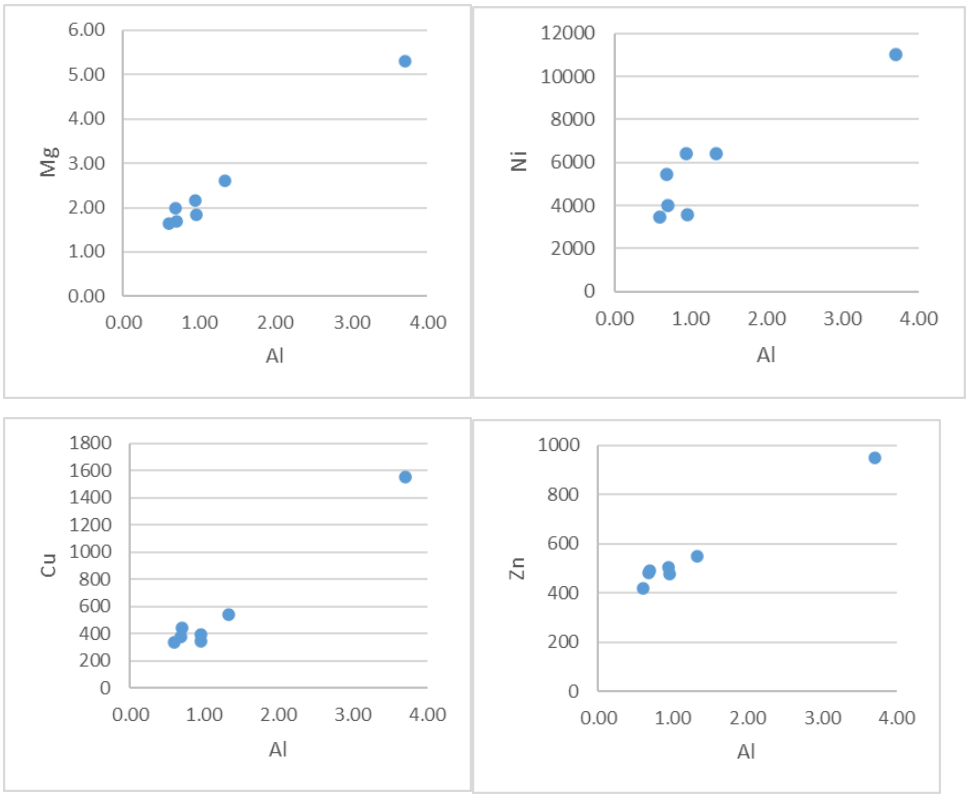

Figure S3: Plot of different metal concentrations showing the outlier sample RGR1_D10_002.

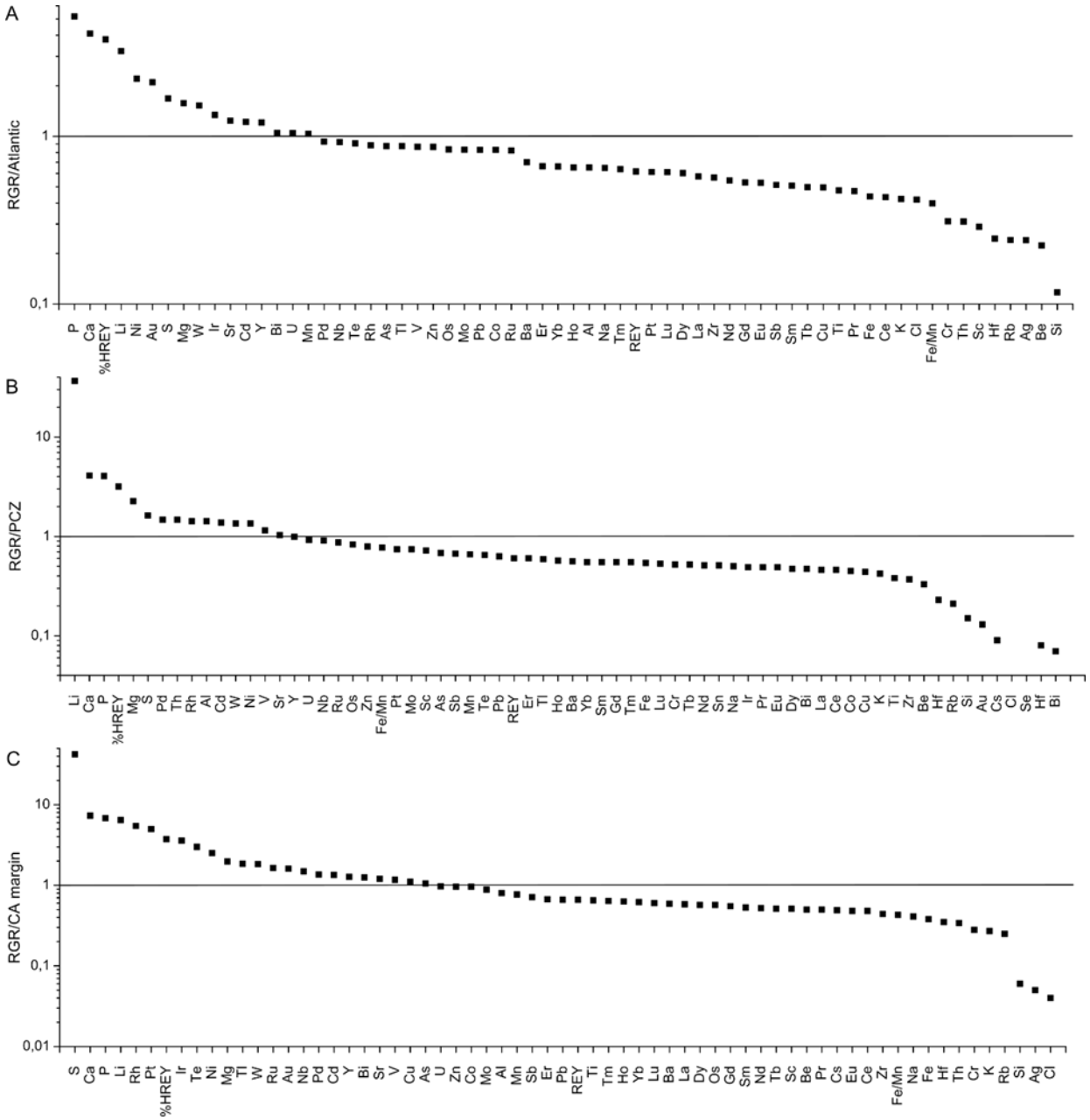

Figure S4: Element enrichments/depletions for (A) mean RGR crusts and mean Atlantic Ocean crusts; (B) mean RGR crusts and mean PCZ crusts; and (C) mean RGR crusts and mean CA margin crusts. Elements above the line are enriched in the RGR crusts. Chemical composition of mean Fe–Mn crusts from the Atlantic Ocean, PCZ, and California margin from Hein et al. (2013) and Conrad et al. (2017).

Table S1: Sorbed water-corrected chemical composition of ferromanganese crust samples.

Sample	RGR1_D02_030_L0-13	RGR1_D02_030_L13-20	RGR1_D02_039_L0-10	RGR1_D02_039_L10-15	RGR1_D05_011_L2-10Mn	RGR1_D05_016_L0-19	RGR1_D06_003_B0-8	RGR1_D07_002_L0-6	RGR1_D07_002_L6-18	RGR1_D07_002_L18-33	RGR1_D07_002_L33-55	RGR1_D07_003_L0-5	RGR1_D07_003_L5-20	RGR1_D09_001_L0-1	RGR1_D09_001_L1-13	RGR1_D09_001_L14-28	RGR1_D09_002_B0-10	RGR1_D10_002_L0-2	RGR1_D10_003-L0-2	RGR1_D10_003-L5-20	RGR1_D11_003-B0-20	RGR1_D15_017-B0-13	RGR1_D17_017-B0-14
Fe wt %	17.4	6.23	16.6	16.9	19.1	4.61	8.34	15.5	5.87	4.34	4.31	16.4	5.84	7.19	3.14	2.57	11.8	9.58	18.2	3.47	2.21	4.88	5.62
Mn	22.6	7.99	22.2	20.2	17.4	14.5	11.5	23.0	13.5	14.8	10.5	24.4	15.2	14.2	7.71	9.07	14.6	22.1	22.9	10.8	5.07	11.6	8.66
Fe/Mn	0.77	0.78	0.75	0.83	1.10	0.32	0.73	0.67	0.43	0.29	0.41	0.67	0.39	0.51	0.41	0.28	0.80	0.43	0.79	0.32	0.44	0.42	0.65
Si	0.75	1.14	0.73	0.81	0.45	0.68	0.47	0.60	0.58	0.47	0.43	0.48	0.56	0.49	0.52	0.49	0.73	0.69	0.56	0.41	0.50	0.83	0.66
Al	0.70	1.78	0.60	0.96	0.78	2.01	0.81	1.33	2.15	1.59	0.84	0.68	2.15	2.20	1.18	0.89	1.76	3.70	0.95	1.18	0.97	2.21	1.47
Si/Al	1.08	0.64	1.22	0.85	0.57	0.34	0.58	0.45	0.27	0.30	0.51	0.70	0.26	0.22	0.44	0.55	0.42	0.19	0.60	0.35	0.51	0.37	0.45
Mg	1.69	2.60	1.65	1.85	1.76	3.41	1.95	2.60	3.22	2.86	1.70	1.98	3.54	3.59	1.97	1.79	2.85	5.31	2.15	1.94	1.42	3.20	2.26
Ca	5.83	23.4	6.17	7.35	10.8	19.2	22.0	5.39	19.1	19.7	25.1	4.97	17.4	16.6	26.5	27.0	14.5	6.04	3.93	24.4	29.4	20.5	24.3
Na	1.30	0.43	1.36	1.20	0.42	0.56	0.60	1.18	0.59	0.83	0.80	1.30	0.68	0.72	0.82	0.79	0.69	0.85	1.24	0.73	0.62	0.57	0.47
K	0.32	0.22	0.32	0.29	0.15	0.26	0.21	0.30	0.20	0.23	0.26	0.31	0.20	0.17	0.17	0.24	0.27	0.20	0.30	0.09	0.12	0.22	0.20
Ti	1.04	0.28	1.00	0.96	0.06	0.21	0.05	1.03	0.21	0.23	0.06	1.05	0.30	0.40	0.15	0.07	0.35	0.67	1.41	0.12	0.10	0.21	0.09
P	0.49	2.90	0.48	0.43	2.50	3.82	5.47	0.70	4.55	6.30	7.07	0.46	4.81	5.60	7.67	7.17	3.20	0.66	0.54	7.47	6.81	5.43	4.88
S	0.37	0.33	0.38	0.43	0.22	0.36	0.41	0.40	0.34	0.46	0.54	0.40	0.41	0.43	0.59	0.58	0.30	0.40	0.39	0.66	0.51	0.40	0.35
V	0.12	0.05	0.10	0.12	0.12	0.05	0.07	0.11	0.06	0.05	0.04	0.12	0.06	0.07	0.03	0.03	0.09	0.10	0.12	0.05	0.02	0.06	0.05
CO^2	4.78	21.9	5.09	6.56	6.36	11.89	10.69	3.80	10.02	5.80	10.00	3.47	7.43	4.78	10.3	11.7	8.28	5.30	2.44	8.66	15.7	9.45	15.28
LOI^1	36.3	28.8	39.8	37.1	20.2	23.8	20.2	36.0	21.6	19.5	18.9	37.3	20.8	20.3	19.7	19.6	25.4	28.7	36.9	17.8	22.1	20.7	23.1
$H2O^-$	19.4	3.7	22.0	18.7	3.50	4.10	2.70	19.3	3.20	4.50	3.10	20.8	3.90	5.00	3.30	2.70	7.30	9.50	21.3	3.00	<0.1	3.60	2.50
$H2O^+$	14.2	7.3	14.8	14.2	9.00	7.70	7.40	15.9	8.50	8.80	6.80	16.4	9.30	10.0	6.90	6.20	10.3	13.4	11.3	6.70	5.00	8.40	6.65
Ag ppm	<0.02	<0.02	<0.02	<0.02	<0.02	<0.02	<0.02	<0.02	<0.02	<0.02	<0.02	<0.02	<0.02	<0.02	<0.02	<0.02	<0.02	<0.02	0.14	0.03	0.03	0.02	0.02
As	524	136	497	349	792	117	202	362	153	96	99	529	143	175	83	65	333	288	621	176	67	165	218
Ba	1453	281	1331	1428	4575	649	2159	1367	542	938	1618	1462	767	627	360	803	962	623	1338	775	180	348	481
Be	3.6	1.2	3.1	5.7	1.2	1.1	1.2	4.5	1.3	1.5	1.0	3.0	1.7	2.0	1.3	0.8	1.8	1.6	4.4	1.2	0.70	1.2	1.0
Bi	54	5.8	62	60	2.1	5.6	0.91	52	5.2	5.8	1.4	65	7.9	9.9	2.8	1.4	12	16	84	3.3	2.4	3.6	1.4
Cd	3.0	2.9	3.1	4.2	2.9	7.4	4.0	4.8	6.0	6.6	4.9	3.4	6.0	4.9	4.6	5.6	6.1	12.5	5.3	2.3	3.2	5.6	4.8
Cl	7943	1134	9017	7279	1083	1507	937	6834	1154	1279	819	7279	1209	1682	983	1076	2320	5794	7939	1271	812	887	938
Co	6825	1244	8586	6395	2396	1625	1454	5634	1555	1402	1017	6812	1832	2138	1046	956	2889	4503	5371	1238	912	1643	1392
Cr	12	16	10	31	30	3.1	28	11	19	7.3	12	10	14	8.4	11	4.1	23	6.6	14	9.3	7.0	29	19
Cs	0.25	0.31	0.13	0.25	<0.1	0.52	0.21	0.25	0.41	0.21	0.21	<0.1	0.31	0.21	0.31	0.31	0.54	0.33	<0.1	0.21	0.3	0.52	0.62
Cu	448	339	334	349	270	737	153	540	550	263	118	376	459	464	148	183	633	1557	391	151	232	711	384
F	340	7862	320	413	6659	9799	14362	1015	11595	14747	16915	308	11140	12512	17253	18539	8091	1161	321	16862	14599	11992	10233
Hf	6.7	0.73	5.8	4.6	0.28	1.0	0.16	5.2	0.36	0.24	0.07	5.9	0.30	3.7	1.1	0.07	0.84	5.4	5.1	0.10	0.78	0.24	0.38
Li	8.7	96	2.6	7.4	44	203	61	61	217	170	78	7.6	208	145	105	101	172	330	8.9	31	81	190	125

Mo	596	283	610	509	172	326	135	523	332	281	165	582	323	326	148	148	320	630	511	221	147	304	228
Nb	92	32	92	96	8.3	29	5.1	108	27	27	5.2	101	39	57	19	8.2	41	88	146	14	12	24	10
Ni	4001	4083	3452	3549	3775	8472	3880	6392	7019	8063	3911	5453	8280	8235	4033	4098	5811	11015	6428	6288	3000	7221	4354
Pb	2646	295	2849	2665	139	474	61	2616	380	480	97	3024	554	735	231	128	785	1055	3633	273	146	274	111
Rb	2.7	5.8	2.6	2.6	0.93	5.9	2.9	2.5	4.5	3.1	3.3	1.6	4.0	2.9	3.7	4.0	5.5	2.9	1.9	2.8	4.0	6.5	6.4
Sb	55	11	55	59	46	11	24	48	11	11	12	52	7.8	19	8.1	9.3	32	26	58	11	6.5	12	18
Sc	3.8	4.4	4.5	6.5	1.1	4.1	1.3	3.5	6.0	6.2	2.4	3.7	7.3	13	10	2.9	4.5	3.0	4.7	4.2	4.9	4.1	2.8
Se	0.25	<0.2	<0.2	<0.2	<0.2	<0.2	<0.2	<0.2	<0.2	<0.2	<0.2	<0.2	<0.2	0.21	0.31	0.21	<0.2	<0.2	<0.2	0.31	<0.2	<0.2	<0.2
Sn	7.1	5.5	7.0	6.8	1.0	4.9	0.41	8.6	7.2	14	0.62	6.4	2.1	7.7	1.8	0.92	3.6	4.8	12.3	1.4	1.5	1.5	9.9
Sr	2079	1241	2060	1918	1561	1145	1487	1740	1216	1671	1721	2101	1426	1478	2047	1807	1200	748	1931	1677	1436	1182	1018
Ta	1.6	0.12	1.5	2.2	0.07	0.10	<0.05	1.6	0.08	0.10	0.06	1.5	0.10	0.86	0.30	0.05	0.17	1.2	1.1	0.06	0.06	<0.05	<0.05
Te	86	20	95	101	10	31	4	86	20	13	5	103	25	37	8	8	36	46	106	5	7	20	11
Th	47	9.7	46	68	2.4	7.7	0.92	32	7.2	4.4	1.3	32	9.5	14	4.6	1.8	13	17	39	2.3	3.3	5.1	2.6
Tl	227	53	174	191	75	98	35	227	62	37	24	154	74	58	23	34	107	165	160	6.8	19	52	30
U	18	6.7	19	16	5.2	6.8	6.4	19	8.2	11	8.8	20	9.4	11	12	8.6	9.0	11	21	12	8.1	8.5	6.1
W	136	88	133	129	63	255	44	138	305	74	38	112	163	132	48	43	202	167	84	49	53	173	144
Zn	490	357	420	476	616	483	603	550	474	826	659	484	620	545	515	441	530	951	504	693	244	417	289
Zr	402	152	337	327	81	126	87	421	144	185	77	407	181	206	131	81	192	238	484	136	90	150	79
La	278	74.8	288	301	29.0	94.3	23.0	213	153	206	56.3	263	201	371	225	57.7	114	79.3	247	113	105	69.0	39.2
Ce	1741	275	1600	2159	58.8	247	34.1	1342	218	288	66.4	1402	335	426	146	82.4	425	570	1933	176	101	184	62.5
Pr	59.0	14.0	60.5	64.6	4.67	17.4	3.6	41.6	27.9	36.1	8.42	51.6	36.3	69.8	38.8	9.10	22.1	15.0	51.3	19.6	19.3	12.9	7.07
Nd	248	63.1	255	264	20.3	77.4	16.1	176	128	168	37.4	213	166	324	178	40.5	97.3	64.9	230	95.7	91.3	61.2	32.3
Sm	54.0	13.9	55.6	57.3	4.35	17.2	3.49	37.9	27.9	36.9	7.53	45.2	36.1	72.7	37.5	8.22	21.6	14.6	44.0	17.4	17.1	11.7	6.15
Eu	10.7	2.95	11.2	11.3	0.93	3.60	0.73	7.93	6.01	8.22	1.71	9.63	8.11	16.4	8.72	1.84	4.71	3.29	9.62	4.01	3.8	2.65	1.39
Gd	48.3	15.9	51.8	49.8	5.22	19.3	4.31	37.4	33.6	46.0	9.89	45.2	44.8	90.0	49.0	10.1	23.4	16.3	44.3	21.5	19.3	14.1	7.24
Tb	7.34	2.28	7.87	7.70	0.80	2.88	0.63	5.79	4.75	6.60	1.34	6.89	6.38	13.1	6.90	1.45	3.58	2.64	6.95	3.07	2.68	2.13	1.09
Dy	42.4	14.4	45.8	43.1	5.26	18.3	4.15	34.8	30.3	42.6	9.30	41.1	40.4	81.8	44.1	9.58	23.2	17.1	44.7	21.1	18.3	14.6	7.22
Y	174	123	192	170	47.3	174	40.7	171	290	429	104	191	386	802	450	110	198	120	224	229	180	154	69.5
Ho	8.49	3.21	9.43	8.52	1.21	4.06	0.95	7.32	6.81	9.80	2.20	8.62	9.05	18.7	10.3	2.26	5.18	3.92	9.66	5.02	4.05	3.40	1.62
Er	24.4	9.50	27.1	24.1	3.76	12.4	2.95	22.6	19.8	29.4	6.81	26.0	26.6	54.9	30.0	6.97	15.9	12.0	28.9	15.2	12.1	10.5	4.86
Tm	3.49	1.28	3.78	3.36	0.52	1.63	0.41	3.14	2.51	3.68	0.88	3.69	3.43	6.95	3.80	0.88	2.18	1.73	4.18	1.98	1.54	1.44	0.68
Yb	22.6	8.00	24.3	21.8	3.47	10.5	2.77	20.7	15.7	23.2	5.88	24.5	21.3	43.1	24.1	5.86	14.5	11.7	25.9	11.6	9.00	8.71	4.21
Lu	3.16	1.18	3.52	3.08	0.52	1.51	0.42	3.04	2.26	3.38	0.90	3.55	3.06	6.20	3.44	0.87	2.15	1.76	3.88	1.67	1.23	1.29	0.47
∑REY[2]	2724	622	2637	3189	186	702	138	2124	967	1337	319	2334	1324	2397	1256	348	974	935	2906	736	586	551	245
%HREY[3]	13	29	14	11	37	35	42	15	43	45	45	15	41	47	50	43	30	20	14	43	43	39	40
Au (ppb)	10	8	17	16	--	13	10	--	--	--	--	13	14	--	13	14	--	--	18	10	--	6	14
Ir	11	3	14	14	--	4	1	--	--	--	--	13	3	--	2	2	--	--	17	1	--	3	2
Os	--	--	4	4	--	--	--	--	--	--	--	--	1	--	--	--	--	--	1	--	--	1	1

Pd	10	4	5	16	--	5	7	--	--	--	--	4	2	--	5	6	--	--	5	3	--	4	2
Pt	666	191	604	626	--	405	49	--	--	--	--	641	252	--	84	91	--	--	765	84	--	273	128
Rh	55	22	64	71	--	21	3	--	--	--	--	67	19	--	6	4	--	--	94	6	--	18	7
Ru	27	6	37	28	--	6	1	--	--	--	--	37	6	--	1	2	--	--	46	3	--	4	3

[1]Loss on ignition at 1000°C

[2]∑ REY = Sum of rare earth elements plus yttrium

[3]Percent of heavy REY (Eu-Lu, +Y) of the total sum of REY

Table S2: Summary statistics for the chemical data.

	Bulk					*Bulk plus layers*					*Non-phosphatized*					*Phosphatized*				
	N	Min	Max	Mean	Std Dev	N	Min	Max	Mean	Std Dev	N	Min	Max	Mean	Std Dev	N	Min	Max	Mean	Std Dev
Fe (wt %)	14	2.21	19.1	8.37	5.2	29	2.21	19.1	9	5.7	6	15.5	18.2	16.8	0.91	16	2.21	19.1	6.22	4.18
Mn	14	5.07	22.1	13.69	5.05	29	5.07	24.4	14.9	5.63	6	20.2	24.4	22.6	1.39	16	5.07	17.4	11.7	3.39
Fe/Mn	14	0.32	1.1	0.56	0.24	29	0.28	1.1	0.56	0.22	6	0.67	0.83	0.75	0.07	16	0.28	1.1	0.52	0.23
Si	14	0.37	0.89	0.6	0.17	29	0.37	1.14	0.6	0.18	6	0.48	0.81	0.66	0.13	16	0.41	1.14	0.59	0.19
Al	14	0.72	3.7	1.46	0.81	29	0.6	3.7	1.36	0.69	6	0.6	1.33	0.87	0.27	16	0.78	2.21	1.5	0.55
Si/Al	14	0.19	1.1	0.5	0.24	29	0.19	1.22	0.53	0.27	6	0.45	1.22	0.82	0.3	16	0.22	0.64	0.42	0.13
Mg	14	1.42	5.31	2.46	1.04	29	1.42	5.31	2.4	0.86	6	1.65	2.6	1.99	0.35	16	1.42	3.59	2.5	0.74
Ca	14	6.04	29.4	17.2	6.97	29	3.93	29.4	16.3	7.94	6	3.93	7.35	5.61	1.15	16	10.8	29.4	21.2	4.96
Na	14	0.42	1.3	0.71	0.23	29	0.42	1.36	0.83	0.29	6	1.18	1.36	1.26	0.07	16	0.42	0.83	0.64	0.13
K	14	0.09	0.31	0.21	0.06	29	0.09	0.32	0.23	0.06	6	0.29	0.32	0.31	0.01	16	0.09	0.27	0.2	0.05
Ti	14	0.05	0.99	0.32	0.29	29	0.05	1.41	0.44	0.4	6	0.96	1.41	1.08	0.16	16	0.05	0.4	0.18	0.11
P	14	0.46	7.07	3.96	2.13	29	0.43	7.67	3.87	2.58	6	0.43	0.7	0.52	0.1	16	2.5	7.67	5.35	1.66
Ca/P	14	3.3	14.2	5.55	3.09	29	2.97	17.1	6.25	3.84	6	7.31	17.12	11.3	3.63	16	2.97	8.05	4.19	1.2
S	14	0.22	0.56	0.4	0.09	29	0.22	0.66	0.42	0.1	6	0.37	0.43	0.4	0.02	16	0.22	0.66	0.43	0.12
V	14	0.02	0.12	0.07	0.03	29	0.02	0.12	0.07	0.03	6	0.1	0.12	0.12	0.01	16	0.02	0.12	0.06	0.02
CO_2	14	5.3	15.7	9.29	3.37	29	2.44	21.9	8.51	4.18	6	2.44	6.56	4.36	1.44	16	4.78	21.9	10.5	4.27
LOI[1]	14	17	38.9	24	6.17	29	17	39.8	25.7	7.66	6	36	39.8	37.2	1.35	16	17.8	28.8	21.4	2.75
H_2O^-	13	2.5	20.9	6.76	5.38	28	2.5	22	8.63	7.31	6	18.7	22	20.2	1.29	15	2.5	7.3	3.74	1.2
H_2O^+	14	5	14.6	8.93	2.89	29	5	16.4	9.73	3.36	6	11.3	16.4	14.5	1.79	16	5	10.3	7.81	1.46
Ag (ppm)	4	0.02	0.04	0.03	0.01	6	0.02	0.14	0.05	0.05	1	0.14	0.14	0.14	-	4	0.02	0.03	0.03	0
As	14	67	792	261	190	29	64.7	792	264	188	6	349	621	480	105	16	65	792	189	174
Ba	14	180	4575	1116	1108	29	180	4575	1059	820	6	1331	1462	1396	58	16	180	4575	1004	1078
Be	14	0.7	3.94	1.61	0.84	29	0.7	5.66	2.03	1.29	6	3.03	5.66	4.04	1.01	16	0.7	2	1.29	0.34
Bi	14	0.91	61.2	13.3	17.1	29	0.91	83.5	20.9	25.4	6	51.5	83.5	62.7	11.3	16	0.91	12.4	4.5	3.31
Cd	14	2.28	12.5	5.00	2.58	29	2.28	12.5	4.75	2	6	2.98	5.26	3.96	0.95	16	2.34	7.43	4.88	1
Cl	14	812	8438	2515	2366	29	812	9017	3176	2939	6	6834	9017	7715	769	16	812	2320	1193	383
Co	14	912	7855	2612	1948	29	912	8586	3056	2395	6	5371	8586	6604	1142	16	912	2889	1546	547
Cr	14	3.13	30.1	15.4	9.08	29	3.13	30.8	14	7.67	6	10.1	30.8	14.8	7.96	16	3.13	30.1	15	9

Cu	14	152	1557	460	372	29	118	1557	398	279	6	334	540	407	76.4	16	118	737	362	209
F	14	351	17110	9228	5054	29	308	18539	8942	6305	6	308	1015	453	278	16	6659	18539	12697	3654
Hf	14	0.16	5.45	1.63	1.95	29	0.07	6.75	2.16	2.34	6	4.55	6.75	5.54	0.76	16	0.07	3.72	0.65	0.9
Li	14	4.17	330	117	88.1	29	2.56	330	99.3	81.7	6	2.56	60.7	16	22	16	30.93	217	127	61
Mo	14	135	630	307	161	29	135	630	340	165	6	509	610	555	45.7	16	135	332	241	78.2
Nb	14	5.14	93.5	35.6	29.8	29	5.14	146.12	46.9	39	6	91.8	146	106	20.6	16	5.14	56.8	22.4	14.8
Ni	14	3000	11015	5469	2304	29	3000	11015	5512	2020	6	3452	6428	4879	1385	16	3000	8472	5658	1967
Pb	14	60.5	2788	717	781	29	60.5	3633	1057	1128	6	2616	3633	2906	389	16	61	785	323	226
Rb	14	0.93	6.54	3.83	1.67	29	0.93	6.54	3.51	1.4	6	1.64	2.73	2.32	0.44	16	0.93	6.54	4.15	2
Sb	14	6.53	56.5	23.3	15.2	29	6.53	58.9	26	19.1	6	48.1	58.9	54.7	3.91	16	6.53	45.7	15.6	10.5
Sc	14	1.14	6.39	3.91	1.57	29	1.14	13.2	4.77	2.48	6	3.47	6.52	4.45	1.12	16	1.14	13.2	4.99	3.18
Se	1	0.24	0.24	0.24	--	6	0.21	0.31	0.25	0.05	1	0.25	0.25	0.25	-	4	0.21	0.31	0.26	0.1
Sr	14	748	2013	1411	342	29	748	2101	1581	355	6	1740	2101	1972	137	16	1018	2047	1457	281
Te	14	4.04	97.1	29.3	26.3	29	4.04	106	39	36	6	86	106	96.3	8.68	16	4.04	37.1	16.3	11.2
Th	14	0.92	53.3	12.1	14.7	29	0.92	68	16.8	18.6	6	31.6	68	44	13.5	16	0.92	13.9	5.59	4.1
Tl	14	19.5	180	80.2	56.6	29	6.84	227	90.6	68.6	6	154	227	189	32.1	16	6.84	107	49.3	28
U	14	5.25	17.9	9.55	3.44	29	5.25	20.5	11.5	4.59	6	16.5	20.5	18.8	1.4	16	5.25	11.7	8.58	2
W	14	44.2	255	121	65.9	29	38.2	305	116	65.5	6	83.9	138	122	20.9	16	38.18	305	117	83.2
Zn	14	244	951	510	168	29	244	951	524	143	6	420	550	487	42.2	16	244	826	520	151.9
Zr	14	79.3	334	165	85.6	29	77.3	484	206	120	6	327	484	396	57.9	16	77.3	206	131	44.7
La	14	23	293	115	76.8	29	23	371	161	96.1	6	213	301	265	31.8	16	23.02	371	121	91.9
Ce	14	34.1	1786	428	504	29	34.1	2159	627	676	6	1342	2159	1696	314	16	34.12	426	195	128
Pr	14	3.62	61.9	22	16.2	29	3.62	69.8	30.9	20.1	6	41.6	64.6	54.8	8.28	16	3.62	69.8	21.7	17.1
Nd	14	16.1	258	97.2	67.9	29	16.1	324	136	85.7	6	176	264	231	32.6	16	16.14	324	99.8	80
Sm	14	3.49	56.2	20.5	14.9	29	3.49	72.7	29	18.8	6	37.9	57.3	49	7.75	16	3.49	72.7	21.2	17.9
Eu	14	0.73	11.24	4.4	3.01	29	0.73	16.4	6.21	3.93	6	7.93	11.3	10.1	1.28	16	0.73	16.4	4.74	4.05
Gd	14	4.31	51.1	22.3	14.1	29	4.31	90	31.4	19.4	6	37.4	51.8	46.1	5.11	16	4.31	90	25.9	22.5
Tb	14	0.63	7.81	3.3	2.1	29	0.63	13.1	4.64	2.89	6	5.79	7.87	7.09	0.75	16	0.63	13.1	3.73	3.23
Dy	14	4.15	44.9	20.8	12.2	29	4.15	81.8	28.8	17.3	6	34.8	45.8	42	3.86	16	4.15	81.8	24	20.2
Y	14	40.7	337	164	81	29	40.7	802	219	151	6	170	224	187	20.6	16	40.7	802	237	199
Ho	14	0.95	9.13	4.58	2.53	29	0.95	18.7	6.33	3.76	6	7.32	9.66	8.67	0.83	16	0.95	18.7	5.49	4.62
Er	14	2.95	26.42	13.63	7.25	29	2.95	54.9	18.7	10.9	6	22.6	28.9	25.5	2.27	16	2.95	54.9	16.3	13.5
Tm	14	0.41	3.64	1.84	0.98	29	0.41	6.95	2.51	1.43	6	3.14	4.18	3.6	0.36	16	0.41	6.95	2.11	1.69
Yb	14	2.77	23.5	11.7	6.33	29	2.77	43.1	16	9.03	6	20.7	25.9	23.3	1.95	16	2.77	43.1	13.2	10.5
Lu	14	0.42	3.37	1.69	0.92	29	0.42	6.2	2.3	1.3	6	3.04	3.88	3.37	0.33	16	0.42	6.2	1.91	1.51
∑REY[2]	14	138	2821	931	742	29	138	3189	1319	940	6	2124	3189	2652	384	16	138	2397	793	582
%HREY[3]	14	13.1	44.7	33.1	9.6	29	10.7	50.2	32.1	12.8	6	10.7	15.4	13.6	1.69	16	29.1	50.2	40.8	5.67
Au (ppb)	8	6.22	16.4	11.5	3.27	18	6.22	17.8	12.5	3.21	5	9.93	17.8	14.6	3.24	9	6.22	14.4	11.5	2.88
Ir	8	1.03	13.9	5.07	4.25	18	1.03	16.5	6.66	5.43	5	11.2	16.5	13.6	1.98	9	1.03	4.17	2.42	1.05

Os	3	1.03	3.79	1.95	1.6	7	1.03	3.85	2.24	1.44	3	1.27	3.85	2.94	1.44	3	1.03	1.04	1.03	0.01
Pd	8	2.05	8.75	5.07	2.61	18	2.05	16	5.62	3.44	5	3.79	16	7.98	5.05	9	2.05	7.19	4.36	1.76
Pt	8	49.3	611	307	196	18	49.3	765	359	245	5	604	765	661	62.6	9	49.3	405	173	117
Rh	8	3.08	66.5	25.4	21	18	3.08	94	34	28.6	5	54.6	94	70.2	14.7	9	3.08	21.8	11.8	7.77
Ru	8	1.03	34.2	11.2	11.2	18	1.03	45.7	15.7	15.1	5	27.3	45.7	35	7.54	9	1.03	6.26	3.69	2.16

[1]Loss on ignition at 1000°C

[2]∑ REY = Sum of rare earth elements plus yttrium

[3]%HREY = percent of heavy REY (Eu-Lu+Y) complement of the total sum of REY

Dash means no statistic available due to low number of samples. H_2O^+ is structural water; H_2O^- is sorbed water

Table S3: Correlation coefficient matrix of the chemical data for non-phosphatized Fe–Mn crusts. Correlation coefficients in bold are within the 99% confidence level for N = 7.

	Fe	Mn	Si	Al	Mg	Ca	Na	K	Ti	P	S	V	CO2	As	Ba	Be	Bi	Cd	Cl	Co	Cr	Cu	F	Hf	In	Li
Fe																										
Mn	0.08																									
Si	-0.08	**-0.88**																								
Al	**-0.96**	-0.16	0.08																							
Mg	**-0.96**	-0.05	-0.03	**0.99**																						
Ca	-0.23	-0.78	0.84	0.13	0.04																					
Na	**0.91**	0.23	-0.09	**-0.98**	**-0.97**	-0.16																				
K	**0.92**	0.24	-0.11	**-0.98**	**-0.97**	-0.18	**0.98**																			
Ti	0.83	0.31	-0.42	-0.68	-0.65	-0.68	0.64	0.67																		
P	-0.61	0.19	-0.23	0.66	0.69	-0.25	-0.65	-0.54	-0.27																	
S	-0.17	-0.49	0.10	0.20	0.16	0.43	-0.34	-0.33	-0.24	-0.06																
V	0.68	0.12	-0.21	-0.57	-0.57	-0.24	0.44	0.49	0.60	-0.50	0.17															
CO2	-0.31	-0.81	0.87	0.22	0.13	**0.99**	-0.24	-0.28	-0.71	-0.25	0.40	-0.27														
As	0.74	0.51	-0.43	-0.68	-0.64	-0.68	0.72	0.68	0.84	-0.47	-0.57	0.48	-0.67													
Ba	**0.94**	0.15	-0.11	**-0.97**	**-0.96**	-0.10	**0.91**	**0.95**	0.66	-0.58	-0.06	0.68	-0.21	0.57												
Be	0.69	-0.43	0.21	-0.58	-0.63	0.16	0.43	0.51	0.52	-0.30	0.45	0.61	0.07	0.10	0.69											
Bi	**0.93**	0.20	-0.31	-0.86	-0.83	-0.45	0.81	0.80	**0.93**	-0.54	-0.09	0.62	-0.51	0.81	0.81	0.61										
Cd	**-0.91**	-0.15	0.03	**0.99**	**0.98**	0.04	**-0.97**	**-0.98**	-0.58	0.63	0.20	-0.53	0.14	-0.59	**-0.97**	-0.56	-0.77									
Cl	0.77	0.03	0.14	-0.81	-0.82	-0.09	**0.88**	0.81	0.57	-0.61	-0.49	0.13	-0.12	0.71	0.65	0.27	0.71	-0.78								
Co	0.54	0.01	0.23	-0.73	-0.73	0.26	0.81	0.73	0.14	-0.66	-0.33	-0.04	0.20	0.39	0.59	0.10	0.41	-0.76	0.84							
Cr	0.41	-0.73	0.49	-0.33	-0.40	0.53	0.18	0.19	0.14	-0.52	0.69	0.51	0.49	-0.15	0.41	0.83	0.32	-0.31	0.09	0.07						
Cu	**-0.96**	-0.08	0.08	**0.99**	**0.99**	0.11	**-0.95**	**-0.96**	-0.71	0.63	0.07	-0.58	0.21	-0.63	**-0.97**	-0.68	**-0.89**	**0.97**	-0.77	-0.67	-0.42					
F	-0.84	-0.07	0.01	0.84	0.85	0.12	-0.84	-0.76	-0.62	**0.90**	0.22	-0.57	0.14	-0.79	-0.74	-0.35	-0.80	0.78	-0.81	-0.68	-0.33	0.81				
Hf	0.10	0.51	-0.05	-0.22	-0.19	-0.16	0.34	0.32	-0.05	-0.17	-0.83	0.01	-0.14	0.41	0.15	-0.50	-0.08	-0.28	0.32	0.41	-0.57	-0.06	-0.27			
In	**-0.90**	-0.29	0.26	**0.95**	**0.93**	0.24	**-0.91**	**-0.96**	-0.70	0.44	0.12	-0.55	0.36	-0.60	**-0.97**	-0.62	-0.83	**0.95**	-0.66	-0.59	-0.25	**0.96**	0.66	-0.12		

Li	**-0.98**	-0.10	0.07	**0.99**	**0.99**	0.13	**-0.96**	**-0.96**	-0.72	0.65	0.12	-0.61	0.22	-0.66	**-0.98**	-0.66	**-0.89**	**0.97**	-0.78	-0.66	-0.41	**1.00**	0.83	-0.12	**0.95**	
Mo	-0.56	0.21	0.12	0.40	0.41	0.16	-0.24	-0.33	-0.62	0.05	-0.51	-0.60	0.23	-0.13	-0.52	**-0.91**	-0.61	0.34	-0.05	0.21	-0.66	0.52	0.17	0.66	0.52	0.50
Nb	0.46	0.27	-0.53	-0.25	-0.21	-0.78	0.19	0.23	0.87	0.09	-0.04	0.42	-0.77	0.59	0.25	0.38	0.69	-0.12	0.18	-0.31	0.05	-0.32	-0.24	-0.35	-0.34	-0.32
Ni	-0.85	0.17	-0.29	**0.92**	**0.95**	-0.26	**-0.90**	**-0.89**	-0.42	0.75	0.09	-0.43	-0.17	-0.44	**-0.88**	-0.61	-0.66	**0.94**	-0.80	-0.82	-0.51	**0.91**	0.79	-0.18	0.81	**0.91**
Pb	**0.94**	0.27	-0.35	**-0.88**	-0.85	-0.48	0.84	0.85	**0.93**	-0.49	-0.15	0.62	-0.55	0.82	0.85	0.59	**0.99**	-0.80	0.71	0.43	0.26	**-0.90**	-0.78	-0.01	**-0.88**	**-0.90**
Rb	-0.49	-0.66	0.83	0.48	0.40	0.69	-0.45	-0.43	-0.66	0.31	-0.04	-0.56	0.73	-0.67	-0.48	-0.14	-0.69	0.40	-0.20	-0.07	0.05	0.49	0.50	0.02	0.55	0.49
Sb	**0.98**	-0.07	0.05	**-0.95**	**-0.97**	-0.07	**0.89**	**0.90**	0.75	-0.69	-0.04	0.65	-0.14	0.64	**0.93**	0.75	**0.90**	**-0.91**	0.77	0.59	0.55	**-0.97**	-0.85	0.00	**-0.88**	**-0.97**
Sc	0.54	-0.69	0.46	-0.46	-0.53	0.43	0.35	0.32	0.29	-0.65	0.54	0.41	0.41	0.06	0.46	0.78	0.51	-0.41	0.38	0.29	**0.93**	-0.55	-0.53	-0.54	-0.34	-0.53
Sn	0.63	0.18	-0.36	-0.42	-0.40	-0.68	0.37	0.42	**0.93**	0.05	-0.17	0.42	-0.70	0.64	0.41	0.51	0.76	-0.32	0.38	-0.12	0.11	-0.48	-0.32	-0.25	-0.49	-0.49
Sr	**0.95**	0.19	-0.10	**-1.00**	**-0.99**	-0.14	**0.98**	**0.98**	0.68	-0.68	-0.21	0.60	-0.23	0.70	**0.97**	0.55	0.85	**-0.99**	0.80	0.72	0.31	**-0.98**	-0.86	0.26	**-0.94**	**-0.99**
Ta	0.30	-0.59	0.56	-0.37	-0.44	0.77	0.27	0.30	-0.20	-0.46	0.56	0.32	0.69	-0.36	0.48	0.65	0.07	-0.45	0.08	0.35	0.80	-0.42	-0.21	-0.25	-0.34	-0.40
Te	**0.94**	0.12	-0.23	**-0.92**	**-0.91**	-0.24	0.86	0.85	0.80	-0.65	0.07	0.66	-0.32	0.68	**0.90**	0.68	**0.96**	-0.86	0.68	0.52	0.46	**-0.95**	-0.82	-0.10	**-0.90**	**-0.95**
Th	0.67	-0.63	0.59	-0.65	-0.72	0.51	0.56	0.55	0.27	-0.72	0.29	0.47	0.47	0.14	0.65	0.78	0.50	-0.65	0.54	0.51	0.86	-0.69	-0.63	-0.20	-0.50	-0.69
Tl	0.19	-0.20	0.41	-0.19	-0.23	0.29	0.14	0.30	-0.06	0.25	-0.17	0.13	0.22	-0.23	0.32	0.39	-0.12	-0.30	0.02	0.05	0.14	-0.18	0.20	0.23	-0.26	-0.19
U	0.87	0.49	-0.49	-0.87	-0.82	-0.58	0.86	**0.88**	0.87	-0.33	-0.31	0.50	-0.66	0.81	0.84	0.44	**0.91**	-0.82	0.69	0.46	0.01	-0.86	-0.66	0.16	**-0.92**	-0.87
W	-0.78	-0.32	0.51	0.66	0.62	0.64	-0.61	-0.59	**-0.94**	0.43	0.05	-0.66	0.67	-0.83	-0.63	-0.47	**-0.94**	0.54	-0.50	-0.14	-0.22	0.69	0.70	0.14	0.66	0.70
Zn	**-0.95**	-0.07	0.02	**0.99**	**0.99**	0.07	**-0.97**	**-0.97**	-0.66	0.65	0.13	-0.51	0.16	-0.63	**-0.96**	-0.63	-0.85	**0.98**	-0.82	-0.74	-0.38	**0.99**	0.82	-0.13	**0.95**	**0.99**
Zr	0.79	0.51	-0.55	-0.68	-0.63	-0.73	0.64	0.71	**0.93**	-0.11	-0.29	0.65	-0.79	0.77	0.72	0.48	0.83	-0.62	0.43	0.09	0.01	-0.69	-0.48	0.10	-0.78	-0.71
La	**0.92**	-0.09	0.15	**-0.96**	**-0.98**	0.11	**0.92**	**0.91**	0.56	-0.78	-0.04	0.56	0.03	0.55	**0.93**	0.66	0.79	**-0.95**	0.80	0.75	0.53	**-0.96**	-0.86	0.12	-0.86	**-0.96**
Ce	**0.91**	-0.32	0.23	-0.82	-0.86	0.06	0.72	0.73	0.68	-0.69	0.12	0.68	0.01	0.50	0.82	0.85	0.82	-0.77	0.65	0.43	0.74	-0.86	-0.78	-0.17	-0.72	-0.87
Pr	**0.91**	-0.18	0.23	**-0.93**	**-0.97**	0.16	**0.90**	**0.88**	0.54	-0.80	-0.04	0.55	0.09	0.53	**0.90**	0.67	0.77	**-0.92**	0.80	0.74	0.57	**-0.94**	-0.87	0.10	-0.81	**-0.94**
Nd	**0.94**	-0.15	0.20	**-0.94**	**-0.97**	0.09	**0.91**	**0.89**	0.61	-0.78	-0.09	0.56	0.02	0.59	**0.90**	0.67	0.81	**-0.92**	0.83	0.72	0.54	**-0.95**	**-0.88**	0.10	-0.82	**-0.95**
Sm	**0.89**	-0.20	0.29	**-0.92**	**-0.96**	0.21	**0.90**	**0.88**	0.49	-0.79	-0.08	0.50	0.14	0.50	**0.88**	0.64	0.72	**-0.92**	0.82	0.78	0.55	**-0.92**	-0.85	0.15	-0.80	**-0.92**
Eu	**0.92**	-0.12	0.19	**-0.95**	**-0.98**	0.11	**0.92**	**0.90**	0.58	-0.79	-0.09	0.53	0.03	0.57	**0.91**	0.64	0.79	**-0.94**	0.83	0.76	0.52	**-0.95**	**-0.88**	0.13	-0.84	**-0.96**
Gd	**0.93**	-0.06	0.13	**-0.97**	**-0.99**	0.06	**0.95**	**0.93**	0.59	-0.77	-0.13	0.51	-0.02	0.61	**0.92**	0.61	0.81	**-0.95**	0.85	0.78	0.46	**-0.96**	**-0.88**	0.16	-0.86	**-0.97**
Tb	**0.94**	-0.07	0.13	**-0.97**	**-0.99**	0.05	**0.94**	**0.92**	0.62	-0.77	-0.11	0.53	-0.03	0.61	**0.92**	0.63	0.83	**-0.95**	0.85	0.76	0.48	**-0.97**	**-0.88**	0.13	-0.86	**-0.97**
Dy	**0.97**	0.02	0.01	**-0.97**	**-0.98**	-0.12	**0.95**	**0.93**	0.74	-0.72	-0.16	0.55	-0.18	0.72	**0.91**	0.62	**0.90**	**-0.93**	0.87	0.70	0.41	**-0.97**	**-0.90**	0.11	**-0.88**	**-0.98**
Y	**0.88**	0.32	-0.40	-0.81	-0.77	-0.57	0.80	0.78	**0.95**	-0.45	-0.24	0.51	-0.62	**0.88**	0.74	0.46	**0.98**	-0.71	0.74	0.41	0.14	-0.83	-0.77	0.01	-0.79	-0.83
Ho	**0.97**	0.11	-0.10	**-0.95**	**-0.95**	-0.24	**0.94**	**0.91**	0.81	-0.67	-0.20	0.53	-0.30	0.78	**0.88**	0.58	**0.95**	**-0.90**	0.87	0.66	0.34	**-0.96**	**-0.89**	0.09	**-0.88**	**-0.96**
Er	**0.96**	0.21	-0.22	**-0.94**	**-0.93**	-0.35	**0.93**	**0.91**	0.85	-0.60	-0.21	0.54	-0.41	0.81	**0.88**	0.56	**0.97**	**-0.88**	0.83	0.61	0.27	**-0.95**	-0.85	0.08	**-0.90**	**-0.95**
Tm	**0.96**	0.23	-0.25	**-0.93**	**-0.91**	-0.39	**0.91**	**0.90**	**0.88**	-0.59	-0.24	0.57	-0.45	0.85	0.86	0.54	**0.98**	-0.86	0.82	0.57	0.25	**-0.93**	-0.86	0.10	**-0.88**	**-0.94**
Yb	**0.96**	0.27	-0.27	**-0.95**	**-0.93**	-0.37	**0.94**	**0.92**	0.84	-0.61	-0.22	0.58	-0.44	0.83	**0.89**	0.53	**0.96**	**-0.89**	0.81	0.61	0.24	**-0.95**	-0.86	0.13	**-0.91**	**-0.96**
Lu	**0.93**	0.31	-0.34	**-0.91**	**-0.88**	-0.45	**0.90**	**0.88**	**0.88**	-0.55	-0.22	0.54	-0.52	0.85	0.85	0.50	**0.98**	-0.84	0.79	0.55	0.19	**-0.92**	-0.82	0.08	**-0.89**	**-0.92**
REY	**0.94**	-0.24	0.19	**-0.88**	**-0.92**	0.04	0.81	0.81	0.69	-0.72	0.05	0.66	-0.02	0.56	0.87	0.80	0.85	-0.84	0.73	0.53	0.67	**-0.92**	-0.83	-0.08	-0.78	**-0.92**
HREY	**-0.88**	0.33	-0.31	0.85	**0.90**	-0.22	-0.77	-0.79	-0.53	0.69	-0.14	-0.64	-0.15	-0.38	**-0.88**	-0.84	-0.72	0.85	-0.64	-0.54	-0.74	**0.89**	0.74	0.08	0.77	**0.89**
Pt	0.91	0.27	-0.45	0.56	0.76	-0.79	-0.40	-0.26	0.96	0.83	-0.19	0.50	-0.75	0.71	-0.28	0.18	0.80	0.77	-0.14	-0.81	-0.13	0.47	-0.26	-0.14	0.09	0.67
Rh	0.64	0.02	-0.43	0.71	0.86	-0.58	-0.52	-0.62	0.85	0.55	0.27	0.24	-0.57	0.40	-0.55	0.40	**0.96**	**0.96**	-0.12	-0.68	0.16	-0.19	-0.07	-0.68	0.06	0.30
Ru	0.39	0.49	-0.71	0.13	0.69	-0.81	0.08	-0.07	0.81	0.70	-0.17	-0.14	-0.82	0.73	-0.67	-0.23	0.92	0.60	0.25	-0.26	-0.43	-0.22	-0.63	-0.25	-0.41	-0.04

Table S6 [continue]

	Sc	Sn	Sr	Ta	Te	Th	Tl	U	W	Zn	Zr	La	Ce	Pr	Nd	Sm	Eu	Gd	Tb	Dy	Y	Ho	Er	Tm	Yb	Lu
Sn	0.23																									
Sr	0.44	0.40																								
Ta	0.67	-0.31	0.36																							
Te	0.60	0.58	**0.91**	0.32																						
Th	**0.91**	0.14	0.63	0.79	0.63																					
Tl	-0.04	0.00	0.18	0.44	-0.06	0.27																				
U	0.17	0.70	0.86	-0.05	0.87	0.26	0.04																			
W	-0.38	-0.81	-0.66	0.15	-0.85	-0.28	0.32	-0.83																		
Zn	-0.53	-0.43	**-0.98**	-0.42	**-0.92**	-0.69	-0.19	-0.85	0.64																	
Zr	0.07	0.84	0.69	-0.17	0.73	0.14	0.15	**0.90**	-0.84	-0.64																
La	0.66	0.31	**0.96**	0.55	**0.89**	0.82	0.19	0.71	-0.57	**-0.97**	0.51															
Ce	0.83	0.53	0.80	0.52	0.86	**0.89**	0.18	0.61	-0.67	-0.84	0.55	**0.89**														
Pr	0.70	0.30	**0.93**	0.57	0.86	0.87	0.20	0.66	-0.54	**-0.95**	0.46	**0.99**	**0.91**													
Nd	0.69	0.38	**0.94**	0.50	**0.88**	0.84	0.18	0.70	-0.60	**-0.95**	0.52	**0.99**	**0.93**	**1.00**												
Sm	0.67	0.25	**0.92**	0.59	0.82	0.87	0.24	0.63	-0.48	**-0.94**	0.42	**0.99**	**0.89**	**1.00**	**0.99**											
Eu	0.66	0.33	**0.95**	0.52	**0.88**	0.83	0.18	0.70	-0.57	**-0.96**	0.50	**1.00**	**0.90**	**1.00**	**1.00**	**0.99**										
Gd	0.62	0.34	**0.96**	0.48	**0.89**	0.79	0.16	0.74	-0.59	**-0.98**	0.53	**0.99**	**0.88**	**0.99**	**0.99**	**0.99**	**1.00**									
Tb	0.64	0.37	**0.96**	0.48	**0.90**	0.80	0.15	0.75	-0.61	**-0.98**	0.54	**0.99**	**0.89**	**0.99**	**0.99**	**0.98**	**1.00**	**1.00**								
Dy	0.59	0.51	**0.96**	0.34	**0.94**	0.72	0.08	0.83	-0.72	**-0.98**	0.65	**0.97**	**0.89**	**0.96**	**0.98**	**0.94**	**0.97**	**0.98**	**0.98**							
Y	0.36	0.79	0.80	-0.11	**0.89**	0.36	-0.18	**0.93**	**-0.94**	-0.80	0.85	0.71	0.71	0.68	0.73	0.64	0.72	0.74	0.76	0.86						
Ho	0.54	0.59	**0.95**	0.22	**0.95**	0.64	0.00	**0.88**	-0.80	**-0.96**	0.71	**0.92**	0.86	**0.91**	**0.94**	**0.89**	**0.93**	**0.95**	**0.95**	**0.99**	**0.92**					
Er	0.47	0.65	**0.94**	0.14	**0.96**	0.55	-0.02	**0.93**	-0.84	**-0.94**	0.78	**0.88**	0.82	0.86	**0.89**	0.83	**0.88**	**0.91**	**0.91**	**0.97**	**0.95**	**0.99**				
Tm	0.45	0.67	**0.92**	0.09	**0.95**	0.52	-0.04	**0.93**	-0.87	**-0.92**	0.80	0.86	0.81	0.83	0.87	0.80	0.86	**0.89**	**0.89**	**0.96**	**0.97**	**0.99**	**1.00**			
Yb	0.43	0.62	**0.95**	0.14	**0.96**	0.52	-0.03	**0.94**	-0.84	**-0.94**	0.79	**0.88**	0.79	0.85	**0.88**	0.82	**0.88**	**0.90**	**0.91**	**0.96**	**0.95**	**0.98**	**1.00**	**1.00**		
Lu	0.40	0.68	**0.91**	0.05	**0.95**	0.45	-0.09	**0.96**	**-0.88**	**-0.90**	0.82	0.82	0.76	0.79	0.83	0.75	0.82	0.85	0.86	**0.93**	**0.98**	**0.97**	**0.99**	**0.99**	**0.99**	
REY	0.78	0.51	0.87	0.51	**0.90**	0.87	0.17	0.68	-0.68	**-0.90**	0.57	**0.94**	**0.99**	**0.95**	**0.97**	**0.93**	**0.95**	**0.93**	**0.95**	**0.94**	0.75	**0.91**	0.87	0.86	0.85	0.81
HREY	-0.79	-0.36	-0.84	-0.68	-0.82	**-0.93**	-0.34	-0.57	0.51	**0.88**	-0.47	**-0.94**	**-0.96**	**-0.95**	**-0.95**	**-0.94**	**-0.94**	**-0.91**	**-0.92**	**-0.88**	-0.60	-0.82	-0.77	-0.75	-0.76	-0.69
Pt	-0.13	0.93	-0.43	-0.66	0.37	-0.36	-0.19	0.60	-0.84	0.74	0.93	-0.81	0.28	-0.65	-0.42	-0.70	-0.68	-0.77	-0.68	0.11	0.75	0.47	0.60	0.71	0.59	0.62
Rh	0.30	0.88	-0.72	-0.45	0.82	-0.15	-0.62	0.51	-0.91	0.41	0.62	-0.60	0.40	-0.49	-0.29	-0.60	-0.52	-0.58	-0.43	0.35	0.82	0.67	0.74	0.76	0.65	0.72
Ru	-0.22	0.75	-0.18	-0.82	0.68	-0.64	-0.81	0.89	-0.86	0.10	0.66	-0.78	-0.19	-0.75	-0.58	-0.77	-0.67	-0.55	-0.49	0.43	**0.98**	0.85	**0.98**	**0.97**	**0.97**	**0.99**

Table S6 [continue]

	REY	HREY	Pt	Rh
HREY	**-0.97**			
Pt	0.19	0.21		
Rh	0.35	0.11	0.76	
Ru	-0.22	0.66	0.61	0.79

Table S4: Correlation coefficient matrix of the chemical data for phosphatized Fe–Mn crusts. Correlation coefficients in bold are within the 99% confidence level for N = 16.

	Fe	Mn	Si	Al	Mg	Ca	Na	K	Ti	P	S	V	CO2	As	Ba	Be	Bi	Cd	Cl	Co	Cr	Cu	F	Hf	Li	Mo
Mn	0.64																									
Si	0.02	-0.15																								
Al	-0.13	0.32	0.59																							
Mg	-0.02	0.54	0.45	**0.95**																						
Ca	**-0.83**	**-0.92**	-0.08	-0.34	-0.50																					
Na	-0.51	-0.10	-0.54	-0.20	-0.14	0.35																				
K	0.01	0.27	0.35	0.32	0.45	-0.22	0.11																			
Ti	0.02	0.33	0.59	**0.82**	**0.79**	-0.41	-0.01	0.36																		
P	**-0.73**	-0.54	-0.57	-0.40	-0.45	**0.76**	**0.77**	-0.29	-0.45																	
S	**-0.74**	-0.54	-0.47	-0.38	-0.43	**0.76**	**0.76**	-0.32	-0.35	**0.95**																
V	**0.95**	**0.77**	0.04	0.06	0.19	**-0.92**	-0.47	0.06	0.15	**-0.74**	**-0.74**															
CO2	-0.31	**-0.72**	**0.64**	0.01	-0.17	0.54	-0.46	0.00	-0.02	-0.14	-0.05	-0.44														
As	**0.96**	0.57	-0.09	-0.22	-0.14	**-0.75**	-0.52	-0.19	-0.14	-0.61	-0.62	**0.90**	-0.33													
Ba	**0.83**	0.55	-0.39	-0.51	-0.33	-0.59	-0.27	-0.10	-0.42	-0.35	-0.39	**0.76**	-0.44	**0.86**												
Be	0.36	**0.65**	0.15	0.52	0.62	**-0.67**	0.14	0.25	**0.75**	-0.38	-0.34	0.51	-0.50	0.20	0.05											
Bi	0.19	0.46	0.40	**0.66**	**0.68**	-0.53	0.05	0.36	**0.94**	-0.48	-0.37	0.30	-0.17	0.02	-0.24	**0.80**										
Cd	-0.19	0.42	0.04	0.57	**0.70**	-0.25	0.30	**0.74**	0.45	-0.08	-0.17	-0.07	-0.34	-0.31	-0.29	0.35	0.44									
Cl	0.32	0.49	0.20	0.36	0.43	-0.54	0.08	0.36	**0.68**	-0.45	-0.32	0.41	-0.25	0.19	-0.04	**0.66**	**0.86**	0.38								
Co	**0.80**	**0.75**	0.16	0.32	0.41	**-0.91**	-0.32	0.24	0.49	**-0.74**	**-0.72**	**0.88**	-0.44	**0.70**	0.44	**0.69**	**0.66**	0.22	**0.73**							
Cr	**0.71**	0.33	0.21	0.06	0.07	-0.55	-0.53	0.01	0.00	-0.52	-0.62	**0.75**	-0.16	**0.65**	0.50	0.30	0.02	-0.22	0.00	0.58						
Cu	0.14	0.42	0.54	**0.85**	**0.83**	-0.50	-0.38	0.43	**0.66**	-0.59	-0.59	0.29	-0.04	0.06	-0.26	0.37	0.61	0.61	0.49	0.55	0.22					
F	**-0.69**	-0.48	-0.58	-0.46	-0.46	**0.73**	**0.80**	-0.18	-0.48	**0.97**	**0.94**	**-0.70**	-0.15	-0.61	-0.28	-0.38	-0.49	-0.04	-0.41	**-0.74**	-0.52	-0.62				
Hf	-0.05	-0.20	0.40	0.25	0.17	0.03	-0.13	0.06	0.42	-0.24	-0.18	-0.15	0.35	-0.11	-0.34	0.12	0.40	0.14	0.35	0.13	-0.21	0.33	-0.31			
Li	-0.16	0.39	0.33	**0.88**	**0.90**	-0.33	0.02	0.53	**0.71**	-0.28	-0.35	0.00	-0.18	-0.28	-0.44	0.48	0.61	**0.86**	0.37	0.31	-0.05	**0.81**	-0.30	0.24		
Mo	0.04	0.51	0.53	**0.95**	**0.94**	-0.51	-0.21	0.37	**0.85**	-0.53	-0.47	0.24	-0.09	-0.06	-0.35	0.61	**0.78**	0.56	0.55	0.48	0.06	**0.84**	-0.56	0.18	**0.83**	
Nb	0.03	0.38	0.55	**0.84**	**0.83**	-0.44	-0.02	0.34	**0.99**	-0.46	-0.36	0.16	-0.05	-0.12	-0.40	**0.75**	**0.93**	0.49	**0.67**	0.49	-0.03	**0.68**	-0.49	0.45	**0.74**	**0.86**
Ni	-0.14	0.61	0.09	**0.79**	**0.88**	-0.43	0.14	0.26	0.62	-0.16	-0.13	0.10	-0.45	-0.18	-0.27	0.56	0.57	**0.68**	0.40	0.30	-0.15	**0.65**	-0.17	-0.02	**0.78**	**0.83**
Pb	0.12	0.53	0.28	**0.69**	**0.74**	-0.53	0.15	0.36	**0.91**	-0.39	-0.30	0.26	-0.31	-0.02	-0.26	**0.80**	**0.97**	0.56	**0.86**	0.62	-0.08	0.64	-0.40	0.37	**0.69**	**0.80**
Rb	-0.36	-0.27	**0.74**	**0.67**	0.53	0.16	-0.26	0.45	0.49	-0.23	-0.22	-0.28	0.51	-0.43	**-0.72**	0.01	0.33	0.42	0.20	0.01	-0.04	**0.69**	-0.29	0.38	0.59	0.56
Sb	**0.96**	0.54	-0.08	-0.29	-0.18	**-0.72**	-0.44	0.02	-0.13	-0.61	-0.64	**0.91**	-0.32	**0.93**	**0.83**	0.25	0.08	-0.22	0.33	**0.76**	**0.69**	0.05	-0.57	-0.08	-0.28	-0.11
Sc	-0.44	-0.13	0.06	0.43	0.36	0.16	0.44	-0.12	0.52	0.29	0.30	-0.40	-0.09	-0.46	-0.57	0.40	0.39	0.28	0.11	-0.15	-0.38	0.10	0.20	0.51	0.45	0.29
Sn	-0.12	0.16	0.19	0.41	0.41	-0.12	-0.05	0.23	0.34	-0.18	-0.26	-0.06	0.05	-0.15	-0.27	0.24	0.26	0.40	0.18	0.02	-0.18	0.22	-0.22	0.07	0.44	0.47
Sr	-0.19	-0.17	-0.61	-0.62	-0.55	0.33	**0.71**	-0.26	-0.40	**0.68**	**0.70**	-0.28	-0.34	-0.12	0.19	-0.11	-0.36	-0.23	-0.27	-0.41	-0.35	**-0.77**	**0.73**	-0.16	-0.49	**-0.65**
Te	0.20	0.48	0.56	**0.80**	**0.82**	-0.57	-0.22	0.52	**0.86**	**-0.65**	-0.57	0.32	-0.04	0.05	-0.24	0.60	**0.87**	0.60	**0.75**	**0.66**	0.08	**0.88**	**-0.65**	0.47	**0.77**	**0.86**
Th	0.15	0.30	0.63	**0.75**	**0.72**	-0.44	-0.15	0.38	**0.95**	-0.59	-0.47	0.22	0.09	-0.02	-0.34	**0.68**	**0.94**	0.39	**0.73**	0.56	0.05	**0.69**	-0.60	0.55	**0.65**	**0.79**
Tl	0.55	**0.69**	0.38	0.55	**0.66**	**-0.79**	-0.35	0.52	0.63	**-0.81**	**-0.76**	0.61	-0.19	0.40	0.20	0.55	**0.72**	0.52	**0.70**	**0.82**	0.27	**0.77**	**-0.76**	0.36	0.60	**0.66**
U	-0.52	-0.13	-0.31	0.06	0.02	0.30	**0.83**	-0.21	0.22	**0.69**	**0.74**	-0.43	-0.38	-0.47	-0.43	0.30	0.20	0.09	0.13	-0.26	-0.46	-0.25	0.64	0.02	0.06	0.02

W	0.07	0.43	0.36	**0.83**	**0.82**	-0.45	-0.31	0.36	0.59	-0.52	-0.54	0.22	-0.06	-0.01	-0.28	0.37	0.56	0.63	0.45	0.46	0.13	**0.89**	-0.53	0.28	**0.84**	**0.83**
Zn	0.20	0.62	-0.51	-0.12	0.10	-0.39	0.51	0.06	0.04	0.16	0.18	0.31	**-0.76**	0.16	0.42	0.52	0.15	0.14	0.21	0.20	-0.02	-0.26	0.22	-0.41	-0.06	0.05
Zr	-0.03	0.39	0.37	**0.74**	**0.74**	-0.39	0.20	0.20	**0.93**	-0.23	-0.15	0.14	-0.26	-0.16	-0.37	**0.83**	**0.87**	0.40	0.62	0.42	-0.01	0.49	-0.27	0.25	0.63	**0.78**
La	-0.35	0.10	-0.12	0.40	0.40	0.01	0.55	-0.10	0.53	0.28	0.28	-0.28	-0.32	-0.38	-0.43	0.53	0.47	0.35	0.21	-0.05	-0.41	0.05	0.22	0.34	0.46	0.34
Ce	0.03	0.40	0.44	**0.73**	**0.74**	-0.43	0.12	0.33	**0.97**	-0.38	-0.26	0.16	-0.14	-0.12	-0.37	**0.78**	**0.97**	0.46	**0.77**	0.51	-0.10	0.59	-0.40	0.37	**0.65**	**0.82**
Pr	-0.33	0.12	-0.07	0.46	0.44	-0.03	0.51	-0.08	0.59	0.22	0.23	-0.26	-0.30	-0.37	-0.45	0.56	0.52	0.37	0.26	-0.01	-0.38	0.12	0.16	0.37	0.50	0.39
Nd	-0.34	0.10	-0.09	0.45	0.43	-0.01	0.51	-0.12	0.57	0.25	0.26	-0.27	-0.30	-0.37	-0.45	0.54	0.50	0.34	0.24	-0.03	-0.39	0.10	0.18	0.36	0.49	0.38
Sm	-0.30	0.16	-0.06	0.47	0.47	-0.07	0.49	-0.04	0.61	0.18	0.19	-0.23	-0.31	-0.35	-0.42	0.59	0.54	0.40	0.27	0.02	-0.37	0.13	0.13	0.36	0.53	0.42
Eu	-0.31	0.14	-0.08	0.45	0.45	-0.04	0.51	-0.06	0.58	0.22	0.22	-0.24	-0.32	-0.35	-0.42	0.58	0.52	0.38	0.25	0.00	-0.37	0.10	0.16	0.36	0.50	0.39
Gd	-0.31	0.14	-0.10	0.43	0.44	-0.04	0.52	-0.06	0.55	0.23	0.23	-0.24	-0.33	-0.36	-0.40	0.57	0.48	0.37	0.21	-0.03	-0.36	0.08	0.18	0.33	0.49	0.37
Tb	-0.30	0.16	-0.08	0.45	0.46	-0.06	0.51	-0.04	0.58	0.21	0.21	-0.22	-0.34	-0.34	-0.40	0.59	0.51	0.39	0.24	0.01	-0.35	0.10	0.15	0.34	0.51	0.39
Dy	-0.31	0.15	-0.09	0.44	0.45	-0.05	0.53	-0.06	0.57	0.23	0.23	-0.24	-0.34	-0.35	-0.41	0.58	0.50	0.38	0.24	0.00	-0.36	0.10	0.17	0.33	0.50	0.38
Y	-0.36	0.12	-0.15	0.39	0.40	0.01	0.58	-0.10	0.50	0.32	0.32	-0.29	-0.37	-0.38	-0.41	0.52	0.42	0.36	0.17	-0.08	-0.39	0.04	0.26	0.28	0.45	0.32
Ho	-0.32	0.14	-0.11	0.42	0.43	-0.03	0.54	-0.07	0.55	0.26	0.26	-0.24	-0.35	-0.35	-0.41	0.57	0.48	0.37	0.23	-0.02	-0.36	0.07	0.20	0.32	0.48	0.36
Er	-0.32	0.15	-0.11	0.43	0.43	-0.04	0.55	-0.06	0.56	0.26	0.26	-0.24	-0.36	-0.35	-0.41	0.58	0.49	0.38	0.24	-0.01	-0.37	0.08	0.20	0.32	0.48	0.37
Tm	-0.31	0.16	-0.08	0.45	0.45	-0.06	0.54	-0.06	0.59	0.24	0.24	-0.22	-0.36	-0.34	-0.41	0.60	0.52	0.38	0.27	0.02	-0.35	0.11	0.17	0.33	0.50	0.40
Yb	-0.28	0.18	-0.08	0.45	0.46	-0.08	0.55	-0.01	0.60	0.22	0.22	-0.20	-0.37	-0.33	-0.40	0.62	0.54	0.41	0.30	0.04	-0.34	0.12	0.16	0.34	0.51	0.40
Lu	-0.27	0.21	-0.08	0.45	0.47	-0.10	0.56	0.01	0.61	0.21	0.22	-0.18	-0.39	-0.32	-0.38	0.64	0.55	0.42	0.32	0.06	-0.33	0.12	0.16	0.33	0.51	0.40
REY	-0.27	0.21	0.03	0.55	0.55	-0.13	0.48	0.02	**0.71**	0.12	0.15	-0.17	-0.31	-0.34	-0.45	**0.66**	**0.65**	0.42	0.39	0.11	-0.35	0.22	0.06	0.37	0.57	0.52
HREY	-0.48	-0.26	**-0.74**	-0.37	-0.36	0.49	0.64	-0.34	-0.52	**0.84**	**0.69**	-0.49	-0.36	-0.36	-0.08	-0.26	-0.55	0.00	-0.57	-0.60	-0.32	-0.56	**0.82**	-0.28	-0.17	-0.51

Table S7 [continue]

	Nb	Ni	Pb	Rb	Sb	Sc	Sn	Sr	Te	Th	Tl	U	W	Zn	Zr	La	Ce	Pr	Nd	Sm	Eu	Gd	Tb	Dy	Y	Ho
Ni	**0.67**																									
Pb	**0.92**	**0.70**																								
Rb	0.47	0.27	0.31																							
Sb	-0.14	-0.25	0.02	-0.36																						
Sc	0.55	0.35	0.45	0.15	-0.55																					
Sn	0.33	0.40	0.32	0.28	-0.13	0.22																				
Sr	-0.40	-0.30	-0.31	**-0.69**	-0.15	0.27	-0.32																			
Te	**0.88**	0.62	**0.86**	0.58	0.09	0.23	0.23	-0.62																		
Th	**0.95**	0.47	**0.87**	0.51	0.00	0.43	0.21	-0.47	**0.92**																	
Tl	**0.67**	0.46	**0.71**	0.28	0.44	-0.03	0.08	-0.53	**0.89**	**0.75**																
U	0.21	0.29	0.29	-0.15	-0.50	**0.69**	0.03	0.59	-0.12	0.04	-0.38															
W	0.63	**0.65**	0.60	0.58	-0.03	0.19	0.33	**-0.72**	**0.79**	**0.64**	**0.69**	-0.19														
Zn	0.05	0.39	0.25	-0.62	0.18	0.05	0.09	0.48	-0.11	-0.12	0.01	0.45	-0.21													
Zr	**0.91**	**0.71**	**0.89**	0.28	-0.16	0.60	0.37	-0.18	**0.68**	**0.79**	0.44	0.48	0.44	0.31												
La	0.57	0.49	0.55	-0.04	-0.46	**0.94**	0.32	0.32	0.23	0.40	0.02	**0.75**	0.18	0.32	**0.68**											
Ce	**0.97**	**0.66**	**0.97**	0.37	-0.10	0.50	0.34	-0.31	**0.84**	**0.91**	0.62	0.32	0.53	0.19	**0.94**	0.57										

Pr	0.62	0.52	0.60	0.00	-0.45	**0.94**	0.34	0.26	0.29	0.46	0.07	**0.72**	0.23	0.29	**0.72**	**1.00**	0.62								
Nd	0.61	0.52	0.58	-0.01	-0.46	**0.94**	0.34	0.27	0.27	0.44	0.04	**0.74**	0.22	0.29	**0.72**	**1.00**	0.60	**1.00**							
Sm	**0.64**	0.54	0.62	0.00	-0.43	**0.93**	0.37	0.24	0.32	0.48	0.11	**0.69**	0.25	0.31	**0.74**	**0.99**	0.64	**1.00**	**1.00**						
Eu	0.62	0.52	0.59	-0.01	-0.43	**0.94**	0.35	0.27	0.28	0.45	0.07	**0.72**	0.22	0.31	**0.72**	**1.00**	0.61	**1.00**	**1.00**	**1.00**					
Gd	0.59	0.52	0.56	-0.04	-0.44	**0.93**	0.35	0.30	0.25	0.42	0.05	**0.71**	0.20	0.34	**0.70**	**1.00**	0.58	**0.99**	**0.99**	**1.00**	**1.00**				
Tb	0.61	0.53	0.59	-0.02	-0.42	**0.93**	0.36	0.28	0.28	0.44	0.08	**0.71**	0.22	0.34	**0.72**	**1.00**	0.61	**1.00**	**0.99**	**1.00**	**1.00**	**1.00**			
Dy	0.60	0.53	0.58	-0.02	-0.43	**0.93**	0.36	0.29	0.27	0.43	0.06	**0.73**	0.21	0.34	**0.72**	**1.00**	0.60	**1.00**	**1.00**	**1.00**	**1.00**	**1.00**	**1.00**		
Y	0.53	0.52	0.52	-0.06	-0.47	**0.93**	0.34	0.36	0.19	0.34	-0.03	**0.78**	0.15	0.37	**0.67**	**0.99**	0.54	**0.99**	**0.99**	**0.98**	**0.99**	**0.99**	**0.99**	**0.99**	
Ho	0.58	0.52	0.57	-0.04	-0.43	**0.93**	0.35	0.31	0.24	0.40	0.03	**0.75**	0.19	0.36	**0.71**	**1.00**	0.58	**0.99**	**0.99**	**0.99**	**1.00**	**1.00**	**1.00**	**1.00**	**1.00**
Er	0.59	0.54	0.58	-0.03	-0.43	**0.93**	0.35	0.31	0.25	0.41	0.04	**0.76**	0.19	0.37	**0.72**	**1.00**	0.60	**0.99**	**0.99**	**0.99**	**1.00**	**1.00**	**1.00**	**1.00**	**1.00**
Tm	0.62	0.55	0.61	-0.01	-0.42	**0.93**	0.35	0.29	0.28	0.44	0.07	**0.75**	0.20	0.36	**0.74**	**0.99**	0.62	**0.99**	**0.99**	**0.99**	**1.00**	**0.99**	**1.00**	**1.00**	**0.99**
Yb	0.63	0.54	0.62	-0.01	-0.39	**0.92**	0.35	0.29	0.31	0.46	0.10	**0.74**	0.21	0.37	**0.75**	**0.99**	0.63	**0.99**	**0.99**	**0.99**	**0.99**	**0.99**	**1.00**	**1.00**	**0.99**
Lu	0.63	0.55	0.64	-0.02	-0.38	**0.91**	0.34	0.30	0.32	0.46	0.11	**0.75**	0.21	0.40	**0.76**	**0.98**	**0.65**	**0.98**	**0.98**	**0.99**	**0.99**	**0.99**	**0.99**	**0.99**	**0.98**
REY	**0.74**	0.61	**0.72**	0.07	-0.40	**0.90**	0.37	0.17	0.43	0.58	0.19	**0.70**	0.30	0.33	**0.83**	**0.97**	**0.75**	**0.98**	**0.98**	**0.99**	**0.98**	**0.97**	**0.98**	**0.98**	**0.96**
HREY	-0.49	-0.09	-0.43	-0.44	-0.42	0.35	-0.06	**0.68**	**-0.68**	**-0.64**	**-0.70**	0.54	-0.38	0.28	-0.28	0.38	-0.48	0.32	0.34	0.30	0.33	0.36	0.34	0.35	0.43

Table S7 [continue]

	Er	Tm	Yb	Lu	REY
Tm	**1.00**				
Yb	**1.00**	**1.00**			
Lu	**0.99**	**1.00**	**1.00**		
REY	**0.98**	**0.98**	**0.98**	**0.98**	
HREY	0.36	0.33	0.32	0.31	0.18

Table S5: $^{87}Sr/^{86}Sr$ isotopic ratio of purified CFA from RGR Fe–Mn crusts and ages based on the age model for the Sr isotopic composition of seawater from McArthur et al. (2012).

Sample ID	$^{87}Sr/^{86}Sr$	%StdErr	2StdErr	2SD	Sr Age
RGR1_D02_030 L17-31	0.708714	0.000276	0.000006	0.00007	16.15
RGR1_D05_016 L0-23	0.708889	0.000205	0.000004	0.000052	9.85
RGR1_D07_002 L1-9	0.708897	0.000741	0.000015	0.000188	9.6
RGR1_D07_002 L9-15	0.708888	0.000606	0.000012	0.000153	9.9
RGR1_D07_002 L15-22	0.70875	0.000853	0.000017	0.000216	15.6
RGR1_D07_002 L22-30	0.70853	0.000543	0.000011	0.000137	18.5
RGR1_D07_002 L30-44	0.708408	0.000674	0.000013	0.00017	20.25
RGR1_D07_003 L9-41	0.708726	0.000199	0.000004	0.00005	15.975
RGR1_D09_001 L1-13	0.708715	0.000228	0.000005	0.000058	16.125
RGR1_D09_001 L1-13 CFA lens	0.70868	0.000242	0.000005	0.000061	16.625

RGR1_D09_001 L14-28	0.708669	0.000214	0.000004	0.000054	16.775
RGR1_D09_001 L14-28 CFA lens	0.708766	0.000284	0.000006	0.000072	15.4
RGR1_D10_003 L5-35	0.708422	0.000224	0.000004	0.000057	20
RGR1_D11_003 L0-6	0.708833	0.000319	0.000006	0.000081	12.25
RGR1_D11_003 L6-13	0.708625	0.00036	0.000007	0.000091	17.35
RGR1_D11_003 CFA lens	0.708615	0.000346	0.000007	0.000088	17.5
RGR1_D15_017	0.708923	0.000288	0.000006	0.000073	8.5
RGR1_D17_017	0.708957	0.000207	0.000004	0.000052	6.8

Table S6: U–Th isotopic data for sample RGR1_D07_002.

Sample	**position (mm)**	**U (ppm)**	**(^{234}U/^{238}U)**	**+/-**	**^{232}Th (ppm)**	**(^{230}Th/^{232}Th)**	**2s unc**	**(^{230}Th/^{238}U)**	**2s unc**	**(^{234}U/^{232}Th)**	**2s unc**	**(^{230}Th/^{234}U)**	**2s unc**	**(^{230}Th_ex/^{232}Th)****	**2s unc**
FeMn-4	0.2	9.6	1.112	0.01	13.6	3.018	0.03	1.389	0.014	2.417	0.036	1.249	0.015	0.602	0.047
FeMn-5	0.2	8.8	1.293	0.01	12.4	3.061	0.031	1.403	0.014	2.821	0.042	1.085	0.013	0.24	0.052
FeMn-6	0.2	8.3	1.095	0.01	11.4	3.027	0.03	1.366	0.014	2.425	0.036	1.248	0.015	0.602	0.047
FeMn-7	0.6	18.3	1.089	0.01	26.9	2.44	0.024	1.173	0.012	2.265	0.034	1.077	0.013	0.175	0.042
FeMn-8	0.6	15.4	1.097	0.01	23.2	2.353	0.024	1.155	0.012	2.235	0.034	1.053	0.013	0.118	0.041
FeMn-9	0.6	19.3	1.07	0.01	27.2	2.352	0.024	1.083	0.011	2.323	0.035	1.013	0.012	0.029	0.042
FeMn-10	1	19.1	1.081	0.01	28.6	2.269	0.023	1.111	0.011	2.208	0.033	1.027	0.012	0.061	0.04
FeMn-11	1	19.5	1.066	0.01	29.2	2.161	0.022	1.056	0.011	2.182	0.033	0.99	0.012	-0.021	0.039
FeMn-12	1	19.1	1.066	0.01	28.5	2.218	0.022	1.08	0.011	2.191	0.033	1.012	0.012	0.027	0.04
FeMn-13	1.4	19.2	1.065	0.01	28.7	2.152	0.022	1.052	0.011	2.179	0.033	0.988	0.012	-0.027	0.039
FeMn-14	1.4	18.9	1.063	0.01	28.5	2.147	0.021	1.06	0.011	2.153	0.032	0.998	0.012	-0.005	0.039
FeMn-15	1.4	19	1.064	0.01	28.6	2.148	0.021	1.059	0.011	2.158	0.032	0.995	0.012	-0.01	0.039
FeMn-16	1.8	18.8	1.057	0.01	26.7	2.228	0.022	1.037	0.01	2.271	0.034	0.981	0.012	-0.043	0.041
FeMn-17	1.8	18.6	1.058	0.01	26.2	2.252	0.023	1.039	0.01	2.293	0.034	0.982	0.012	-0.041	0.041
FeMn-18	1.8	19.2	1.058	0.01	27	2.261	0.023	1.045	0.01	2.289	0.034	0.988	0.012	-0.028	0.041
FeMn-19*	<0.1	18.9	1.104	0	28.8	4.021	0.013	1.999	0.045	1.813	0.041	1.813	0.041	2.209	0.043

* Measured at UCSC

** (^{230}Th$_{ex}$/^{232}Th) = (^{230}Th/^{232}Th) - (^{234}U/^{232}Th)

Table S7: Comparison between the chemical composition of Fe–Mn crusts from the RGR and Fe–Mn deposits from elsewhere, as compiled by Conrad et al. (2017) and Hein and Koschinsky (2014).

	Atlantic Ocean		Indian Ocean		Prime Crust Zone		South Pacific Ocean		CA margin		CCZ nodules		Peru Basin nodules	RGR crusts					
														All		Non-phosphatized		Phosphatized	RGR1_D10_002_L0-2
	N	Mean	N	Mean	N	Mean	N	Mean	N	Mean	N	Mean	Mean	N	Mean	N	Mean	N	Mean
Fe (wt.%)	43	20.9	23	22.3	362	16.9	286	18.1	225	23.8	66	6.16	6.12	29	9	6	16.8	16	6.22	9.58
Mn	43	14.5	23	17	362	22.8	321	21.7	225	19.5	66	28.4	34.2	29	14.9	6	22.6	16	11.7	22.1
Fe/Mn	43	1.44	23	1.31	362	0.74	286	0.83	225	1.33	0	0	0.18	29	0.56	6	0.75	16	0.52	0.43
Si	43	5.21	23	6.82	303	4.05	255	4.75	225	10.8	12	6.55	4.82	29	0.6	6	0.66	16	0.59	0.69
Al	43	2.2	23	1.83	351	1.01	241	1.28	225	1.79	65	2.36	1.5	29	1.36	6	0.87	16	1.5	3.7
Si/Al	43	2.37	23	3.73	303	4	241	3.72	225	6.18	0	-	3.21	29	0.53	6	0.82	16	0.42	0.19
Mg	43	1.58	23	1.25	328	1.1	192	1.32	225	1.26	66	1.89	1.71	29	2.4	6	1.99	16	2.5	5.31
Ca	43	4.03	23	2.27	328	4.03	256	3.53	225	2.25	66	1.7	1.82	29	16.3	6	5.61	16	21.2	6.04
Na	43	1.26	23	1.55	303	1.64	88	1.52	225	1.97	66	1.99	2.65	29	0.83	6	1.26	16	0.64	0.85
K	43	0.54	23	0.63	303	0.55	156	0.63	225	0.85	66	0.99	0.81	29	0.23	6	0.31	16	0.2	0.2
Ti	43	0.92	23	0.88	345	1.16	230	1.12	225	0.67	66	0.32	0.16	29	0.44	6	1.08	16	0.18	0.67
P	43	0.75	23	0.38	328	0.96	265	0.78	225	0.57	66	0.21	0.15	29	3.87	6	0.52	16	5.35	0.66
S	31	0.25	9	0.15	43	0.26	40	0.12	40	0.01	12	0.17	-	29	0.42	6	0.4	16	0.43	0.4
V	43	0.08	23	0.06	328	0.06	177	0.07	223	0.06	66	0.04	431	29	0.07	6	0.12	16	0.06	0.1
CO2	0	-	0	-	263	0.74	7	0.83	0	-	0	-	-	29	8.51	6	4.36	16	10.5	5.3
LOI	43	26	23	26.6	185	32	55	18.5	172	16.4	12	26.5	16.2	29	25.7	6	37.2	16	21.4	28.7
H2O-	43	10.6	23	14.1	303	19.5	53	19.8	224	18.3	12	11.6	-	28	8.63	6	20.2	15	3.74	9.5
H2O+	0	-	0	-	263	7.99	7	10.2	0	-	7	8.8	-	29	9.73	6	14.5	16	7.81	13.4
Ag (ppm)	18	0.2	9	0.37	0	-	13	0.97	169	0.9	12	0.17	0.005	6	0.05	1	0.14	4	0.03	<0.02
As	42	308	19	207	328	393	84	287	225	257	12	67	65	29	264	6	480	16	189	288
Ba	43	1556	23	1533	328	1934	143	1705	225	1838	66	3500	3158	29	1059	6	1396	16	1004	623
Be	43	8.98	23	6.93	43	6.07	59	5.38	181	3.99	12	1.9	1.4	29	2.03	6	4.04	16	1.29	1.6
Bi	38	19.3	22	30.2	34	42.9	46	22.4	182	16.2	12	8.8	3.3	29	20.9	6	62.7	16	4.5	16
Cd	34	4.07	18	3.47	285	3.59	62	4.14	223	3.7	12	16	19	29	4.75	6	3.96	16	4.88	12.5
Cl	31	7400	19	10000	43	9200	40	10800	14	7400	12	2700	>0.50	29	3176	6	7715	16	1193	5794
Co	43	3608	23	3291	362	6662	321	6167	223	3131	66	2098	475	29	3056	6	6604	16	1546	4503
Cr	40	46.8	18	22.3	272	27.9	79	35	225	51.9	12	17	16	29	14	6	14.8	16	15	6.6
Cu	43	861	23	1105	362	976	321	1082	223	383	66	10714	5988	29	398	6	407	16	362	1557
Hf	30	8.71	15	9.78	43	9.43	81	9.15	184	6.12	66	4.7	4.7	29	2.16	6	5.54	16	0.65	5.4
Li	42	33.1	22	8.34	33	2.92	36	3.46	33	16.6	66	131	311	29	99.3	6	16	16	127	330
Mo	43	409	23	392	328	461	67	418	223	385	66	590	547	29	340	6	555	16	241	630
Nb	43	50.9	23	61.3	43	51.6	46	59.2	184	31.5	66	22	13	29	46.9	6	106	16	22.4	88
Ni	43	2581	23	2563	362	4209	321	4643	223	2269	66	13002	13008	29	5512	6	4879	16	5658	11015
Pb	43	1238	23	1371	326	1641	113	1057	223	1565	66	338	121	29	1057	6	2906	16	323	1055
Rb	24	15	17	15.8	12	17	27	10.6	184	14.6	66	23	12	29	3.51	6	2.32	16	4.15	2.9

Sb	30	51.1	15	39.9	43	39.3	73	35.4	184	36.9	12	41	61	29	26	6	54.7	16	15.6	26
Sc	43	16.4	23	12.5	43	6.55	82	9.29	182	9.36	66	11	7.6	29	4.77	6	4.45	16	4.99	3
Se	10	0.44	10	1.73	1	14.8	14	5.06	175	2	12	0.72	0.5	6	0.25	1	0.25	4	0.26	<0.2
Sr	43	1262	23	1201	303	1510	67	1483	202	1302	66	645	687	29	1581	6	1972	16	1457	748
Te	37	43	22	31	43	60	38	38	184	13	66	3.6	1.7	29	39	6	96.3	16	16.3	46
Th	42	52	18	56	40	11	67	15	177	48	66	15	6.9	29	16.8	6	44	16	5.59	17
Tl	38	104	22	95.4	34	155	46	154	182	49	12	199	129	29	90.6	6	189	16	49.3	165
U	35	10.9	18	10.3	38	12.4	67	12	177	11.7	66	4.2	4.4	29	11.5	6	18.8	16	8.58	11
W	35	79	18	80	36	89	56	97	184	66	66	62	75	29	116	6	122	16	117	167
Zn	43	614	23	531	325	668	181	698	223	554	66	1366	1845	29	524	6	487	16	520	951
Zr	38	362	22	535	43	548	46	754	184	464	66	307	325	29	206	6	396	16	131	238
La	42	272	21	290	83	339	75	204	187	270	66	114	68	29	161	6	265	16	121	79.3
Ce	42	1392	21	1469	83	1322	75	818	223	1264	66	284	110	29	627	6	1696	16	195	570
Pr	20	63.8	12	66.2	83	61.3	31	40.8	187	60.3	66	33.4	14.1	29	30.9	6	54.8	16	21.7	15
Nd	42	243	21	259	83	258	67	184	187	253	66	140	63	29	136	6	231	16	99.8	64.9
Sm	20	55.5	12	60.8	83	51.5	67	38.1	187	53.5	66	34	14	29	29	6	49	16	21.2	14.6
Eu	42	11.5	21	12.5	83	12.5	75	17.5	187	12.7	66	8.03	3.87	29	6.21	6	10.1	16	4.74	3.29
Gd	20	57.9	12	67.2	83	56.2	31	43.9	187	55.5	66	31.8	15.6	29	31.4	6	46.1	16	25.9	16.3
Tb	20	9.17	12	9.99	82	8.79	53	5.98	187	8.92	66	4.98	2.52	29	4.64	6	7.09	16	3.73	2.64
Dy	20	47.1	12	55.6	83	60	30	40.7	187	49.6	66	28.5	15.8	29	28.8	6	42	16	24	17.1
Y	43	181	23	178	294	221	49	177	223	172	66	96	69	29	219	6	187	16	237	120
Ho	41	9.61	13	10.6	82	10.9	17	8.45	187	10	66	5.35	3.42	29	6.33	6	8.67	16	5.49	3.92
Er	20	28	12	29.3	83	31	31	26.5	187	27.9	66	14.6	10	29	18.7	6	25.5	16	16.3	12
Tm	20	3.91	12	4.03	82	4.55	17	3.6	187	3.9	66	2.11	1.5	29	2.51	6	3.6	16	2.11	1.73
Yb	42	23.9	21	24.8	83	28.5	75	21.9	187	25.3	66	13.7	10.3	29	16	6	23.3	16	13.2	11.7
Lu	20	3.74	12	4.05	40	4.29	75	3.33	186	3.81	66	2.05	1.61	29	2.3	6	3.37	16	1.91	1.76
∑REY2	20	2402	12	2541	82	2470	17	1634	186	2270	66	813	403	29	1319	6	2652	16	793	935
%HREY3	20	15.6	12	15.6	82	17.7	17	21.4	186	16.3	66	25.5	130	29	32.1	6	13.6	16	40.8	20
Au (ppb)	2	5.99	2	20.7	7	99.7	38	33.1	17	7.8	9	4.5	-	18	12.5	5	14.6	9	11.5	-
Ir	2	4.8	5	6.8	56	13	3	2.5	9	1.8	11	2	-	18	6.66	5	13.6	9	2.42	-
Os	1	2.4	3	4	4	2.4	1	2.5	11	3.5	0	-	-	7	2.24	3	2.94	3	1.03	-
Pd	2	6	6	15	54	3.8	14	7	28	4.1	12	8	-	18	5.62	5	7.98	9	4.36	-
Pt	2	567	6	211	60	470	15	465	30	70	12	128	40	18	359	5	661	9	173	-
Rh	2	37	6	20	59	23	15	33	29	6	12	9	-	18	34	5	70.2	9	11.8	-
Ru	2	18	6	20	58	17	6	13	15	9	12	12	-	18	15.7	5	35	9	3.69	-

[1]Loss on ignition at 1000°C

[2]∑ REY = Sum of rare earth elements plus yttrium

[3]Percent of heavy REY (Eu-Lu. +Y) of the total sum of REY

3 MIOCENE PHOSPHATIZATION OF ROCKS FROM THE SUMMIT OF RIO GRANDE RISE (CHAPTER II)

Manuscript published on the Paleoceanography and Paleoclimatology

Mariana Benites[1], James R. Hein[2], Kira Mizell[2], Luigi Jovane[1]

[1]Instituto Oceanográfico da Universidade de São Paulo, Praça do Oceanográfico 191, 05508-120 São Paulo, SP, Brazil.

[2]U.S. Geological Survey, PCMSC, 2885 Mission St., Santa Cruz, CA 95060, USA.

Abstract

Marine phosphorites are an important part of the oceanic phosphorus cycle and are related to the effects of long-term global climate changes. We use petrography, mineralogy, rare earth elements contents, and $^{87}Sr/^{86}Sr$-determined carbonate fluorapatite (CFA) and calcite ages to investigate the paragenesis and history of phosphatization of carbonate sediments, limestones, FeMn crusts, and ironstones from the summit of Rio Grande Rise (RGR), Southwest Atlantic Ocean. Phosphatization of all the rock types occurred throughout the Miocene from 20.2 - 6.8 million years ago (Ma), and occasionally during the Quaternary, mainly through the cementation of carbonate sediments by cryptocrystalline CFA, likely involving the dissolution of the smaller size fraction of foraminifera-nannofossil ooze. Porosity/permeability and abundance of fine calcite material were important factors determining the intensity of phosphatization of the various rock types. Phosphatization was initiated during a transition to a more dynamic circulation system in the South Atlantic Ocean, which remobilized phosphorus from deeper waters and increased primary productivity that culminated with the middle-Miocene Climatic Optimum between ~17 - 14.8 Ma. The relatively shallow-water depth of RGR summit during the Miocene provided proximity to the oxygen minimum zone, a reservoir for reactive phosphorus, especially during periods of enhanced phosphorus cycling spurred by surface primary productivity. The cessation of phosphatization at RGR resulted from a rapidly cooling and dry climate that characterized the Miocene-Pliocene transition. Our results support previous observations that periods of broadly intensified ocean circulation and local hydrodynamic changes were the key paleoceanographic links to phosphorite formation.

3.1 Introduction

Phosphate is an essential nutrient and energy carrier for living organisms and a limiting nutrient for ocean productivity. On a long-term basis, the phosphorus cycle controls oceanic

primary production and has a feedback mechanism with global climate, environment, and ecology (Follmi, 1996; Tyrrell, 1999; Elser et al., 2007). Marine phosphorites and phosphate-rich rocks are an important sink of P in the oceans (Follmi, 1996). Thus, determining the timing of the formation of phosphate-rich seafloor deposits can shed light on past climatic changes and the global P cycle.

Although marine phosphorites have been more extensively studied in areas of high P and organic matter input to sediments from strong primary productivity along continental margins, significant phosphorite deposits also formed in more oxygenated low-organic-carbon environments at open-ocean seamounts, plateaus, and banks (Burnett et al., 1987; Baturin, 1989; Hein et al., 1993; Glenn et al., 1994; Rao et al., 2008). Some previous studies addressed the mechanism and timing of phosphatization of open-ocean seamounts (e.g., Hein et al., 1993; Benninger and Hein, 2000; Jiang et al., 2020); however, many questions still remain.

Seamount phosphatization generally involves the formation of carbonate fluorapatite (CFA) as the phosphate phase (approximate formula $Ca_5(PO_4,CO_3)_3F$); CFA is a thermodynamically stable form of apatite in carbonate-rich fluids such as seawater (Jahnke, 1984) and is a term extensively used in many studies (e.g., Knudsen and Gunter, 2002; Kraal et al., 2012). At seamounts, authigenic formation of CFA occurs mainly at depths where these seafloor features intersected the oxygen minimum zone (OMZ) which is a source of reactive P (Kraal et al., 2012). Phosphorite forms by precipitation of CFA as a cement in sediment pores and void spaces of host rocks and the impregnation or replacement of pre-existing minerals by CFA, most commonly calcite (McArthur et al., 1990; Glenn et al., 1994). Most seamount rocks can be impacted by phosphatization (e.g., limestone, basalt, breccia, conglomerate, hyaloclastite); however, carbonate sediments and rocks are the most easily phosphatized (Glenn et al., 1994; Benninger and Hein, 2000; Filippelli, 2011).

CFA formation may also be concomitant with the formation of other authigenic phases, mainly Fe and Mn oxyhydroxides (Baturin, 1989; Benninger and Hein, 2000). Commonly, seamount/plateau phosphorites occur at the same locations as FeMn crusts (i.e., Campbell Plateau and north Tasman seamounts, Pacific and Atlantic seamounts; Glasby and Summerhayes, 1975; Hein et al., 1993; Jones et al., 2002), where CFA has impregnated the lower portion of thick FeMn crusts (Koschinsky et al., 1997; Hein et al., 2000, 2016a). The phosphorite-FeMn-oxide mineral combination has been also found on Rio Grande Rise (RGR; Benites et al., 2020; Sousa et al., 2021). Whether the summit and upper flanks of oceanic rises are in the proximity of the OMZ, a reservoir of reactive P and metals, will favor the precipitation of CFA or FeMn crusts over geologic time depending on the prevailing redox condition (Burnett

et al., 1987; Koschinsky et al., 1997; Hein et al., 2016a). Younger, non-phosphatized crusts may then grow after each phosphatization event, which varied in time for different parts of the global ocean.

Seamount phosphatization broadly occurred during two main periods around the global ocean: the Eocene-Oligocene transition and the Oligocene-Miocene transition, along with other minor events (Hein et al., 1993; Hyeong et al., 2013). Some equatorial Atlantic seamounts and banks show younger events throughout the Miocene, in many places related to upwelling near the paleo-equator (Jones et al., 2002). Thus, seamount, bank, and plateau phosphorites are vital recorders of past ocean biogeochemical conditions (Glenn et al., 1994).

This study provides the first investigation of the phosphatization of rocks from the summit of the RGR, a prominent ridge offshore Brazil that hosts heavily phosphatized FeMn crusts (Benites et al., 2020; Sousa et al., 2021) and other phosphatized rocks, which can shed light on past oceanographic and climate conditions in the area of the Southwest Atlantic Ocean. Mineralogy and chemical compositions reflect the extent of mineral replacement, Sr isotopes determine ages of precipitation of CFA and calcite, rare earth elements composition reveal the nature of the phosphatizing fluid and redox conditions, and petrographic and SEM observations elucidate the paragenesis of mineral deposition. These data are used together to infer the paleoceanographic context of phosphatization at RGR.

3.2 Environmental setting

Rio Grande Rise is an aseismic ridge that rises from the surrounding 4000 m-deep abyssal plain to 600 m water depth at the top of the central plateau. The rise is located 1000 km offshore the closest point of the Brazil coast and is isolated from the continental margin by the Vema Channel (Figure 1).

The modern water column in the region is marked by an oxygen maximum that corresponds to the Antarctic Intermediate Water (AAIW; ~700-1000 m), sandwiched between the less oxygenated South Atlantic Central Water (SACW; ~200-700 m) above and the oxygen-poor Upper Circumpolar Deep Water (UCDW; ~1300-1700 m) below (Tsuchiya et al., 1994) (Figure 1). The AAIW is a tongue of well-oxygenated and phosphate-rich water from the Southern Ocean, centered at 900 m depth at 30°S near RGR (Tsuchiya et al., 1994; Poggemann et al., 2017), which may have provided the conditions necessary for phosphatization of rocks at RGR in the past.

Little information is available about sediment coverage on RGR, but compiled information suggests that most RGR seafloor is covered with fine-grained carbonate ooze

(Montserrat et al., 2019). The transition between the Vema Channel and the western margin of RGR is marked by a switch from red mud with Mn micronodules and nodules to a carbonate ooze (up to 85% carbonate, 50% of the sediment is sand-sized); FeMn crusts occur where rocks crop out along the flanks of RGR (Melguen and Thiede, 1974). Additionally, phosphatized FeMn crusts and phosphate-rich rocks occur along the top of the RGR plateau (Cavalcanti et al., 2015; Benites et al., 2020; Sousa et al., 2021).

Enhanced primary biological productivity and sedimentation rates of biogenic particles occurred during the late Oligocene and early Miocene on RGR (Florindo et al., 2015). Peaks of organic carbon exported to RGR sediments occurred around 19.1, 15.5, 5.4 – 4.6, and 4.4 - 4.2 million years ago (Ma) (Berggren et al., 1983; Emelyanov and Trimonis, 1983) as determined from sediment cores collected by the Deep Sea Drilling Program (DSDP) at site 516 on northern RGR.

3.3 Materials and Methods

3.3.1 Samples

The phosphorites and phosphatized rocks used in this research were dredged from the summit of RGR during expedition RGR1 onboard the R/V Alpha Crucis of the Instituto Oceanográfico da Universidade de São Paulo, between 30 January and 20 February 2018 (Table 1; Jovane et al., 2019a). The samples studied here include 23 phosphatized FeMn crusts (17 layer samples, delineated by visual changes in color and texture and accordingly subsampled, and six bulk samples), 11 phosphorite rocks and lenses within FeMn crusts, five limestones (breccias, coralline algal balls, and substrate for FeMn crusts), and four ironstones (Figure 2).

3.3.2 Methods

3.3.2.1. X-ray Diffraction (XRD)

The mineralogy of the samples was identified by XRD using a Panalytical X'Pert3 Powder diffractometer at the United States Geological Survey, Pacific Coastal and Marine Science Center, Santa Cruz, California. Powder aliquots were drilled from the samples using a diamond-coated drill bit and ground using an agate mortar and pestle to approximately 75 µm. The powder was wet mounted on zero-diffraction sample holders using alcohol and measured using a Cu-kα radiation source and graphite monochromator. Each sample was scanned from 4° to 70° 2θ at 40 kV and 45 mA. The diffractograms were interpreted using the Philips High Score Plus software and the International Centre for Diffraction Database. Semi-quantitative

percentages of mineral phases were calculated based on the intensities of the peaks and weighting factors relative to quartz (Cook et al., 1975; Hein et al., 1988).

3.3.2.2 Petrography and Microscopy

Polished thin sections were observed under a petrographic microscope using transmitted and reflected light. The thin sections were later carbon-coated for observations using a scanning electron microscope from Leo Electron Microscopy Ltd (Leo 440i) at the Laboratory of Scanning Electron Microscopy (LabMEV), Instituto de Geociências da Universidade de São Paulo, in Brazil. Backscatter Electron (BSE) and Secondary Electron (SE) images were taken under high vacuum with Electron High Tension (EHT) of 20 keV at a work distance of 25 mm, and ion probe current of 1 to 2 nA. The Energy Dispersive Spectroscopy (EDS) mode was used with a Si (Li) solid-state detector and with INCA 300 software from Oxford Microanalysis to perform chemical element identification and mapping.

3.3.2.3 Chemical leaching for CFA purification

A sequence of chemical leaches was performed to isolate the CFA from the different rock types for chemical and Sr isotopic analyses using the procedure of Ruttenberg (1992). FeMn oxyhydroxides were removed by leaching 3 g of powdered (<75 μm) samples in 1 L of a leaching solution of Na-citrate, Na-bicarbonate, and Na-dithionite (pH 8) for 24 hours. The solution was then filtered (2.7 μm paper filter), the residue washed in a 1 M MgCl2 solution (pH 8), and filtered again. For calcite removal, the residue from the previous step was stirred in a 0.5 M triammonium citrate solution (pH 8.1) for 10 hours, after the procedure of Silverman et al. (1952). After calcite leaching, the solution was filtered (2.7 μm paper filter), and the residues washed in Mili-Q water, centrifuged, and placed in a sonic bath (repeated five times). Finally, the organic matter was removed by stirring the residues with a 30% H2O2 solution.

Eighteen CFA-containing FeMn layers from nine hand samples were treated with all the above procedures to isolate CFA from the FeMn crust since high content of Sr may also be associated especially with Mn oxides (Koschinsky and Hein, 2003). Seven phosphorites were treated for calcite and organic matter removal so that the Sr measured would be only from CFA. Three carbonate (calcite) samples were treated only for the removal of organic matter since the calcite was the final phase of interest on those samples.

XRD confirmed the removal of each phase at the end of each step. One FeMn crust hand sample (D07_002) had the CFA isolated from five different stratigraphic layers to

investigate if phosphatization affected all layers during a single phosphatization event or multiple events at different times throughout the past.

3.3.2.4 Sr Isotopes

Strontium was isolated from the purified CFA residues by column chemistry at the University of California, Santa Cruz, W.M. Keck Isotope Facility. The residues were digested in concentrated HNO3 on a hot plate at 90°C. Remnant undigested solid (mainly silicate phases) was separated from the solution by centrifuge since silicates were not the material of interest in this study. The digested solution was evaporated and dried to a small bead and brought up in 1 mL using 7N HNO3. A 0.5 mL aliquot of the sample was then loaded onto pre-conditioned columns containing 0.5 mL of Sr-SPEC resin followed by rinsing with three 1 mL aliquots of 7N HNO3. The residual solution containing Sr was eluted from the columns using four 1 mL aliquots of 0.05N HNO3 and collected in Teflon vials. Sr isotopes were measured by Thermal Ionization Mass Spectrometry (TIMS) in an IsotopX Phoenix x62 system at the W.M. Keck Isotope Facility. Analytical precision, expressed by the standard error, was less than 0.0000086 for all samples. The 87Sr/86Sr ratio of the samples was compared to the Cenozoic seawater curve, and corresponding calibrated ages were determined using the data of McArthur et al. (2012).

3.3.2.5 Chemical composition

The REE compositions of leached CFA from three FeMn crusts, two coralline algal balls, and the CFA rim of a calcareous phosphorite sample, D12_004, were determined. The REE elements Dy, Er, Eu, Gd, Ho, La, Sm, Tb, and Tm, plus Y were determined by Inductively Coupled Plasma-Mass Spectroscopy (ICP-MS) using lithium metaborate fused discs, while Ce, Lu, and Yb were determined by ICP-MS from multi-acid digested aliquots, all at SGS Mineral Services, Canada. Precision and accuracy were better than 20% for all elements.

Micro X-ray Fluorescence (µ-XRF) scans were carried out on polished thin sections of FeMn samples at the XRF beamline at the Brazilian Synchrotron Light Laboratory, Campinas, Brazil. Step mode µ-XRF scans were performed every 0.025 mm, with a 4000 ms time per point, under white synchrotron light using a Double Crystal Si(111)/Si(220) channel-cut type monochromator, a Silicon Drift Detector (SSD), collimator, and a six-µm-thick Fe filter to reduce the dead time. The X-ray beam was 12x22 µm in size. The PyMCA free software for XRF data analysis from the European Synchrotron Radiation Facility was used to calibrate and fit the fluorescence peaks to corresponding chemical elements.

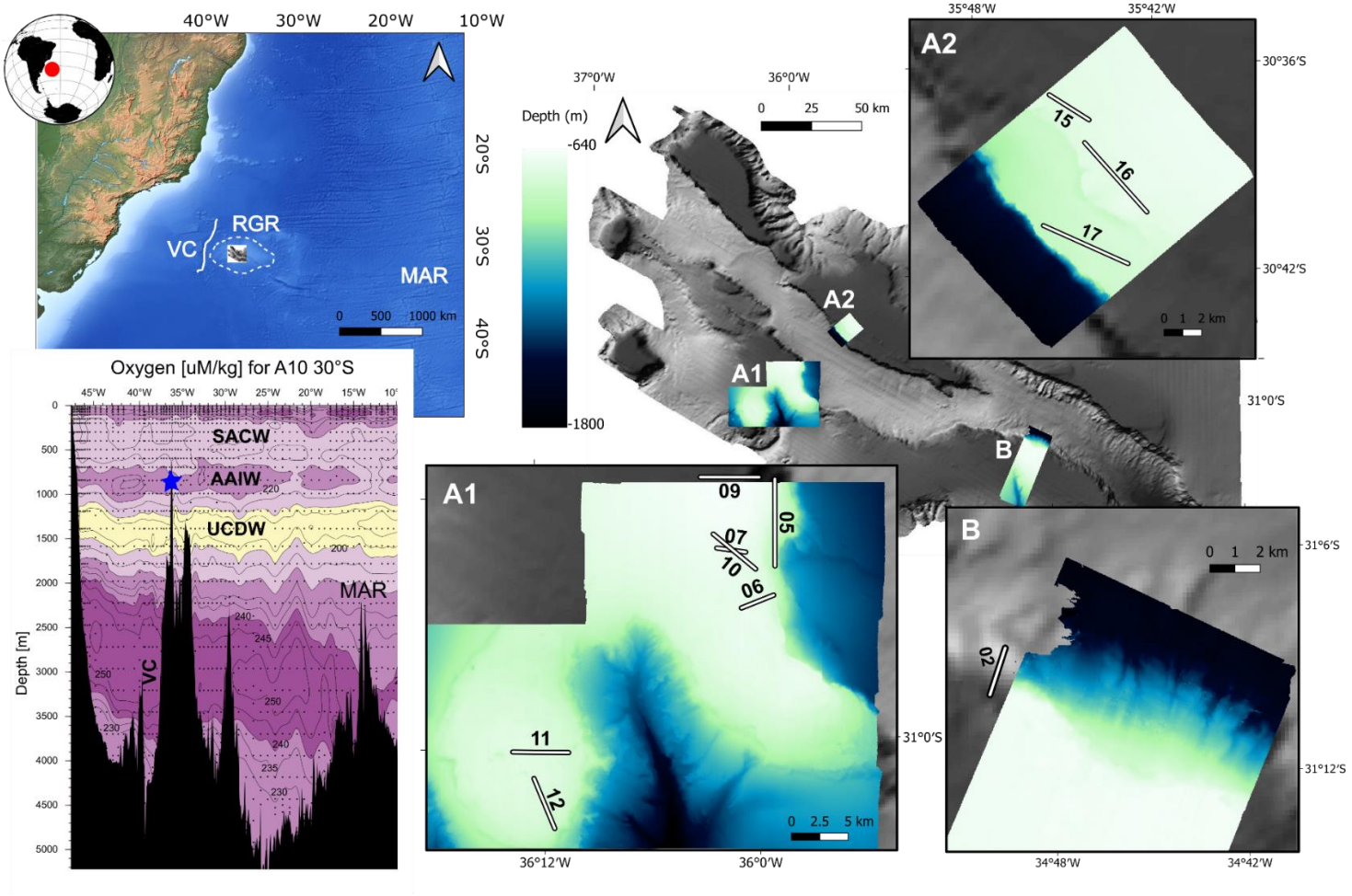

Figure 1: Upper left, location of RGR in the South Atlantic Ocean, in which the dashed circle delineates the area of RGR and the filled white square encompasses the surveyed area. RGR = Rio Grande Rise; VC = Vema Channel; MAR = Mid Atlantic Ridge; upper right, multibeam surveyed areas A1, A2, and B, each shown in detail with numbered dredge track lines indicated; lower left, transect of dissolved oxygen profile and main water masses in the region; the star marks the position of the top of RGR at about 800 m; contours correspond to oxygen concentration, which is also depicted by the colors: dark purple (<240 µM/kg), medium purple (220–240 µM/kg), light purple (200–220 µM/kg) and yellow (<200 µM/kg). Modified from the Electronic Atlas A10 of WOCE (Mueller, 1997). SACW = South Atlantic Central Water; AAIW = Antarctic Intermediate Water; UCDW = Upper Circumpolar Deep Water.

Table 1. Description, Location, and Mineralogy of Samples

Sample name	Portion analysed	Rock type	Longitude	Latitude	Avg water depth (m)	Major minerals	Moderate minerals	Minor mineral
RGR1_D02_022	L10-15	Phosphatized Fe-Mn crust	34°49,803'W	31°9,351'S	825.5	δ-MnO2 and asbolane	Calcite and CFA	-
RGR1_D02_022	Substrate	Limestone	34°49,803'W	31°9,351'S	825.5	Calcite	-	Quartz
RGR1_D02_030	L13-20	Phosphatized Fe-Mn crust	34°49,803'W	31°9,351'S	825.5	δ-MnO2, asbolane and CFA	Calcite	-
RGR1_D05_011	L2-10	Phosphatized Fe-Mn crust	35°58,853'W	30°53,367'S	739	Asbolane and pyrolusite	CFA and calcite	Quartz
RGR1_D05_011	L10-19	Ironstone	35°58,853'W	30°53,367'S	739	Goethite	CFA	Quartz
RGR1_D05_016	L0-1	Phosphatized Fe-Mn crust	35°58,853'W	30°53,367'S	739	Asbolane, δ-MnO2 and CFA	Calcite	-
RGR1_D05_016	L0-23	Phosphatized Fe-Mn crust	35°58,853'W	30°53,367'S	739	Goethite	CFA	Calcite
RGR1_D05_016	L23-24	Ironstone	35°58,853'W	30°53,367'S	739	δ-MnO2, asbolane and CFA	-	-
RGR1_D06_003	Bulk	Phosphatized Fe-Mn crust	35°59,932'W	30°53,634'S	716.5	δ-MnO2 and asbolane	CFA	Calcite
RGR1_D06_013	Bulk	Phosphatized Fe-Mn crust	35°59,932'W	30°53,634'S	716.5	δ-MnO2, asbolane and CFA	Calcite	-
RGR1_D06_019	Bulk	Phosphorite	35°59,932'W	30°53,634'S	716.5	CFA and calcite	-	Quartz
RGR1_D07_001	Substrate	Phosphorite	36°1,319'W	30°51,135'S	684	CFA and calcite	-	Quartz
RGR1_D07_002	L18-33 lens	Phosphatized detritus	36°1,319'W	30°51,135'S	684	Calcite and CFA	-	Quartz
RGR1_D07_002	L6-18	Phosphatized Fe-Mn crust	36°1,319'W	30°51,135'S	684	δ-MnO2, asbolane and CFA	Calcite	Minor quartz
RGR1_D07_002	L18-33	Phosphatized Fe-Mn crust	36°1,319'W	30°51,135'S	684	δ-MnO2 and asbolane	CFA	Quartz and calcite
RGR1_D07_002	L33-55	Phosphatized Fe-Mn crust	36°1,319'W	30°51,135'S	684	δ-MnO2, asbolane and CFA	-	-
RGR1_D07_003	Upper L5-18	Phosphatized Fe-Mn crust	36°1,319'W	30°51,135'S	684	δ-MnO2, asbolane and CFA	-	-
RGR1_D07_003	Lower L5-18	Phosphatized Fe-Mn crust	36°1,319'W	30°51,135'S	684	CFA and δ-MnO2	Calcite and asbolane	-
RGR1_D07_003	L5-18 lens	Phosphatized detritus	36°1,319'W	30°51,135'S	684	CFA and calcite	-	Quartz
RGR1_D07_020	L0-15	Phosphatized Fe-Mn crust	36°1,319'W	30°51,135'S	684	δ-MnO2, asbolane and CFA	Calcite and Mg-calcite	Quartz
RGR1_D07_020	L15-33	Phosphatized Fe-Mn crust	36°1,319'W	30°51,135'S	684	CFA, δ-MnO2 and asbolane	Calcite	-
RGR1_D09_001	L0-1	Phosphatized Fe-Mn crust	36°1,398'W	30°47,638'S	650.5	δ-MnO2 and asbolane	CFA	-
RGR1_D09_001	L1-13	Phosphatized Fe-Mn crust	36°1,398'W	30°47,638'S	650.5	CFA and δ-MnO2	Calcite and asbolane	-
RGR1_D09_001	L14-28	Phosphatized Fe-Mn crust	36°1,398'W	30°47,638'S	650.5	CFA and calcite	δ-MnO2 and asbolane	Quartz and plagioclase
RGR1_D09_001	CFA lens	Phosphatized detritus	36°1,398'W	30°47,638'S	650.5	CFA and calcite	-	Quartz
RGR1_D09_003	L1-3 lens	Carbonate lens	36°1,398'W	30°47,638'S	650.5	Goethite	-	CFA and calcite
RGR1_D09_005	Bulk	Ironstone	36°1,398'W	30°47,638'S	650.5	Calcite, Mg-calcite	-	Minor CFA

RGR1_D09_011	Bulk	Phosphorite	36°1,398'W	30°47,638'S	650.5	Calcite	CFA	Quartz
RGR1_D09_023	Bulk	Ironstone	36°1,398'W	30°47,638'S	650.5	Goethite	CFA, calcite and Mg-calcite	-
RGR1_D09_025	Center	Phosphorite	36°1,398'W	30°47,638'S	650.5	Calcite and CFA	-	Quartz
RGR1_D10_002	Center	Phosphatized carbonate sand	36°1,146'W	30°51,205'S	686.5	CFA	Calcite	Quartz
RGR1_D10_003	L2-5	Ironstone	36°1,146'W	30°51,205'S	686.5	Calcite	-	CFA and quartz
RGR1_D10_003	L5-20	Phosphatized Fe-Mn crust	36°1,146'W	30°51,205'S	686.5	Calcite	-	CFA and quartz
RGR1_D10_003	Substrate	Carbonate breccia	36°1,146'W	30°51,205'S	686.5	CFA	-	Calcite and pyrolusite
RGR1_D10_003	Substrate	Carbonate	36°1,146'W	30°51,205'S	686.5	CFA	Goethite, δ-MnO2 and calcite	Ramsdellite-like mineral
RGR1_D11_003	Bulk	Phosphatized Fe-Mn crust	36°12,494'W	31°0,539'S	751	CFA	Asbolane and calcite	Goethite and δ-MnO2
RGR1_D11_004	Bulk	Phosphatized Fe-Mn crust	36°12,494'W	31°0,539'S	751	δ-MnO2 and asbolane	CFA	Calcite
RGR1_D11_004	Center	Phosphorite	36°12,494'W	31°0,539'S	751	Calcite	CFA	Quartz
RGR1_D11_020	Bulk	Carbonate algae ball	36°12,494'W	31°0,539'S	751	Calcite	-	CFA and quartz
RGR1_D12_004	Edge	Phosphorite	36°11,972'W	31°2,729'S	762.5	CFA	-	-
RGR1_D12_004	Center	Phosphorite	36°11,972'W	31°2,729'S	762.5	CFA	Calcite	-
RGR1_D12_008	Bulk	Carbonate algae ball	36°11,972'W	31°2,729'S	762.5	Calcite	-	Quartz and CFA
RGR1_D15_017	Bulk	Phosphatized Fe-Mn crust	30°37,517'S	35°45,711'W	648	Vernadite, asbolane and CFA	Calcite	Quartz
RGR1_D17_017	Bulk	Phosphatized Fe-Mn crust	30°39,275'S	35°43,327'W	633.5	Calcite	Asbolane, vernadite and CFA	-
RGR1_D17_018	Center	Phosphorite	30°39,275'S	35°43,327'W	633.5	Calcite	CFA	-

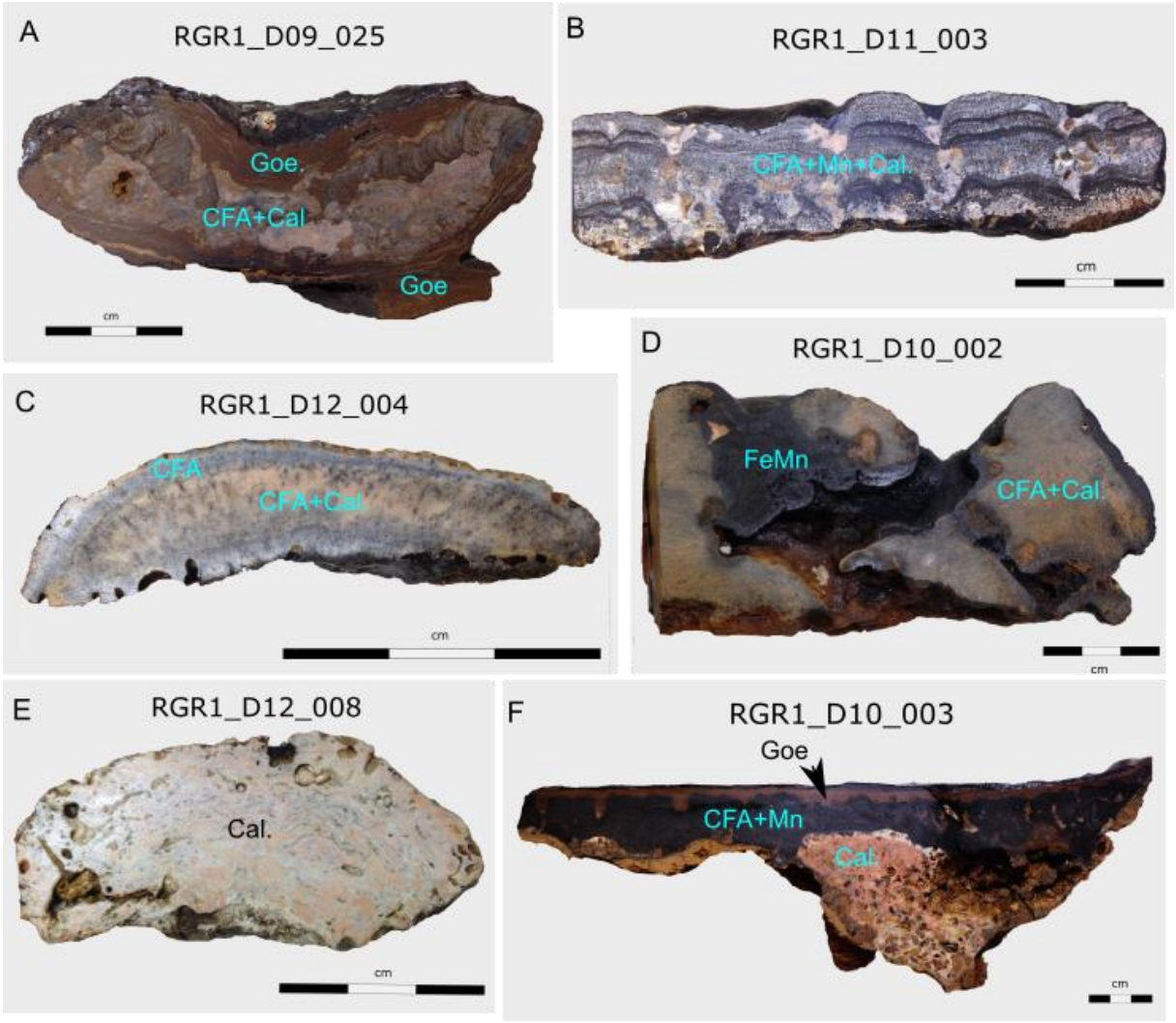

Figure 2: Phosphorite and phosphatized rocks from Rio Grande Rise. (a) Phosphorite central layer enveloped by ironstone; (b) pervasively phosphatized FeMn crust; (c) phosphorite; (d) phosphatized sandy limestone (CFA + Cal.) impregnated by FeMn oxyhydroxides; (e) coralline algal ball; (f) carbonate breccia covered by phosphatized FeMn crust and an ironstone layer (arrow). Goe. = goethite; CFA = carbonate fluorapatite; Cal. = calcite; FeMn = Fe and Mn (oxyhydr)oxides.

3.4 Results and Discussion

3.4.1 Different rock types affected by phosphatization

According to the XRD data, not only the phosphorites contain CFA, but also the limestones, coralline algal balls, FeMn crusts, and ironstones contain variable amounts of CFA (Table 1), which means that all the rock types studied were affected by phosphatization to some degree.

Phosphorites contain moderate to major amounts of CFA (Table 1) and moderate to major amounts of calcite, suggesting the rock was originally calcareous and was phosphatized to varying degrees. On the other hand, the limestones are composed of major calcite and minor amounts to no CFA (Table 1), reflecting minor phosphatization. Limestones are common substrate rocks for FeMn crusts along the RGR summit, and they are frequently covered by

phosphatized FeMn crusts. The coralline algal balls D11_020 and D12_008 (Figure 2E) are also made of calcite and contain minor CFA and quartz, indicating minor phosphatization.

Sixteen phosphatized FeMn crust layers out of the 23 layers studied contain CFA as a major mineral phase (Table 1); four of those samples have more CFA than the Fe and Mn (oxyhydr)oxide component (vernadite, asbolane, pyrolusite, goethite) (Table 1), which is evidence of pervasive phosphatization of these samples. Moderate to major amounts of calcite also occur in the phosphatized FeMn crust layers, indicating incomplete phosphatization of all extant calcite or continued deposition of bio-calcite in the crusts throughout their growth history. According to a µ-XRF scan across the phosphatized FeMn crust D07_002 (Figure 3), the relative P content is distinct at each stratigraphic depth (Age), illustrating that CFA formation was episodic and resulted in a different distribution of CFA within each of the centimeter-scale stratigraphic layers that also show discrete mineralogical and textural properties (Figure 3). The FeMn crusts dredged from the slope of the central rift valley of RGR at about 825 m water depth (dredge D02) are less intensely phosphatized compared to FeMn crusts from the summit at <750 m water depth (Table 1).

Ironstones are composed of goethite and minor to moderate amounts of CFA and calcite (Table 1), suggesting that phosphatization was less pervasive than for the FeMn crusts and phosphorites.

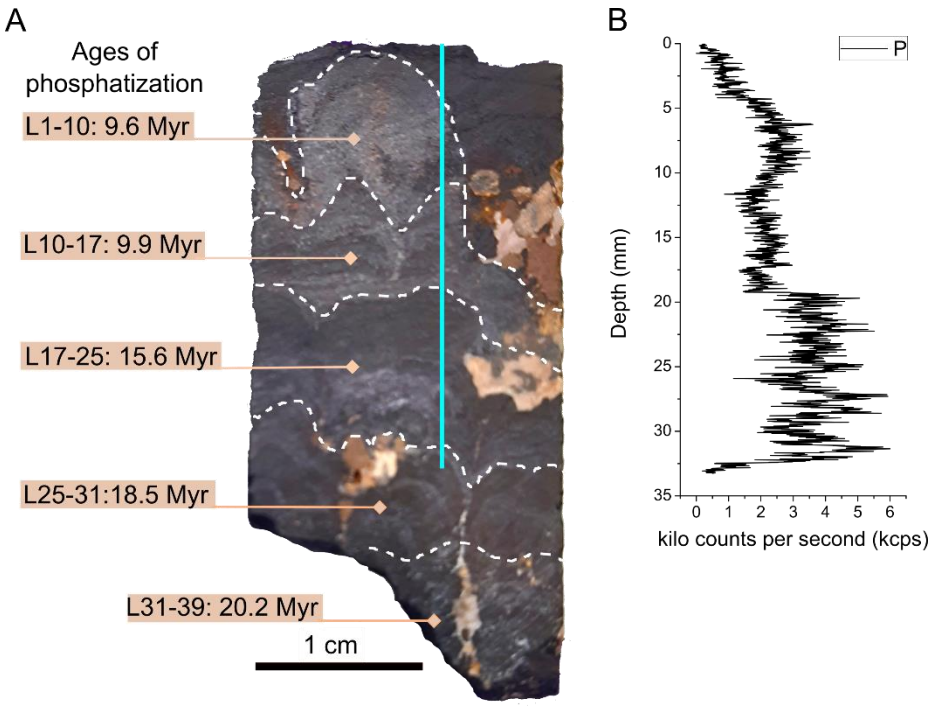

Figure 3: (a) A cross-section of phosphatized FeMn crust sample D07_002 displaying different macroscopic layers and the corresponding age of carbonate fluorapatite carbonate fluorapatite (CFA) (phosphatization) based on the 87Sr/86Sr ratio of CFA leached from each layer; the blue line shows where the micro-X-ray Fluorescence (XRF)

profile was taken; (b) a micro-XRF profile of P counts through the same sample, showing the high variability of phosphatization on the micrometer scale.

3.4.2 Petrography and mineral paragenesis during phosphatization

3.4.2.1 Degree of phosphatization and timing of oxide precipitation in FeMn crusts

The CFA content of FeMn crusts reflects changes in the texture and the number of bioclasts within the FeMn crust matrix. Mildly phosphatized FeMn crusts often have laminated and botryoidal texture, and they lack bioclasts, for example, sample D02_030 from the slope (Figure 4A, B). In contrast, moderately phosphatized FeMn crust layers have botryoidal and columnar textures with abundant bioclasts, as in the phosphatized portion of sample D07_002 (Figure 4C, D). Further, pervasively phosphatized FeMn crusts have an acicular texture with extremely high amounts of foraminifera tests, as in sample D11_003 (Figure 4E). In this latter sample, some layers have such abundant foraminifera, with only sparse FeMn dendrites, that they are better described as phosphatized foraminifera ooze that was impregnated by Fe and Mn (oxyhydr)oxides as a post-depositional process (Supporting Information Figure S1A, B).

In such highly phosphatized samples, the foraminifera are within cryptocrystalline CFA cement, in which diffuse Fe and Mn oxyhydroxides appear sparsely or form thin columns (Figure 4D). When these thin columns are longer, they have a needle-like macroscopic appearance resulting in a coarse acicular texture (Figure 4C). In sample D11_003, the acicular-textured, foraminifera-rich layers alternate with thin parallel laminae with sparse foraminifers (Figure 4E), suggesting alternating periods of high and low pelagic sedimentation; the foraminifera-rich layers were probably originally carbonate ooze. The parallel laminae are composed of CFA, but Fe- or Mn-rich thin laminae are also present (Supporting Information Figure S1C, D).

The high content of biogenic particles within FeMn crusts from RGR coincides with the high intensity of phosphatization and reinforces the interpretation that the formation of CFA is best facilitated by replacing biogenic calcite. However, CFA also filled pore space in the FeMn crusts, illustrating multiple CFA formation pathways within one sample type. The phosphatization of FeMn crusts may also have been facilitated by the phosphate pump trap that has been described for seafloor sediments, in which the phosphate scavenged by poorly crystalline Fe-oxyhydroxides in seawater is released under reducing conditions (Berner, 1973; Heggie et al., 1990; Lucotte et al., 1994; Knudsen and Gunter, 2002). Fe-rich sediments adsorb the phosphate from seawater and at far greater amounts than carbonate sediments (Berner, 1973). This recycling process provides a large amount of dissolved phosphate and fluoride that

can lead to CFA mineralization in the top centimeters of the sediment (Krom and Berner, 1981; Heggie et al., 1990) and may also promote CFA formation in FeMn crusts. Stronger remobilization of FeOOH over MnO2 in phosphatized FeMn crusts is a common observation (Koschinsky et al., 1997; Hein et al., 2016a), which also occurred in FeMn crusts from RGR (Benites et al., 2020), and may represent a version of the phosphate pump trap applied to phosphatized FeMn crusts.

The co-occurrence of CFA cement and FeMn oxyhydroxides poses the question of the order of mineralization. Previous studies suggested that accessory minerals in phosphatized rocks, such as the FeMn oxyhydroxides and other authigenic minerals, formed before, during, and after CFA formation (Benninger and Hein, 2000). The cryptocrystalline CFA matrix of phosphorites from the Pacific Ocean seamounts is commonly intergrown with FeMn oxyhydroxide dendrites (Benninger and Hein, 2000). In seamount phosphorites from the equatorial Atlantic Ocean, some clasts were coated and impregnated by Fe oxyhydroxides (Jones et al., 2002), which were likely mineralized before their incorporation as clasts into the phosphorite breccias – a phenomenon also observed in phosphorite sample D10_003 from RGR. In RGR, FeMn mineralization occurred before phosphatization as depicted by FeMn crust layers with subsequent carbonate sediment filling the space between columns in the crusts that were then phosphatized and resulted in phosphorite lenses. Also, abundant Fe oxide, and less abundant Mn oxide, separate curved laminae within the fossil backfill burrow and line the margin of the entire burrow structure (Figure 4G, H), which probably precipitated before phosphatization.

FeMn mineralization also occurred after phosphatization as illustrated by non-phosphatized FeMn laminae overlying phosphatized FeMn laminae (Figure 3A) and FeMn coating the phosphorites and enveloping phosphorite clasts (Supporting Information Figure S2A, C, D, E). Finally, FeMn mineralization likely occurred very soon after phosphatization via diffusion as suggested by sparse Fe and Mn stains, fronts, and dendrites within CFA cement and foraminifera chambers as showed by EDS point analyses (Figure 5B, #7 and #9; 5C, #1 and #7; Supporting Information Figure S1B, D).

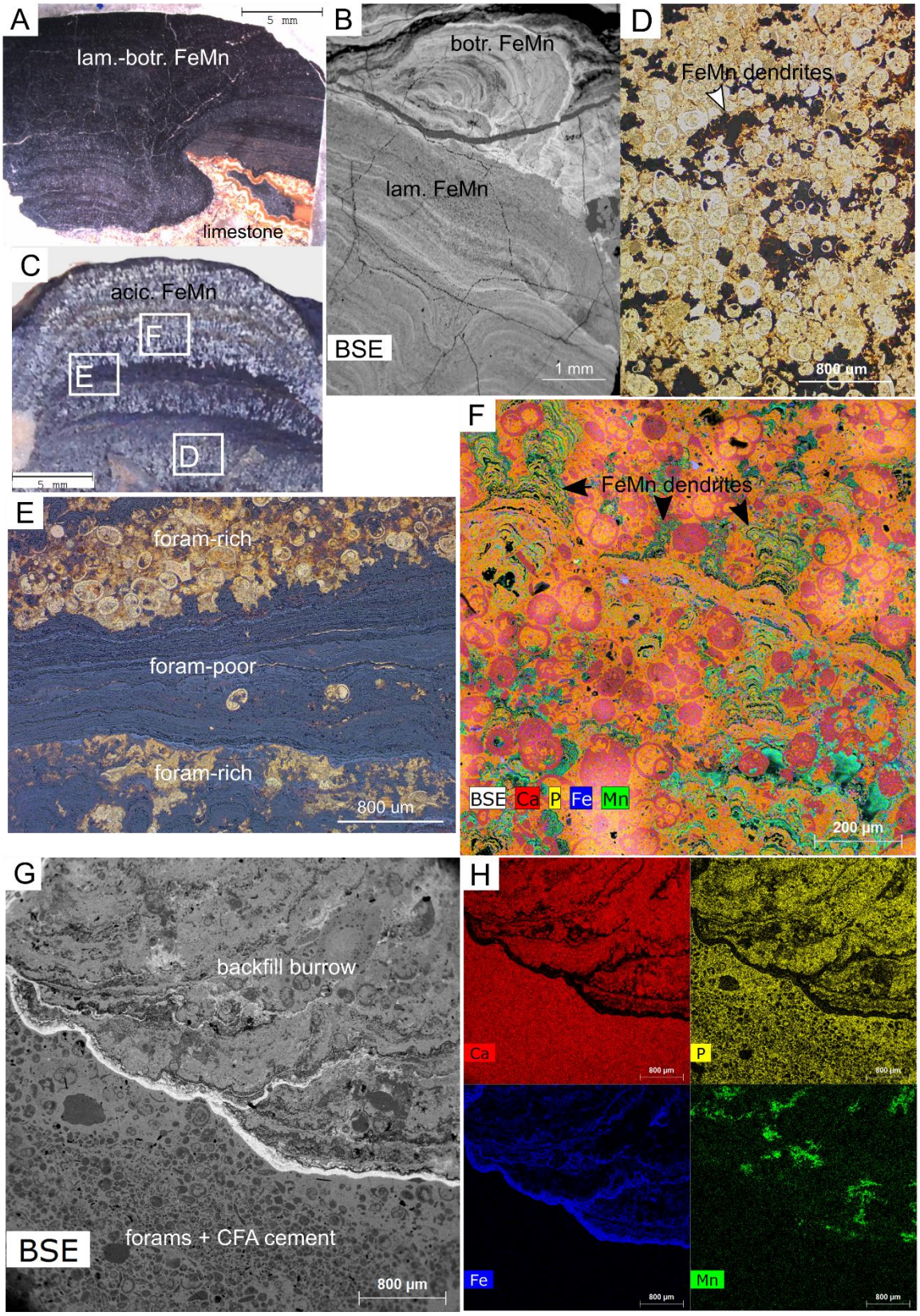

Figure 4: Images of different textures in phosphatized FeMn crusts. (a) Optical microscope image of phosphatized FeMn crust sample D02_030 showing laminated, botryoidal textures; the substrate rock is limestone; (b) scanning electron microscopy (SEM) image of the laminated-botryoidal texture in the phosphatized FeMn crust from D07_002 showing that no foraminifera are present and carbonate fluorapatite (CFA) instead forms laminations and fills pore space; (c) optical microscope image of phosphatized FeMn crust D11_003 showing a botryoidal structure with alternation of acicular and laminated layers; (d) optical microscope image of foraminifera-rich

acicular layer of (c); (e) optical microscope image showing in detail the contact between the foraminifera-rich acicular layers and the foraminifera-poor laminated layer; (f) SEM image overlaid by Energy Dispersive Spectroscopy (EDS) map of Ca, P, Mn, Fe of the acicular layer in (e) that is foraminifera-rich, resembling a carbonate ooze; Fe-Mn oxyhydroxide dendrites are evident; (g) SEM image and (h) EDS maps of phosphorite sample D09_025 showing abundant foraminifera supported by a cryptocrystalline CFA cement and a trace fossil backfilled burrow that cuts through the sample, within which Fe-oxide-rich, thin, curved laminae separate the thicker CFA-rich laminae. Foram. = foraminifera; Lam. = laminated; botr. = botryoidal; acic. = acicular; colum. = columnar; FeMn = FeMn crust.

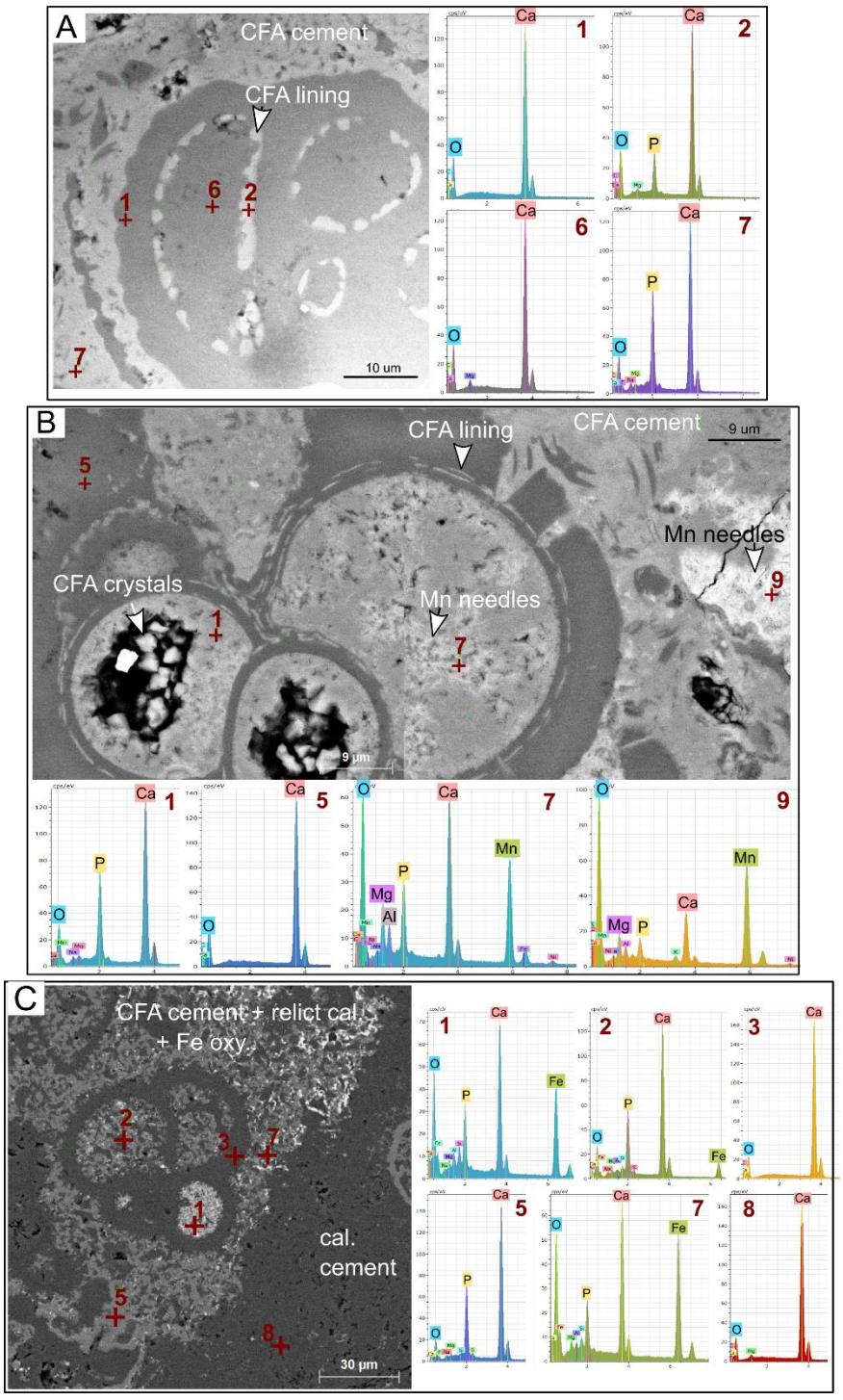

Figure 5: Images of carbonate fluorapatite (CFA) replacement of calcite in foraminifera tests. (a) and (b) scanning electron microscopy (SEM) images and Energy Dispersive Spectroscopy (EDS) point analyses (+) of foraminifera tests within the acicular and laminated textured portions of FeMn crust sample D11_003, respectively; (a) the calcite foraminifer test (gray) shows chamber wall rim cement of CFA (white), the remainder of the chambers are

filled with secondary calcite (gray), and the test is in a matrix is cryptocrystalline CFA (white, pale gray); (b) a calcite foraminifer test (dark gray) with CFA precipitated in pore spaces along lines parallel to the chamber walls (pale gray) and CFA cement filling the chambers (EDS #1); CFA crystals are seen in one chamber (white-pale gray); Mn oxyhydroxide needles fill the center of the bigger chamber (#7) and are also present in the CFA matrix (#9); (c) SEM images and EDS point analyses of foraminifera tests from phosphorite sample D09_025; a calcite foraminifera test (#3) filled with CFA (#2) within a phosphorite matrix (#5), with some regions containing Fe oxides (#7) including the filling of one of the foraminifer chambers (#1); the phosphorite matrix is surrounded by a calcite matrix (#8); relict calcite (dark gray grains) is widespread within the phosphorite matrix (light gray). Forams. = foraminifera; Cal. = calcite; Fe oxy. = Fe oxyhydroxide.

3.4.2.2 Resistance to phosphatization by limestones and ironstones at RGR

The limited CFA content of the limestones from RGR is in contrast to the abundant CFA in both the phosphorite originated from unconsolidated sediment and the FeMn crusts. The pervasive phosphatization of FeMn crusts that grew on only mildly phosphatized limestone substrates is shown in EDS maps (Supporting Information Figure S3A,B) and supports the notion that lithified limestones were less prone to phosphatization. Apart from larger clasts and grains (Figure 6A and Supporting Information Figure S3C), the limestones contain abundant bioclasts, as in the limestone breccia sample D10_003, which is composed of mollusk shells and foraminifera tests (Figure 6B) in a calcite cement with interference colors evident under polarized light (Figure 6B, colorful area). EDS maps reveal that the breccia matrix has almost no P (Figure 6C) and that P is restricted to phosphorite rock fragment clasts (Ca+P) within the breccia (Figure 6C), which correspond to bioclasts supported by CFA cement (Figure 6A), similar to the phosphorite samples. So, the mild phosphatization of the limestones is likely due to the characteristics of their calcite, namely the low porosity and large grain size of the calcite that cemented and lithified the rock.

Calcite cementation may occur at the seafloor or shallow subsurface at the top of guyots, plateaus, platform margins, and continental shelf and slope at rapid rates of 10 to 104 years under oxidizing conditions, low sedimentation rates, and stable strata with sufficient exchange with seawater (Milliman, 1974; James and Choquette, 1987). In the Northeast Atlantic seamounts, carbonate lithification was triggered by carbonate ion diffusion from supersaturated seawater into the sediment pore fluid (Noé et al., 2006). The Atlantic tropical and subtropical surface seawater is supersaturated with respect to calcite up to 2000 m water depth (Broecker and Takahashi, 1977; Takahashi et al., 1981, 2014), which encompasses the locality of the summit of RGR. Besides, based on the Sr age of 22 Ma for limestone D10_003, as discussed below, the summit of RGR was likely shallower at the time of calcite cementation. Finally, a relatively strong bottom current (50 cm s-1) at the RGR seafloor (Harlamov et al., 2015; Lisniowski et al., 2017) would facilitate seafloor carbonate cementation and hardground formation because the vigorous bottom currents enhance diffusion and the exhumation of

lithified carbonates, and prevent fine-grained sedimentation (Noé et al., 2006). As a result, the decreased porosity and permeability of the lithified limestone may have prevented or minimized phosphatization, which contrasts with the unconsolidated pelagic sediment in which phosphatization was facilitated by high porosity and permeability. In contrast, the coralline algal balls are highly porous, and yet they were only mildly phosphatized, which may be related to the susceptibility of the calcite to replacement by CFA because of the coarser grain size of the coral and mollusk fragments.

Laboratory experiments have shown the transformation of calcite to CFA involving rapid calcite dissolution in the presence of phosphate and F (Ekamparam and Singh, 2020). Nathan and Lucas (1972) showed that the replacement of calcite by CFA occurs first by the dissolution of calcite, which increases the Ca/Mg ratio of the solution and drives the crystallization of Ca-phosphate (apatite). According to the paragenetic model of phosphatization of limestone of Benninger and Hein (2000), during moderate to intense phosphatization, calcite is dissolved, and precipitation of CFA is pervasive. Phosphatization of RGR samples also followed this model and began with the dissolution of the smaller and more fragile fraction of a foraminifera-nannofossil ooze followed by subsequent formation of cryptocrystalline CFA cement. According to the paragenetic model, for mild phosphatization of limestones, calcite is sometimes not dissolved, and precipitation of CFA occurs in original pore spaces (Benninger and Hein, 2000); this is true for the mildly phosphatized limestones from RGR.

The mild phosphatization of the ironstones is likely due to their high rock/water ratio and consequently low porosity and permeability. The ironstones are composed of Fe-oxyhydroxide (goethite), are dense, and have massive and laminated textures with a lack of pore space available for CFA pore filling (Figure 6D). In addition, they do not contain fine-grained calcite to serve as a host for CFA replacement, which also hinders phosphatization. EDS maps of the ironstone show that the goethite laminae comprise Fe and oxygen and that CFA is limited to parallel and perpendicular veins and fractures between the goethite layers (Figure 6E). EDS point analyses of one of these veins show that the CFA (Figure 6F, #5) encapsulates grains of calcite (#1) that are probably relict calcite not completely dissolved/replaced; this suggests that CFA replaced the original calcite that was deposited within and between the goethite laminae. The carbonate sediment in veins and fractures between the goethite layers was mostly replaced by CFA.

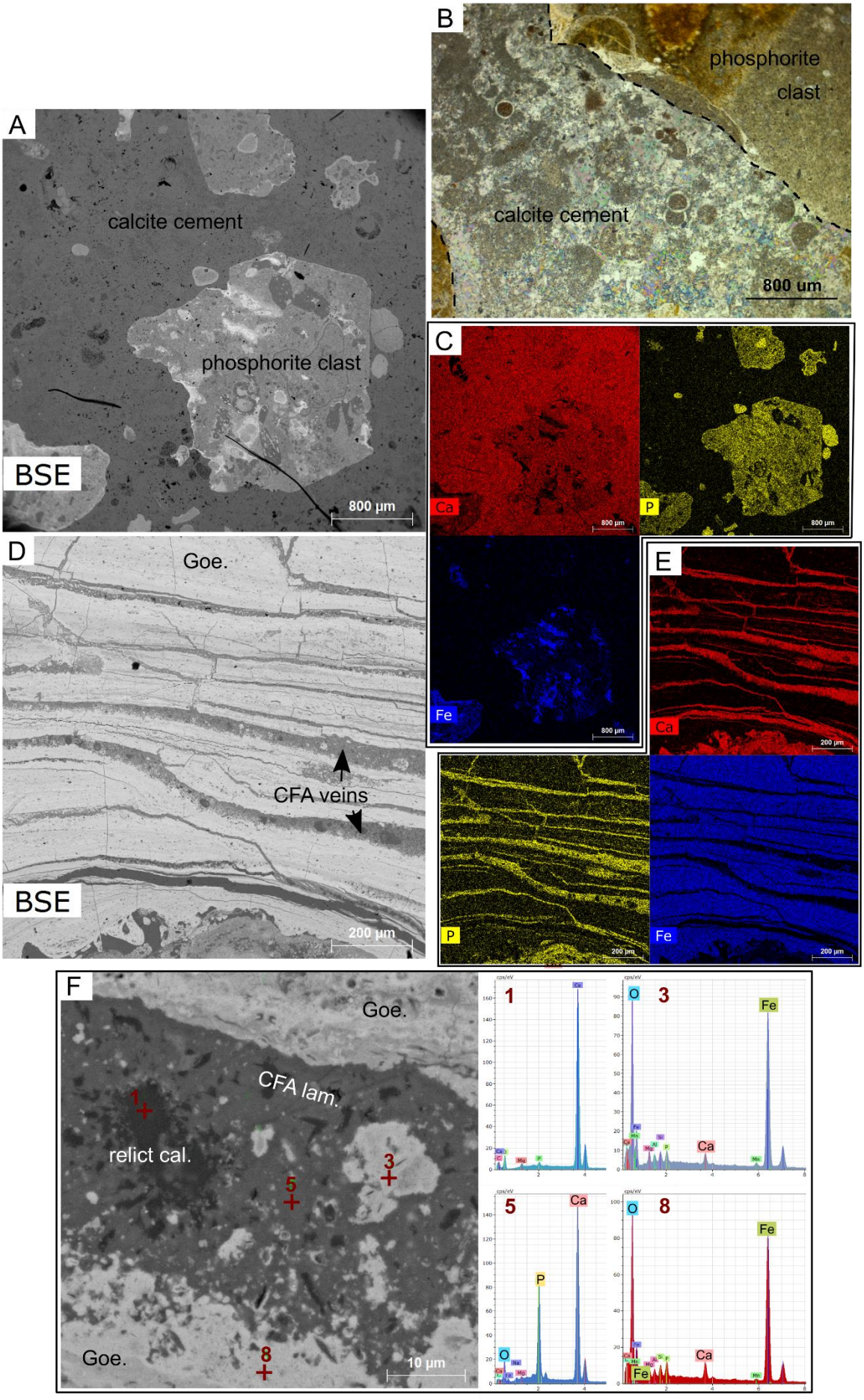
A
calcite cement
phosphorite clast
BSE
800 µm
B
phosphorite clast
calcite cement
800 um
C
Ca
P
Fe
800 µm
D
Goe.
CFA veins
BSE
200 µm
E
Ca
P
Fe
200 µm
F
Goe.
CFA lam.
relict cal.
Goe.
10 µm
1
3
5
8
O
Ca
Fe
P

Figure 6: Images of mineral boundaries in phosphatized limestone breccia and ironstone (a) scanning electron microscopy (SEM) image of the limestone breccia sample D10_003; (b) optical microscope image of recrystallized (secondary) calcite cement (multi-colored) supporting the limestone breccia and containing foraminifera; the multi-colored calcite is due to interference colors of coarse-grained calcite; dashed black lines mark the contact between calcite cement and phosphorite fragments (brown to greenish-brown) within the breccia; (c) Energy Dispersive Spectroscopy (EDS) maps of the same area in 'A' showing various phosphorite fragments in the calcite cement-supported breccia; (d) SEM Backscatter Electron image of ironstone layers composed of goethite with alternating carbonate fluorapatite (CFA) laminae; (e) EDS maps showing the goethite laminae (Fe) and CFA filling fractures and forming laminae that separate ironstone laminae; (f) SEM image of a CFA lamina of a CFA vein of D and EDS point analysis of the contact between goethite laminae (pale gray), a CFA vein (dark gray) that contains remnant calcite (very dark gray/black) from the original carbonate sediment that was replaced by CFA during phosphatization.

3.4.2.3 Detailed carbonate replacement mechanisms

From optical and electron microscopy, the phosphorite samples correspond to cemented pelagic sediments with abundant bioclastic material, dominantly planktonic and benthic foraminifera (Figure 4G and Supporting Information Figure S2B, F, G) and, less often, larger mollusk shells (Supporting Information Figure S2G, H). This is in accordance with the dominant type of sedimentation on RGR that took place since the Eocene being largely pelagic carbonates, a foraminifera-nannofossil ooze (Emelyanov and Trimonis, 1983; Florindo et al., 2015). EDS maps reveal the cement is CFA (Ca and P, Figure 4H and Supporting Information Figure S2D), which is more frequently cryptocrystalline (crystals are too small to be distinguished). Less frequently, granular CFA cement is also observed in areas of phosphorite sample D09_011 (Figure 5C), in which isolated calcite grains (dark grey) and etched foraminifera tests and other larger calcite fragments are seen, indicating the dissolution and replacement of original calcite by CFA. Based on these observations, the phosphorites from RGR best correspond to the phosphatization of unconsolidated foraminifera ooze. The presence of a trace fossil backfilled burrow cutting through sample D09_025 (Figure 4G and Supporting Information Figure S2E) and a series of curved laminae resulted from the movement of an organism through unconsolidated sediment support originally unconsolidated sediment. The phosphorite lenses within the phosphatized FeMn crusts also consist of bioclasts, mainly foraminifera tests (Supporting Information Figure S4) cemented by cryptocrystalline CFA, suggesting the accumulation of pelagic sediments in the troughs of the FeMn crusts surface before cementation.

In general, the calcite foraminifera tests within the FeMn crusts show good preservation with little evidence of dissolution, recrystallization, and replacement of the test wall (Figure 5A,B), which generally contains only CaCO3 (Figure 5A, #1; 5B, #5). The same is generally true for foraminifera tests within the phosphorites, although in a few areas the tests show etched walls or signs of recrystallization (Figure 5C and Supporting Information Figure

S2H). Pore-lining (pale grey) and chamber filling by CFA occur within the calcite foraminifera walls (dark grey) as seen in Figure 5A #2, and the inner wall of some chambers shows CFA lining with distinguishable CFA crystals (Figure 5B), suggesting that CFA filled open space. The foraminifera chambers are generally filled with CFA and calcite (Figure 5A,B,C), and less frequently Mn-oxide needles (Figure 5B, #7) and Fe oxide (Figure 5C, #1), which are also present in the matrix outside of the foraminifera chambers (Figure 5B, #9 and 5C, #7).

It is well known that CFA can form through the replacement of calcite, especially in carbonate sediments (Ames, 1959; Knudsen and Gunter, 2002; Filippelli, 2011). The foraminifera tests – a significant fraction of the carbonate sediments - escaped dissolution or replacement by CFA in general. However, these processes may have occurred to the smaller size fraction of the carbonate sediments, for example, nannofossils and smaller, delicate foraminifera tests. Phosphatized foraminifera-nannofossil-rich sediments are one of the most abundant types of seamount phosphorite found on central Pacific seamounts, in which clasts, foraminifera, and nannofossil tests are supported in a cryptocrystalline CFA matrix (Benninger and Hein, 2000). Similarly, cryptocrystalline CFA pervasively replaced bio-carbonate material and carbonate cement in limestones from Atlantic seamounts and banks (Jones et al., 2002).

3.4.3 Phosphatization and the rare earth elements plus Yttrium (REY) patterns

The total REY concentration in RGR phosphorite (15 ppm, Table 2) is relatively low compared to the mean total REY of continental-margin phosphorites (161 ppm) and pure CFA rocks (calcite removed) from other seamounts (935 ppm) reported by Hein et al. (2016b). Phosphatization at highly productive continental margins, with an anoxic water mass bounded by suboxic transition zones due to high organic matter flux, generally takes only thousands of years, whereas seamount phosphatization typically occurs over millions of years in relatively more oxygenated, low carbon, deeper open-ocean waters (Baturin, 2004; Filippelli, 2011; Hein et al., 2016b). Consequently, seamount phosphorites are more enriched in REY, except Ce, compared to continental-margin phosphorites because of the scavenging of REY for longer durations (Hein et al., 1993, 2016b) and the increase of dissolved REY in ocean water with increasing water depth (De Baar et al., 1985; Alibo and Nozaki, 1999). Compared to other seamounts/plateau phosphorites, the very low total REY content of CFA in RGR phosphorite deposits likely reflects their relatively shallow-water depth of phosphatization. The low REY contents may also indicate that phosphatization at RGR occurred over a relatively short timeframe. Compared to the phosphatization of Pacific seamount deposits–where most of the studies have been conducted—RGR phosphorites may have experienced a shorter time for REY

to sorb, substitute, or co-precipitate in the CFA (Hein et al., 2016b); this may indicate that RGR has experienced strong diagenetic redox zonation in the past. The total REY content of CFA leached from FeMn crusts at RGR (686 ppm) is lower compared to phosphorite rocks from other seamounts (935 ppm), but an order of magnitude higher than the phosphatized rocks at RGR (~ 15 ppm), which may indicate that REY can become more enriched in CFA that is forming within the chemical environment of the FeMn crust matrix. This hypothesis could be investigated in future works.

The shale-normalized REY (REYsn) patterns of the CFA leached from FeMn crusts, calcareous phosphorite, bulk phosphatized FeMn crusts, and limestones all resemble that of seawater (Figure 7), with heavier REYsn enrichment, Ce depletion leading to a negative Cesn anomaly, and positive Gdsn and Ysn anomalies. The similarity among the REYsn patterns with that of seawater indicates seawater as the phosphatizing fluid, which is a universal feature of seamount phosphorites (Hein et al., 1993; Koschinsky et al., 1997; Baturin and Yushina, 2007; Jiang et al., 2020), while continental-margin upwelling phosphorites have a shale-like REYsn pattern (Kolodny, 1981; Burnett et al., 1983, 1987). Modern seawater is enriched in dissolved heavy rare earth elements (HREE) because the light rare earth elements (LREE) are more particle reactive and tend to adsorb onto particulate matter (Sholkovitz et al., 1994; Alibo and Nozaki, 1999). The Cesn anomaly can further inform the redox conditions of CFA formation (German and Elderfield, 1990; Koschinsky et al., 1997; Auer et al., 2017). A positive Ce anomaly for CFA from phosphatized FeMn crusts has been argued to reflect dysoxic/suboxic conditions caused by Ce enrichment in the phosphatizing fluid liberated from FeMn oxyhydroxide reduction (Koschinsky et al., 1997). On the other hand, a strong negative Ce anomaly typically reflects oxic conditions for CFA formation (German and Elderfield, 1990; Auer et al., 2017) inherited from oxic seawater where fractionation of Cesn relative to the adjacent REE is due to the oxidation and accumulation of Cesn on the surface of FeMn oxides in the global ocean (Figure 7; Baturin and Yushina, 2007). The Ce anomaly of our phosphorites and phosphatized rocks is negative, which suggests phosphatization occurred at relatively oxic conditions (Garnit et al., 2012; Auer et al., 2017); however, the negative Cesn anomaly is not as pronounced as that for oxic seawater. Further, the presence of 10 Å manganates in the phosphatized FeMn crusts from RGR (Benites et al., 2020; Sousa et al., 2021) indicates the modification of the Mn oxides under lower redox potential than oxic seawater (Koschinsky et al., 1997; Wegorzewski et al., 2015; Hein et al., 2016a), which may occur within microenvironments of the rock during phosphatization. Thus, we suggest phosphatization occurred under intermediate oxic–suboxic conditions at RGR.

3.4.4 $^{87}Sr/^{86}Sr$ ratios and ages of phosphatization

The three predominantly calcite limestones samples show $^{87}Sr/^{86}Sr$ ratios from 0.708296 ±0.000004 to 0.708480 ±0.000004, which correspond to calibrated ages between 22.25 ±0.10 and 19.10 ±0.05 Ma (Table 3). Minor amounts of CFA are present in the limestones, so the resulting $^{87}Sr/^{86}Sr$ value is a combination of both calcite and any minor CFA in the sample, which would decrease the age from pure primary calcite; thus, these represent approximate but minimum depositional ages for the limestones. Still, the limestones are older than most CFA isolated from the phosphorites, FeMn crusts, and ironstones (spanning 20.25 ±0.10 Ma to 1.37 ±0.07 Ma.), which means they likely formed before the phosphatization events we observe at RGR.

The calibrated $^{87}Sr/^{86}Sr$ ages of CFA from phosphorites, leached FeMn crusts, and the phosphorite lenses within crusts range from 20.25 ±0.25 to 6.8 ±0.12 Ma. The ages of the CFA from phosphorite lenses match the age of the CFA leached from the corresponding FeMn crust stratigraphic level in which the phosphorite lens is contained, indicating phosphatization during the same paleoceanographic event. For example, D09_001 L1-13 CFA lens (16.62 ±0.07 Ma) and D09_001 L1-13 CFA from the crust (16.12 ±0.07 Ma) (note others in Table 3). Also, the five stratigraphic layers from FeMn crust D07_002 show CFA ages that are progressively younger from the bottom to the top (Figure 3A), indicating at least three phosphatization events. Although several phosphatization events occurred within a single crust, it is apparent that successive events did not result in Sr isotope re-equilibration in the previously formed CFA since the age of CFA from deeper/older stratigraphic layers is older than the shallower/younger stratigraphic layers. The CFA in the two ironstone samples (D09_005 and D10_003 L2-5) have similar calibrated $^{87}Sr/^{86}Sr$ ages, indicating both formed about 6.8 Ma. Much younger CFA ages were obtained from two phosphorite samples, the pervasively phosphatized semi-consolidated foraminifera ooze D10_002 at 1.97 ±0.15 Ma, and calcareous phosphorite D12_004 at 1.37 ±0.07 Ma (Quaternary).

Apart from the two Quaternary ages, the phosphatization of the rocks analyzed from the RGR summit started at ~20.2 Ma and ended ~6.8 Ma within the Miocene. This set of phosphatization ages is one of the most extensive published to date. Nevertheless, it should be noted that the distribution of ages reflects the degree of sampling; additional ages might be found with additional sampling and Sr-isotope analyses.

Table 2 Composition of rare earth elements plus Y of CFA leached from phosphatized FeMn crusts, carbonate algal balls, and phosphorite.

Sample name	Type	P (wt.%)	Total REY[1] (ppm)	La	Ce	Pr	Nd	Sm	Eu	Gd	Tb	Dy	Y	Ho	Er	Tm	Yb	Lu	%HREY[2]
D09_001	Leached CFA	10.5	347	78.8	61.5	12.9	57.3	11.1	2.46	12.91	1.97	12.81	153	2.97	9.05	1.18	7.10	1.07	58.9
D10_003	Leached CFA	9.69	686	142	141	23.0	105	20.8	4.72	25.7	3.81	25.17	295	5.88	17.9	2.27	13.6	2.02	57.7
D11_003	Leached CFA	11.7	636	167	67.6	28.3	126	24.5	5.52	28.6	4.19	26.4	284	5.99	18.0	2.27	13.3	1.89	61.3
D11_020	Carb. Algal ball	0.05	17.0	4.00	3.52	0.79	3.10	0.6	0.13	0.64	0.1	0.68	6.50	0.14	0.43	0.06	0.40	0.05	53.7
D12_004	Phosphorite	13.7	13.0	2.00	1.87	0.49	1.80	0.4	0.08	0.51	0.07	0.54	60	0.12	0.39	0.05	0.40	0.05	63.2
D12_008	Carb. Algal ball	0.05	10.0	2.55	1.68	0.51	1.90	0.4	0.08	0.385	0.06	0.40	4.50	0.08	0.24	<0.05	0.20	0.03	60.4

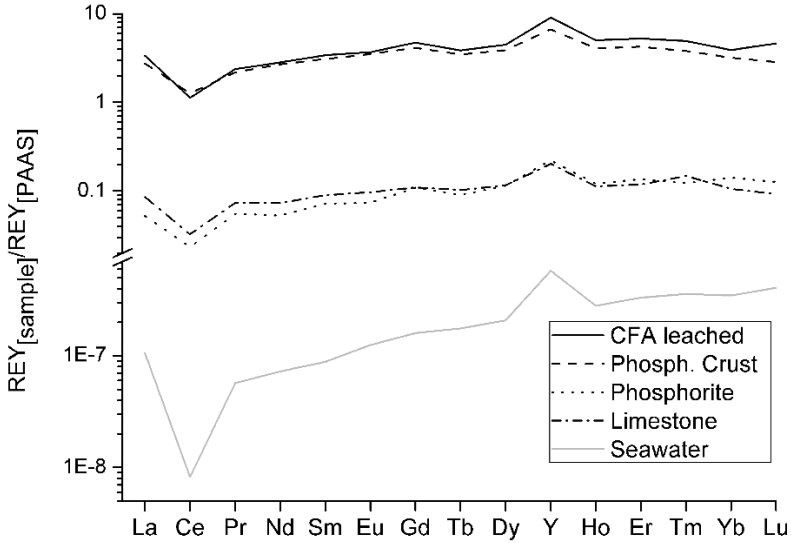

Figure 7 Post Archean Australian Shale (PAAS) normalized rare earth elements plus Yttrium (REY) patterns of RGR samples: average CFA leached from FeMn crusts (solid black); bulk phosphatized FeMn crust (dashed); phosphorite sample (dot); an average of two limestones (dashed dot); seawater at 800 m water depth off Japan from Alibo and Nozaki (1999) (solid grey).

Table 3 $^{87}Sr/^{86}Sr$ values and corresponding ages from the Sr-isotope seawater curve based on McArthur et al. (2012)[1]

Sample ID	Sample type	Mineral analyzed[2]	$^{87}Sr/^{86}Sr$	%StdErr	2StdErr	2SD	Sr Age (Ma)	± Ma

D12_004 Edge	Phosphorite	CFA	0.709115	0.000214	0.000004	0.000054	1.375	0.075
D10_002 Center	Phosphorite	CFA	0.709085	0.000278	0.000006	0.000070	1.975	0.150
D09_005	Ironstone	CFA	0.708957	0.000209	0.000004	0.000053	6.800	0.138
D17_017	FeMn crust	CFA	0.708957	0.000207	0.000004	0.000052	6.800	0.125
D10_003 L2-5	Ironstone	CFA	0.708956	0.000343	0.000007	0.000087	6.825	0.213
D15_017	FeMn crust	CFA	0.708923	0.000288	0.000006	0.000073	8.500	0.325
D07_002 L1-9	FeMn crust	CFA	0.708897	0.000741	0.000015	0.000188	9.600	0.513
D05_016 L0-23	FeMn crust	CFA	0.708889	0.000205	0.000004	0.000052	9.850	0.138
D07_002 L9-15	FeMn crust	CFA	0.708888	0.000606	0.000012	0.000153	9.900	0.413
D06_019	Phosphorite	CFA	0.708837	0.000613	0.000012	0.000155	12.000	0.675
D11_003 L0-6	FeMn crust	CFA	0.708833	0.000319	0.000006	0.000081	12.250	0.400
D07_001 substrate	Phosphorite	CFA	0.708794	0.000696	0.000014	0.000176	14.800	0.600
D09_001 L14-28 CFA lens	FeMn crust	CFA	0.708766	0.000284	0.000006	0.000072	15.400	0.087
D09_011	Phosphorite	CFA	0.708765	0.000569	0.000011	0.000144	15.400	0.175
D07_002 L15-22	FeMn crust	CFA	0.708750	0.000853	0.000017	0.000216	15.600	0.263
D07_003 L9-41	FeMn crust	CFA	0.708726	0.000199	0.000004	0.000050	15.975	0.062
D09_001 L1-13	FeMn crust	CFA	0.708715	0.000228	0.000005	0.000058	16.125	0.075
D02_030 L17-31	FeMn crust	CFA	0.708714	0.000276	0.000006	0.000070	16.150	0.075
D09_025 Center	Phosphorite	CFA	0.708704	0.000224	0.000004	0.000057	16.300	0.050
D09_001 L1-13 CFA lens	FeMn crust	CFA	0.708680	0.000242	0.000005	0.000061	16.625	0.075
D11_004 substrate	Phosphorite	CFA	0.708670	0.000857	0.000017	0.000217	16.750	0.238
D09_001 L14-28	FeMn crust	CFA	0.708669	0.000214	0.000004	0.000054	16.775	0.063
D11_003 L6-13	FeMn crust	CFA	0.708625	0.000360	0.000007	0.000091	17.350	0.088
D11_003 CFA lens	FeMn crust	CFA	0.708615	0.000346	0.000007	0.000088	17.500	0.100
D07_002 L22-30	FeMn crust	CFA	0.708530	0.000543	0.000011	0.000137	18.500	0.113
D10_003 Substrate 1	Limestone	Calcite[3]	0.708480	0.000203	0.000004	0.000051	19.100	0.050
D10_003 Substrate 2	Limestone	Calcite[3]	0.708448	0.000225	0.000005	0.000057	19.550	0.075
D10_003 L5-35	FeMn crust	CFA	0.708422	0.000224	0.000004	0.000057	20.000	0.075
D07_002 L30-44	FeMn crust	CFA	0.708408	0.000674	0.000013	0.000170	20.250	0.250
D11_020	Limestone	Calcite[3]	0.708296	0.000204	0.000004	0.000052	22.250	0.075

[1]%StdErr is percentage standard error; 2StdErr is two times the standard error; 2SD is two times the standard deviation

[2]Samples were treated to remove Fe and Mn oxyhydroxides, calcite, and organic matter (see Methods section)

[3]Samples were treated to remove organic matter

3.4.5 Phosphatization and past oceanographic conditions at Rio Grande Rise

Most CFA ages are confined to the Miocene, indicating that this Epoch provided the conditions necessary for repeated episodes of phosphatization along the RGR summit. However, phosphatization on RGR before the Miocene cannot be excluded due to phosphorite intraclasts embedded in the limestone breccia RGR1_D10_003 that gave calcite plus CFA combined age of 22 Ma (Early Miocene). Other seamount and plateau phosphorites also formed during the Miocene, for example, in the equatorial eastern Atlantic (Jones et al., 2002); along the South African continental margin (Siesser, 1978); in the Arabian sea (Rao et al., 2008); on Chatham Rise (Glasby and Summerhayes, 1975; Glasby and Wright, 1990); along the southern California continental margin (Mullins and Rasch, 1985); and along the Blake Plateau in the Atlantic Ocean off Florida (Manheim et al., 1980). Thus, the Miocene was a significant time for phosphogenesis globally.

Important global phosphogenesis events coincided with two significant global climatic shifts: (1) during the Eocene-Oligocene boundary (~34 Ma), when climate shifted from a warmer to a glacial Earth and (2) the late Oligocene–early Miocene transition (~27 to 21 Ma) during a shift from a glacial to warmer Earth (Hein et al., 1993; Hyeong et al., 2013; Schöllhorn et al., 2019; Jovane et al., 2020). According to Sheldon (1980), major climatic shifts initiated phosphogenesis in the oceans because they promoted intense oceanic vertical mixing that mobilized high amounts of phosphorus stored in the deep ocean after long periods of sluggish vertical mixing. The Oligocene–early Miocene global phosphatization event, for example, was associated with an increased oceanic equator-to-pole and vertical temperature gradient (Baldauf, 1992), leading to intensified ocean circulation, upwelling intensification, and increased primary productivity (Diester-Haass et al., 2011). The input of phosphorus to sediments on oceanic elevations during climatic shifts then occurred in two ways. First, intensified vertical mixing (obstructional upwelling) delivered inorganic P directly from the deep to carbonate sediments draping seamounts at shallower depths. Second, vertical mixing fertilized the euphotic zone with phosphorus and other nutrients, which was utilized for local primary productivity. With intensified primary productivity, the OMZ below the euphotic zone likely expanded and intensified due to respiration providing high storage of remineralized inorganic P. This biological P sequence may also have triggered phosphatization upon contact of the P-rich OMZ with seamounts (Hein et al., 1993; Koschinsky et al., 1997). We can infer periods of stronger OMZ in the RGR in the early to middle Miocene from enhanced biological productivity and organic carbon peaks in the sediments. For example, DSDP site 516 sediment cores at RGR revealed enhanced biological productivity from 23.9 – 22.9 Ma based on the accumulation of

foraminifera tests (Florindo et al., 2015) and organic carbon peaks at about 19.1 Ma and 15 Ma (Berggren et al., 1983; Emelyanov and Trimonis, 1983). In addition, stable C and O isotopes compositions ($\delta^{18}O$ and $\delta^{13}C$) of the planktonic foraminifers and alkenones data all point to an incursion of a cold, nutrient-rich intermediate water mass from high southern latitudes at ~20.3 Ma in the RGR area, caused by more dynamic circulation in the early Miocene in the South Atlantic (Pagani et al., 2000).

The late Oligocene–early Miocene phosphogenic episode was found to be diachronous throughout the Pacific Ocean to the central Atlantic Ocean, suggesting regional differences in the transfer of P (Schöllhorn et al., 2019) that may explain the lack of Oligocene phosphatization ages at RGR. During the first period of phosphatization on RGR in our dataset (early to mid-Miocene), the Antarctic ice sheet was ephemeral, with prominent oscillations in its volume and extent (Zachos et al., 2001b; Foster et al., 2012; Gasson et al., 2016; Jovane et al., 2019b). Evidence of variations in the influence of a proto-AAIW through the mid-Miocene in the RGR region was presented by Pagani et al. (2000). Thus, these strong oscillations in the overall circulation in the South Atlantic Ocean in the early Miocene potentially impacted nutrient supply, primary productivity, strength of the OMZ, and P cycling at RGR that promoted phosphatization.

The next phosphatization ages cluster between 17.5 and 14.8 Myr coinciding with the middle Miocene Climatic Optimum (MMCO) (Figure 8), which also promoted phosphatization along Pacific Ocean seamounts (e.g., Chatham Rise and Campbell Plateau; Glasby and Summerhayes, 1975; Hein et al., 1993). The MMCO comprises a short period of global warmth and retraction of the Antarctic Ice Sheet due to high atmospheric CO_2 (Foster et al., 2012). These conditions lead to changes in the global carbon reservoir resulting in lower seawater pH and marine carbonate dissolution (Holbourn et al., 2015; Kochhann et al., 2016; Sosdian et al., 2018, 2020), with dissolution events reported to have occurred in the South Atlantic Ocean (Kender et al., 2009). In a more substantial calcite dissolution scenario, CFA formation through calcite replacement could have been facilitated due to the high stability of CFA. In addition, the higher ocean-water temperature during the MMCO may have promoted lower solubility of CFA and, thus, enhanced phosphorite formation (Kolodny and Kaplan, 1970; Glasby and Summerhayes, 1975). After the MMCO, phosphatization in the RGR diminished between 14.8 and 12.2 Ma, coinciding with the middle Miocene Climate Transition (~14 Ma) (Figure 8) marked by a decline in atmospheric CO_2 after its highest level during the MMCO (Kürschner et al., 2008; Zhang et al., 2013).

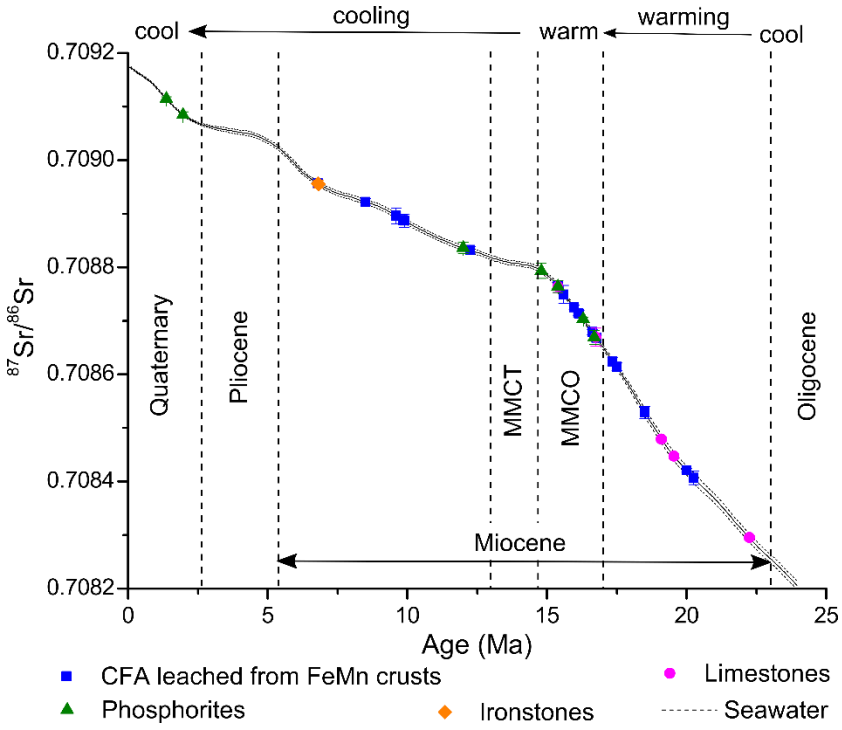

Figure 8: $^{87}Sr/^{86}Sr$ isotopic ratio of samples from the Rio Grande Rise plotted on the seawater curve (gray line); seawater $^{87}Sr/^{86}Sr$ values and calibrated ages after McArthur et al. (2012). MMCO = middle Miocene Climate Optimum; MMCT = middle Miocene Climate Transition.

The late Miocene phosphatization along RGR (12 – 6.8 Ma) and its cessation at ~6.8 Ma matches phosphatization along Chatham Rise, Blake Plateau, northwest Africa, southwest Africa, and southern California (Manheim et al., 1980; Glasby and Wright, 1990). In the Atlantic Ocean, the cessation of phosphatization along RGR at 6.8 Ma agrees with cessation in the equatorial eastern Atlantic (6 Ma) (Jones et al., 2002) and coincides with a more rapidly cooling climate and ice sheet expansion along West Antarctica and in the Arctic around 6 Ma (Zachos et al., 2001a). The late Miocene experienced more intense mid- and high-latitude cooling and glacial events and a decline in atmospheric pCO_2 that reduced continental weathering (Hodell and Kennett, 1986; Si and Rosenthal, 2019). This cooling was accompanied by periods of continental aridity in South America at the Miocene-Pliocene transition (Amidon et al., 2017). Therefore, the cessation of phosphatization along Atlantic seamounts at the Miocene-Pliocene transition seems to have been related to the dry, cooling climate, diminished weathering, and consequent diminished labile P input from rivers. In western and central Pacific seamounts, the cessation of phosphatization at 12 Ma was also linked to these factors (Hyeong et al., 2013).

The two quaternary ages (1.9 and 1.4 Ma) of phosphatization along the RGR summit are inserted in the cold climate context of glacial/interglacial periods that prevailed since the early Pleistocene in the subtropical South Atlantic Ocean (1.83–0.87 Ma) (Becquey and

Gersonde, 2002). The ages also match sedimentation hiatus intervals from 2.5 – 1.9 Ma and 1.6 – 0.8 Ma in the vicinity of RGR resulting from more vigorous contour currents (Ivanova et al., 2016, 2020) that also removed the sediment record of the last 2.5 Ma in the Weddell and Cape Basins (Ledbetter and Ciesielski, 1982). In this more vigorous contour current scenario, vertical mixing may have promoted the cycling of nutrients, including P, adjacent to oceanic elevations such as the RGR, thereby driving phosphatization locally.

A general conclusion for the feedback mechanism between phosphatization events and climate is challenging to make since the P cycle appears to respond to warm climate, such as during the MMCO, and to dynamic glacial activity in the early Miocene shown here and by others (e.g., Follmi, 1996). However, our results corroborate previous observations of an accelerated P cycle and broad phosphorite formation during periods of intensified ocean circulation and hydrodynamism (Filippelli, 2011; Hyeong et al., 2013).

3.4.5 The role of water depth

Water depth is strongly correlated with phosphatization of FeMn crusts from Pacific seamounts (Koschinsky et al., 1997; Hein et al., 2000), where a higher number of FeMn crusts and seamount rocks from shallower water depths tend to be phosphatized compared to deeper depths. Consistent with these observations, the FeMn crusts studied here – from 650-825 m water depths – are highly phosphatized, while crusts collected from the São Paulo plateau, located nearby RGR at 2871 m, have not been phosphatized at all (Goto et al., 2017). RGR summit crusts are also more intensely phosphatized than phosphatized crusts from deeper seamounts, for example, from >3000 m at Ninetyeast Ridge in the Indian Ocean (Hein et al., 2016a) and ~1500-2500 m on mid-Pacific seamounts (Koschinsky et al., 1997; Hein et al., 2000). The shallow-water depth of the RGR summit played a crucial role in providing the conditions for intense phosphatization, principally, proximity to a prolonged supply of reactive P from the OMZ that formed in response to increased surface primary productivity during the climatic conditions that corresponded to the phosphatization events. We note that the OMZ is a comparative term for the oxygen concentrations in the water column, and our data indicate that the OMZ at RGR remained oxic-suboxic throughout the history of phosphatization.

Notably, the paleodepth of the RGR summit was potentially even shallower during the Miocene. This is evidenced by the presence of coralline algal balls typically formed in the euphotic zone (this study), photosynthetic algae structures, the presence of large benthic foraminifera found in RGR phosphorites characteristic of shallow water (Sousa et al., 2021), and other sedimentological evidence (Barker, 1983; Camboa and Rabinowitz, 1984). Although

assemblages of planktonic foraminifera lacking photosynthetic organisms in RGR sediments indicate greater water depths since the Miocene (Sousa et al., 2021), these water depths could still have been shallower than the modern summit of RGR.

3.5 Conclusions

Miocene phosphatization events recorded in Southwest Atlantic Ocean RGR rocks produced phosphorites and phosphatized FeMn crusts, limestone, ironstone, and carbonate algal concretions. RGR FeMn crusts phosphatization is among the most pervasive ever discovered and produced a white-haze appearance not found in phosphatized crusts from other locations.

Petrographic and microscopic analyses reveal that phosphatization along the summit of RGR occurred mainly via CFA cementation and replacement of pelagic sediments. These formation mechanisms likely involved the dissolution of the smaller size fraction of foraminifera-nannofossil ooze and, less importantly, through the precipitation of CFA in pore space including foraminifera chambers. The intense phosphatization of FeMn crusts resulted from the high quantity of entrained biological carbonate particles from pelagic sedimentation and high crust porosity/permeability. Lithified limestones, carbonate algal balls, and ironstones were less intensely phosphatized due to their lower porosity-permeability (higher rock/water ratios), as well as larger calcite grain sizes. REY_{sn} patterns of the samples reveal that the phosphatizing fluid was ambient seawater under oxic-suboxic conditions that were likely provided by the OMZ that was in close proximity to the shallow summit of RGR, currently at 650-825 m water depth, which was likely shallower during the Miocene.

Phosphatization accompanied major shifts in the South Atlantic Ocean during the Miocene, including dynamic glacial activity during the early Miocene and increased temperature and atmospheric CO_2 related to the middle-Miocene Climatic Optimum. These periods of more dynamic circulation in the South Atlantic Ocean likely remobilized P from greater water depths and increased productivity in surface waters, both of which enhanced the P cycle. Most of the phosphatization apparently ceased at the Miocene-Pliocene transition due to a rapidly cooling and dry climate. However, minor Quaternary phosphatization corresponded with vigorous bottom currents that typically increase upwelling along topographic highs and could have promoted phosphatization.

This research provides the most extensive set of $^{87}Sr/^{86}Sr$ based phosphatization ages and correlated paleoclimatic/paleoceanographic conditions published to date. The P cycle appears to respond to both warm climate conditions, as for the MMCO, and to dynamic glacial activity in the early Miocene. Therefore, instead of establishing a link for phosphatization to a

specific type of historical climate regime, our results corroborate previous observations that intensified ocean circulation and hydrodynamism can initiate widespread development of phosphorites on seamounts due to vertical mixing and contact with an expanded/intensified OMZ caused by enhanced local primary productivity. Further sampling of rocks from the flanks and summit of RGR would help determine whether the full range of phosphatization ages in this unique seafloor feature has been fully represented. It is clear from this research that RGR represented an important phosphorous sink throughout the last ~20 Ma and an excellent setting for the study of P cycling in the Atlantic Ocean.

References

Alibo, D.S., and Nozaki, Y., 1999, Rare earth elements in seawater: Particle association, shale-normalization, and Ce oxidation: Geochimica et Cosmochimica Acta, v. 63, p. 363–372, doi:10.1016/S0016-7037(98)00279-8.

Ames, L.L., 1959, The genesis of carbonate apatites: Economic Geology, v. 54, p. 829–841, doi:10.2113/gsecongeo.54.5.829.

Amidon, W.H., Fisher, G.B., Burbank, D.W., Ciccioli, P.L., Alonso, R.N., Gorin, A.L., Silverhart, P.H., Kylander-Clark, A.R.C., and Christoffersen, M.S., 2017, Mio-Pliocene aridity in the south-central Andes associated with Southern Hemisphere cold periods: Proceedings of the National Academy of Sciences, v. 114, p. 6474–6479, doi:10.1073/pnas.1700327114.

Auer, G., Reuter, M., Hauzenberger, C.A., and Piller, W.E., 2017, The impact of transport processes on rare earth element patterns in marine authigenic and biogenic phosphates: Geochimica et Cosmochimica Acta, v. 203, p. 140–156, doi:10.1016/j.gca.2017.01.001.

De Baar, H.J.W., Bacon, M.P., Brewer, P.G., and Bruland, K.W., 1985, Rare earth elements in the Pacific and Atlantic Oceans: Geochimica et Cosmochimica Acta, v. 49, p. 1943–1959, doi:10.1016/0016-7037(85)90089-4.

Baldauf, J.G., 1992, Middle Eocene through early Miocene diatom floral turnover, *in* Prothero, D.R. and Berggren, W.A. eds., Eocene-Oligocene Climatic and Biotic Evolution, Princeton, Princeton University Press, p. 310–326, doi:10.1515/9781400862924.310 2525.

Barker, P.F., 1983, Tectonic evolution and subsidence history of the Rio Grande Rise.: Initial reports DSDP, Leg 72, Santos, Brazil, p. 953–976, doi:10.2973/dsdp.proc.72.151.1983.

Baturin, G.N., 2004, Thallium in oceanic phosphorites: Doklady Earth SciencesEarth Science, v. 394, p. 68–72.

Baturin, G.N., 1989, The origin of marine phosphorites: International Geology Review, v. 31, p. 327–342, doi:10.1080/00206818909465885.

Baturin, G.N., and Yushina, I.G., 2007, Rare earth elements in phosphate-ferromanganese crusts on Pacific seamounts: Lithology and Mineral Resources, v. 42, p. 101–117, doi:10.1134/s0024490207020010.

Becquey, S., and Gersonde, R., 2002, Past hydrographic and climate changes in the Subantarctic Zone of the South Atlantic - the Pleistocene record from ODP site 1090: Palaeogeography, Palaeoclimatology, Palaeoecology, v. 182, p. 221–239, doi:10.1016/S0031-0182(01)00497-7.

Benites, M., Hein, J.R., Mizell, K., Blackburn, T., and Jovane, L., 2020, Genesis and Evolution of Ferromanganese Crusts from the Summit of Rio Grande Rise, Southwest Atlantic Ocean: Minerals, v. 10, p. 349, doi:10.3390/min10040349.

Benninger, L.M., and Hein, J.R., 2000, Diagenetic evolution of seamount phosphorite: Marine Authigenesis: From Global to Microbial, p. 245–256, doi:10.2110/pec.00.66.0245.

Berggren, W.A., Aubry, M.P., and Hamilton, N., 1983, Neogene magnetobiostratigraphy of Deep Sea Drilling Project Site 516 (Rio Grande Rise, South Atlantic):, doi:10.2973/dsdp.proc.72.130.1983.

Berner, R.A., 1973, Phosphate removal from sea water by adsorption on volcanogenic ferric oxides: Earth and Planetary Science Letters, v. 18, p. 77–86, doi:10.1016/0012-821X(73)90037-X.

Broecker, W.S., and Takahashi, T., 1977, The Solubility of Calcite in Sea Water, *in* Fraser, D.G. ed., Thermodynamics in Geology, Dordrecht, Springer, doi:10.1007/978-94-010-1252-2_18.

Burnett, W.C., Cullen, D.J., and McMurtry, G.M., 1987, Open-ocean phosphorites - in a class by themselves?, *in* Teleki, P.G., Dobson, M.R., Moore, J.R., and von Stackelberg, U. eds., Marine Minerals. NATO ASI Series (Series C: Mathematical and Physical Sciences), Dordrecht, Springer, p. 119–134, doi:10.1007/978-94-009-3803-8_10.

Burnett, W.C., Roe, K.K., and Piper, D.Z., 1983, Upwelling and phosphorite formation in the ocean, *in* Suess, E. and Thiede, J. eds., Coastal upwelling: its sediment record. NATO Conference Series (IV Marine Sciences), Boston, MA, Springer, v. 10B, p. 377–397, doi:10.1007/978-1-4615-6651-9.

Camboa, L.A.P., and Rabinowitz, P.D., 1984, The evolution of the Rio Grande Rise in the southwest Atlantic Ocean: Marine Geology, v. 58, p. 35–58, doi:10.1016/0025-3227(84)90115-4.

Cavalcanti, A.J.D., da Silva, J.C.B., Christian, S., Lacasse, M., Nereu, J., Rojas, L., and Nobrega, M., 2015, Potential Mineral Resources of Phosphates and Trace Elements on the Rio Grande Rise , South Atlantic Ocean: Nearshore Underwater Mining: Critical Commodities for the Future. 44th Underwater Mining Conference · 1-6 November 2015, Tampa Bay, Florida USA, p. 11 pp., https://www.researchgate.net/profile/Jose_Dias_Cavalcanti/publication/284178203_Potential_Mineral_Resources_of_Phosphates_and_Trace_Elements_on_the_Rio_Grande_Rise_South_Atlantic_Ocean/links/564e257908aeafc2aab19e2f.pdf.

Cook, H.E., Johnson, P.D., Matti, J.C., and Zemmels, I., 1975, Methods of sample preparation and X-ray data analysis (X-ray mineralogy laboratory, Deep Sea Drilling Project, University of California Riverside).:

Diester-Haass, L., Billups, K., and Emeis, K., 2011, Enhanced paleoproductivity across the Oligocene/Miocene boundary as evidenced by benthic foraminiferal accumulation rates:

Palaeogeography, Palaeoclimatology, Palaeoecology, v. 302, p. 464–473, doi:10.1016/j.palaeo.2011.02.006.

Ekamparam, A.S.S., and Singh, A., 2020, Transformation of calcite to fluorapatite at room temperature: Impact of initial phosphate and fluoride levels: Geochimica et Cosmochimica Acta, v. 288, p. 16–35, doi:10.1016/j.gca.2020.07.039.

Elser, J.J., Bracken, M.E.S., Cleland, E.E., Gruner, D.S., Harpole, W.S., Hillebrand, H., Ngai, J.T., Seabloom, E.W., Shurin, J.B., and Smith, J.E., 2007, Global analysis of nitrogen and phosphorus limitation of primary producers in freshwater, marine and terrestrial ecosystems: Ecology Letters, v. 10, p. 1135–1142, doi:10.1111/j.1461-0248.2007.01113.x.

Emelyanov, E.M., and Trimonis, E.S., 1983, Geochemical investigation of sediments from the Brazil Basin and the Rio Grande Rise:, doi:10.2973/dsdp.proc.72.112.1983.

Filippelli, G.M., 2011, Phosphate rock formation and marine phosphorus geochemistry: The deep time perspective: Chemosphere, v. 84, p. 759–766, doi:10.1016/j.chemosphere.2011.02.019.

Florindo, F., Gennari, R., Persico, D., Turco, E., Villa, G., Lurcock, P.C., Roberts, A.P., Winkler, A., Carter, L., and Pekar, S.F., 2015, New magnetobiostratigraphic chronology and paleoceanographic changes across the Oligocene-Miocene boundary at DSDP Site 516 (Rio Grande Rise, SW Atlantic): Paleoceanography, v. 30, p. 659–681, doi:10.1002/2014PA002734.

Follmi, K.B., 1996, The phosphorus cycle, phosphogenesis phosphate-rich deposits: Earth-Science Reviews, v. 40, p. 55–124, doi:10.1016/0012-8252(95)00049-6.

Foster, G.L., Lear, C.H., and Rae, J.W.B., 2012, The evolution of pCO 2, ice volume and climate during the middle Miocene: Earth and Planetary Science Letters, v. 341–344, p. 243–254, doi:10.1016/j.epsl.2012.06.007.

Garnit, H., Bouhlel, S., Barca, D., and Chtara, C., 2012, Application of LA-ICP-MS to sedimentary phosphatic particles from Tunisian phosphorite deposits: Insights from trace elements and REE into paleo-depositional environments: Chemie der Erde, v. 72, p. 127–139, doi:10.1016/j.chemer.2012.02.001.

Gasson, E., DeConto, R.M., Pollard, D., and Levy, R.H., 2016, Dynamic Antarctic ice sheet during the early to mid-Miocene: Proceedings of the National Academy of Sciences, v. 113, p. 3459–3464, doi:10.1073/pnas.1516130113.

German, C.R., and Elderfield, H., 1990, Application of the Ce anomaly as a paleoredox indicator: The ground rules: Paleoceanography, v. 5, p. 823–833, doi:10.1029/PA005i005p00823.

Glasby, G.P., and Summerhayes, C.P., 1975, Sequential deposition of authigenic marine minerals around new zealand: Paleoenvironmental significance: New Zealand Journal of Geology and Geophysics, v. 18, p. 477–490, doi:10.1080/00288306.1975.10421548.

Glasby, G.P., and Wright, I.C., 1990, Marine mineral potential in New Zealand's exclusive economic zone: Proceedings of the Annual Offshore Technology Conference, v. 1990-May, p. 479–490, doi:10.4043/6326-MS.

Glenn, C.R. et al., 1994, Phosphorus and phosphorites: sedimentology and environments of formation: Eclogae Geologicae Helvetiae, v. 87, p. 747–788.

Goto, K.T., Nozaki, T., Toyofuku, T., Augustin, A.H., Shimoda, G., Chang, Q., Kimura, J.I., Kameo, K., Kitazato, H., and Suzuki, K., 2017, Paleoceanographic conditions on the São Paulo Ridge, SW Atlantic Ocean, for the past 30 million years inferred from Os and Pb isotopes of a hydrogenous ferromanganese crust: Deep-Sea Research Part II: Topical Studies in Oceanography, v. 146, p. 82–92, doi:10.1016/j.dsr2.2016.10.010.

Harlamov, V. et al., 2015, Preliminary results on mid-depth circulation features on Rio Grande Rise, *in* 2015 IEEE/OES Acoustics in Underwater Geosciences Symposium (RIO Acoustics), Rio de Janeiro, p. 0–7, doi:10.1109/RIOAcoustics.2015.7473647.

Heggie, D.T., Skyring, G.W., O'Brien, G.W., Reimers, C., Herczeg, A., Moriarty, D.J.W., Burnett, W.C., and Milnes, A.R., 1990, Organic carbon cycling and modern phosphorite formation on the East Australian continental margin: An overview: Geological Society Special Publication, v. 52, p. 87–117, doi:10.1144/GSL.SP.1990.052.01.07.

Hein, J., Conrad, T., Mizell, K., Banakar, V.K., Frey, F.A., and Sager, W.W., 2016a, Controls on ferromanganese crust composition and reconnaissance resource potential, Ninetyeast Ridge, Indian Ocean: Deep-Sea Research Part I, v. 110, p. 1–19, doi:10.1016/j.dsr.2015.11.006.

Hein, J., Gunn, H., Sliter, V., and Benninger, M., 1993, Two major Cenozoic episodes of phosphogenesis recorded in Equatorial Pacific seamounts deposits: Paleoceanography, v. 8, p. 293–311, doi:10.1029/93PA00320.

Hein, J.R., Koschinsky, A., Bau, M., Manheim, F.T., Kang, J., and Roberts, L., 2000, Cobalt-rich ferromanganese crusts in the Pacific, *in* Cronan, D.S. ed., Handbook of Marine Mineral Deposits, Boca Raton, Florida, CRC Marine Science Series. CRC Press, p. 239–279.

Hein, J., Koschinsky, A., Mikesell, M., Mizell, K., Glenn, C., and Wood, R., 2016b, Marine phosphorites as potential resources for heavy rare earth elements and yttrium: Minerals, v. 6, p. 88, doi:10.3390/min6030088.

Hein, J.R., Schwab, W.C., and Davis, A.S., 1988, Cobalt- and platinum-rich ferromanganese crusts and associated substrate rocks from the Marshall Islands: Marine Geology, v. 78, p. 255–283, doi:10.1016/0025-3227(88)90113-2.

Hodell, D.A., and Kennett, J.P., 1986, Late Miocene–Early Pliocene stratigraphy and paleoceanography of the South Atlantic and southwest Pacific oceans: A synthesis: Paleoceanography, v. 1, p. 285–311, doi:10.1029/pa001i003p00285.

Holbourn, A., Kuhnt, W., Kochhann, K.G.D., Andersen, N., and Sebastian Meier, K.J., 2015, Global perturbation of the carbon cycle at the onset of the Miocene Climatic Optimum: Geology, v. 43, p. 123–126, doi:10.1130/G36317.1.

Hyeong, K., Kim, J., Yoo, C.M., Moon, J.W., and Seo, I., 2013, Cenozoic history of phosphogenesis recorded in the ferromanganese crusts of central and western Pacific seamounts: Implications for deepwater circulation and phosphorus budgets: Palaeogeography, Palaeoclimatology, Palaeoecology, v. 392, p. 293–301, doi:10.1016/j.palaeo.2013.09.012.

Ivanova, E., Borisov, D., Dmitrenko, O., and Murdmaa, I., 2020, Hiatuses in the late Pliocene–Pleistocene stratigraphy of the Ioffe calcareous contourite drift, western South Atlantic: Marine and Petroleum Geology, v. 111, p. 624–637, doi:10.1016/j.marpetgeo.2019.08.031.

Ivanova, E., Murdmaa, I., Borisov, D., Dmitrenko, O., Levchenko, O., and Emelyanov, E., 2016, Late Pliocene-Pleistocene stratigraphy and history of formation of the Ioffe calcareous contourite drift, Western South Atlantic: Marine Geology, v. 372, p. 17–30, doi:10.1016/j.margeo.2015.12.002.

Jahnke, R.A., 1984, The synthesis and solubility of carbonate fluorapatite.: American Journal of Science, v. 284, p. 58–78, doi:10.2475/ajs.284.1.58.

James, N.P., and Choquette, P.W., 1987, Diagenesis 6. Limestones - the sea floor diagenetic environment: Geoscience Canada, v. 10, p. 162–179.

Jiang, X.-D., Sun, X.-M., Chou, Y.-M., Hein, J.R., He, G.-W., Fu, Y., Li, D., Liao, J.-L., and Ren, J.-B., 2020, Mineralogy and geochemistry of carbonate fluorapatite in seamount Fe Mn crusts from the Pacific Ocean: Marine Geology, v. 423, p. 106135, doi:10.1016/j.margeo.2020.106135.

Jones, E.J.W., Boudagher-Fadel, M.K., and Thirlwall, M.F., 2002, An investigation of seamount phosphorites in the eastern Equatorial Atlantic: Marine Geology, v. 183, p. 143–162, doi:10.1016/S0025-3227(01)00254-7.

Jovane, L. et al., 2019a, Multidisciplinary Scientific Cruise to the Rio Grande Rise: Frontiers in Marine Science, v. 6, p. 1–7, doi:10.3389/fmars.2019.00252.

Jovane, L. et al., 2019b, Miocene Glacial Dynamics Recorded by Variations in Magnetic Properties in the ANDRILL-2A Drill Core: Journal of Geophysical Research: Solid Earth, v. 124, p. 2297–2312, doi:10.1029/2018JB016865.

Jovane, L., Florindo, F., Wilson, G., de Almeida Pecchiai Saldanha Leone, S., Hassan, M., Rodelli, D., and Cortese, G., 2020, Magnetostratigraphic Chronology of a Cenozoic Sequence From DSDP Site: Frontiers in Earth Science, v. 8, p. 1–16, doi:10.3389/feart.2020.563453.

Kender, S., Peck, V.L., Jones, R.W., and Kaminski, M.A., 2009, Middle Miocene oxygen minimum zone expansion offshore West Africa: Evidence for global cooling precursor events: Geology, v. 37, p. 699–702, doi:10.1130/G30070A.1.

Knudsen, A.C., and Gunter, M.E., 2002, Sedimentary Phosphorites — An Example: Phosphoria Formation, Southeastern Idaho, USA: Reviews in Mineralogy and Geochemistry, v. 48, p. 363–389, doi:10.2138/rmg.2002.48.9.

Kochhann, K.G.D., Holbourn, A., Kuhnt, W., Channell, J.E.T., Lyle, M., Shackford, J.K., Wilkens, R.H., and Andersen, N., 2016, Eccentricity pacing of eastern equatorial Pacific carbonate dissolution cycles during the Miocene Climatic Optimum: Paleoceanography, v. 31, p. 1176–1192, doi:10.1002/2016pa002988.

Kolodny, Y., 1981, Phosphorites, *in* Emiliani, C. ed., The Sea, VII, The Oceanic Lithosphere, New York, Wiley Interscience, p. 981–1023.

Kolodny, Y., and Kaplan, I.R., 1970, Carbon and oxygen isotopes in apatite CO2 and co-

existing calcite from sedimentary phosphorite: Journal of sedimentary Petrology, v. 40, p. 954–959, doi:10.1306/74D720EF-2B21-11D7-8648000102C1865D.

Koschinsky, A., and Hein, J.R., 2003, Uptake of elements from seawater by ferromanganese crusts: Solid-phase associations and seawater speciation: Marine Geology, v. 198, p. 331–351, doi:10.1016/S0025-3227(03)00122-1.

Koschinsky, A., Stascheit, I.A., Bau, M., and Halbach, P., 1997, Effects of phosphatization on the geochemical and mineralogical composition of marine ferromanganese crusts: Geochimica et Cosmochimica Acta, v. 6, p. 4079–4094.

Kraal, P., Slomp, C.P., Reed, D.C., Reichart, G.J., and Poulton, S.W., 2012, Sedimentary phosphorus and iron cycling in and below the oxygen minimum zone of the northern Arabian Sea: Biogeosciences, v. 9, p. 2603–2624, doi:10.5194/bg-9-2603-2012.

Krom, M., and Berner, R., 1981, The diagenesis of phosphorus in a nearshore marine sediment: Geochimica et Cosmochimica Acta, v. 45, p. 207–216, doi:10.1016/0016-7037(81)90164-2.

Kürschner, W.M., Kvaček, Z., and Dilcher, D.L., 2008, The impact of Miocene atmospheric carbon dioxide fluctuations on climate and the evolution of terrestrial ecosystems: Proceedings of the National Academy of Sciences, v. 105, p. 449–453, doi:10.1073/pnas.0708588105.

Ledbetter, M.T., and Ciesielski, P.F., 1982, Bottom-current erosion along a traverse in the South Atlantic sector of the Southern Ocean: Marine Geology, v. 46, p. 329–341, doi:10.1016/0025-3227(82)90087-1.

Lisniowski, M.A., Pessanha, I.B.M., and Neto, A.A., 2017, Sediment Waves on the Rio Grande Rise, *in* 2017 IEEE/OES Acoustics in Underwater Geosciences Symposium (RIO Acoustics), Rio de Janeiro, IEEE, p. 1–5, doi:10.1109/RIOAcoustics.2017.8349731.

Lucotte, M., Mucci, A., Hillaire-Marcel, C., and Tran, S., 1994, Early diagenetic processes in deep Labrador Sea sediments; reactive and nonreactive iron and phosphorus: Canadian Journal of Earth Sciences, v. 31, p. 14–27, doi:10.1139/e94-003.

Manheim, F.T., Pratt, R.M., and McFarlin, P.F., 1980, Composition and origin of phosphorite deposits of the Blake Plateau: SEPM special publication, v. 29, p. 117–137, doi:10.2110/pec.80.29.0117.

McArthur, J., Howarth, R.J., and Shields, G.A., 2012, Strontium isotope stratigraphy, *in* Gradstein, F., Ogg, J.G., Schmitz, M.D., and Ogg, G.M. eds., The Geologic Time Scale 2012, Oxford, UK, Elsevier, p. 127–144, doi:10.1017/CBO9780511536045.008.

McArthur, J.M., Sahami, A.R., Thirlwall, M., Hamilton, P.J., and Osborn, A.O., 1990, Dating phosphogenesis with strontium isotopes: Geochimica et Cosmochimica Acta, v. 54, p. 1343–1351, doi:10.1016/0016-7037(90)90159-I.

Melguen, M., and Thiede, J., 1974, Facies distribution and dussolution depths of surface sediment components from the Vema channel and the Rio Grande Rise (southwest Atlantic Ocean): Marine Geology, v. 17, p. 341–353, doi:10.1016/0025-3227(74)90096-6.

Milliman, J.D., 1974, Precipitation and Cementation of Deep-Sea Carbonate Sediments: Deep-Sea Sediments, p. 463–476, doi:10.1007/978-1-4684-2754-7_23.

Montserrat, F. et al., 2019, Deep-sea mining on the Rio Grande Rise (Southwestern Atlantic): A review on environmental baseline, ecosystem services and potential impacts: Deep-Sea Research Part I, v. 145, p. 31–58, doi:10.1016/j.dsr.2018.12.007.

Mueller, T.J., 1997. CTD data from section A10, Cruise 06MT22_5. Accessed from http://whp-atlas.ucsd.edu/atlantic/a10/sections/printatlas/A10_OXYGEN.pdf. Access date 2021-07-23.

Mullins, H.T., and Rasch, R.F., 1985, Sea-floor phosphorites along the central California continental margin.: Economic Geology, v. 80, p. 696–715, doi:10.2113/gsecongeo.80.3.696.

Nathan, Y., and Lucas, J., 1972, Synthese de l'apatite a partir du gypse: application au probleme de la formation des apatites carbonatees par precipitation directe: Chemical Geology, v. 9, p. 99–112, doi:10.1016/0009-2541(72)90040-X.

Noé, S., Titschack, J., Freiwald, A., and Dullo, W.C., 2006, From sediment to rock: Diagenetic processes of hardground formation in deep-water carbonate mounds of the NE Atlantic: Facies, v. 52, p. 183–208, doi:10.1007/s10347-005-0037-x.

Pagani, M., Arthur, M.A., and Freeman, K.H., 2000, Variations in Miocene phytoplankton growth rates in the Southwest Atlantic: Evidence for changes in ocean circulation: Paleoceanography, v. 15, p. 486–496, doi:10.1029/1999PA000484.

Poggemann, D.W., Hathorne, E.C., Nürnberg, D., Frank, M., Bruhn, I., Reißig, S., and Bahr, A., 2017, Rapid deglacial injection of nutrients into the tropical Atlantic via Antarctic Intermediate Water: Earth and Planetary Science Letters, v. 463, p. 118–126, doi:10.1016/j.epsl.2017.01.030.

Rao, V.P., Hegner, E., Naqvi, S.W.A., Kessarkar, P.M., Ahmad, S.M., and Raju, D.S., 2008, Miocene phosphorites from the Murray Ridge, northwestern Arabian Sea: Palaeogeography, Palaeoclimatology, Palaeoecology, v. 260, p. 347–358, doi:10.1016/j.palaeo.2007.12.003.

Ruttenberg, K.C., 1992, Development of a sequential extraction method for different forms of phosphorus in marine sediments: Limnology and Oceanography, v. 37, p. 1460–1482, doi:10.4319/lo.1992.37.7.1460.

Schöllhorn, I., Houben, A., Gertsch, B., Adatte, T., Alexey, U., de Kaenel, E., Spangenberg, J.E., Janssen, N., Schwennicke, T., and Föllmi, K.B., 2019, Enhanced upwelling and phosphorite formation in the northeastern Pacific during the late Oligocene: Depositional mechanisms, environmental conditions, and the impact of glacio-eustacy: GSA Bulletin, p. 1–23, doi:10.1130/b32061.1.

Sheldon, R.P., 1980, Episodicity of Phosphate Deposition and Deep Ocean Circulation-A Hypothesis (Y. K. Bentor, Ed.): Marine Phosphorites—Geochemistry, Occurrence, Genesis, v. 29, p. 0, doi:10.2110/pec.80.29.0239.

Sholkovitz, E.R., Landing, W.M., and Lewis, B.L., 1994, Ocean particle chemistry: The fractionation of rare earth elements between suspended particles and seawater: Geochimica et Cosmochimica Acta, v. 58, p. 1567–1579, doi:10.1016/0016-

7037(94)90559-2.

Si, W., and Rosenthal, Y., 2019, Reduced continental weathering and marine calcification linked to late Neogene decline in atmospheric CO2: Nature Geoscience, p. 1–6, doi:10.1038/s41561-019-0450-3.

Siesser, W.G., 1978, Age of phosphorites on the South African continental margin: Marine Geology, v. 26, p. M17–M28, doi:10.1016/0025-3227(78)90053-1.

Silverman, S., Fuyat, R., and Weiser, J., 1952, Quantitative determination of calcite associated with carbonate-bearing apatites: American Mineralogist, v. 37, p. 211–222.

Sosdian, S.M., Babila, T.L., Greenop, R., Foster, G.L., and Lear, C.H., 2020, Ocean Carbon Storage across the middle Miocene: a new interpretation for the Monterey Event: Nature Communications, v. 11, p. 134, doi:10.1038/s41467-019-13792-0.

Sosdian, S.M., Greenop, R., Hain, M.P., Foster, G.L., Pearson, P.N., and Lear, C.H., 2018, Constraining the evolution of Neogene ocean carbonate chemistry using the boron isotope pH proxy: Earth and Planetary Science Letters, v. 498, p. 362–376, doi:10.1016/j.epsl.2018.06.017.

Sousa, I.M.C., Santos, R. V., Koschinsky, A., Bau, M., Wegorzewski, A. V., Cavalcanti, J.A.D., and Dantas, E.L., 2021, Mineralogy and chemical composition of ferromanganese crusts from the Cruzeiro do Sul Lineament - Rio Grande Rise, South Atlantic: Journal of South American Earth Sciences, v. 108, p. 103207, doi:10.1016/j.jsames.2021.103207.

Takahashi, T., Broecker, W.S., and Bainbridge, A.E., 1981, The alkalinity and total carbon dioxide concentration in the world oceans: Carbon cycle modelling, SCOPE, v. 16, p. 271–286, http://data.ieda.org.cn/upload/fckeditor/SCOPE_16_1.5.07_Takahashi_271-286.pdf.

Takahashi, T., Sutherland, S.C., Chipman, D.W., Goddard, J.G., and Ho, C., 2014, Climatological distributions of pH, pCO2, total CO2, alkalinity, and CaCO3 saturation in the global surface ocean, and temporal changes at selected locations: Marine Chemistry, v. 164, p. 95–125, doi:10.1016/j.marchem.2014.06.004.

Tsuchiya, M., Talley, L.D., and McCartney, M.S., 1994, Water-mass distributions in the western South Atlantic; a section from South Georgia Island (54S) northward across the equator: Journal of Marine Research, v. 52, p. 55–81, doi:10.1357/0022240943076759.

Tyrrell, T., 1999, The relative influences of nitrogen and phosphorus on oceanic primary productivity: Nature, v. 400, p. 525–531, doi:10.1038/22941.

Wegorzewski, A. V., Kuhn, T., Dohrmann, R., Wirth, R., and Grangeon, S., 2015, Mineralogical characterization of individual growth structures of Mn-nodules with different Ni+Cu content from the central Pacific Ocean: American Mineralogist, v. 100, p. 2497–2508, doi:10.2138/am-2015-5122.

Zachos, J., Pagani, H., Sloan, L., Thomas, E., and Billups, K., 2001a, Trends, rhythms, and aberrations in global climate 65 Ma to present: Science, v. 292, p. 686–693, doi:10.1126/science.1059412.

Zachos, J.C., Shackleton, N.J., Revenaugh, J.S., Pälike, H., and Flower, B.P., 2001b, Climate

response to orbital forcing across the oligocene-miocene boundary: Science, v. 292, p. 274–278, doi:10.1126/science.1058288.

Zhang, Y.G., Pagani, M., Liu, Z., Bohaty, S.M., and Deconto, R., 2013, A 40-million-year history of atmospheric CO(2).: Philosophical transactions. Series A, Mathematical, physical, and engineering sciences, v. 371, p. 20130096, doi:10.1098/rsta.2013.0096.

3.6 Supplementary Material

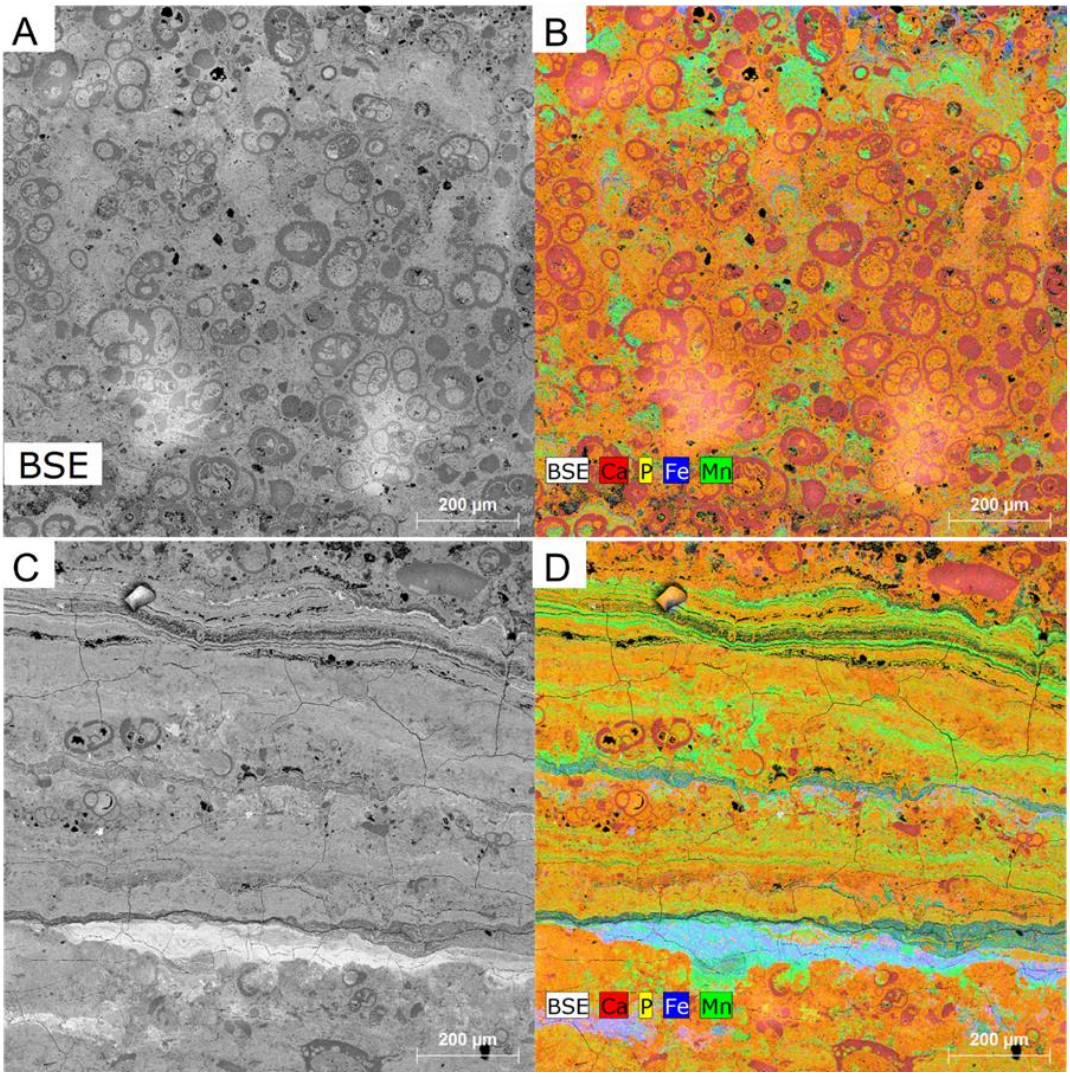

Figure S1. (A) BSE image and (B) EDS map of Ca, P, Fe, and Mn of foraminifera-rich layer of sample D11_003. Fe and Mn dendrites are seen; (C) BSE image and (D) EDS map of Ca, P, Fe, and Mn of foraminifera-poor parallel laminations of sample D11_003. Fe, Mn oxyhydroxide mineralization fronts are seen.

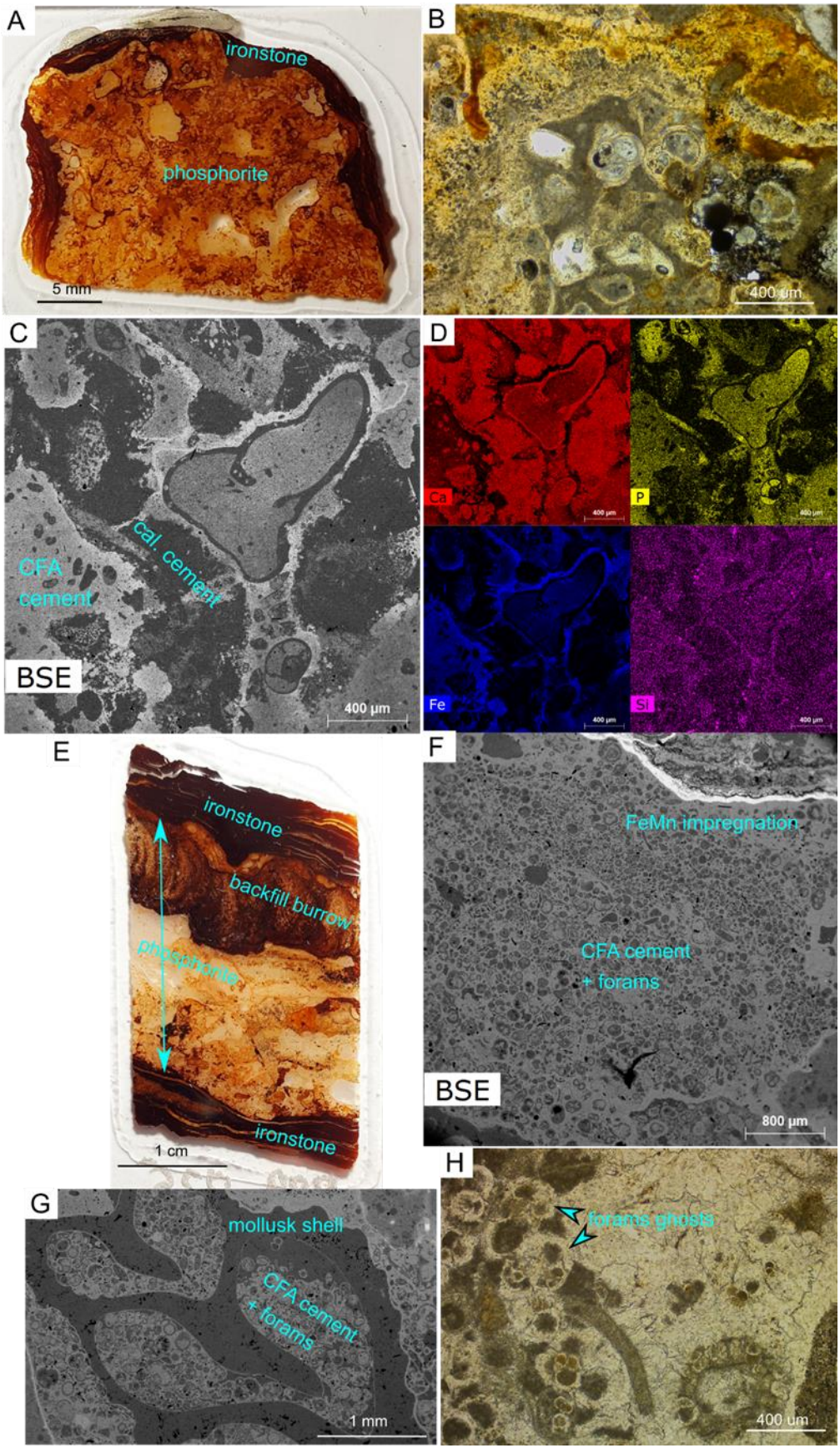

Figure S2. (A) photo of a thin section of phosphorite sample RGR1_D09_011; (B) optical microscope image of phosphorite sample RGR1_D09_011 showing foraminifera tests in a grey cement surrounded by an orange cement; (C) SEM image and (D) EDS maps showing a complex phosphorite structure, in which there are areas of CFA

cement containing many clasts, and areas of calcite cement; Fe oxyhydroxide, silicates (clay minerals?) are present mainly within the CFA cement, especially at their margins; note the large phosphorite clast in the upper right quadrant was first rimed by calcite, then Fe oxyhydroxide; (E) photo of a thin section of phosphorite sample RGR1_D09_025, enveloped by ironstone; the back-fill burrow is observed; (F) SEM image of RGR1_D09_025 showing the phosphorite matrix composed of abundant foraminifera in a cryptocrystalline CFA cement; Fe and Mn impregnation is observed marking the edge of the back-fill burrow; (G) SEM image of RGR1_D09_025 showing a mollusk shell filled with foraminifera and cryptocrystalline CFA cement; (H) optical microscope image of RGR1_D09_025 showing foraminifera molds in a coarse matrix, probably secondary calcite.

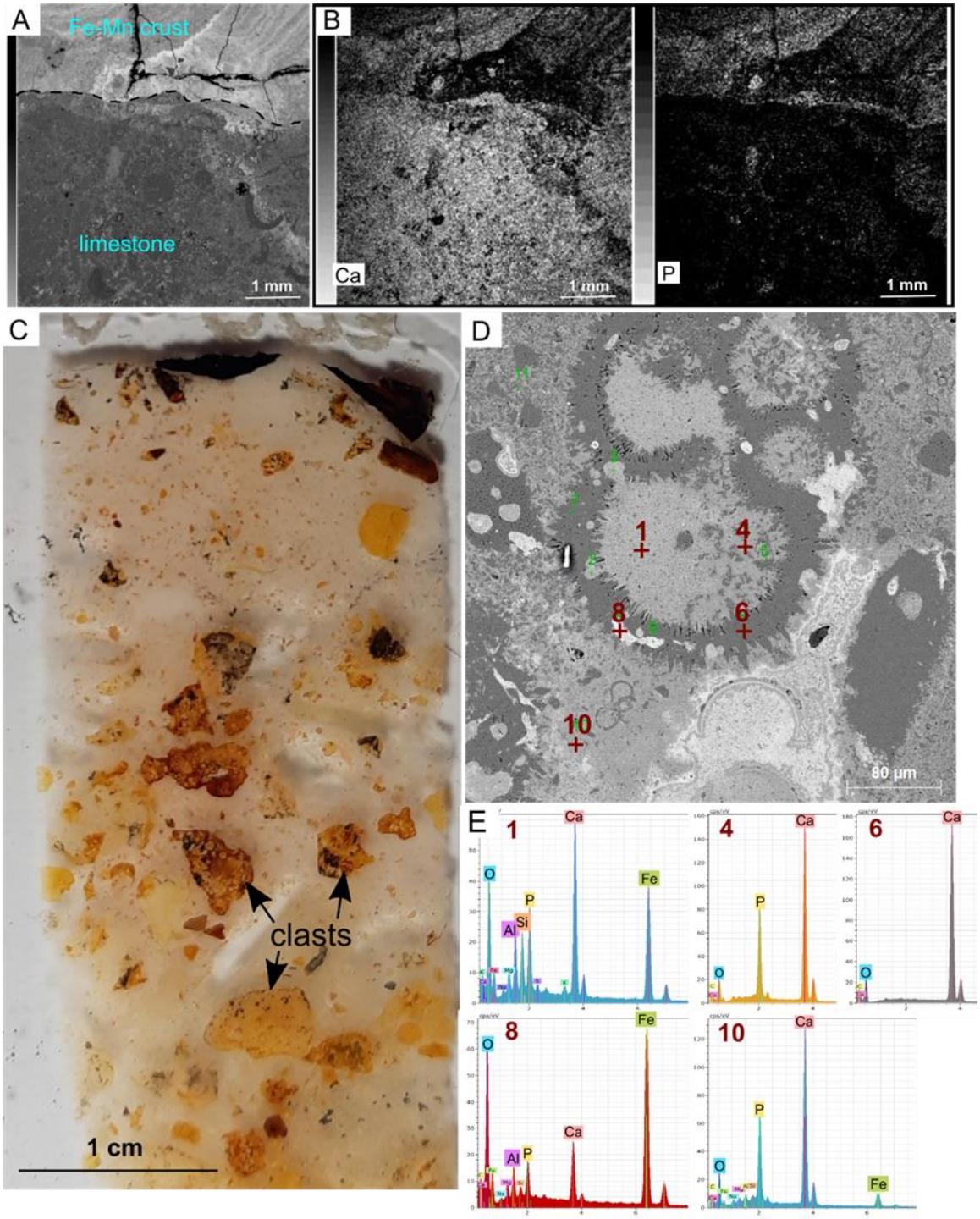

Figure S3. (A) SEM image and (B) EDS Ca and P maps of the contact between a mildly phosphatized limestone substrate, and phosphatized Fe-Mn crust (upper 1-2 mm) of sample RGR1_D02_030; (C) thin section of mildly phosphatized limestone breccia RGR1_10_003 which is the substrate of a phosphatized Fe-Mn crust; (D) SEM

image and (E) EDS point analyses of a foraminifera test in a cryptocrystalline CFA matrix (#10) of a phosphorite fragment within the limestone breccia; the calcite foraminifer wall (#6) is significantly etched both inside, outside the chambers, contain Fe oxyhydroxide impregnation at several points (#8); the chambers are filled with CFA, Fe oxyhydroxide, a Si-Al-silicate (#1, probably clay minerals), cryptocrystalline CFA replaced relict calcite grains (dark grey; #4).

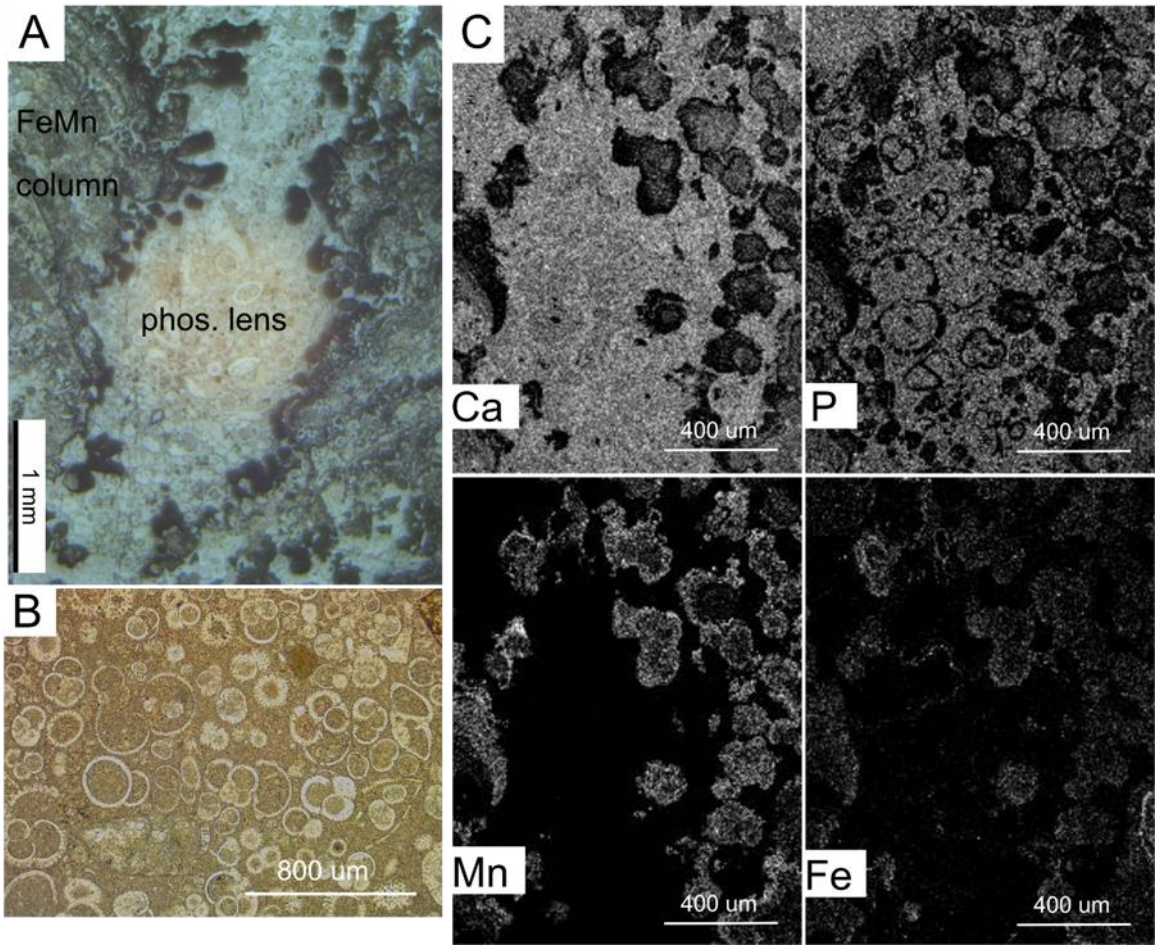

Figure S4. (A) optical microscope image of a phosphorite lens between Fe-Mn crust columns, which replaced carbonate sediment in sample RGR1_D07_002; note the small Fe-Mn columns projecting from the main Fe-Mn columns into the original carbonate sediment; (B) optical microscope, close-up of (A), showing moderately to well-preserved foraminifera tests; (C) EDS maps of the same sample showing carbonate sediment that was partly replaced by CFA, which is surrounded by the Fe-Mn oxyhydroxides that comprise the crust; note the foraminifera are not replaced by CFA, they are still calcite (Ca, not P).

4 GEOCHEMICAL INSIGHTS INTO FORMATION OF ENIGMATIC IRONSTONES FROM THE THE RIO GRANDE RISE, SOUTH ATLANTIC OCEAN (CHAPTER III)

Manuscript published on Marine Geology

Mariana Benites[1], James R. Hein[2], Kira Mizell[2], Kenneth A. Farley[3], Jonathan Treffkorn[3], Luigi Jovane[1]

[1] Institute of Oceanography, University of São Paulo, Praça do Oceanográfico 191, 05508-120 São Paulo, SP, Brazil

[2] U.S. Geological Survey Retired, PCMSC, 2885 Mission St., Santa Cruz, CA 95060, USA

[3] Division of Geological and Planetary Sciences, California Institute of Technology, Pasadena, CA 91125, USA

Abstract

Rio Grande Rise (RGR) is an intraplate oceanic elevation in the South Atlantic Ocean that formed at a hotspot on the Mid-Atlantic Ridge during the Cretaceous. In spreading center and hotspot environments, ironstones form mainly by biomineralization of reduced Fe from hydrothermal fluids or oxidation of sulfide deposits. However, RGR has been considered aseismic and volcanically inactive for the past 46 Ma. Here, we investigate the origin of ironstones collected from the summit of RGR using multiple techniques: petrographic observations, X-ray diffraction, U-Th/He geochronology, and chemical composition. The ironstones from RGR consist of finely laminated goethite containing igneous rock fragments, carbonate fluorapatite, and calcite. Our results suggest that Fe oxyhydroxides were precipitated by Fe-oxidizing bacteria forming bacterial mats. The bacterial Fe mats underwent compaction, dewatering, goethite crystallization, and cementation that created the ironstone deposits. U-Th/He geochronology reveals protracted goethite minimum ages extending from the late Miocene to the Quaternary, probably due to multiple generations of mats, slow mineralization rates, and Fe-oxide dissolution-reprecipitation cycles. Flame-like goethite structures underneath FeMn crusts and a chimney-shaped goethite sample with a central channel indicate that the dewatering fluid flowed upward through the deposits, or a thermal fluid source may have been introduced from below the ironstone deposits. High Fe/Mn ratios, low trace metals contents (Ni+Co+Cu), and very low Fe/REY ratios suggest ironstone precipitation from a hydrothermal fluid; however, REY_{SN} plots and bivariate Ce_{SN} /Ce_{SN}* versus Y_{SN}/Ho_{SN} and Ce_{SN} /Ce_{SN}* versus Nd plots are inconclusive, and a proximal source of magma was unlikely

during the period of mat formation. Given this evidence, we hypothesize that a geothermal circulation system may have facilitated ironstone mineralization at RGR.

4.1 Introduction

Rio Grande Rise (RGR) is a large intraplate oceanic rise in the Southwest Atlantic Ocean hosting a broad variety of mineralized rocks resulting from multiple formation mechanisms, predominantly hydrogenetic ferromanganese crusts and diagenetic phosphorite mineralization (Figure 1) (Benites et al., 2018, 2020, 2021; Montserrat et al., 2019; Sousa et al., 2021). Ironstones have also been found along the summit of RGR during multiple expeditions, but their origin has not been investigated. Ironstones are reddish-brown chemical sedimentary rocks that contain a significant amount of Fe (> 15%, Kimberley, 1978) and typically form by direct precipitation of or replacement of pre-existing minerals by Fe^{3+} oxyhydroxides.

Most commonly, marine ironstones form along continental margins through the precipitation of ferruginous stromatolites, oncoids, and ooids in intertidal environments (Kimberley, 1978; Helba et al., 2001; Planavsky et al., 2009; Salama et al., 2012, 2013, 2014) or at volcanically active areas along tectonic plate boundaries through precipitation from hydrothermal fluids of original moderate temperature (Rona, 1984, 1986; Hein et al., 1997; Rona, 2003; Zeng et al., 2012). Fe-rich nodules also precipitate from fluids influenced by hydrocarbon degradation along continental margins (González et al., 2012, 2016; Zhong et al., 2017, 2021). However, the occurrence of ironstones at intraplate open-ocean rises like RGR derives dominantly from low-temperature hydrothermal fluid exhalation at hotspot islands and seamounts (Alt, 1988; Stoffers et al., 1992; Hein et al., 1994, 2005; Pichler et al., 1999; Edwards et al., 2011; Johannessen et al., 2017; González et al., 2020). Moreover, Fe oxyhydroxides can precipitate from cold seawater to form ironstones with contributions from nearby hydrothermal plumes (Kuhn et al., 1998; Usui et al., 1999; Baioumy et al., 2014; Marino et al., 2019).

In most settings listed above, petrographic observations of texture indicate that microbial mats contributed to the formation of the reddish ironstones (Dahanayake and Krumbein, 1986; Little et al., 2004; Reolid and Abad, 2019). Moreover, fossil microbial-related structures are well-preserved in ironstones (Little et al., 2004; Crosby et al., 2014; Chan et al., 2016; Reolid and Abad, 2019). In modern seafloor settings, neutrophilic (i.e., living at pH close to neutral) Fe-oxidizing bacteria (FeOB) form thick Fe-oxyhydroxide-rich mats at focused-flow hydrothermal vents and diffusive/ultra-diffusive hydrothermal discharge at the seafloor (Emerson and Moyer, 2002; Edwards et al., 2011; Zeng et al., 2012; Carey et al., 2016;

Johannessen et al., 2017; González et al., 2020). Therefore, a plausible mechanism for ironstone formation can include the buildup of FeOB mats and eventual lithification (Baele et al., 2008; Salama et al., 2013).

Due to unique formation mechanisms, ironstones contain important information about the thermal, organic carbon, and microbial history of the regions where they occur. For RGR, the volcanic ridge has been considered aseismic and inactive since 46 Ma (million years ago) (Thiede, 1977; Camboa and Rabinowitz, 1984; Ussami et al., 2012; Rohde et al., 2013). By investigating the mechanism and timing of ironstone formation at RGR and the role of microbial activity in this process, we can elucidate information about the oceanographic and geologic history of this open ocean edifice and contribute to the plausible genetic models for marine ironstones formed in this type of setting.

4.2 Geological setting of the Rio Grande Rise

RGR is located between Brazil and the Mid-Atlantic Ridge and is an intraplate aseismic ridge rising from the surrounding abyssal plains at 4000 to 600 m water depth at the summit platform. RGR is divided into the West RGR (WRGR), an elliptical body with a central plateau, and the East RGR (ERGR), an elongated N-S hook-shaped feature at greater water depths (Figure 1). A 10-20 km wide and 1-2 km deep NW-SE rift cuts both the WRGR and ERGR, which is called the Cruzeiro do Sul Rift (CSR) (Mohriak et al., 2010; Constantino et al., 2017; Montserrat et al., 2019).

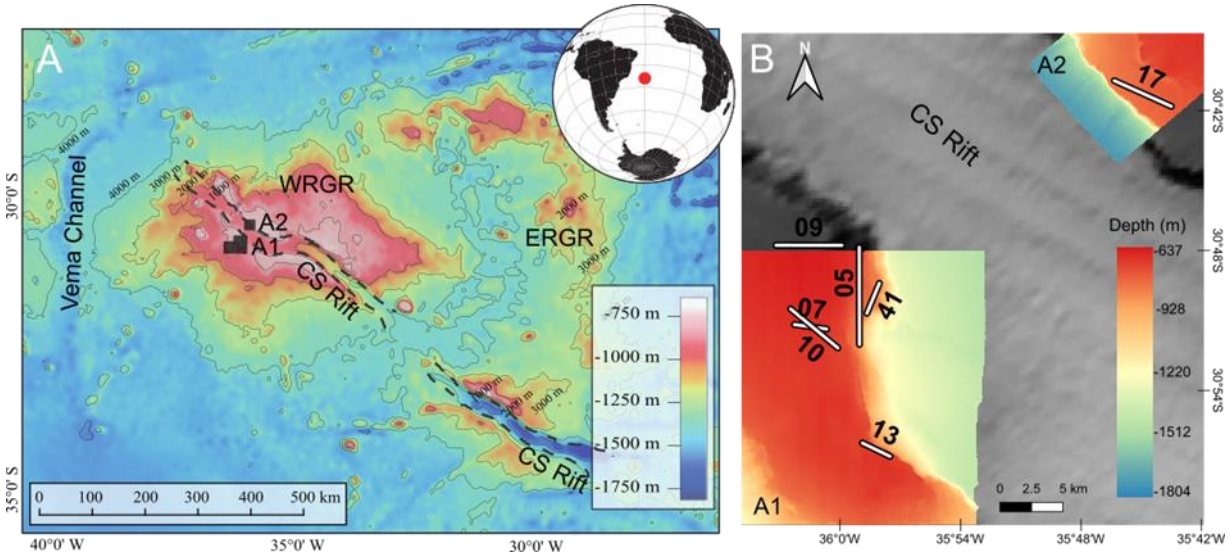

Figure 1: (A) Bathymetric map and geomorphology of Rio Grande Rise (RGR) in the Southwest Atlantic Ocean; (B) location of dredges in areas A1 and A2, both along the margins of the Cruzeiro do Sul Rift (CSR) that cuts the West Rio Grande Rise (WRGR); ERGR = East Rio Grande Rise.

RGR was the western part of a single large volcanic edifice, the Walvis Ridge-RGR volcanic system, that formed along the South Atlantic Ocean spreading axis at about 80 Ma (Thiede, 1977; Barker, 1983; Camboa and Rabinowitz, 1984; O'Connor and Duncan, 1990; Ussami et al., 2012; Galvão and de Castro, 2017; Graça et al., 2019; Santos et al., 2019). As seafloor spreading between the African and South American plates continued, the Walvis Ridge-RGR system drifted apart and underwent subsidence due to cooling (Thiede, 1977; Ussami et al., 2012). At about 70 Ma, the spreading-axis migrated westward, and some research suggests that it jumped position several times between 90 and 50 Ma, resulting in the fragmented RGR that we see today (Graça et al., 2019); the N-S structures correspond to the extinct spreading center (Constantino et al., 2017). Eocene magmatic rejuvenation occurred around 46 Ma at RGR, which caused uplift and subaerial exposure of portions of the ridge (Barker, 1983; Camboa and Rabinowitz, 1984; Ussami et al., 2012; Rohde et al., 2013).

The last tectonic activity to have occurred along RGR was Neogene plate reorganization involving extensional rift structures over a large area around the ridge (Mohriak et al., 2010; Galvão and de Castro, 2017; Praxedes et al., 2019). The CSR probably formed as an accommodation zone due to transtensional movements along a shear zone during plate reorganization (Mohriak et al., 2010; Galvão and de Castro, 2017). Deep normal faults exist along the CSR and offset the uppermost sediment layer, indicating extensional tectonic activity since the Late Cretaceous to at least the Miocene and probably until the present (Praxedes et al., 2019). Igneous intrusions were facilitated by the intense fracturing of the crust (Mohriak et al., 2010; Praxedes et al., 2019).

4.3 Material and methods

4.3.1 Samples

Fourteen ironstone hand samples were used in this study, from which 13 samples were dredged on cruise RGR1 onboard the RV Alpha Crucis in 2018 (Universidade de São Paulo, Brazil) (Jovane et al., 2019); and one sample was dredged on cruise DY094 on board the RRS Discovery (National Oceanographic Centre Southampton, UK) in 2018. Both cruises used dredges to target collection of FeMn crusts from rock outcrops at the CSR borders and RGR main plateau at water depths between 600 and 800 m; however, ironstones were also unexpectedly retrieved. Most of the ironstones collected showed wavy laminations (Figure 2A), parallel laminations (Figure 2B), and some showed flame-like structures (Figure 2C) associated with other rock types (FeMn crusts, phosphorites). One breccia sample (Figure 2D) and one

small chimney-shaped sample with concentric laminations around a central conduit (Figure 2E, F) were also selected for this study.

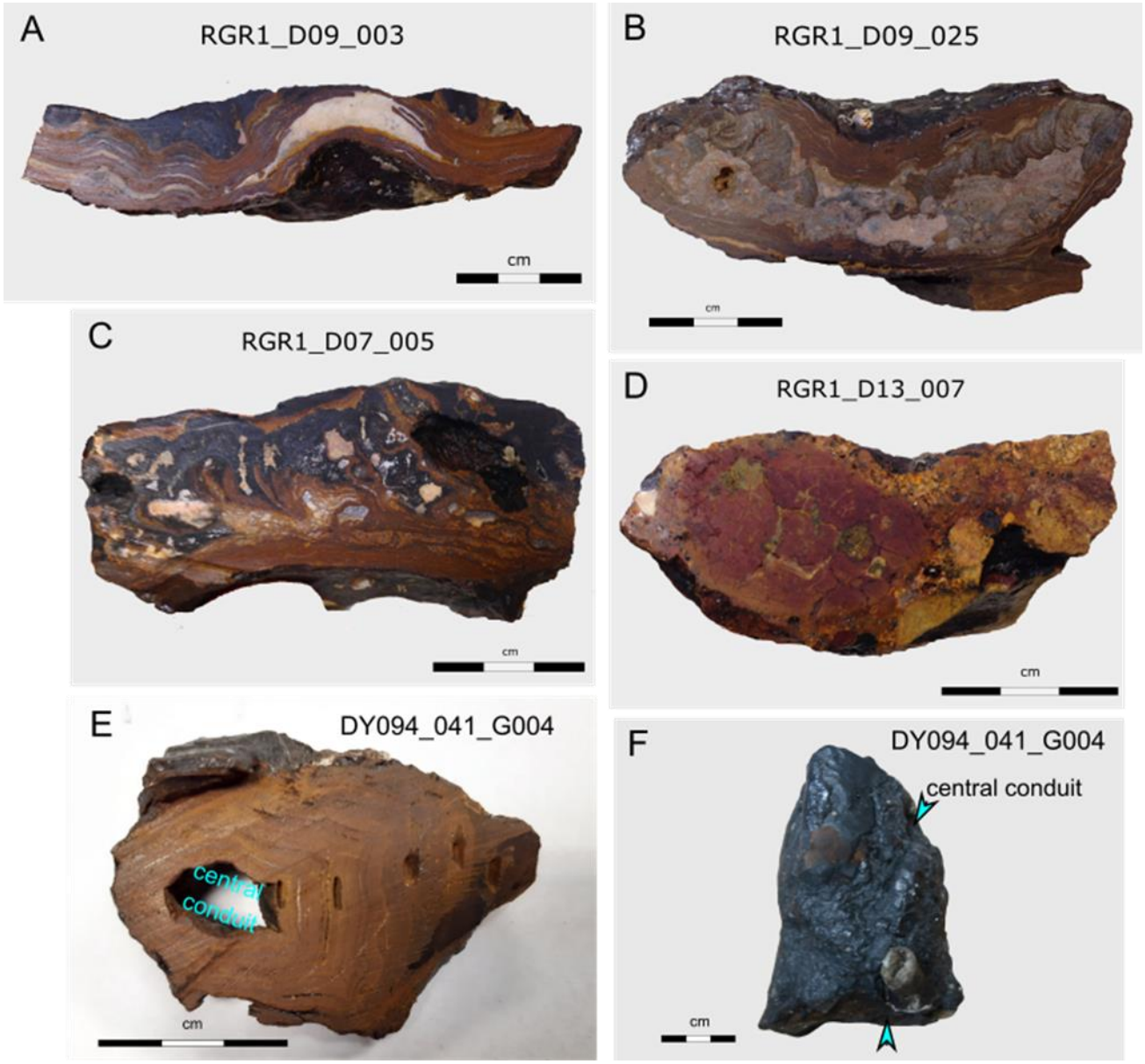

Figure 2: Ironstones from RGR occur as (A) wavy laminations enveloping a carbonate lens; (B) parallel laminations enveloping phosphorite; (C) flame-like laminae in association with FeMn crust; (D) breccia of igneous rock fragments; and (E) concentric laminations around a large central conduit; a slice of the chimney-like structure in "F," (F) vertical chimney-shaped structure; the original photograph has had its brightness level increased so that the surface texture can be better distinguished.

4.3.2 Methods

4.3.2.1 X-ray Diffraction

X-ray diffraction analyses were performed using a Panalytical X'Pert3 Powder diffractometer with Cu-kα radiation and carbon monochromator at the U.S. Geological Survey, Pacific Coastal and Marine Science Center, Santa Cruz, California. Powder aliquots were drilled from the samples using a diamond-coated drill bit and ground to approximately 75 µm

using an agate mortar and pestle. Each powder sample was mounted wet on zero-diffraction sample holders using alcohol and scanned from 4° to 70° 2θ at 40 kV and 45 mA. Semi-quantitative percentages of each mineral phase identified were determined based on the intensity of the peaks and weight factors relative to quartz, following Cook et al. (1975) and Hein et al. (1988).

4.3.2.2 Petrography

Polished thin sections were observed under a petrographic microscope using transmitted and reflected light. The thin sections were then Pt-coated and analyzed in a Quanta650 FEG electron microscope from FEI, equipped with an Energy Dispersion X-ray Spectrometer (EDS) Quantax 400 (technology SDD – Silicon Drift Detector) and software Esprit from Bruker at the Laboratório de Caracterização Tecnológica from the Escola Politécnica, Universidade de São Paulo. A high vacuum was used with an Electron High Tension (EHT) of 20 keV, Work Distance of 14 mm, a spot size of 4.0 µm, magnifications from 100x to 400x, and Ion probe current of 1 – 2 nA.

Additional SEM observations, using the secondary electron (SE) mode, were performed on approximately 1x1x1 mm ironstone fragments broken from four different hand samples (RGR1_D09_018, RGR1 _D09_025, RGR1_D10_003, and DY094_D41_004G) in order to verify the presence of microbial-related structures in the ironstones. The observations were made at high vacuum at 5.0 kV, spot size of 2.0-4.0 µm, working distance between 8 and 12 mm, and magnifications from 5000x to 100,000x.

4.3.2.3 Chemical composition

Thirteen ironstone samples were analyzed by a range of analytical techniques. The major elements Al, Ca, Fe, K, Mg, Mn, Na, P, Si, and Ti were determined using a borate fused disc and X-ray Fluorescence (XRF); Loss on Ignition was determined at 1000°C; Ag, As, Ba, Be, Bi, Cd, Ce, Cr, Cu, Hf, Li, Mo, Ni, Pb, S, Sb, Sc, Sr, V, and Zn were determined by multi-acid digestion and Inductively Coupled Plasma-Mass Spectrometry (ICP-MS); Co, Cs, Dy, Er, Eu, Ho, La, Lu, Nb, Nd, Pr, Rb, Sm, Tb, Th, Tm, U, Y, Yb, and Zr were determined using a Lithium metaborate fused disc and ICP-MS; Cl and F were determined by Ion Specific Probe; H2O- was determined by gravimetry and H_2O^+ by Penfield-infrared method. Precision was better than 20% for all elements except K (40%) and Ag (57%). Accuracy was better than 20% for all compounds excepting H_2O^+ (26%) and P (28%) and was not determined for H2O-, Co, Cs, Nb, Rb, and Zr because no certified values were available.

Rare earth elements plus Yttrium (REY) were plotted with contents normalized to Post-Archean Australian Shale (PAAS; Bau and Dulski, 1996; McLennan, 2018). The Ce anomaly (Ce*) and Eu anomaly (Eu*) were calculated from PAAS-normalized (SN) data using the equations $Ce_{SN}^* = Log (Ce_{SN}/ (2/3La_{SN} + 1/3Nd_{SN})$ and $Eu_{SN}^* = 2Eu_{SN}/(Sm_{SN} + Gd_{SN})$.

Two ironstone samples (RGR1_D09_005 and RGR1_D10_003) were analyzed for total organic carbon (TOC). The total carbon (TC) content was measured using a furnace, while the total inorganic carbon (TIC) was measured by acid digestion, at the U.S. Geological Survey, Pacific Coastal and Marine Science Center, Santa Cruz, California. The TOC was obtained by subtracting the TIC from the TC content.

4.3.2.4 U-Th/He

U-Th/He geochronology has been applied successfully to date supergene goethite from weathering profiles on land (Shuster et al., 2005; Heim et al., 2006; Vasconcelos et al., 2013; Monteiro et al., 2014). A major source of uncertainty is the possibility of diffusive ^{4}He loss over the sample history. However, ^{4}He/^{3}He diffusivity experiments with these supergene goethites showed good ^{4}He retentivity (with less than 10% ^{4}He loss) and that (U–Th)/He ages are probably accurate to within ±10%. (Shuster et al., 2005; Heim et al., 2006; Vasconcelos et al., 2013). We tentatively adopt the same uncertainty figure for the goethites analyzed here and do not correct for possible diffusive loss. Should diffusive loss be greater in our samples than in supergene goethites, the resulting ages would be lower limits.

The U-Th/He analysis focused on six laminated ironstone hand samples from which the chimney-shaped sample DY094_041 had two different stratigraphic layers selected for analysis - an inner layer closer to the central hollow and an outer layer. Three to four aliquots of goethite grains were taken from each selected sample, totaling 22 aliquots. Reddish grains were taken from the hand sample by scraping it with a pen knife over weighing paper, with special care to guarantee that the scraped area was constrained to the same stratigraphic lamina of the sample. The grains were transferred to an agate mortar and were softly crushed to approximately 1x1 mm size. XRD confirmed the mineralogy of the aliquots. The U-Th/He analyses and determination of ^{4}He and ^{3}He in two aliquots were performed at Caltech using the methods described by Monteiro et al. (2014).

4.4 Results

4.4.1 Structure, mineralogy, and textural features

The ironstones from RGR are compact, dense, and medium to dark orange-brown with little porosity. Most samples are laminated and composed dominantly of goethite (FeOOH) with variable amounts of calcite (Table 1). A few samples have minor to moderate amounts of carbonate fluorapatite (CFA). Samples RGR1_D07_017 and RGR1_D05_014 contain minor amounts of Mn oxides (vernadite and 10Å manganate). Minor amounts of quartz present in a few samples indicate overall weak terrigenous detritus input to the ironstones.

The laminated ironstones consist of fine, parallel goethite laminae with fractures perpendicular to the direction of accretion, probably the result of compression and dewatering (Figure 3A, B). Macroscopic (Figure 2A) and microscopic (Figure 3A) calcite laminae are often observed alternating with goethite laminae. Moreover, a rhythmic alternation between foraminifera-rich and foraminifera-poor goethite laminae is observed in the troughs of wavy layers in ironstone sample RGR1_D09_002 (Figure 3C), pointing to episodic deposition of more and less pelagic sediment. Goethite laminae also alternate with CFA laminae in sample D09_025 (Figure 3B), where CFA comprises veins and fills fractures between the goethite laminae, suggesting diagenetic replacement of the original calcite by CFA. Complex flame-like goethite structures often occur at the base of FeMn crusts (Figure 3D). These structures are generally accompanied by rounded clastic particles at their base, and they swirl and disappear within the FeMn crusts matrix (Figure 3D, E).

The breccia sample RGR1_D13_007 differs from the description above and consists of igneous rock fragments cemented by goethite (Figure 4A). The igneous fragments are medium-grained in texture with abundant elongated Si-Al-K minerals (Figure 4D,F), most likely K-feldspar, suggesting a felsic host. The rim cement comprises fine goethite needles attached to aluminosilicate minerals (Figure 4B, C), which are basaltic host rock fragments and products of their alteration. Alteration of the igneous rock is clear from Fe mineralization fronts around fragments (Figure 4D). EDS analysis shows mild Fe mineralization at the core of an igneous rock fragment but intense Fe mineralization at its margins (Figure 4E). Fe mineralization of the igneous rock seems to have occurred by replacement of minerals with Fe oxyhydroxide and precipitation along fractures (Figure 4F).

Table 1: Location, mineralogy, and texture of ironstones collected during the RGR1 and DY094 cruises. The sample from DY094 (sample DY094_041_G004) was processed into five subsamples, #1 to #5.

Sample ID	Latitude	Longitude	Depth (m)	Area	Major	Moderate	Minor	Texture
RGR1_D05_011	30°53,367'S	35°58,853'W	739.0	A1	Goethite	CFA	Quartz	Laminated
RGR1_D05_014	30°53,367'S	35°58,853'W	739.0	A1	Goethite	-	Calcite, 10Å manganate	Laminated
RGR1_D05_016	30°53,367'S	35°58,853'W	739.0	A1	Goethite	CFA	Calcite	Laminated, flames
RGR1_D07_005	30°51,1355'S	36°1,319'W	684.0	A1	Goethite	-	Calcite	Laminated, flames
RGR1_D07_017	30°51,1355'S	36°1,319'W	684.0	A1	Goethite, calcite	Vernadite, 10Å manganate	Quartz	Finely laminated
RGR1_D09_002	30°47,638'S	36°1,398'W	650.5	A1	Goethite	-	CFA, calcite	Laminated, wavy
RGR1_D09_003	30°47,638'S	36°1,398'W	650.5	A1	Goethite	-	Calcite	Laminated, wavy
RGR1_D09_005	30°47,638'S	36°1,398'W	650.5	A1	Goethite	-	Calcite	Laminated, folded
RGR1_D09_023	30°47,638'S	36°1,398'W	650.5	A1	Goethite	CFA, calcite	-	Laminated
RGR1_D09_025	30°47,638'S	36°1,398'W	650.5	A1	Goethite	-	Calcite	Laminated
RGR1_D10_003	30°51,205'S	36°1,146'W	686.5	A1	Goethite	Calcite	-	Finely laminated
RGR1_D13_007	30°56,327'S	57,846'W	707.5	A1	Goethite, calcite	-	-	Breccia
RGR1_D17_016	30°41,498'S	35°44,508'W	697.0	A2	Goethite	-	Calcite	Laminated
DY094_041_G004	30°49,782'S	35°58,260'W	927	A1				
#1					Goethite	-	Calcite	Laminated, concentric
#2					Goethite	-	Calcite	Laminated, concentric
#3					Goethite	-	Calcite	Laminated, concentric
#4					Goethite	-	Calcite	Laminated, concentric
#5					Goethite	-	Calcite	Laminated, concentric

Mineralogy: major denotes >25%, moderate 5 to 25%, minor <5%.

CFA = carbonate fluorapatite.

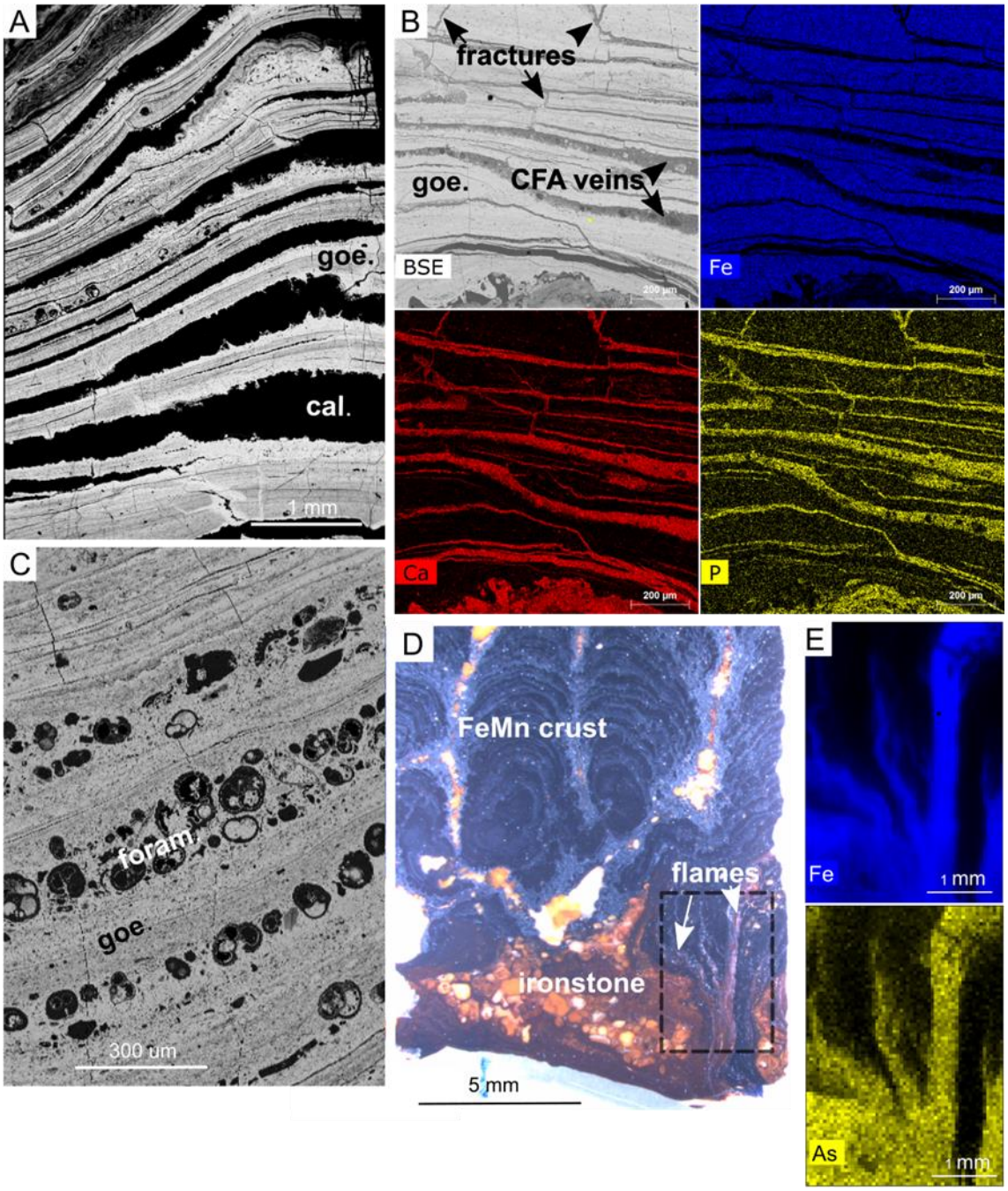

Figure 3: (A) SEM image of alternating goethite and calcite laminae in sample RGR1_D09_002; (B) SEM image and EDS maps of Fe, Ca, and P of goethite laminae showing veins and fractures filled with CFA in sample RGR1_D09_025; (C) SEM image of alternating foraminifera-rich and foraminifera-poor goethite laminae in sample RGR1_D09_002; note that goethite fills or partially fills some foraminifera tests; (D) Ironstone lamina forming flame-like structures at the base of FeMn crust in sample RGR1_D07_002. Rock clasts are present within the ironstone; (E) SEM-EDS maps of Fe and As in the area constrained by the rectangle in (D).

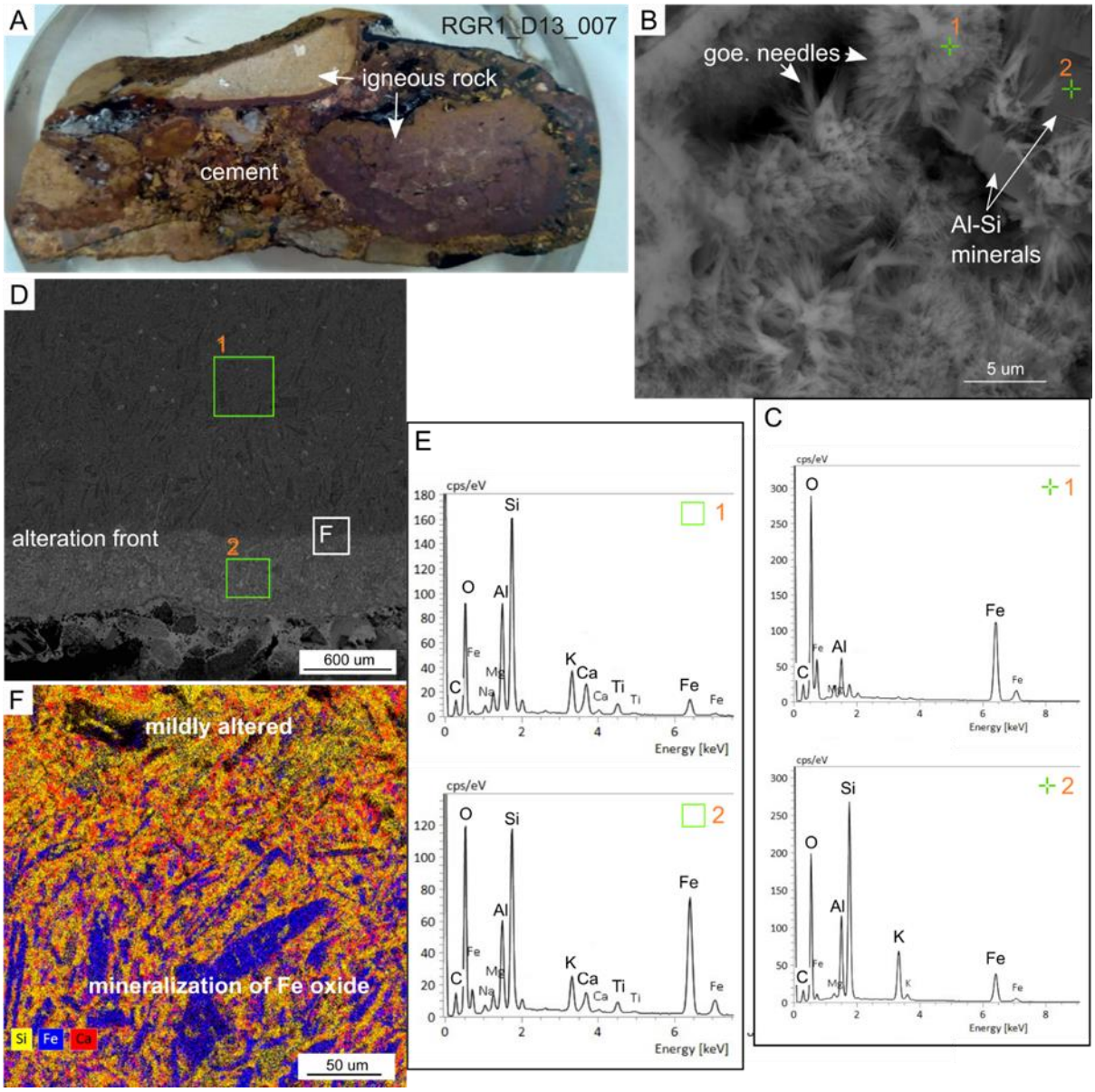

Figure 4: (A) Ironstone breccia RGR1_D13_007 composed of volcanic rock fragments cemented by goethite; (B) SEM image and (C) EDS point analyses showing the cements consist of fine goethite needles (#1) with aluminosilicates minerals (#2); (D) SEM image of one volcanic rock fragment displaying an alteration rind; (E) EDS analyses of areas 1 and 2 displayed in D, revealing that the rind around the volcanic rock fragment (#2) is enriched in Fe oxide in comparison to its core (#1); (F) EDS chemical map of Si, Fe, and Ca corresponding to the white square in D, showing the transition across the alteration front.

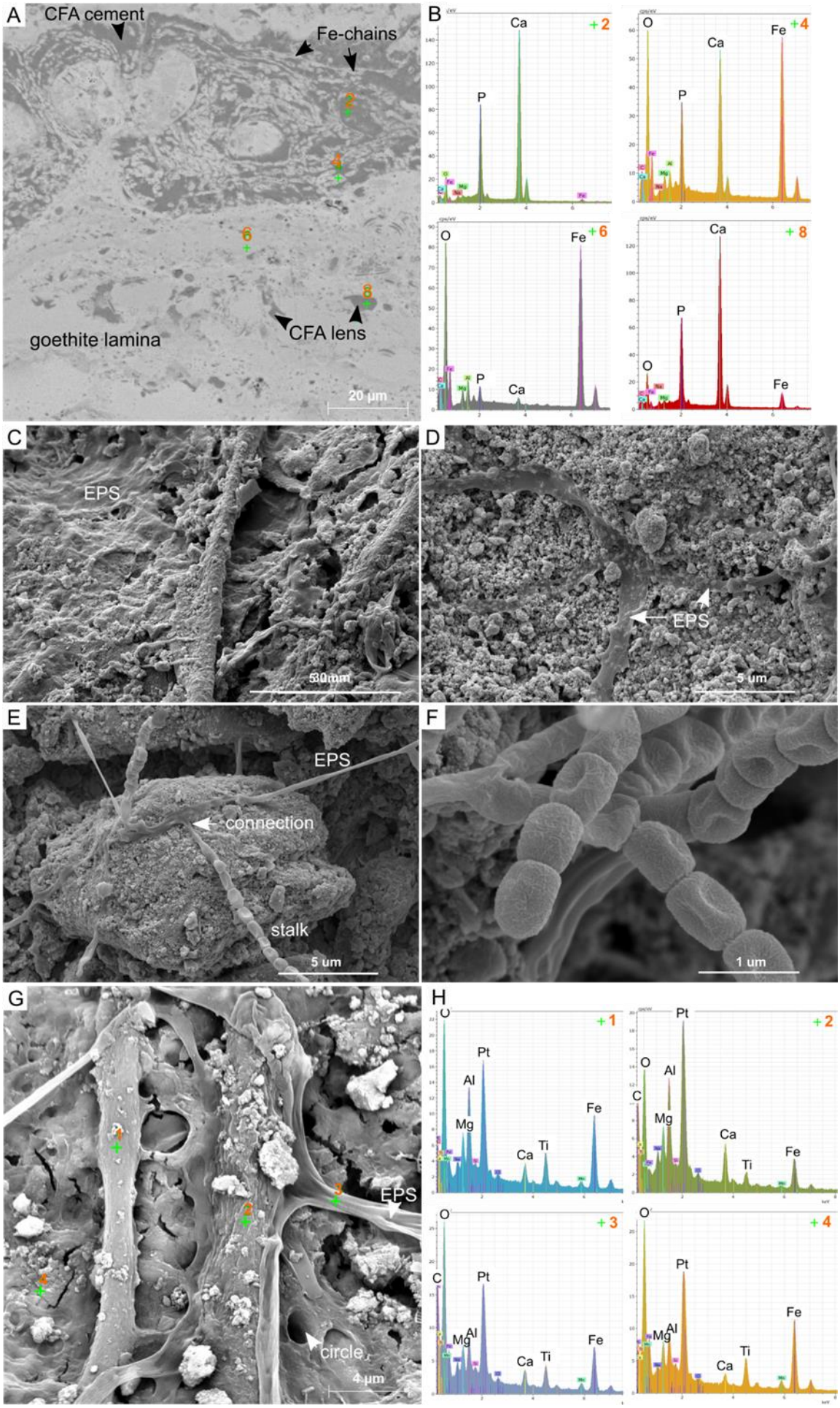
A
CFA cement
Fe-chains
goethite lamina
CFA lens
20 µm
B
Ca
P
O
Fe
C
EPS
D
EPS
5 µm
E
EPS
connection
stalk
5 um
F
1 um
G
EPS
circle
4 µm
H
Pt
Al
Mg
Ca
Ti
Fe
C

Figure 5: (A) Backscatter electron SEM image of Fe-oxide chains with the appearance of bacillus; the chains are within a CFA cement between goethite laminae; (B) EDS chemical spectra of points in A showing the composition of Fe-oxide (#4,#6) and CFA (#2,#4,#8); (C) secondary electron SEM image of veil-like feature resembling mineralized extracellular polymeric substance (EPS) in sample RGR1_D09_025; (D) mineralized EPS in sample DY094_041_004; (E) mineralized EPS connected to a bacteria stalk in sample RGR1_D10_003; (F) detail of mineralized bacteria stalk in E showing individual cells; (G) backscatter electron SEM image of mineralized EPS with circular holes that may be imprints left by nannofossils in sample RGR1_D09_025; (H) EDS point analyses of (G); goethite matrix (Fe, O) with sorbed elements or mixture of accessory minerals containing Ca, Mg, Ti, and Al. C is possibly from fossilized organic compounds of EPS; note that the Pt is from the coating preparation on the sample.

Microbial-related features include bacillus-shaped Fe-oxyhydroxide chains within the interior of sample RGR1_D09_011 (Figure 5A, B), which may be imprints of fossil bacteria coated by the Fe oxyhydroxides. Moreover, SEM observations reveal a veil feature and web of long filaments that branch and intercept each other on the surface and interior of four laminated ironstone samples analyzed (Figure 5C, D), which resemble extracellular polymeric substance (EPS). One filament is directly connected to a bacteria stalk in sample RGR1_D10_003 (Figure 5E, F). The filaments are covered by the goethite matrix (Figure 5B), indicating a genetic linkage between them rather than surficial bacterial colonization after sample formation or sample collection. EDS point analyses reveal that the filaments contain C as one of the main constituents (Figure 5G, H), pointing to an organic composition. No EPS and microbial structures were observed in the breccia sample.

4.4.2 Chemical composition

4.4.2.1 Major and trace elements

The laminated ironstones contain 71.4 to 52.5% Fe, while the ironstone breccia contains 35.3% Fe (Table 2). Apart from Fe, the ironstone breccia D13_007 shows a distinct chemical composition compared to the laminated ironstones; thus, it was not included in the summary statistics (Table 2) and is described separately later in this section. The Fe/Mn ratios of the ironstones, including the breccia, range from 23.9 to 302, indicating a strong fractionation between Fe and Mn. The laminated ironstones show variable amounts of calcite as indicated by Ca and CO3 contents of 3.42 – 14.9% and 2.59 – 12.6%, respectively, and variable contributions from CFA (P contents of 3.29 – 9.26%) as well as some Ca and CO3 also occur in the CFA. The content of Mn oxides is low (average Mn content of 0.90%). The highest trace element contents in the laminated ironstones are (followed by the mean content) Cl (3619 ppm), F (3347 ppm), V (1704 ppm), As (1684 ppm), Ni (569 ppm), Co (408 ppm), Zn (396 ppm), Sr (374 ppm), and Cr (230 ppm). The ironstone breccia shows a much higher content of the aluminosilicate-related elements Si (20.3%), Al (5.55%), Ti (2.26%), and K (2.55%), reflecting the presence of igneous rock fragments that are absent in the laminated ironstones. In addition,

the breccia sample has lower V, As, Cl, W, Te, and Pb, and higher contents of Ba, Hf, Li, Nb, Nd, Rb, Sc, U, LREE (La-Eu) than the laminated ironstones.

A micro-XRF chemical map of a flame-like ironstone structure in sample RGR1_D07_002 reveals a close association between the As and Fe distribution (Figure 3).

4.4.2.2 Rare earth elements plus yttrium

The sum of rare earth elements plus Y (∑REY) ranges from 82 to 184 ppm in the laminated ironstones, with one sample (RGR1_D10_003) showing a higher ∑REY content of 409 ppm (Table 2)—this sample also has the highest Mn content, which then may reflect minor contamination of Mn oxides. From total REY, 44.1% correspond to the heavy rare earth elements plus Y (%HREY) complement in the laminated ironstones. The breccia sample show ∑REY of 258 ppm and is depleted in the HREY complement compared to the laminated ironstones (%HREY of 24.3%).

The PAAS shale normalized REY (REYsn) plots of laminated ironstones show an increasing trend from light REYsn to medium REYsn, especially from Prsn to Gdsn, and a relatively flat trend from Gdsn to Ybsn with a positive Ysn anomaly (Figure 6, gray lines). The Cesn anomalies are mostly slightly negative (7 samples), slightly positive in two samples, and absent in four samples, ranging from -0.45 to 0.19 (Table 2). The ironstone breccia presents an overall flat REYsn pattern, with no Cesn anomaly, a pronounced positive Eusn anomaly (Eusn anomaly of 1.35, Table 2), and a weak positive Ysn anomaly.

4.4.2.3 Total organic carbon (TOC)

The TOC content of the laminated ironstones samples D09_005 and D10_003 L2-5 is 0.31 and 0.23%, respectively.

Table 2: Chemical composition of ironstones from RGR. The summary statistics do not include the ironstone breccia due to its distinct composition.

	Laminated ironstones												Breccia	Summary statistics (laminated ironstones)			
Sample	RGR1_D05_011 L10-19	RGR1_D05_014 Bulk	RGR1_D05_016 L23-34	RGR1_D07_005 Bulk	RGR1_D07_017 Bulk	RGR1_D09_002 L8-14	RGR1_D09_003 L1-3	RGR1_D09_005 Bulk	RGR1_D09_023 Bulk	RGR1_D09_025	RGR1_D10_003 L2-5	RGR1_D17_016 Bulk	RGR1_D13_007 L0-20	N	Max	Min	Mean
Fe (wt%)	59.6	62.2	55.1	55.0	63.2	52.5	55.9	65.0	54.9	71.4	55.6	65.2	35.3	12	71.4	52.5	59.6
Mn	1.62	0.52	0.84	0.50	0.21	0.67	1.04	1.03	0.40	0.53	2.33	1.10	0.73	12	2.33	0.21	0.90
Al	0.82	0.71	0.93	0.95	1.82	0.91	1.08	0.71	0.94	0.67	1.21	1.32	5.55	12	1.82	0.67	1.01
Si	1.51	1.66	1.24	1.30	1.57	1.05	1.21	1.12	1.17	1.34	1.99	1.07	20.3	12	1.99	1.05	1.35
Si/Al	1.85	2.35	1.34	1.37	0.86	1.15	1.12	1.58	1.23	2.00	1.65	0.81	3.65	12	2.35	0.81	1.44
Mg	1.96	2.55	2.56	2.80	2.80	2.46	2.68	2.39	2.48	2.43	2.65	3.02	3.42	12	3.02	1.96	2.56
Ca	10.5	9.00	12.8	13.8	6.84	14.9	12.0	7.28	13.6	3.42	11.0	5.01	7.38	12	14.9	3.42	10.0
Na	0.33	0.24	0.22	0.21	0.22	0.21	0.25	0.18	0.22	0.19	0.24	0.22	0.61	12	0.33	0.18	0.23
K	0.03	0.03	0.03	0.01	0.02	0.04	0.06	0.03	0.03	0.03	0.08	0.03	2.55	12	0.08	0.01	0.03
Ti	0.08	0.14	0.12	0.06	0.18	0.14	0.16	0.10	0.09	0.10	0.39	0.16	2.26	12	0.39	0.06	0.15
P	6.79	4.64	4.12	3.94	4.98	4.60	5.00	3.47	5.07	3.29	3.48	4.00	2.58	12	6.79	3.29	4.45
Ca/P	1.55	1.94	3.12	3.50	1.37	3.23	2.40	2.10	2.69	1.04	3.15	1.25	2.86	12	3.50	1.00	2.30
S	0.16	0.10	0.10	0.10	0.10	0.10	0.10	0.06	0.10	0.05	0.10	0.08	0.10	12	0.16	0.05	0.10
CO_2	2.50	4.37	8.16	9.00	2.42	9.26	6.82	4.51	7.65	1.90	7.59	2.77	3.51	12	9.26	1.90	5.58
CO_3[1]	3.41	5.96	11.1	12.3	3.31	12.6	9.30	6.15	10.4	2.59	10.3	3.77	4.78	12	12.6	2.59	7.61
LOI[2]	16.4	18.4	22.0	22.6	19.0	22.2	20.5	18.7	20.9	17.4	20.6	20.3	14.7	12	22.6	16.4	19.9
$H2O^-$	2.90	2.60	3.40	4.30	4.30	3.10	3.40	2.90	3.10	3.00	3.50	4.90	2.80	12	4.90	2.60	3.45
$H2O^+$	11.2	12.0	12.0	11.5	13.8	11.4	12.3	12.3	12.3	13.6	11.0	14.9	9.60	12	14.9	11.0	12.4
Ag (ppm)	0.05	0.04	0.04	0.04	0.06	0.09	0.11	0.08	0.05	0.04	0.06	0.07	0.06	12	0.11	0.04	0.06
As	1025	993	1625	1517	915	1637	1847	2325	1028	2388	2847	2064	265	12	2847	915	1684
Ba	242	25.7	69.4	18.8	7.31	42.3	44.5	63.9	15.5	14.4	89.1	112	391	12	242	7.31	62.1
Be	1.54	2.16	2.80	2.51	3.13	2.79	4.24	3.30	2.27	2.27	3.01	5.36	3.19	12	5.36	1.54	2.95
Bi	1.53	1.21	1.60	0.93	2.22	3.83	3.98	1.52	1.80	2.03	8.77	2.52	1.22	12	8.77	0.93	2.66
Cd	0.81	0.83	1.15	0.89	0.65	1.35	1.31	1.24	1.00	1.03	1.82	1.00	0.53	12	1.82	0.65	1.09
Cl	3182	3005	3022	3742	2869	2697	3261	3476	3699	5996	2255	6223	1550	12	6223	2255	3619
Co	559	242	411	163	159	485	519	542	299	534	470	512	202	12	559	159	408
Cr	89.6	375	271	194	341	214	199	162	183	131	244	358	101	12	375	89.6	230
Cu	77.4	56.9	16.8	27.5	24.8	33.5	96.3	42.5	20.6	71.9	89.5	27.7	72.1	12	96.3	16.8	48.8
F	7025	4094	3043	3090	4148	3332	3559	2064	4102	1425	2307	1976	3207	12	7025	1425	3347
Hf	0.41	0.31	1.82	1.38	0.59	1.32	1.22	1.13	0.42	1.23	2.28	2.30	4.33	12	2.30	0.31	1.20
Li	8.24	10.3	10.4	8.4	5.2	11.4	17.6	12.4	8.3	13.4	15.5	11.6	32.9	12	17.6	5.22	11.0

Mo	31.3	19.0	15.9	19.3	11.4	14.1	31.1	25.4	14.6	24.2	36.1	28.9	18.7	12	36.1	11.4	22.6
Nb	8.24	14.4	17.6	9.40	20.9	15.5	15.5	15.4	10.3	12.4	29.0	23.1	39.1	12	29.0	8.24	16.0
Ni	1041	411	464	278	268	530	640	693	393	566	980	558	214	12	1041	268	569
Pb	78.8	79.4	87.2	47.5	59.2	209	287	126	81.2	188	311	117	64.3	12	311	47.5	139
Rb	0.62	0.51	0.72	0.21	0.31	1.75	2.59	0.82	1.03	0.93	3.42	0.74	24.3	12	3.42	0.21	1.14
Sc	1.34	1.54	2.07	1.25	2.19	1.65	2.28	1.13	1.65	1.24	3.21	2.26	8.64	12	3.21	1.13	1.82
Sr	442	315	870	526	215	366	400	265	301	157	426	211	362	12	870	157	374
Te	6.92	3.36	4.03	2.10	3.50	13.0	14.6	6.62	4.62	9.51	12.91	8.09	2.40	12	14.6	2.10	7.44
Th	1.44	1.75	1.76	0.73	0.94	1.86	2.38	1.65	1.44	1.65	7.05	2.52	5.14	12	7.05	0.73	2.10
U	5.31	3.28	3.91	3.65	6.55	3.56	4.28	2.67	4.05	2.61	4.54	4.79	14.7	12	6.55	2.61	4.10
V	1420	1479	1848	1459	1255	1933	1921	2101	1593	1975	1362	2113	377	12	2113	1255	1705
W	32.9	16.7	25.9	15.0	16.0	49.0	47.8	52.3	28.8	49.3	35.6	25.7	4.32	12	52.3	15.0	32.9
Zn	441	501	305	542	677	266	293	233	356	288	437	416	131	12	677	233	396
Zr	82.3	72.0	96.0	86.0	133.8	68.1	86.0	64.4	79.3	66.9	132	104	241	12	134	64.4	89.2
La	24.1	20.1	22.7	17.2	9.82	13.6	21.8	16.8	15.1	19.8	59.3	16.5	43.7	12	59.3	9.82	21.4
Ce	45.6	28.2	41.7	14.6	7.63	31.7	48.3	55.5	24.7	55.7	90.7	36.4	91.9	12	90.7	7.63	40.1
Pr	4.52	4.14	4.67	3.35	2.16	3.36	4.88	3.48	3.31	4.27	12.2	3.56	9.92	12	12.2	2.16	4.49
Nd	21.2	19.4	20.8	15.7	10.2	15.4	22.6	15.8	15.4	19.4	58.0	16.2	42.5	12	58.0	10.2	20.8
Sm	4.22	3.90	4.35	3.13	2.40	3.30	4.76	3.30	3.30	4.12	11.6	3.79	7.41	12	11.6	2.40	4.35
Eu	0.94	0.92	1.01	0.76	0.59	0.79	1.10	0.81	0.73	0.99	2.78	0.96	2.04	12	2.78	0.59	1.03
Gd	4.88	4.69	5.30	3.97	3.20	4.10	5.88	4.23	4.11	4.84	14.2	5.18	6.77	12	14.2	3.20	5.39
Tb	0.75	0.73	0.84	0.62	0.54	0.63	0.92	0.67	0.63	0.80	2.11	0.86	0.97	12	2.11	0.54	0.84
Dy	5.05	5.10	5.55	4.51	3.96	4.19	6.38	4.49	4.41	5.35	14.2	5.88	5.84	12	14.2	3.96	5.76
Y	42.8	47.1	41.9	38.2	34.5	29.4	55.8	32.6	36.1	38.8	121	44.2	39.0	12	121	29.4	46.9
Ho	1.17	1.18	1.23	1.01	0.92	0.93	1.46	1.01	0.99	1.12	3.15	1.29	1.19	12	3.15	0.92	1.29
Er	3.51	3.56	3.56	3.10	2.88	2.66	4.62	2.95	2.93	3.44	9.30	4.03	3.32	12	9.30	2.66	3.88
Tm	0.46	0.49	0.49	0.44	0.41	0.37	0.65	0.40	0.40	0.45	1.24	0.56	0.46	12	1.24	0.37	0.53
Yb	3.09	3.08	3.00	2.82	2.82	2.27	3.93	2.57	2.68	2.89	7.36	3.47	2.78	12	7.36	2.27	3.33
Lu	0.51	0.53	0.41	0.45	0.25	0.13	0.43	0.18	0.20	0.47	1.17	0.59	0.46	12	1.17	0.13	0.44
∑REY[3]	163	143	158	110	82	113	184	145	115	162	409	143	258	12	409	82.3	161
%HREY[4]	38.8	47.1	40.2	50.9	60.8	40.3	44.2	34.5	46.3	36.4	43.3	46.7	24.3	12	60.8	34.5	44.1
Ce*	-0.04	-0.18	-0.06	-0.39	-0.45	0.01	0.00	0.19	-0.13	0.12	-0.15	0.01	-0.01	12	0.2	-0.5	-0.1
Eu*	0.96	1.00	0.98	1.00	0.97	1.00	0.96	1.00	0.92	1.03	1.00	0.99	1.35	12	1.0	0.9	1.0
∑REY/Fe	0.0003	0.0002	0.0003	0.0002	0.0001	0.0002	0.0003	0.0002	0.0002	0.0002	0.0007	0.0002	0.0007	12	0.0007	0.0001	0.0003
Fe/Mn	36.9	118.8	65.7	109.6	302.5	78.3	54.0	63.1	136.4	135.9	23.9	59.0	48.3	12	303	23.9	98.7
Co/Zn	1.27	0.48	1.35	0.30	0.23	1.82	1.77	2.33	0.84	1.86	1.08	1.23	1.54	12	2.3	0.23	1.21

[1]Calculated from measured CO_2 content

[2]Loss on ignition at 1000°C

[3]∑ REY = Sum of rare earth elements plus yttrium

[4]Percent of heavy REY (Eu-Lu, +Y) of the total sum of REY

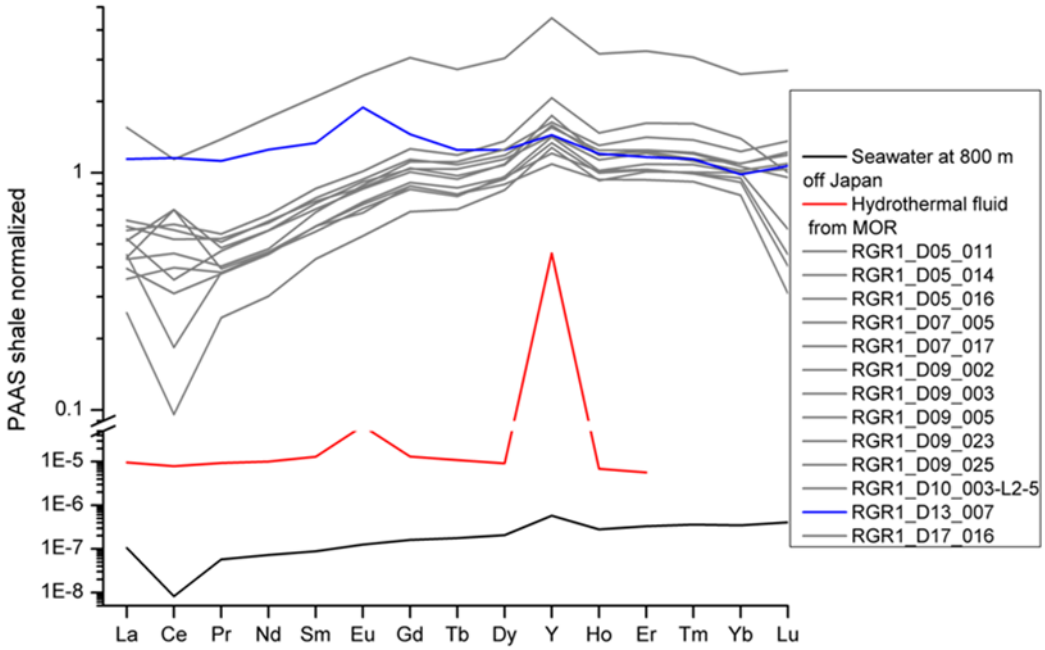

Figure 6: Shale normalized (Post Archean Australian Shale) rare earth elements and Y plot for laminated ironstones samples (gray) and ironstone breccia sample D13_007 (blue). Plots of REY in seawater at 800 m water depth off Japan (black) from Alibo and Nozaki (1999) and hydrothermal fluid from middle ocean ridges (red) from Klinkhammer et al. (1994).

4.4.3 U-Th/He ages of goethite

The ages of 19 goethite aliquots from the 22 aliquots analyzed by the U-Th/He method range between 1.65 and 7.68 Ma (Table 3). The ages of the three remaining aliquots have been discredited because two aliquots are chemically different (very low U contents and high Th/U) and consequently yield ages inconsistent with the rest of the suite; and one aliquot has a chemical composition very distinct from goethite based on the Fe, Al, Si, U, Th, Sm, and He contents (Table 3), probably because it contained a different mineral other than goethite.

For each hand sample, the ages of the three different aliquots vary significantly, with differences of up to 3.7 Ma for sample RGR1_D07_005 (Table 3). Since the analytical uncertainty of the method is small (Table 3), the age variability in a single sample indicates goethite crystallization, recrystallization, and maturation at different times, suggesting prolonged growth and/or Fe recycling (see discussion below).

For the chimney-shaped sample DY094_041, the inner stratigraphic layer (conduit proximal) shows average age of 3.07 Ma while the outer one shows an older average age of 5.96 Ma, indicating that the chimney-shaped structure grew outward away from the central conduit with the newest material forming along the conduit (Figure 7). The breccia sample was not analyzed because it was only recognized as being unique from the other samples after the U-Th/He analyzes were done on a random set of samples that did not include the breccia.

Table 3: Chemical composition and derived U-Th/He geochronology ages of goethite fragments from ironstones from RGR. The pale gray text in italic refers to aliquots potentially containing terrigenous material (#16 and #10) and chemical composition distinct from goethite (#13).

Sample name	Aliquot	(U-Th-Sm)/He age [Ma]	± σ	goe [ug]	± σ	Fe [mol-%]	Al [mol-%]	Si [mol-%]	Mn [mol-%]	U [ppm]	± σ	Th [ppm]	± σ	Sm [ppm]	± σ	He [mol/g]	± σ
	1	3.4	0.0	48	1	93.7	3.9	2.2	0.2	5.1	0.1	0.6	0.0	3.6	0.3	9.72E-11	9.68E-12
	8	7.2	0.2	67	1	90.1	6.9	2.3	0.8	5.0	0.1	1.2	0.0	4.4	0.2	2.04E-10	1.37E-11
RGR1_D07_005	15	4.7	0.1	66	1	97.8	1.9	0.2	0.2	3.0	0.1	1.6	0.0	4.7	0.3	8.79E-11	5.25E-12
	2	3.5	0.1	29	0	93.3	2.7	1.9	2.2	3.6	0.1	3.1	0.1	2.7	0.2	8.30E-11	1.05E-11
	9	4.1	0.0	37	0	94.1	3.2	2.3	0.4	4.7	0.1	2.3	0.1	4.6	0.3	1.16E-10	1.69E-11
RGR1_D09_002	*16*	*11.1*	*0.3*	*64*	*1*	*95.3*	*2.3*	*2.2*	*0.3*	*0.4*	*0.0*	*1.5*	*0.0*	*4.6*	*0.3*	*4.34E-11*	*5.72E-12*
	3	4.4	0.1	64	1	92	5.1	1.6	1.2	4.2	0.1	2.7	0.0	2.8	0.2	1.15E-10	1.00E-11
	10	*16.3*	*0.2*	*66*	*1*	*92.7*	*5.3*	*1.7*	*0.3*	*0.1*	*0.0*	*5.8*	*0.1*	*5.9*	*0.3*	*1.28E-10*	*1.14E-11*
	17	2.5	0.0	58	1	92.5	5.6	1.5	0.4	5.5	0.1	3.0	0.1	3.0	0.2	8.29E-11	9.92E-12
RGR1_D09_003	22	1.7	0.0	73	1	94.6	3.3	1.9	0.2	5.7	0.1	1.2	0.0	4.0	0.3	5.44E-11	3.43E-12
	4	4.5	0.1	110	1	95.1	3.3	1.3	0.3	3.2	0.1	1.8	0.0	3.6	0.2	8.85E-11	7.14E-12
	11	4.3	0.0	121	1	96.8	2.5	0.3	0.4	2.7	0.0	1.9	0.0	4.2	0.3	7.43E-11	7.20E-12
RGR1_D09_005	18	3.3	0.1	90	1	95	2.6	2.1	0.4	2.6	0.0	1.6	0.0	3.8	0.2	5.42E-11	5.85E-12
	5	3.7	0.1	73	1	93.4	5.6	0.5	0.4	3.3	0.1	2.1	0.0	5.4	0.3	7.56E-11	6.61E-12
	12	2.1	0.0	108	1	90.6	7.3	1.8	0.3	6.7	0.1	4.3	0.1	4.9	0.3	8.77E-11	8.32E-12
RGR1_D17_016	19	1.7	0.0	108	1	90.9	7	1.7	0.4	6.6	0.1	5.6	0.1	4.8	0.3	7.12E-11	6.43E-12
	6	7.7	0.1	56	1	97.6	2	0.1	0.2	2.1	0.0	0.4	0.0	4.7	0.3	9.23E-11	1.02E-11
	13	*337.3*	*16.6*	*15*	*0*	*71.9*	*12*	*16*	*0.1*	*0.2*	*0.0*	*3.0*	*0.1*	*27.7*	*1.6*	*1.71E-09*	*5.58E-11*
DY094_041_5	20	4.2	0.1	110	1	97.7	1.4	0.6	0.3	3.1	0.0	0.5	0.0	2.7	0.2	7.43E-11	7.15E-12
	7	3.1	0.1	69	1	98	0.5	1.2	0.3	3.3	0.1	0.1	0.0	1.2	0.1	5.49E-11	6.62E-12
	14	1.7	0.0	77	1	97.8	0.5	1.5	0.2	3.4	0.1	0.1	0.0	1.1	0.1	3.12E-11	3.26E-12
DY094_041_1	21	4.5	0.1	109	2	98.2	0.5	1	0.3	1.3	0.0	0.2	0.0	1.3	0.1	3.21E-11	3.02E-12

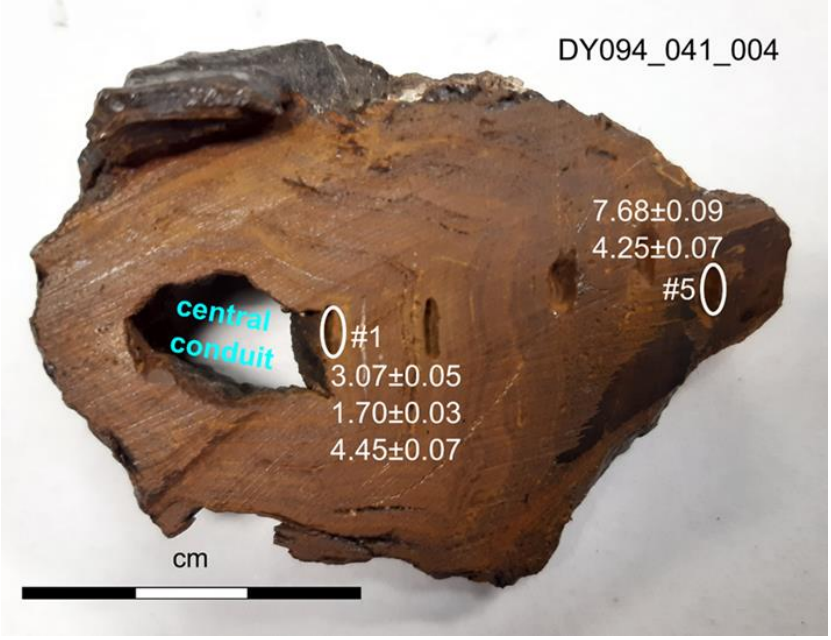

Figure 7: Cross-section of the chimney-shaped ironstone sample DY094_041_004 with a large central conduit. Three ironstone grains from each of the two sample areas were analyzed for U-Th/He geochronology ages.

4.5 Discussion

4.5.1 Geochemical clues regarding the source of metals and formation of ironstones from RGR

4.5.1.1 Major element signatures

Fe oxyhydroxides have a high metal sorption capacity. In ferromanganese precipitates, Cr, As, P, and V (enriched in RGR ironstones) are mostly sorbed on the FeOOH (González et al., 2009, 2012) while Ni, Co, and Zn are preferentially associated with Mn oxides, and S, Cl, and F with CFA (Koschinsky et al., 1995; Koschinsky and Hein, 2003; Mohwinkel et al., 2014; Marino et al., 2018). Thus, the most effective controls on which elements will be enriched in the ironstones from RGR are their availability in the mineralizing fluids for sorption onto the FeOOH and the presence of CFA, calcite, MnO2, and associated elements. The average Ca/P of the ironstones (2.30) is similar to seamount phosphorites (Hein et al., 2016) and suggests Ca is predominantly in the form of CFA. However, we acknowledge that some P can be associated to Fe oxyhydroxides apart from CFA, which would imply that more Ca would then be linked to calcite; due to the multiple ways for Ca and P to be incorporated in the ironstones, we primarily rely on the XRD results that indicate calcite and CFA contents satisfy the Ca and P concentrations.

Incorporated detrital material can also influence ironstone composition, namely the Si and Al contents. The laminated ironstones show low Si/Al ratios compared to igneous rocks -

e.g., 3.37 for basalts (Dasgupta et al., 2010) and 3.82 for average upper continental crust (Rudnick and Gao, 2013) - which indicates little detrital aluminosilicate fraction or preferential sorption of Al relative to Si on the iron minerals. This contrasts with the Si/Al ratio of the Fe-cemented breccia, which is typical of average upper continental crust (Rudnick and Gao, 2013), representing the inclusion of detrital aluminosilicate minerals.

4.5.1.2 Trace element enrichments

The strong fractionation between Fe and Mn combined with low trace element contents (Co+Ni+Cu of < 0.17 wt.%) of the ironstones from RGR are characteristics of seafloor hydrothermal ferromanganese deposits (Bonatti et al., 1972; Toth, 1980; Lyle, 1981; Rona et al., 1983; Dymond et al., 1984; Manheim and Lane-Bostwick, 1988; Hein et al., 1994), which results in the ironstones plotting within the hydrothermal field on the ternary discrimination diagram of Bonatti et al. (1972) (Figure 8). The ironstones from RGR also plot in the hydrothermal field of the Fe, Mn, Cu, Ni, Zr, Y, and Ce ternary discrimination diagram of Josso et al. (2017) (Figure 8). The ironstones from RGR generally have low trace element contents except for Cl, F, As, Zn, Cr, Ni, V, Sr, and S. Fluorine, S, and Cl may be linked to the variable amounts of CFA and were sourced from seawater. As, Zn, Cr, Ni, V, and Sr are enriched in hydrothermal Fe and Mn deposits from elsewhere in the global ocean (Hein et al., 1994, 1997; Fitzgerald and Gillis, 2006; Hein et al., 2008; Pecoits et al., 2009). Arsenic, Fe, and Ni are sourced from the hydrothermal fluids that produced ironstones from Pacific seamounts (Hein et al., 1994), and high Ni content is found at hydrothermal fluids from Loihi Seamount in Hawaii (Sedwick et al., 1992). A Co/Zn ratio close to 0.15 can also indicate hydrothermal influence, whereas values close to 2.5 indicate a hydrogenetic origin with no hydrothermal input (Toth, 1980). Ironstones from RGR have Co/Zn ranging from 0.23 to 2.32, at intermediate values between the hydrothermal and hydrogenetic end members.

4.5.1.3 Rare earth element plus yttrium patterns

The influence of a hydrothermal solution is also suggested by very low REY/Fe ($\leq$ 0.0007) of the ironstones from RGR, similar to purely hydrothermally precipitated Fe oxyhydroxides from the Tagoro submarine volcano (REE/Fe of <0.0009) (González et al., 2020). However, the average total REY of the ironstones studied here (161 ppm) is intermediate between the values typical for hydrothermal origin (15–149 ppm) and diagenetic origin (110–489 ppm) reported by Bau et al. (2014). Furthermore, the ironstones from RGR cluster closer to the hydrothermal field on the bivariate discrimination diagram of Ce_{SN}/Ce_{SN}^* versus

Y_{SN}/Ho_{SN} from Bau et al. (2014), but within the diagenetic field on the Ce_{SN}/Ce_{SN}^* versus Nd plot, although some samples overlap with the hydrothermal field (Figure 9). This intermediate REY behavior may reflect a mixture of potentially hydrothermal goethite and diagenetic CFA, since CFA can host high contents of REY (Hein et al., 2016).

The PAAS shale-normalized REY plots of the RGR ironstones resemble that of seawater (Bau et al., 1996), except for the absence of or slightly positive Ce_{SN} anomalies in 8 of 13 samples. The Ce_{SN} anomaly is not a definitive indicator of hydrothermal influence since hydrothermal deposits may bear either positive or negative Ce_{SN} anomalies, although no anomaly or negative Ce_{SN} anomalies are most common (Toth, 1980; Hein et al., 1994; González et al., 2020). Moderate positive to weak negative Ce_{SN} anomalies, similar to ironstones from RGR, may suggest a transitional suboxic redox state of the fluid, indicating a redox front (Slack et al., 2007). The REY plots of hydrothermal Fe deposits usually show a positive Eu_{SN} anomaly (Stoffers et al., 1992; Bau and Dulski, 1996; González et al., 2020) since hydrothermal fluids are Eu-rich with an Eu_{SN} anomaly typically between 6.3 and 19.7 (Michard and Albarède, 1986). Most of our ironstone samples display no Eu_{SN} anomaly, but the breccia sample RGR1_D13_007 shows a weak positive anomaly (1.35). Absent or weak EuSN anomalies do not negate a hydrothermal origin. For example, low-to-moderate temperature hydrothermal fluids (<250°C) may not display an Eu anomaly or may display values close to 1 (Bau and Dulski, 1996). Also, biomineralized Fe-deposits formed from diffuse-flow, low-temperature hydrothermal fluids show a negative Eu_{SN} anomaly at the Jan Mayen Vent Field (Johannessen et al., 2017). Negative Eu* can result from the absence of leaching of plagioclase by the hydrothermal fluids at depth or to precipitation of Eu-rich minerals (such as barite or anhydrite) from the fluids at depth, before the mineralization at or near the seafloor (Hein et al., 2000). Fe-oxyhydroxide mineralized samples from the Tagoro submarine volcano field show Eu_{SN} anomalies of 1.3 (González et al., 2020), similar to RGR sample RGR1_D13_007.

We note that none of the published ferromanganese oxide discrimination diagrams used here were constructed using data for Fe-rich bacterial mats and their geologic end-products. Consequently, there is no field in the plots designated to represent the geochemical signature of those types of deposits, or elements used that might best discriminate that type of deposit (see next section) from hydrothermal, hydrogenetic, and diagenetic deposits.

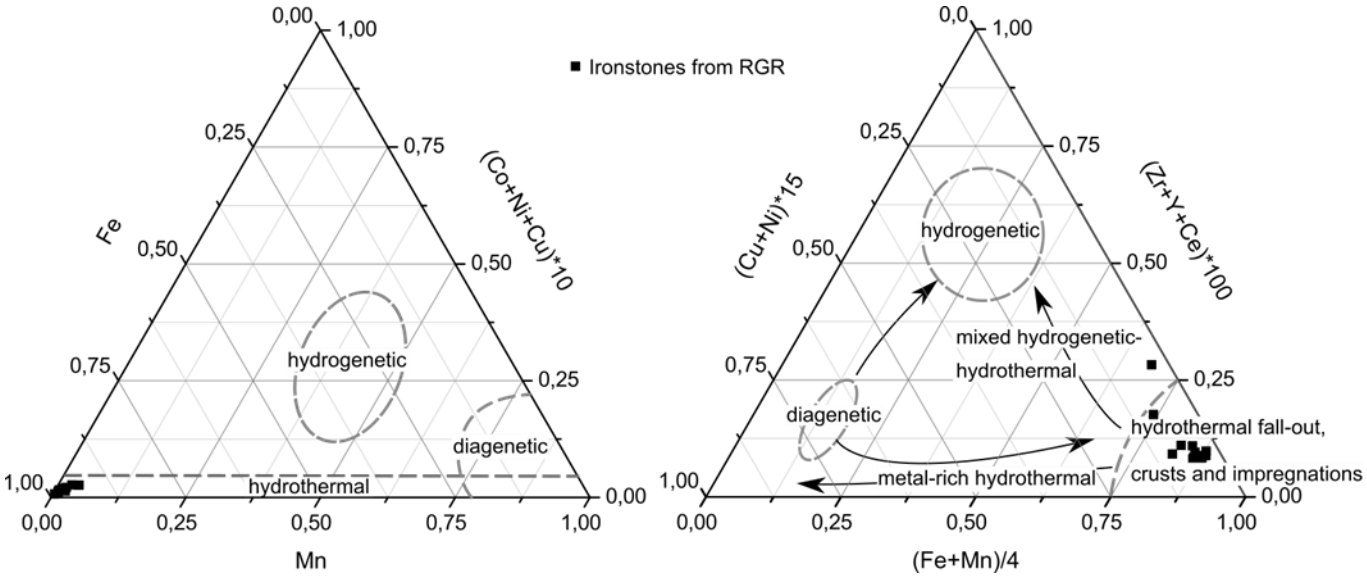

Figure 8: Discrimination ternary diagrams based on the content of major (Fe and Mn) and trace (Cu, Co, Ni) elements from Bonatti et al. (1972) (left) and on the content of major (Fe and Mn), trace (Cu and Ni), and high field strength and rare earth elements (Zr, Y, and Ce) from Josso et al. (2017). Ironstones from RGR plot in the hydrothermal field.

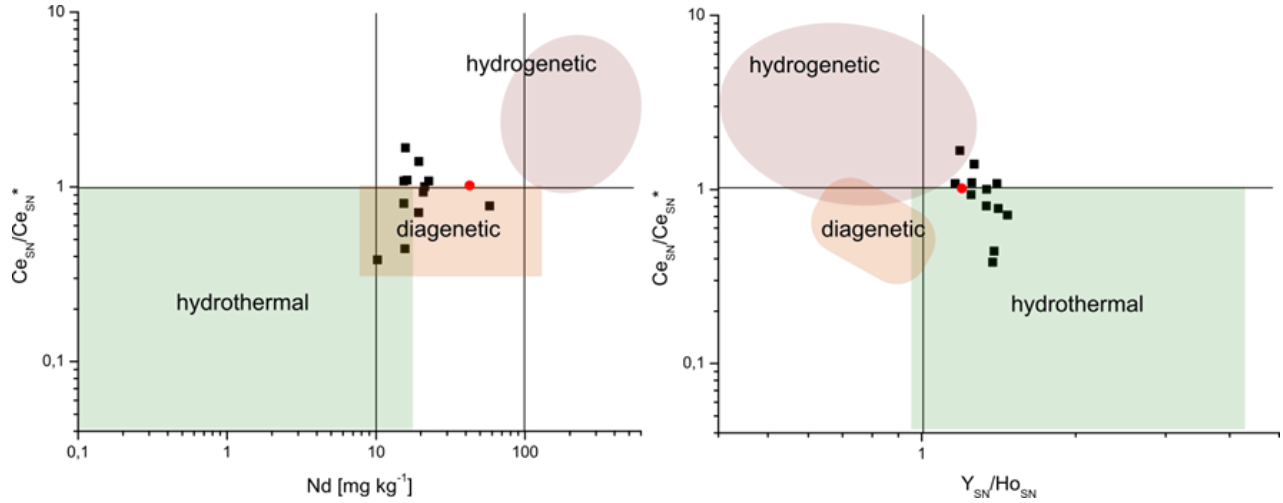

Figure 9: Ironstones from RGR plotted on the bivariate discrimination diagrams of Ce_{SN}/Ce_{SN}* ratio vs. Nd concentration (left) and Ce_{SN}/Ce_{SN}* ratio vs. Y_{SN}/Ho_{SN} (right) from Bau et al. (2014). Black squares refer to laminated ironstones, and the red square refers to the breccia sample RGR1_D13_007.

4.5.2 Evidence of microbial mats contribution to RGR ironstones formation

4.5.2.1 Physical observations

Microbial structures from FeOB mats recognizable in rocks from elsewhere by microscopy include twisted stalks, straight sheaths, long rod-shaped microorganisms, filamentous branching bodies, stromatolitic structures, and EPS (Chan et al., 2016; Heim et al., 2017; González et al., 2020). Among these, only morphology reminiscent of EPS was consistently found in the different RGR ironstone samples, but we cannot exclude that other microbial-related forms were present but not preserved in the fossil record. EPS is an essential

component of biofilms and is composed dominantly of polysaccharides (Reolid and Abad, 2019), which explains the C content in the EDS point analyses of the RGR samples. EPS is known to increase chemical gradients across biofilms (Reolid and Abad, 2019), and the microbial community is often involved in the precipitation of specific metals, such as Fe (Emerson et al., 2007; Heim et al., 2017). EPS structures similar to those observed here were identified in fossil microbialites from the Tethys Western End associated with past hydrothermal activity (Reolid and Abad, 2019), such as the RGR bacteria stalk connected to EPS in Figure 5E.

FeOB produce mats of orange color up to 1.5 m thick, which underlie FeMn crusts at Loihi Seamount (Hawaii) and Tagoro submarine volcano (Canary Islands) (Edwards et al., 2004; González et al., 2020). After compression and dewatering, the Fe-oxyhydroxide rock produced by these FeOB mats would not differ from the ironstones from RGR in appearance, mineralogy, and chemical composition.

4.5.2.2 Ironstone composition and mineral paragenesis

Studying microbially mediated ironstone facies, Salama et al. (2012) found enrichment in Zn, V, Mo, U, S, and Cl; four (Zn, V, S, Cl) of which are strongly enriched in RGR ironstones. Remains of organic carbon are also linked to the role of microbes in the formation of ironstones (Salama et al., 2012). In addition, it is known that bacterially mediated Fe oxidation contributes significantly to Fe oxidation, and FeOB accelerate the rate of Fe oxidation under microaerobic conditions ($O_2 < 50$ μM) (Edwards et al., 2004; Emerson et al., 2010; McAllister et al., 2019).

Goethite is a more ordered phase transformed after the dehydration and recrystallization of ferrihydrite, the primary mineral that precipitates in modern Fe microbial mats (Hughes, 1989; Baele et al., 2008; Raiswell, 2011; Salama et al., 2013). Thus, it is plausible that the thin laminations of RGR ironstones reflect past primary precipitation of Fe oxyhydroxide from solution within soft, living Fe-rich mats. The macroscopic and microscopic calcite laminae between goethite laminae were probably deposited between episodes of bacterial mat activity. The lithification of mats to form ironstone probably involved the crystallization of goethite from a precursor Fe oxyhydroxide upon dewatering and compaction as newly added material accumulated on old FeOB mat material. Later, diagenetic CFA replaced part of the carbonate during phosphatization (Benites et al., 2021).

The presence of planktonic foraminifera within the goethite laminae suggests precipitation at the seafloor. On the other hand, the swirling goethite lamina at the base of FeMn crusts suggests that Fe-mineralization also occurred in the subsurface through upflow. In this

case, a fluid flowing from deeper levels and leaching underlying rocks was likely, which is also indicated for the chimney-like sample DY094_D04_041.

Alteration of igneous rock fragments in the ironstone breccia may also be related to microbial activity. It is known that reduced elements, such as Fe(II), can be accessed by microbes from volcanic rocks under oligotrophic conditions (Adams et al., 1992; Staudigel et al., 1998; Bailey et al., 2009; Konhauser et al., 2011). Cockell et al. (2011) suggested that minerals such as pyroxene and olivine in crystalline basalts provide a source of reduced Fe for the FeOB bacteria growing in streams in Iceland. Basalt glass weathering experiments have shown that more Si is released to solution in the presence of FeOB, suggesting enhanced weathering (Edwards et al., 2004). Different from the poorly crystalline goethite in the laminated ironstone, the goethite cement of the igneous rock fragments corresponds to acicular micro-crystallites and was probably precipitated inorganically based on morphology and the lack of observed structures similar to EPS.

4.5.3 Ages of mineralization

The goethite ages derived from the U-Th/He method indicate mineralization must have started by 7.68 Ma, with a wide range of ages from different goethite grains taken in proximity from a single sample. The conversion of amorphous to crystalline Fe oxyhydroxides takes time and may not be homogenous among grains. Thus, goethite U-Th/He ages spanning millions of years within a few mm is a common observation in authigenic goethite cement and reflects various goethite generations closely intergrown, revealing a prolonged history of mineral precipitation and maturation instead of an isolated event (Vasconcelos et al., 2013; Monteiro et al., 2014). Besides, He diffusion may occur due to Fe oxyhydroxide dissolution and reprecipitation and/or diagenesis processes. For these reasons, the U-Th/He ages provide a minimum estimate for the age of the initiation of ironstone mineralization.

The composition of fluid inclusions in the ironstones have the potential of impacting the U-Th/He ages. However, the ironstone grains analyzed in this study were small and the fluid inclusions smaller yet. Based on the genesis of the ironstones discussed in the next section, for which magmatic hydrothermal input is highly unsupported, the fluid inclusions in goethite grains are likely composed predominantly of seawater. The mean ^{4}He content of the two ironstone aliquots analyzed is $137x10^{-8}$ CC/g (see Supplementary Material S1), which is two orders of magnitude higher than the ^{4}He of seawater ($4x10^{-8}$ CC/g; Ostlund et al., 1987). Thus, fluid inclusions are considered inconsequential to the determination of ages using the U-Th/He method.

The ironstones from RGR underwent diagenesis, as evidenced by the CFA replacement of carbonates (Benites et al., 2021). The $^{87}Sr/^{86}Sr$ ratio and calibrated ages of CFA in two of the ironstones samples from RGR studied here (RGR1_D09_005 and RGR1_D10_003) revealed that CFA formed around 6.8 Ma in these samples (Benites et al., 2021), which is in agreement with the oldest goethite U-Th/He age. Thus, based on the ironstone ages from RGR, goethite mineralization minimum ages correspond to the late Miocene at around 7.68 Ma or earlier. The goethite in ironstones from RGR may have continued to mineralize from at least the late Miocene into the Quaternary. Alternatively, it is also possible that Fe cycling through dissolution and reprecipitation of Fe oxyhydroxides occurred until more recently based on the Quaternary goethite ages found here.

4.5.4 Proposed source of the mineralizing fluid for ironstone formation

Geochemical, petrographic, and geochronology data of the ironstones studied here suggest a prolonged formation history since the late Miocene or slightly earlier, under the influence of low-temperature mineralizing fluids. Although the last significant magmatism along RGR dates from the Eocene (~46 Ma) (Thiede, 1977; Camboa and Rabinowitz, 1984; Ussami et al., 2012; Rohde et al., 2013), we cannot exclude the possibility of more recent unidentified magmatic events. However, we favor a geothermal system as the source of the low-temperature fluids.

The combination of faults providing a pathway and high-heat flow providing low-temperature geothermal fluids may have facilitated the seafloor FeMn mineralization, which occurs for example on thinned oceanic crust in the East Pacific Ocean (Hein et al., 2005). Even though the oceanic crust at RGR is thick (up to 25 km, Graça et al., 2019), a series of deep faults along the CSR could have facilitated a geothermal circulation cell. There is evidence that these faults have been reactivated from the Late Cretaceous to the early Miocene and probably by younger extensional events (Mohriak et al., 2010; Galvão and de Castro, 2017; Praxedes et al., 2019). Geothermal circulation cells can develop at extensional and transtensional basins with fractures and faults functioning as an open network for fluid circulation (Stimac et al., 2015). Within a system of faults and fractures, seawater can easily percolate to depths of several kilometers and ascend back to the seafloor once heated and attaining buoyancy, carrying heat and solutes (Stimac et al., 2015). For example, temperatures of 90 to 200°C occur at 1 km depth along an East Pacific Ocean rifted continental margin, and the deep-seated circulating fluids can leach basement rocks providing many metals to the seabed (Ag, Ba, S, Sr, Hg, Cd, Tl, Li, Cr, As, Sb, among others; Hein et al., 2005, 2007). The tholeiitic to alkaline basement basalts

from the RGR are enriched in trace metals like V, Zr, Nb, Sr, Cr, Co, Ni, and the LREE, apart from Fe (Thompson et al., 1981; O'Connor and Duncan, 1990), some of which are enriched in the ironstones. Reactivated faults have driven high geothermal gradients and deep-seated fluid circulation venting in the area of Galicia Bank, providing dissolved and colloidal Fe and other metals from leaching of basement rocks for mineralization at and near the seafloor (González et al., 2016). Moreover, hotspot and volcanic-arc geothermal systems can generate chloride and As-rich waters (Stauffer and Thompson, 1984; Stimac et al., 2015), compounds significantly enriched in RGR ironstones. Biomineralization of As-rich hydrous ferric oxides have been found at chloride-rich geothermal springs from Yellowstone (Donahoe-Christiansen et al., 2004; Inskeep et al., 2004), a terrestrial hotspot in the western USA, and could also have occurred within the RGR Fe mats, explaining the close association between Fe and As distribution.

FeOB mats grow at oxic-suboxic fronts where Fe2+-rich fluids flow from basement rocks into oxygenated waters (Cockell et al., 2011; Edwards et al., 2011; Gonzalez et al., 2020; Emerson et al., 2010; Emerson and Moyer, 2002). It is plausible that Fe mineralization by FeOB bacteria occurred along a redox front in the shallow subsurface below the pre-existing FeMn crusts, producing the flame-like ironstone structures. This process also occurs at environmental temperatures lower than 10°C (Emerson and Revsbech, 1994; Cockell et al., 2011), closer to the seawater temperature of RGR seafloor at 700 m (6°C; Jovane et al., 2019). Thus, it is also likely that FeOB mats were present at the seafloor near the discharge of Fe^{2+}-rich geothermal fluids. The chimney-shaped ironstone with central conduit directly supports this idea.

An alternative Fe^{2+} source of fluid venting could be from hydrocarbon reservoirs. This phenomenon is observed in the Gulf of Cadiz and in the South China Sea, where goethite nodules form nearby hydrocarbon fluid seepage or cold seeps (González et al., 2012; Zhong et al., 2021). In this case, the same RGR fault system previously mentioned would facilitate the ascension of deep-seated hydrocarbon fluids to the surface, feeding a bacterial community and driving mineralization at the seafloor. However, the presence of a hydrocarbon reservoir in the RGR has not been reported and it is implausible that, even if present, it would develop at the summit of RGR where the sediment cover is thin. In addition, the sediment records from RGR consist of pelagic carbonate and terrigenous debris with low organic carbon contents in general (Emelyanov and Trimonis, 1983), which would limit the formation of hydrocarbon compounds. Finally, no accessory minerals typically found in proximity to cold seeps were observed in the ironstones or elsewhere along the summit of RGR (e.g., ankerite, dolomite, pyrite, chalcopyrite; Gonzalez et al., 2009). Thus, it is unlikely that the Fe^{2+}-rich fluid was linked to a hydrocarbon reservoir.

We favor a model in which the exhalation of a Fe2+-rich geothermal fluid occurred on RGR via fluid circulation along CSR-related faults and an appropriate geothermal gradient (Figure 10A). The sample distribution may support this model since ironstones were retrieved only from dredges collected near the margins of the CSR. In this genetic model, metals and other compounds would have been provided to living microbial mats by the geothermal fluid exhaling at the seafloor (Fe^{2+}, As^{3+}, Ni^{2+}, Zn^{2+}, $HVO4^{2-}$, $CrO4^{2-}$, among others) and by seawater (Cl^{-}, F^{-}, NO^{3-}, $HPO4^{2-}$, HCO3-, Ca^{2+}, Mg^{2+}, Fe^{2+}, among others) (Figure 10B). Within the living microbial mat, FeOB oxidized Fe^{2+} to Fe^{3+} producing ferrihydrite (FeOOH) in the process, to which many metals were adsorbed (Figure 10C). Episodic periods of enhanced primary productivity triggered increased input of pelagic sediments to the seafloor that hindered mat growth, creating hiatuses in mat growth. The pilling up of dead mats and carbonate sediments led to dewatering (Figure 10D). With time, compaction, diagenesis, and lithification occurred, producing the ironstone (Figure 10E), which also involved the decomposition of organic matter associated with the mats, mineralization of goethite, and subsequent variable phosphatization of the carbonates.

4.6 Conclusions

Geochemical investigations reveal that ironstones from RGR formed by precipitation of Fe oxyhydroxides that eventually formed laminated goethite pavements and cement around igneous rock fragments in a breccia sample. Our preferred model for their formation involves biomineralization by FeOB mats on the seafloor and within the shallow subsurface. Upon bacterial mat death and accumulation of a series of intercalated dead mats and carbonate sediments, compaction and dewatering caused the crystallization of goethite and formation of ironstone. Goethite mineralization occurred over several million years from the late Miocene (7.65 Ma) or slightly before and extending into the Quaternary (1.68 Ma), likely because of formation of several generations of bacterial mats, slow goethite mineralization rates, and Fe cycling (dissolution-reprecipitation). The mineralizing fluid most likely flowed upward, as indicated by the flame-like goethite laminae below FeMn crusts and the chimney-shaped sample with a central conduit.

The strong fractionation between Fe and Mn, low trace elements content (Ni+Cu+Co) except for Cl and As, and very low REY/Fe ratios suggest a hydrothermal fluid, while the EuSN anomalies and the bivariate Ce_{SN}/Ce_{SN}* versus Y_{SN}/Ho_{SN} and Ce_{SN}/Ce_{SN}* versus Nd plots are inconclusive. However, no proximal source of magma has been identified at RGR during Fe-rich bacterial mat formation. As an alternative, we propose that the mineralizing fluid may have

been generated by a geothermal circulation system associated with faults along the CSR. Within this system, seawater would have percolated into the RGR edifice where it would have been heated and enriched in solutes (e.g., Fe^{2+}, As^{3+}, Ni^{2+}, Zn^{2+}, $HVO4^{2-}$, $CrO4^{2-}$) and ascended back to the seafloor providing the conditions for microbial mats to flourish. Our proposed genetic model can be better constrained with further data, such as heat-flow measurement to corroborate the possibility of geothermal circulation at RGR, Fe isotopes, identification of organic remains (e.g., proteinaceous compounds, lipids, carbohydrates, and carotenoids), and microbiological studies in the ironstones to corroborate biogenicity.

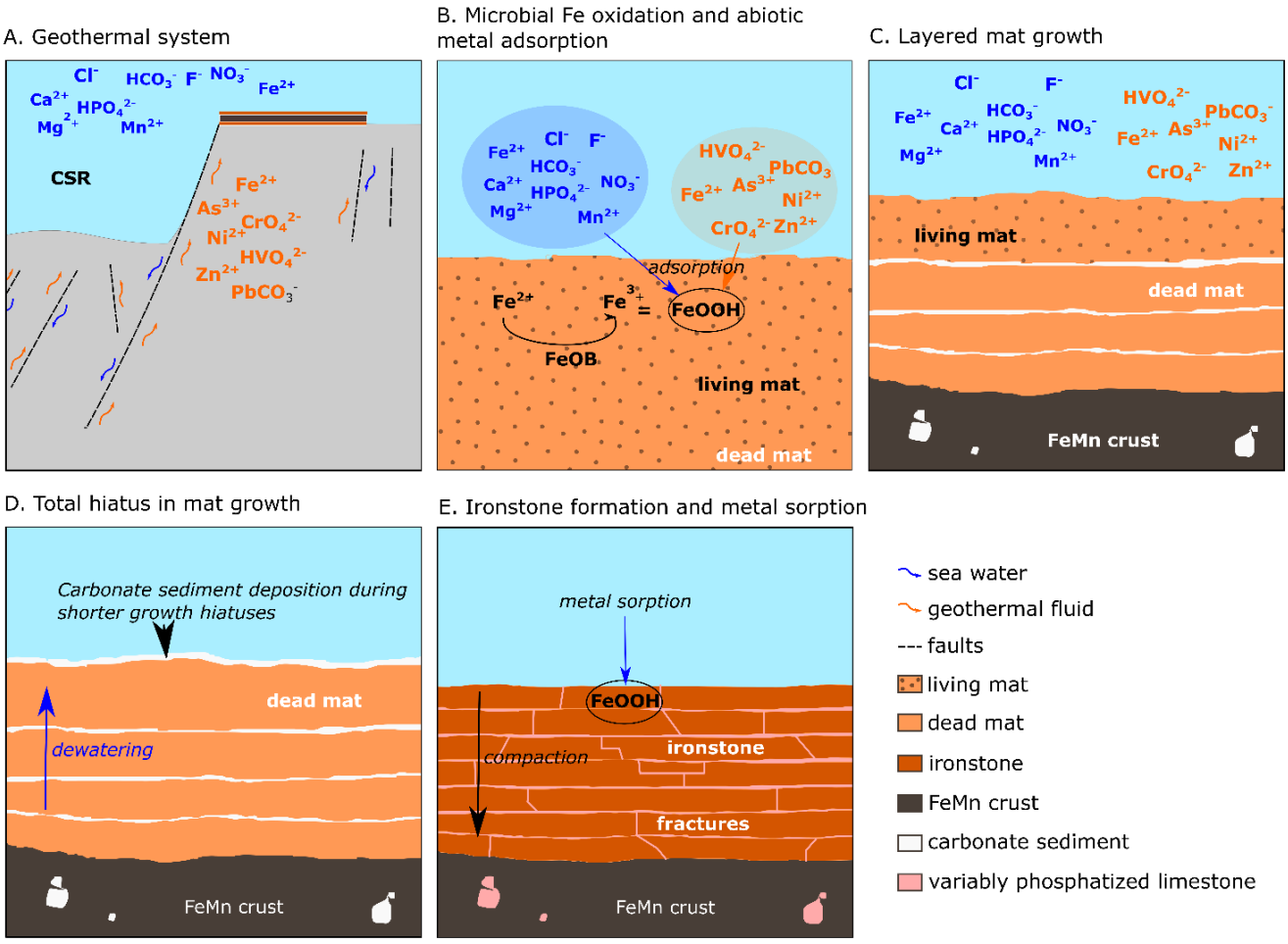

Figure 10: Proposed model of ironstone formation at the summit of Rio Grande Rise. (A) Fe^{2+} and other metals are sourced to living microbial mats by a geothermal circulation cell (orange) and by seawater (blue); (B) Fe-oxidizing bacteria (FeOB) within living microbial mat oxidizes Fe^{2+} to Fe^{3+} forming FeOOH. Many other metals are adsorbed to the surface of the FeOOH; (C) Mat growth via successive layers of dead mats and carbonate sediments; (D) carbonate deposition occurs during hiatus in microbial mat growth. The mass of the accumulating material leads to dewatering of the dead mats and carbonates; (E) upon compaction and diagenesis (phosphatization), the dead mats thinned, fractured, and lithified as ironstone. Metals sorption continues after lithification.

References

Adams, J.B., Palmer, F., and Staley, J.T., 1992, Rock weathering in deserts: mobilization and concentration of ferric iron by microorganisms: Geomicrobiology Journal, v. 10, p. 99–114, doi:10.1080/01490459209377910.

Alibo, D.S., and Nozaki, Y., 1999, Rare earth elements in seawater: Particle association, shale-normalization, and Ce oxidation: Geochimica et Cosmochimica Acta, v. 63, p. 363–372, doi:10.1016/S0016-7037(98)00279-8.

Alt, J.C., 1988, Hydrothermal oxide and nontronite deposits on seamounts in the eastern Pacific: Marine Geology, v. 81, p. 227–239, doi:10.1016/0025-3227(88)90029-1.

Baele, J.-M., Bouvain, F., De Jong, J., Matielli, N., Papier, S., and Préat, A., 2008, Iron microbial mats in modern and phanerozoic environments: Instruments, Methods, and Missions for Astrobiology XI, v. 7097, p. 70970N, doi:10.1117/12.801597.

Bailey, B., Templeton, A., Staudigel, H., and Tebo, B.M., 2009, Utilization of substrate components during basaltic glass colonization by Pseudomonas and Shewanella Isolates: Geomicrobiology Journal, v. 26, p. 648–656, doi:10.1080/01490450903263376.

Baioumy, H.M., Ahmed, A.H., and Khedr, M.Z., 2014, A mixed hydrogenous and hydrothermal origin of the Bahariya iron ores, Egypt: evidences from the trace and rare earth element geochemistry: Journal of Geochemical Exploration, v. 146, p. 149–162, doi:10.1016/j.gexplo.2014.08.008.

Barker, P.F., 1983, Tectonic evolution and subsidence history of the Rio Grande Rise: Initial reports DSDP, Leg 72, Santos, Brazil, p. 953–976, doi:10.2973/dsdp.proc.72.151.1983.

Bau, M., and Dulski, P., 1996, Distribution of yttrium and rare-earth elements in the Penge and Kuruman iron-formations, Transvaal Supergroup, South Africa: Precambrian Research, v. 79, p. 37–55, doi:10.1016/0301-9268(95)00087-9.

Bau, M., Koschinsky, A., Dulski, P., and Hein, J.R., 1996, Comparison of the partitioning behaviours of yttrium, rare earth elements, and titanium between hydrogenetic marine ferromanganese crusts and seawater: Geochimica et Cosmochimica Acta, v. 60, p. 1709–1725, doi:10.1016/0016-7037(96)00063-4.

Bau, M., Schmidt, K., Koschinsky, A., Hein, J., Kuhn, T., and Usui, A., 2014, Discriminating between different genetic types of marine ferro-manganese crusts and nodules based on rare earth elements and yttrium: Chemical Geology, v. 381, p. 1–9, doi:10.1016/j.chemgeo.2014.05.004.

Benites, M., Hein, J.R., Mizell, K., Blackburn, T., and Jovane, L., 2020, Genesis and evolution of ferromanganese crusts from the summit of Rio Grande Rise, Southwest Atlantic Ocean: Minerals, v. 10, p. 349, doi:10.3390/min10040349.

Benites, M., Hein, J.R., Mizell, K.L., and Jovane, L., 2021, Miocene phosphatization of rocks from the summit of Rio Grande Rise, Southwest Atlantic Ocean [in press]: Paleoceanography and Paleoclimatology, doi:10.1029/2020PA004197.

Benites, M., Millo, C., Hein, J., Nath, B.N., Murton, B., Galante, D., and Jovane, L., 2018, Integrated geochemical and morphological data provide insights into the genesis of ferromanganese nodules: Minerals, v. 8, p. 1–16, doi:10.3390/min8110488.

Bonatti, E., Kraemer, T., and Rydell, H., 1972, Classification and genesis of submarine iron-manganese deposits, in Horn, D.R. ed., Ferromanganese deposits on the ocean floor, Alexandria, VA, USA, NSF, p. 149–166.

Camboa, L.A.P., and Rabinowitz, P.D., 1984, The evolution of the Rio Grande Rise in the Southwest Atlantic Ocean: Marine Geology, v. 58, p. 35–58, doi:10.1016/0025-3227(84)90115-4.

Carey, S. et al., 2016, Hydrothermal venting and mineralization in the crater of Kick'em Jenny submarine volcano, Grenada (Lesser Antilles): Geochemistry, Geophysics, Geosystems, v. 17, p. 1000–1019, doi:10.1002/2015GC006060.

Chan, C.S., McAllister, S.M., Leavitt, A.H., Glazer, B.T., Krepski, S.T., and Emerson, D., 2016, The architecture of iron microbial mats reflects the adaptation of chemolithotrophic iron oxidation in freshwater and marine environments: Frontiers in Microbiology, v. 7, p. 1–18, doi:10.3389/fmicb.2016.00796.

Cockell, C.S., Kelly, L.C., Summers, S., and Marteinsson, V., 2011, Following the kinetics: iron-oxidizing microbial mats in cold icelandic volcanic habitats and their rock-associated carbonaceous signature: Astrobiology, v. 11, p. 679–694, doi:10.1089/ast.2011.0606.

Constantino, R.R., Hackspacher, P.C., de Souza, I.A., and Lima Costa, I.S., 2017, Basement structures over Rio Grande Rise from gravity inversion: Journal of South American Earth Sciences, v. 75, p. 85–91, doi:10.1016/j.jsames.2017.02.005.

Cook, H.E., Johnson, P.D., Matti, J.C., and Zemmels, I., 1975, Methods of sample preparation and X-ray data analysis: X-ray mineralogy laboratory, Deep Sea Drilling Project, University of California Riverside, p. 999–1007.

Crosby, C.H., Bailey, J. V., and Sharma, M., 2014, Fossil evidence of iron-oxidizing chemolithotrophy linked to phosphogenesis in the wake of the Great Oxidation Event: Geology, v. 42, p. 1015–1018, doi:10.1130/G35922.1.

Dahanayake, K., and Krumbein, W.E., 1986, Microbial structures in oolitic iron formations: Mineralium Deposita, v. 21, p. 85–94, doi:10.1007/BF00204266.

Dasgupta, R., Jackson, M.G., and Lee, C.T.A., 2010, Major element chemistry of ocean island basalts - Conditions of mantle melting and heterogeneity of mantle source: Earth and Planetary Science Letters, v. 289, p. 377–392, doi:10.1016/j.epsl.2009.11.027.

Donahoe-Christiansen, J., D'Imperio, S., Jackson, C.R., Inskeep, W.P., and McDermott, T.R., 2004, Arsenite-oxidizing hydrogenobaculum strain isolated from an acid-sulfate-chloride geothermal spring in Yellowstone National Park: Applied and Environmental Microbiology, v. 70, p. 1865–1868, doi:10.1128/AEM.70.3.1865-1868.2004.

Dymond, J., Lyle, M., Finney, B., Piper, D.Z., Murphy, K., Conard, R., and Pisias, N., 1984, Ferromanganese nodules from MANOP Sites H, S, and R - control of mineralogical and chemical composition by multiple accretionary processes: Geochimica et Cosmochimica Acta, v. 48, p. 931–949, doi:10.1016/0016-7037(84)90186-8.

Edwards, K.J. et al., 2011, Ultra-diffuse hydrothermal venting supports Fe-oxidizing bacteria and massive umber deposition at 5000 m off Hawaii: ISME Journal, v. 5, p. 1748–1758, doi:10.1038/ismej.2011.48.

Edwards, K.J., Bach, W., McCollom, T.M., and Rogers, D.R., 2004, Neutrophilic iron-oxidizing bacteria in the ocean: their habitats, diversity, and roles in mineral deposition, rock alteration, and biomass production in the deep-sea: Geomicrobiology Journal, v. 21, p. 393–404, doi:10.1080/01490450490485863.

Emelyanov, E.M., and Trimonis, E.S., 1983, Geochemical investigation of sediments from the Brazil Basin and the Rio Grande Rise:, doi:10.2973/dsdp.proc.72.112.1983.

Emerson, D., Fleming, E.J., and McBeth, J.M., 2010, Iron-oxidizing bacteria: an environmental and genomic perspective: Annual Review of Microbiology, v. 64, p. 561–583, doi:10.1146/annurev.micro.112408.134208.

Emerson, D., and Moyer, C.L., 2002, Neutrophilic Fe-oxidizing bacteria are abundant at the Loihi Seamount hydrothermal vents and play a major role in Fe oxide deposition: Applied and Environmental Microbiology, v. 68, p. 3085–3093, doi:10.1128/AEM.68.6.3085-3093.2002.

Emerson, D., Rentz, J.A., Lilburn, T.G., Davis, R.E., Aldrich, H., Chan, C., and Moyer, C.L., 2007, A novel lineage of proteobacteria involved in formation of marine Fe-oxidizing microbial mat communities: PLoS ONE, v. 2, p. e667, doi:10.1371/journal.pone.0000667.

Emerson, D., and Revsbech, N.P., 1994, Investigation of an iron-oxidizing microbial mat community located near Aarhus, Denmark: Field studies: Applied and Environmental Microbiology, v. 60, p. 4022–4031, doi:10.1128/aem.60.11.4022-4031.1994.

Fitzgerald, C.E., and Gillis, K.M., 2006, Hydrothermal manganese oxide deposits from Baby Bare seamount in the Northeast Pacific Ocean: Marine Geology, v. 225, p. 145–156, doi:10.1016/j.margeo.2005.09.005.

Galvão, I.L.G., and de Castro, D.L., 2017, Contribution of global potential field data to the tectonic reconstruction of the Rio Grande Rise in the South Atlantic: Marine and Petroleum Geology, v. 86, p. 932–949, doi:10.1016/j.marpetgeo.2017.06.048.

González, F.J. et al., 2020, Low-temperature, shallow-water hydrothermal vent mineralization following the recent submarine eruption of Tagoro volcano (El Hierro, Canary Islands): Marine Geology, v. 430, p. 106333, doi:10.1016/j.margeo.2020.106333.

González, F.J., Somoza, L., Hein, J.R., Medialdea, T., León, R., Urgorri, V., Reyes, J., and Martín-Rubí, J.A., 2016, Phosphorites, Co-rich Mn nodules, and Fe-Mn crusts from Galicia Bank, NE Atlantic: reflections of cenozoic tectonics and paleoceanography: Geochemistry, Geophysics, Geosystems, v. 17, p. 346–374, doi:10.1002/2015GC00586 1.

González, F.J., Somoza, L., León, R., Medialdea, T., de Torres, T., Ortiz, J.E., Lunar, R., Martínez-Frías, J., and Merinero, R., 2012, Ferromanganese nodules and micro-hardgrounds associated with the Cadiz Contourite Channel (NE Atlantic): palaeoenvironmental records of fluid venting and bottom currents: Chemical Geology, v. 310–311, p. 56–78, doi:10.1016/j.chemgeo.2012.03.030.

González, F.J., Somoza, L., Lunar, R., Martínez-Frías, J., Martín Rubí, J.A., Torres, T., Ortiz, J.E., Díaz del Río, V., Pinheiro, L.M., and Magalhães, V.H., 2009, Hydrocarbon-derived ferromanganese nodules in carbonate-mud mounds from the Gulf of Cadiz: Mud-breccia sediments and clasts as nucleation sites: Marine Geology, v. 261, p. 64–81, doi:10.1016/j.margeo.2008.11.005.

Graça, M.C., Kusznir, N., and Stanton, N.S.G., 2019, Crustal thickness mapping of the central South Atlantic and the geodynamic development of the Rio Grande Rise and Walvis Ridge: Marine and Petroleum Geology, v. 101, p. 230–242, doi:10.1016/j.marpetgeo.2018.12.011.

Heim, C., Quéric, N.V., Ionescu, D., Schäfer, N., and Reitner, J., 2017, Frutexites-like structures formed by iron oxidizing biofilms in the continental subsurface (Äspö Hard Rock Laboratory, Sweden): PLoS ONE, v. 12, p. 1–22, doi:10.1371/journal.pone.0177542.

Heim, J.A., Vasconcelos, P.M., Shuster, D.L., Farley, K.A., and Broadbent, G., 2006, Dating paleochannel iron ore by (U-Th)/He analysis of supergene goethite, Hamersley province, Australia: Geology, v. 34, p. 173–176, doi:10.1130/G22003.1.

Hein, J.R., Clague, D.A., Koski, R.A., Embley, R.W., and Dunham, R.E., 2008, Metalliferous sediment and a silica-hematite deposit within the Blanco Fracture Zone, Northeast Pacific: Marine Georesources and Geotechnology, v. 26, p. 317–339, doi:10.1080/10641190802430986.

Hein, J.R., Hsueh-Wen, Y., Gunn, S.H., Gibbs, A.E., and Chung-ho, W., 1994, Composition and origin of hydrothermal ironstones from central Pacific seamounts: Geochimica et Cosmochimica Acta, v. 58, p. 179–189, doi:10.1016/0016-7037(94)90455-3.

Hein, J.R., Koschinsky, A., Halbach, P., Manheim, F.T., Bau, M., Kang, J., and Lubick, N., 1997, Iron and manganese oxide mineralization in the Pacific, in Nicholson, K., Hein, J.R., Buhn, B., and Dasgupta, S. eds., Manganese Mineralisation: Geochemistry and Mineralogy of Terrestrial and Marine Deposits, Geological Society Special Publication, v. 119, p. 123–138.

Hein, J.R., Koschinsky, A., and McIntyre, B.R., 2005, Mercury- and silver-rich ferromanganese oxides, Southern California borderland: deposit model and environmental implications: Economic Geology, v. 100, p. 1151–1168, doi:10.2113/gsecongeo.100.6.1151.

Hein, J., Koschinsky, A., Mikesell, M., Mizell, K., Glenn, C., and Wood, R., 2016, Marine phosphorites as potential resources for heavy rare earth elements and yttrium: Minerals, v. 6, p. 88, doi:10.3390/min6030088.

Hein, J.R., Schwab, W.C., and Davis, A.S., 1988, Cobalt- and platinum-rich ferromanganese crusts and associated substrate rocks from the Marshall Islands: Marine Geology, v. 78, p. 255–283, doi:10.1016/0025-3227(88)90113-2.

Hein, J.R., Stamatakis, M.G., and Dowling, J.S., 2000, Trace metal-rich Quaternary hydrothermal manganese oxide and barite deposit, Milos Island, Greece: Applied Earth Science, v. 109, p. 67–76, doi:10.1179/aes.2000.109.2.67.

Hein, J.R., Zierenberg, R.A., Maynard, J.B., and Hannington, M.D., 2007, Barite-forming environments along a rifted continental margin, Southern California Borderland: Deep-Sea Research Part II: Topical Studies in Oceanography, v. 54, p. 1327–1349, doi:10.1016/j.dsr2.2007.04.011.

Helba, A.A., El Aref, M., and Saad, F., 2001, Lutetian oncoidal and ooidal ironstone sequences; Egyption Journal of Geology, v. 45, p. 325–351.

Hughes, C.R., 1989, The application of analytical transmission electron microscopy to the study of oolitic ironstones: a preliminary study: Geological Society Special Publication, v. 46, p. 121–131, doi:10.1144/GSL.SP.1989.046.01.12.

Inskeep, W.P., Macur, R.E., Harrison, G., Bostick, B.C., and Fendorf, S., 2004, Biomineralization of As(V)-hydrous ferric oxyhydroxide in microbial mats of an acid-sulfate-chloride geothermal spring, Yellowstone National Park: Geochimica et Cosmochimica Acta, v. 68, p. 3141–3155, doi:10.1016/j.gca.2003.09.020.

Johannessen, K.C., Vander Roost, J., Dahle, H., Dundas, S.H., Pedersen, R.B., and Thorseth, I.H., 2017, Environmental controls on biomineralization and Fe-mound formation in a low-temperature hydrothermal system at the Jan Mayen Vent Fields: Geochimica et Cosmochimica Acta, v. 202, p. 101–123, doi:10.1016/j.gca.2016.12.016.

Josso, P., Pelleter, E., Pourret, O., Fouquet, Y., Etoubleau, J., Cheron, S., and Bollinger, C., 2017, A new discrimination scheme for oceanic ferromanganese deposits using high field strength and rare earth elements: Ore Geology Reviews, v. 87, p. 3–15, doi:10.1016/j.oregeorev.2016.09.003.

Jovane, L. et al., 2019, Multidisciplinary scientific cruise to the Rio Grande Rise: Frontiers in Marine Science, v. 6, p. 1–7, doi:10.3389/fmars.2019.00252.

Kimberley, M.M., 1978, Paleoenvironmental classification of iron formations: Economic Geology, v. 73, p. 215–229, doi:10.2113/gsecongeo.73.2.215.

Klinkhammer, G.P., Elderfield, H., Edmond, J.M., and Mitra, A., 1994, Geochemical implications of rare earth element patterns in hydrothermal fluids from mid-ocean ridges: Geochimica et Cosmochimica Acta, v. 58, p. 5105–5113, doi:10.1016/0016-7037(94)90297-6.

Konhauser, K.O., Kappler, A., and Roden, E.E., 2011, Iron in microbial metabolisms: Elements, v. 7, p. 89–93, doi:10.2113/gselements.7.2.89.

Koschinsky, A., Van Gerven, M., and Halbach, P., 1995, First investigations of massive ferromanganese crusts in the NE Atlantic in comparison with hydrogenetic pacific occurrences: Marine Georesources and Geotechnology, v. 13, p. 375–391, doi:10.1080/10641199509388294.

Koschinsky, A., and Hein, J.R., 2003, Uptake of elements from seawater by ferromanganese crusts: solid-phase associations and seawater speciation: Marine Geology, v. 198, p. 331–351, doi:10.1016/S0025-3227(03)00122-1.

Kuhn, T., Bau, M., Blum, N., and Halbach, P., 1998, Origin of negative Ce anomalies in mixed hydrothermal-hydrogenetic Fe-Mn crusts from the Central Indian Ridge: Earth and Planetary Science Letters, v. 163, p. 207–220.

Little, C.T.S., Glynn, S.E.J., and Mills, R.A., 2004, Four-hundred-and-ninety-million-year record of bacteriogenic iron oxide precipitation at sea-floor hydrothermal vents: Geomicrobiology Journal, v. 21, p. 415–429, doi:10.1080/01490450490485845.

Lyle, M., 1981, Formation and growth of ferromanganese oxides on the Nazca plate: Memoir of the Geological Society of America, v. 154, p. 269–294, doi:10.1130/MEM154-p269.

Manheim, F.T., and Lane-Bostwick, C.M., 1988, Cobalt in ferromanganese crusts as a monitor of hydrothermal discharge on the Pacific sea floor: Nature, v. 335, p. 59–62.

Marino, E. et al., 2019, Hydrogenetic, diagenetic and hydrothermal processes forming ferromanganese crusts in the Canary Island seamounts and their influence in the metal recovery rate with hydrometallurgical methods: Minerals, v. 9, doi:10.3390/min9070439.

Marino, E., González, F.J., Lunar, R., Reyes, J., Medialdea, T., Castillo-Carrión, M., Bellido, E., and Somoza, L., 2018, High-resolution analysis of critical minerals and elements in Fe–Mn crusts from the canary island seamount province (Atlantic ocean): Minerals, v. 8, p. 1–36, doi:10.3390/min8070285.

McAllister, S.M., Moore, R.M., Gartman, A., Luther, G.W., Emerson, D., and Chan, C.S., 2019, The Fe(II)-oxidizing Zetaproteobacteria: Historical, ecological and genomic perspectives: FEMS Microbiology Ecology, v. 95, p. 1–18, doi:10.1093/femsec/fiz015.

McLennan, S.M., 2018, Rare earth elements in sedimentary rocks: influence of provenance and sedimentary processes, in Lipin, B.R. and McKay, G.A. eds., Geochemistry and Mineralogy of Rare Earth Elements, Berlin, Boston, De Gruyter, v. 21, p. 169–200, doi:10.1515/9781501509032-010.

Michard, A., and Albarède, F., 1986, The REE content of some hydrothermal fluids: Chemical Geology, v. 55, p. 51–60, doi:10.1016/0009-2541(86)90127-0.

Mohriak, W.U., Nobrega, M., Odegard, M.E., Gomes, B.S., and Dickson, W.G., 2010, Geological and geophysical interpretation of the Rio Grande Rise, south-eastern Brazilian margin: extensional tectonics and rifting of continental and oceanic crusts: Petroleum Geoscience, v. 16, p. 231–245, doi:10.1144/1354-079309-910.

Mohwinkel, D., Kleint, C., and Koschinsky, A., 2014, Phase associations and potential selective extraction methods for selected high-tech metals from ferromanganese nodules and crusts with siderophores: Applied Geochemistry, v. 43, p. 13–21, doi:10.1016/j.apgeochem.2014.01.010.

Monteiro, H.S., Vasconcelos, P.M., Farley, K.A., Spier, C.A., and Mello, C.L., 2014, (U – Th)/He geochronology of goethite and the origin and evolution of cangas: Geochimica et Cosmochimica Acta, v. 131, p. 267–289, doi:10.1016/j.gca.2014.01.036.

Montserrat, F. et al., 2019, Deep-sea mining on the Rio Grande Rise (Southwestern Atlantic): A review on environmental baseline, ecosystem services and potential impacts: Deep-Sea Research Part I, v. 145, p. 31–58, doi:10.1016/j.dsr.2018.12.007.

O'Connor, J.M., and Duncan, R.A., 1990, Evolution of the Walvis Ridge-Rio Grande Rise hot spot system: implications for African and South American plate motions over plumes: Journal of Geophysical Research, v. 95, doi:10.1029/jb095ib11p17475.

Ostlund, H.G., Craig, H., Broecker, W.S., and Spencer, D., 1987, Shorebased data and graphics. GEOSECS Atlantic, Pacific, and Indian Ocean Expeditions: Washington, DC, National Science Foundation, v. 7.

Pecoits, E., Gingras, M.K., Barley, M.E., Kappler, A., Posth, N.R., and Konhauser, K.O., 2009, Petrography and geochemistry of the Dales Gorge banded iron formation: paragenetic sequence, source and implications for palaeo-ocean chemistry: Precambrian Research, v. 172, p. 163–187, doi:10.1016/j.precamres.2009.03.014.

Pichler, T., Veizer, J., and Hall, G.E.M., 1999, Natural input of arsenic into a coral-reef ecosystem by hydrothermal fluids and its removal by Fe(III) oxyhydroxides: Environmental Science and Technology, v. 33, p. 1373–1378, doi:10.1021/es980949+.

Planavsky, N., Rouxel, O., Bekker, A., Shapiro, R., Fralick, P., and Knudsen, A., 2009, Iron-oxidizing microbial ecosystems thrived in late Paleoproterozoic redox-stratified oceans: Earth and Planetary Science Letters, v. 286, p. 230–242, doi:10.1016/j.epsl.2009.06.033.

Praxedes, A.G.P., de Castro, D.L., Torres, L.C., Gambôa, L.A.P., and Hackspacher, P.C., 2019, New insights of the tectonic and sedimentary evolution of the Rio Grande Rise, South Atlantic Ocean: Marine and Petroleum Geology, v. 110, p. 335–346, doi:10.1016/j.marpetgeo.2019.07.035.

Raiswell, R., 2011, Iron transport from the continents to the open ocean: the aging-rejuvenation cycle: Elements, v. 7, p. 101–106, doi:10.2113/gselements.7.2.101.

Reolid, M., and Abad, I., 2019, Jurassic non-carbonate microbialites from the Betic-Rifian Cordillera (Tethys western end): textures, mineralogy, and environmental reconstruction: Minerals, v. 9, doi:10.3390/min9020088.

Rohde, J.K., van den Bogaard, P., Hoernle, K., Hauff, F., and Werner, R., 2013, Evidence for an age progression along the Tristan-Gough volcanic track from new 40Ar/39Ar ages on phenocryst phases: Tectonophysics, v. 604, p. 60–71, doi:10.1016/j.tecto.2012.08.026.

Rona, P.A., 1984, Hydrothermal mineralization at seafloor spreading centers: Earth Science Reviews, v. 20, p. 1–104, doi:10.1016/0012-8252(84)90080-1.

Rona, P.A., 1986, Mineral deposits from sea-floor hot springs: Scientific American, v. 254, p. 84–93.

Rona, P.A., 2003, Resources of the sea floor: Science, v. 299, p. 673–674, doi:10.1126/science.1080679.

Rona, P.A., Boström, K., Laubier, L., and Smith, K.L., 1983, Hydrothermal processes at seafloor spreading centers: New York, Springer.

Rudnick, R.L., and Gao, S., 2013, Composition of the continental crust, in Holland, H.D. and Turekian, K.K. eds., Treatise on Geochemistry: Second Edition, Elsevier Ltd., v. 4, p. 1–51, doi:10.1016/B0-08-043751-6/03016-4.

Salama, W., El Aref, M., and Gaupp, R., 2014, Facies analysis and palaeoclimatic significance of ironstones formed during the Eocene greenhouse: Sedimentology, v. 61, p. 1594–1624, doi:10.1111/sed.12106.

Salama, W., El Aref, M.M., and Gaupp, R., 2013, Mineral evolution and processes of ferruginous microbialite accretion - an example from the Middle Eocene stromatolitic and ooidal ironstones of the Bahariya Depression, Western Desert, Egypt: Geobiology, v. 11, p. 15–28, doi:10.1111/gbi.12011.

Salama, W., El Aref, M., and Gaupp, R., 2012, Mineralogical and geochemical investigations of the Middle Eocene ironstones, El Bahariya Depression, Western Desert, Egypt: Gondwana Research, v. 22, p. 717–736, doi:10.1016/j.gr.2011.11.011.

Santos, R.V., Ganade, C.E., Lacasse, C.M., Costa, I.S.L., Pessanha, I., Frazão, E.P., Dantas, E.L., and Cavalcante, J.A., 2019, Dating Gondwanan continental crust at the Rio Grande Rise, South Atlantic: Terra Nova, v. 31, p. 424–429, doi:10.1111/ter.12405.

Sedwick, P.N., McMurtry, G.M., and Macdougall, J.D., 1992, Chemistry of hydrothermal solutions from Pele's Vents, Loihi Seamount, Hawaii: Geochimica et Cosmochimica Acta, v. 56, p. 3643–3667, doi:10.1016/0016-7037(92)90159-G.

Shuster, D.L., Vasconcelos, P.M., Heim, J.A., and Farley, K.A., 2005, Weathering geochronology by (U-Th)/He dating of goethite: Geochimica et Cosmochimica Acta, v. 69, p. 659–673, doi:10.1016/j.gca.2004.07.028.

Slack, J.F., Grenne, T., Bekker, A., Rouxel, O.J., and Lindberg, P.A., 2007, Suboxic deep seawater in the late Paleoproterozoic: evidence from hematitic chert and iron formation related to seafloor-hydrothermal sulfide deposits, central Arizona, USA: Earth and Planetary Science Letters, v. 255, p. 243–256, doi:10.1016/j.epsl.2006.12.018.

Sousa, I.M.C., Santos, R. V., Koschinsky, A., Bau, M., Wegorzewski, A. V., Cavalcanti, J.A.D., and Dantas, E.L., 2021, Mineralogy and chemical composition of

ferromanganese crusts from the Cruzeiro do Sul Lineament - Rio Grande Rise, South Atlantic: Journal of South American Earth Sciences, v. 108, p. 103207, doi:10.1016/j.jsames.2021.103207.

Staudigel, H., Yayanos, A., Chastain, R., Davies, G., Verdurmen, E.A.T., Schiffman, P., Bourcier, R., and De Baar, 1998, Biologically mediated dissolution of volcanic glass in seawater: Earth and Planetary Science Letters, v. 164, p. 233–244, papers3://publication/uuid/2E154618-E071-425F-AF3B-01D322F65C35.

Stauffer, R.E., and Thompson, J.M., 1984, Arsenic and antimony in geothermal waters of Yellowstone National Park, Wyoming, USA: Geochimica et Cosmochimica Acta, v. 48, p. 2547–2561, doi:10.1016/0016-7037(84)90305-3.

Stimac, J., Goff, F., and Goff, C.J., 2015, Intrusion-related geothermal systems, in Sigurdsson, H. ed., The Encyclopedia of Volcanoes, Elsevier Inc., p. 799–822, doi:10.1016/b978-0-12-385938-9.00046-8.

Stoffers, P., Glasby, G.P., Stuben, D., Renner, R.M., Pierre, T.G., Webb, J., and Cardile, C.M., 1992, Comparative mineralogy and geochemistry of hydrothermal iron rich crusts from the Pitcairn, Teahitia-mehetia, and Macdonald hot spot areas of the S.W. Pacific: Marine Georesources and Geotechnology, v. 11, p. 45–86, doi:10.1080/10641199309379905.

Thiede, J., 1977, Subsidence of aseismic ridges: evidence from sediments on Rio Grande Rise (Southwest Atlantic Ocean): AAPG Bulletin (American Association of Petroleum Geologists), v. 61, p. 929–940, doi:10.1306/c1ea43a6-16c9-11d7-8645000102c1865d.

Thompson, G., Humphris, S., and Schilling, J., 1981, Petrology and geochemistry of basaltic rocks from Rio Grande Rise, South Atlantic: Deep Sea Drilling Project leg 72, hole 516F1: v. 3, p. 31, https://books.google.be/books?id=dzyy3XlmUS0C&dq=physiologie+humaine+hervé+guénard&hl=fr&sa=X&ved=0ahUKEwjpl_m3sLziAhWEaFAKHUkiBEkQ6AEIKDAA.

Toth, J.R., 1980, Deposition of submarine crusts rich in manganese and iron: Geological Society of America Bulletin, v. 91, p. 44, doi:10.1130/0016-7606(1980)91<44:doscri>2.0.co;2.

Ussami, N., Chaves, C.A.M., Marques, L.S., and Ernesto, M., 2012, Origin of the Rio Grande Rise-Walvis Ridge reviewed integrating palaeogeographic reconstruction, isotope geochemistry and flexural modelling, in Mohriak, W.U., Danforth, A., Post, P.J., Brown, D.E., Tari, G.C., Nemcok, M., and Sinha, S.T. eds., Conjugate Divergent Margins, London, Geological Society Special Publication, p. 369, doi:10.1144/SP369.10.

Usui, A., Ishizuka, O., and Yuasa, M., 1999, Mode of occurrence of iron-manganese crusts on inactive seamounts in the Northwestern Pacific back-arc setting, in Third ISOPE Ocean Mining Symposium, Goa, India.

Vasconcelos, P.M., Heim, J.A., Farley, K.A., Monteiro, H., and Waltenberg, K., 2013, 40Ar/39 Ar and (U-Th)/He – 4He/3He geochronology of landscape evolution and channel iron deposit genesis at Lynn Peak , Western Australia: Geochimica et Cosmochimica Acta, v. 117, p. 283–312, doi:10.1016/j.gca.2013.03.037.

Zeng, Z., Ouyang, H., Yin, X., Chen, S., Wang, X., and Wu, L., 2012, Formation of Fe-Si-Mn oxyhydroxides at the PACMANUS hydrothermal field, Eastern Manus Basin: mineralogical and geochemical evidence: Journal of Asian Earth Sciences, v. 60, p. 130–146, doi:10.1016/j.jseaes.2012.08.009.

Zhong, Y., Chen, Z., González, F.J., Hein, J.R., Zheng, X., Li, G., Luo, Y., Mo, A., Tian, Y., and Wang, S., 2017, Composition and genesis of ferromanganese deposits from the northern South China Sea: Journal of Asian Earth Sciences, v. 138, p. 110–128, doi:10.1016/j.jseaes.2017.02.015.

Zhong, Y., Chen, Z., González, F.J., Ortiz, J.E., Blanco, L., Marino, E., and Liu, Q., 2021, Insights into the origin of ferromanganese-rich deposits associated with South China Sea contourite depositional systems: Marine and Petroleum Geology, v. 133, doi:10.1016/j.marpetgeo.2021.105257.

Supplementary Material

Table S1: Measurements of 3He and 4He in samples D17-016 and D07-005 and in reference materials.

Name	Mass (mg)	Mass (g)	4He Blank (nCC)	3He Blank (pCC)	BC 4He (nCC)	BC 3He (pCC)	[4He] (nCC/g)	[3He] (pCC/g)
1AIR-6044			0.010907667	0.000637				
HB			0.010907667	0.000637				
D17-016	1.55	0.00155	0.010907667	0.000637	2.108432333	0.000792	1360.278925	0.510967742
HB			0.010907667	0.000637				
D07-005	1.82	0.00182	0.010907667	0.000637	2.497039333	0.000905	1371.9996	0.3500
1AIR-6045			0.010907667	0.000637				
HB			0.010907667	0.000637				

5 CONTROLS ON THE CHEMICAL COMPOSITION OF FERROMANGANESE CRUSTS FROM DEEP-WATER TO THE SUMMIT OF THE THE RIO GRANDE RISE, SOUTH ATLANTIC OCEAN (CHAPTER IV)

Manuscript submitted to Marine Geology

Mariana Benites[1], Javier González[2], James Hein[3], Egidio Marino[2], Jesus Reyes[2], Christian Millo[1], Luigi Jovane[1]

[1]Institute of Oceanography, University of São Paulo, Praça do Oceanográfico 191, 05508-120 São Paulo, SP, Brazil

[2]Geological Survey of Spain, (IGME), C/ Ríos Rosas, 23, 28003 Madrid, Spain

[3]U.S. Geological Survey Retired, PCMSC, 2885 Mission St., Santa Cruz, CA 95060, USA

Abstract

Ferromanganese (FeMn) crusts at the summit of Rio Grande Rise (RGR) (625 – 850 m) in the southwest Atlantic Ocean consistently show two contrasting generations, the older, typically thicker one, that is strongly phosphatized, and a younger thinner crust. Here, we investigate for the first time a suite of deep-water FeMn crusts from RGR at 1505 – 5060 m to evaluate the extent of phosphatization and the controls on the chemical composition. For this, we use a range of analytical techniques to study the mineralogy, chemical composition, and petrography of the crusts. Deep-water (>1500 m) RGR FeMn crusts are hydrogenetic, composed of vernadite and goethite with minor amounts of 10Å manganates in a few samples. Aluminosilicates (feldspar, clay minerals) and quartz are among the main components in some crusts below 4000 m. In general, these crusts are characterized by high contents of hydrogenetic metals (e.g., As, Be, Co, Cu, Mo, Sb, Se, Ti, Th, Tl, U, Zn, rare earth elements) and absence of calcite and phosphate minerals, which contrasts to the crusts from the summit. The contents of Mn, Co, V, As, Ni, Mo, Tl, U, Zn, Sb, P, and Ca in crusts decrease from 2008 to 5218 m due to oxygenation from the North Atlantic Deep Water (NADW) and Antarctic Bottom Water (AABW), mineral-phase association, and episodes of increased paleoproductivity and expanded/intensified oxygen minimum zone. On the other hand, increased Si, Al, K, Cu, and Th contents in the deeper-water crusts reflect entrained detrital material, the characteristic dissolved Cu seawater profile, and the presence of the silicate-rich AABW. Carbonate fluorapatite was identified in two crusts, from 1523 and 2190 m water depth. Subsidence played a key role in the temporal increase in contents of Mn, Co, and Mo in crust D20-1, due to exposure to more oxidizing conditions. Subsidence was possibly responsible also for the time gap between the initiation age of the non-

phosphatized generation of crust D28-32 at 2190 m (20.1 Ma) and of crusts at the summit (<14.7 Ma). The oldest initiation age of the deep-water crusts at RGR is estimated to be about 47 Ma. From a resource point of view, the deep-water crusts would be a better target for higher contents of Mn, Co, V, As, Mo, Tl, U, Zn, and Sb and to avoid the presence of phosphates. On the other hand, crusts from the summit would be a better target for exploration for phosphatized rocks rich in Ni, Li, and Y.

Keywords: ferromanganese crusts; phosphatization; Rio Grande Rise; metal resources; Atlantic Ocean.

5.1 Introduction

Ferromanganese (FeMn) oxide crusts precipitate from seawater onto oceanic elevations like seamounts, ridges, and plateaus. Because hydrogenetic precipitation rates are very slow (1 – 10 mm/Ma), the Fe and Mn oxyhydroxides with high specific surface areas adsorb and concentrate a wide variety of metals over their concentrations in seawater (Hein et al., 2013; Hein and Koschinsky, 2014; Mizell and Hein, 2018). The most recent estimate of the FeMn crusts global tonnage is $93x10^{10}$ dry tons, which highlights their importance as metal deposit (Mizell et al., 2022). It is known that oceanographic parameters (e.g., water depth, proximity to the continent, surface primary productivity, and proximity to the oxygen minimum zone (OMZ)) have a control on the physical characteristics of FeMn crusts such as thickness, texture, and, more importantly on chemical composition and therefore contents of metals of economic interest (Mizell et al., 2020; Usui et al., 2017). Further, regional and local paleoenvironmental conditions influence the temporal chemical and mineralogical variations along the growth axis of crusts (Usui et al., 2017; Marino et al., 2017).

FeMn crusts in the Atlantic Ocean have been more extensively studied in the northeast sector, comprising the Canary Island Seamount Province (CISP), off the Iberian coast, and off the Madeira and Azores Islands (González et al., 2022, 2016, 2014; Josso et al., 2021, 2020; Kfouri et al., 2021; Koschinsky et al., 1996, 1995; Marino et al., 2017, 2019, 2018; Muiños et al., 2013, 2008; Yeo et al., 2018). In the South Atlantic Ocean, FeMn crusts had been only sparsely studied until recently, for example at four occurrences along the Mid-Atlantic Ridge and to the east in the Angola and Cape basins (Dubinin et al., 2018) and one sample from the São Paulo Ridge in the vicinity of Rio Grande Rise (RGR) (Goto et al., 2017). The RGR is the first location in the South Atlantic Ocean to gain visibility regarding deep-sea Fe-Mn-oxide mineral deposits. Previous ROV dives showed a broad occurrence of FeMn crusts and

biodiversity on the main plateau (Corrêa et al., 2022), and the FeMn crusts from the RGR summit area were the first to undergo detailed geochemical and microbiological studies (Benites et al., 2020; Bergo et al., 2021; Sousa et al., 2021).

FeMn crusts from the RGR plateau at water depths of 600 – 1300 m have two generations of growth, an older phosphatized generation and a young non-phosphatized one (Benites et al., 2020; Sousa et al., 2021). These generations contrast significantly regarding their mineralogy and chemical composition, especially with reference to rare metals contents (Benites et al., 2020). The phosphatized generation is dominated by carbonate fluorapatite (CFA) and calcite, with minor 10Å manganates, up to 7.7 wt.% P, and high Mn, Ni, and Li contents; the younger non-phosphatized generation encompassing the top few millimeters is typical of hydrogenetic crusts composed of Fe oxyhydroxide and vernadite and is significantly enriched in critical metals (Bi, Nb, Ni, Te, Y, Pt, rare earth elements (REE)) (Benites et al., 2020). Because the phosphatized generation makes up most of the crust volume, the bulk FeMn crusts from the RGR plateau are depleted in the hydrogenetic metals of greatest economic interest (Co, REE, Mo, Te, Zr) but are the most enriched in P, Ni, and Li compared to the average for FeMn crusts from the Atlantic Ocean, Indian Ocean, Prime Crust Zone, and California Margin and manganese nodules from the Peru Basin and the Clarion-Clipperton Zone (Benites et al., 2020 and references therein). This dual structure has been previously described for other seamounts (Halbach et al., 1989; Nishi et al., 2017; Usui et al., 2017) and linked to global Miocene phosphatization (Hein et al., 1993; Hyeong et al., 2013) with the phosphorus source being primary productivity and the reservoir being the OMZ, which is also true for RGR (Benites et al., 2021). The younger generation, then, formed after the phosphatization event(s). However, a FeMn crust from 2871 m from the São Paulo Plateau studied by Goto et al. (2017) is 30 Ma old and was not phosphatized, indicating that phosphatization affected crusts only above a specific water depth. Thus, FeMn crusts from greater water depths are potentially more enriched in metals of economic interest.

Here, we use high-resolution techniques to investigate the petrography, mineralogy, and chemical composition of FeMn crusts from greater water depths (~1500 – 5000 m) along the RGR and surrounding seamounts and compare those with FeMn crusts from the RGR plateau (600 – 1300 m) previously studied by Benites et al. (2020). We evaluate the oceanographic controls on crust compositions, especially how the contents of metals of economic interest vary with water depth.

5.2 The study area

5.2.1 Geological setting of RGR

RGR is one of the most prominent bathymetric features in the South Atlantic Ocean, rising from 5000 m to 600 m water depths. It consists of a group of topographic highs composed of a plateau to the West (WRGR) and an N-S ridge to the East (ERGR), with a basin between the two structures and several smaller seamounts (Figure 1). Both WRGR and ERGR are cut by the Cruzeiro do Sul Lineament (CSL), a NW-SE rift channel that deepens about 1000 m from the summit in the WRGR, but more than 3000 m in the ERGR.

The formation of WRGR occurred jointly with the Walvis Ridge about 87 - 80 Myr ago when both rises formed on top of the Mid-Atlantic Ridge (MAR), like Iceland (Hoyer et al., 2022; Ussami et al., 2012). Continuous ocean spreading separated the two rises and the southward displacement of the mantle plume led to the formation of the N-S oriented ERGR most likely from 83 to 70 Myr ago (Rohde et al., 2013). Several ridge jumps formed the basin between the WRGR and ERGR and isolated the RGR as part of the South American Plate (Graça et al., 2019).

The ERGR and old parts of WRGR consist of tholeiitic basalt moderately enriched in trace metals while the crest of WRGR along the CSL is younger and consist of alkalic lavas (Hoyer et al., 2022). The alkaline volcanic activity occurred between 51 and 46 Myr ago (Hoyer et al 2022), when the WRGR was uplifted and subaerially exposed (Barker, 1983; Camboa and Rabinowitz, 1984); the CSL probably formed during this period (Hoyer et al 2022).

The most likely target area for FeMn crusts exploration consist of FeMn pavements at the plateau along the CSL (Corrêa et al., 2022; Montserrat et al., 2019; Sergipe et al., 2023). ROV images in the WRGR plateau reveal that the FeMn crust pavements occur on calcarenite substrate, with scattered thin sediment cover, but also FeMn crust debris, irregular FeMn crusts, and FeMn coated volcanic rock outcrops occur along the rift walls and occasional FeMn coated boulders and cobbles (Corrêa et al., 2022).

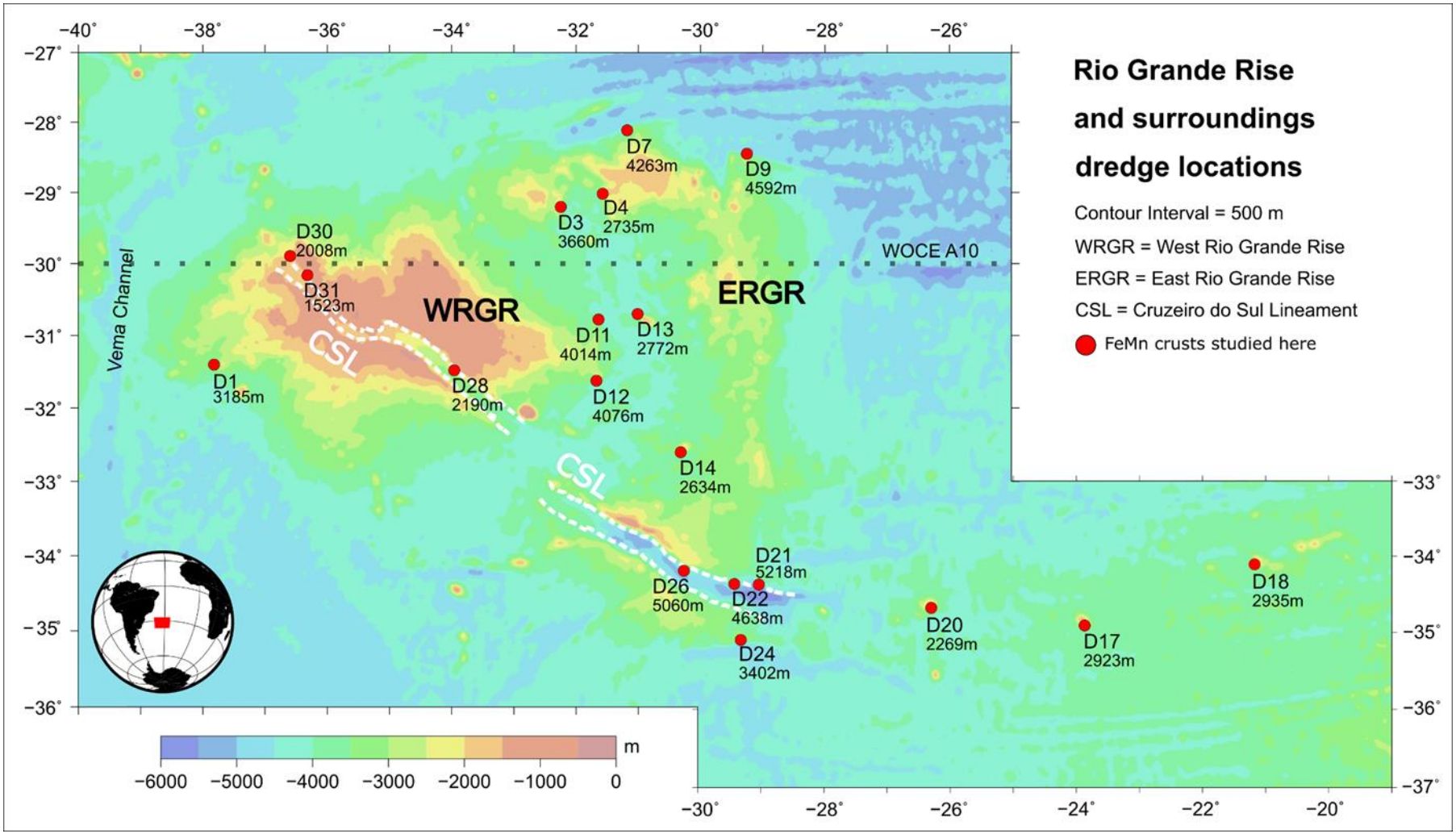

Figure 1: Topography of RGR area showing the location of dredges from cruise NBP1808 (red dots) followed by the water depth. Dashed white lines represent the Cruzeiro do Sul Lineament (CSL). Dashed black line displays the A10 transect from World Ocean Circulation Experiment (WOCE). WRGR = West RGR; ERGR = East RGR.

5.2.2 Modern oceanographic conditions at RGR

The wide range of water depths of FeMn crusts studied here (1500 – 5000 m) and by Benites et al. (2020) and Jovane et al. (2019) (600 – 800 m) includes samples bathed by multiple water masses with different temperatures, dissolved oxygen contents, and nutrient contents. The South Atlantic Central Water (SACW; 100 - 600 m) comprises a local oxygen minimum of ~4.7 mL/L O_2. Below it, the Antarctic Intermediate Water (AAIW; 600 – 1100 m) is nutrient-rich and comprises an oxygen maximum of ~5.1 mL/L O_2 at around 800–900 m. The Upper Circumpolar Water (UCPW; 1100 – 1600 m) marks a second local oxygen minimum of ~4.2 mL/L O_2 and a silicate and phosphate maximum. The North Atlantic Deep Water (NADW; 1600 – 3500 m) is oxygenated, but nutrient-poor. Finally, the Antarctic Bottom Water (AABW; >3500m) is a cold high density well-oxygenated water mass with potential temperature < 0.2°C below 4000 m and close to 0°C around 5000 m (da Silveira et al., 2020; Reid et al., 1977; Stramma and England, 1999).

5.3 Material and methods

5.3.1 Samples

FeMn crusts were dredged from the seafloor during the NBP1808 cruise onboard the R/V Nathaniel B. Palmer (Cruise DOI: 907974) from 3 October to 12 December 2018 and provided to us by the Marine and Geology Repository, Oregon State University, USA. Twenty-two samples were used in this work from 19 dredge hauls from water depths between 1523 and 5218 m and locations ranging from the plateau of WRGR to seamounts east of the ERGR (Figure 1). Samples were cut into slices onboard and subsampled afterwards at the laboratory using a chisel.

For mineralogical and chemical composition analyses, 18 hand samples were selected from which seven hand samples were subsampled into two or three layers, and the remaining 11 hand samples were not subsampled (Figure 2), resulting in 11 bulk crusts and 16 crust layers for a total of 27 samples (Table 1). Layers were differentiated based on macroscopic changes in crust color, texture, density and/or porosity of the crusts. The subsamples were ground to a fine powder in an automatic mill inside an agate bowl. In addition, polished thin sections of 12 FeMn crust samples were prepared for petrographic observations and chemical microanalyses.

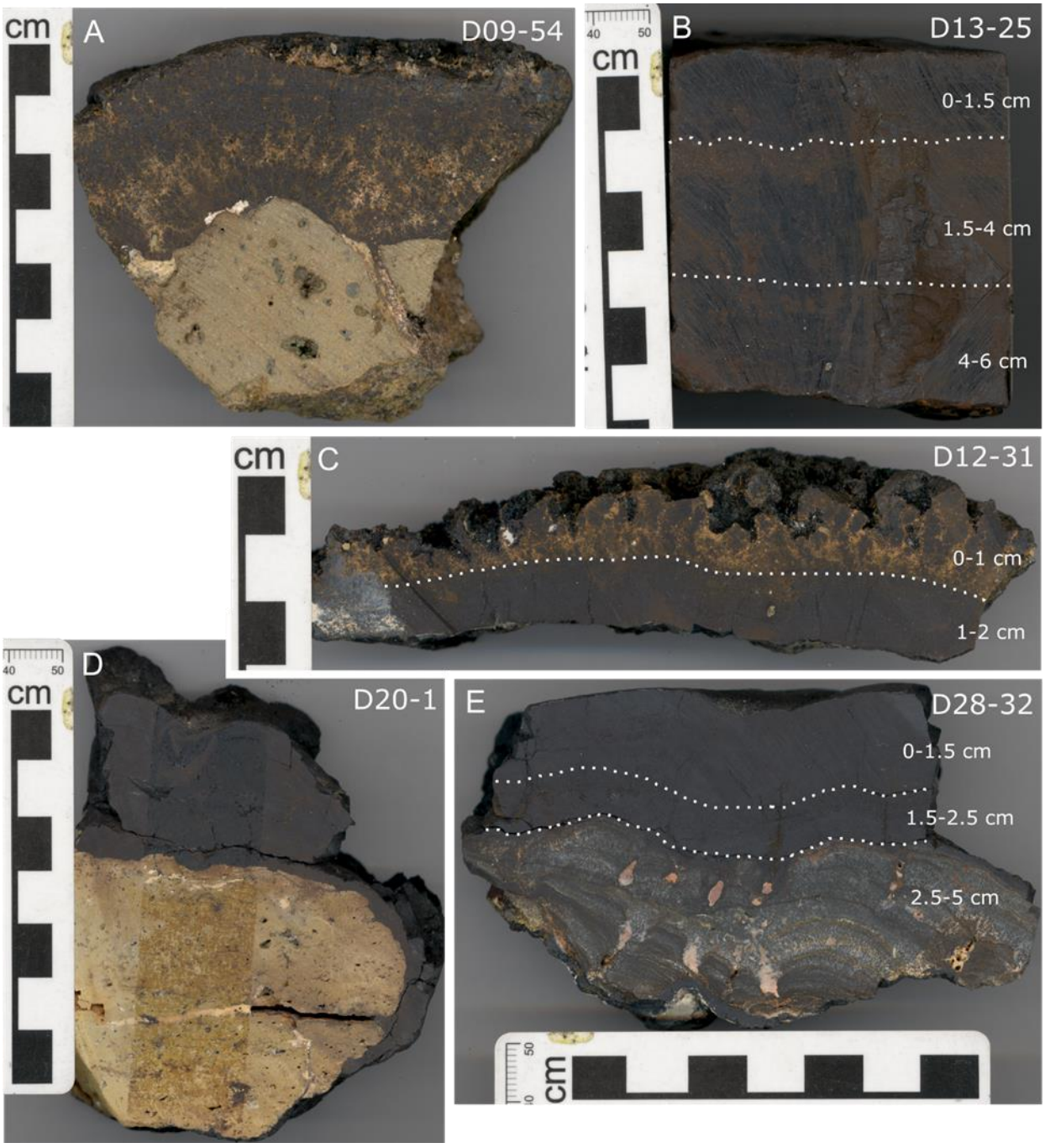

Figure 2: FeMn crust samples from cruise NBP1808 used in this study. (A) Sample D9-54 contains entrained detrital material and basaltic substrate; (B) The thickest sample D13-25 (6 cm) was subsampled in three layers; (C) Sample D12-31 has two layers of different colors, detrital material content, and texture. Note the pristine upper surface; (D) Sample D20-1 is homogenously black and fractured and has a volcanic rock substrate; (E) Sample D28-32 has two generations of FeMn crust, phosphatized lower layer covered by two non-phosphatized layers.

Table 1: Sample list with sample type, sampling interval, geographic coordinates, water depth, and mineral composition. The growth rate (GR) was determined using the Co-chronometer of Manheim and Lane-Bostwick (1988). Calculated ages are based on the GR and thickness of samples in mm.

Sample ID	Type	Interval (mm)	Latitude	Longitude	Water depth (m)	Substrate rock	Principal minerals	Accessory minerals	GR (mm/Myr)	Age* (Myr)
D1_1	bulk	0-6	-31.400	-37.820	3185	phosphorite	vernadite, goethite	quartz, todorokite	3.00	2.00
D3_11	bulk	?	-29.200	-32.240	3660	not present	vernadite, goethite	quartz, feldspars	1.11	-
D4_13	thin section	0-20	-29.020	-31.570	2735	phosphorite	-	-	-	-
D4_19	bulk	0-20	-29.020	-31.570	2735	phosphorite	vernadite, goethite	-	1.41	14.2
D5_2	thin section	0-22	-28.700	-32.110	2855	volcanic rock	-	-	-	-
D7_25	bulk	0-25	-28.110	-31.180	4263	volcanic rock	goethite; quartz	vernadite, feldspars, clay minerals(?)	2.48	10.1
D9_7A	layer	0-10	-28.110	-31.180	4592	volcanic rock	vernadite, goethite	quartz, feldspars, clay minerals(?)	2.23	4.48
D9_7B	layer	10-30	-28.450	-29.250	4592	volcanic rock	vernadite, goethite	quartz, feldspars, clay minerals(?)	2.57	12.3
D9_54	thin section	0-27	-28.450	-29.250	4592	volcanic rock	-	-	-	-
D11_2	bulk	0-8	-30.780	-31.640	4014	phosphorite	vernadite, goethite	quartz, feldspars, clay minerals(?)	1.34	5.99
D12_31A	layer/thin section	0-10	-30.780	-31.640	4076	volcanic rock	vernadite, goethite, quartz	feldspars	2.63	3.80
D12_31B	layer/thin section	10-20	-31.620	-31.670	4076	volcanic rock	vernadite, goethite	quartz, feldspars	3.45	6.70
D12_41	thin section	0-30	-31.620	-31.670	4076	not present	-	-	-	-
D13_25A	layer	0-15	-31.620	-31.670	2772	not present	vernadite, goethite	calcite	0.98	15.2
D13_25B	layer	15-40	-31.620	-31.670	2772	not present	vernadite, goethite	calcite(?)	1.24	35.5
D13_25C	layer	40-60	-30.700	-31.010	2772	not present	vernadite, goethite	-	1.64	47.7
D14_1A	layer	0-10	-30.700	-31.010	2634	volcanic rock	vernadite, goethite	quartz	0.94	10.7
D14_1B	layer	10-20	-32.600	-30.320	2634	volcanic rock	vernadite, goethite	calcite	0.98	20.9
D16-7	thin section	0-15	-34.670	-26.240	2405	volcanic rock	-	-	-	-
D17_5	bulk	0-12	-34.920	-23.890	2923	volcanic rock	vernadite, goethite	quartz, feldspars, calcite	1.50	8.02
D17-8	thin section	0-10	-34.920	-23.890	2923	volcanic rock	-	-	-	-
D18_6	bulk	0-6	-34.150	-21.170	2935	volcanic rock	vernadite, goethite	quartz, feldspars	1.33	4.50
D20_1	thin section	0-27	-34.690	-26.290	2269	volcanic rock	-	-	1.63	6.15
D20_6A	layer	0-10	-34.690	-26.290	2269	not present	vernadite, goethite	quartz	1.74	14.8

D20_6B	layer	10-25	-34.690	-26.290	2269	not present	vernadite, goethite	quartz, feldspars	-	-
D21_8	bulk	0-30	-34.380	-29.060	5218	volcanic rock	goethite, quartz	feldspars, vernadite, 10Å phyllomanganates	4.65	6.45
D21-14	thin section	0-25	-34.380	-29.060	5218	phosphorite	-	-	-	-
D22_31	bulk	0-10	-34.380	-29.450	4638	volcanic rock	goethite, vernadite, quartz	feldspars, clay minerals(?)	3.18	3.14
D24_1	bulk	0-20	-35.120	-29.350	3402	volcanic rock	vernadite, goethite	quartz, feldspars, 10Å phyllomanganates	0.88	22.7
D26_4	bulk	0-25	-34.200	-30.260	5060	volcanic rock	vernadite, goethite	quartz, feldspars	0.86	29.1
D26-39	thin section	0-35	-34.200	-30.260	5060	not present	-	-	-	-
D28_32A	layer	0-15	-34.200	-30.260	2190	not present	vernadite, goethite	quartz, 10Å phyllomanganates	1.31	11.5
D28_32B	layer	15-25	-34.200	-30.260	2190	not present	vernadite, goethite	quartz, calcite, 10Å phyllomanganates	1.15	20.1
D28_32C	layer	25-50	-31.480	-33.950	2190	not present	CFA, calcite	todorokite, magnetite	1.99	32.7
D30_34A	layer	0-10	-31.480	-33.950	2008	volcanic rock	vernadite, goethite	-	0.79	12.6
D30_34B	layer	10-20	-29.890	-36.590	2008	volcanic rock	vernadite, goethite	-	0.89	23.9
D31_9	thin section	0-35	-30.160	-36.310	1523	not present	-	-	-	-
D32-5	thin section	0-17	-30.190	-36.280	1505	phosphorite	-	-	-	-

5.3.2 Analytical methods

5.3.2.1 X-ray Diffraction

FeMn crust powdered samples were mounted in zero background sample holders and inserted in a PANalytical X'Pert PRO X-ray diffractometer from Malvern Panalytical with Cu-Kα radiation, carbon monochromator and automatic slit (PTRX-004) at the Central Laboratories of the Geological Survey of Spain (IGME-CSIC). Samples were scanned from 2° to 70° (2θ) at a step size and time of 0.0170° and 0.5 °/min, respectively. Measurements were performed at 40 kV and 30 mA using a curved graphite secondary monochromator. The diffractograms were processed and interpreted using the HighScore software from PANalytical loaded with the ICDD database. Six samples were thermally treated at 300°C for 24 h and were reanalyzed to verify the collapse of 10 Å manganese oxide minerals.

4.3.2.2 Chemical composition

A variety of analytical procedures were applied to determine the chemical composition of powdered FeMn crust samples at the Central Laboratories of the Geological Survey of Spain (IGME-CSIC).

The major elements Fe, Mn, Si, Al, Mg, Ca, K, Ti, and P were determined by X-ray Fluorescence (XRF) on fused disks prepared with lithium metaborate using a PANalytical ZETIUM spectrometer with a rhodium tube and SuperQ software. A calibrated XRF protocol for Fe oxides was used. The analyses were performed at 50 kV voltage and 50 mA current. The international reference material NOD-A-1 (USGS) was analyzed to determine the accuracy of the analyses. Sorbed water and loss on ignition (LOI) were determined by heating at 105° and 950°C, respectively. Lithium, Na, Co, and Ni were determined by inductively coupled plasma – atomic emission spectroscopy (ICP-AES) using a VARIAN VISTA-MPX spectrometer on sample solutions prepared by fusion with lithium metaborate followed by acid digestion.

The trace elements Be, V, Cr, Cu, Zn, As, Mo, Ag, Cd, Sb, Tl, Th, and U, as well as the rare earth elements La, Ce, Pr, Nd, Sm, Eu, Gd, Tb, Dy, Ho, Er, Tm, Yb, and Lu plus Y (REY) were determined by triacid digestion inductively coupled plasma mass spectrometry (ICP-MS). The ICP-MS measurements were performed in an AGILENT 7900 CE spectrometer, and several standard materials (GBW07103, GBW07105 GBW07108, Geopt 22, TMDA-62.3, and TM 9.2) were used to validate the analytical procedure. Quality Control was determined by participation in the international proficiency test GeoPT program organized by the International Association of Geoanalyst (IAG). Moreover, certified reference materials were analyzed during routine laboratory work on a regular basis. The precision obtained during chemical analyses

was lower than 10% and the accuracy was in the range of 90–110% for most studied elements. All chemical element, except H2O- and LOI, concentrations were normalized to 0% sorbed water.

Multivariate statistical methods applied to the chemical dataset consisted of a correlation matrix and factor analysis; Li was excluded from both due to values below the detection limit. A Pearson correlation coefficient matrix was generated using R Studio. Correlations between chemical composition of FeMn crusts with geographic location, water depth, latitude, and longitude were included to the correlation matrix. Q-mode factor analyses was performed to identify common groups of elements (factors) using MATLAB according to the procedures of Pisias et al. (2013). Each variable was scaled to the percent of the maximum value and factors were derived from orthogonal rotations of principal component eigenvectors using the Varimax method (Klovan and Imbrie, 1971). The communality values, a measure of how efficient the reduced set of factors is on accounting for the original variance, for all samples are > 0.98. Factor scores between -0.13 and +0.13 are not statistically significant and were discarded. Together with the mineralogy and correlation of elements, the factors are interpreted to represent one specific mineral phase or group of minerals that host the elements contained in that factor.

The Co-chronometer empirical equations of Manheim and Lane-Bostwick (1988) (Eq.1) were used to calculate the growth rates and minimum ages of non-phosphatized FeMn crusts:

$GR = 0.68/Co_n^{1.67}$, where $Co_n = Co * (50/Fe + Mn)$ (Eq.1)

This method assumes that Co supply to the ocean is constant and that Co incorporation in the FeMn crusts is solely hydrogenetic. The Co empirical equations have been extensively used in the past decades and have been shown to generally provide age estimates consistent with isotopic age dating methods (Frank et al., 1999; Josso et al., 2019; Yi et al., 2020). However, they are unable to account for potential hiatuses and erosion during crust growth; therefore, the resulting growth rates should be taken as maximum estimates and derived ages taken as minimum estimates (Hein et al., 1990). The equation of Manheim and Lane-Bostwick is used instead of the equation of Halbach and Puteanus (1988) because the Co contents of samples are <0.7%.

4.3.2.3 Petrography and chemical microanalyses

The microstructure of FeMn crusts was observed on polished thin sections under reflected light using a DM2700P Leica microscope coupled to a DFC550 digital camera. Three

thin sections were selected for chemical microanalyses. For this, they were carbon-coated and analyzed by Electron Microprobe (EPMA) in a JEOL JXA-8900M WDS/EDS microanalyzer composed by 4 wavelength dispersion spectrometers with crystals TAP, LIF, PETJ, PETH, at the Centro Nacional de Microscopía Electrónica, Complutense University of Madrid (CNME-UCM), Spain. The WDS measurements were performed at 15 kV, 20 nA, with a spot size of 5 µm, for 10 s per peak and 5 s per background. Corrections were made applying a ZAF matrix. Certified standards used comprised pure metals and natural and synthetic minerals (Al – sillimanite; Mn, Fe – almandine; P – apatite; Sr – strontianite; Na, Si – albite; Ti, Mg – kaersutite; Ca – dolomite; pure Mo, Ni, Cu, Co, and Zn; Pb – galena; Ba – benitoite; K – microcline; V - vanadinite). Accuracy and precision were better than ± 5%.

An EPMA transect along the growth axis of sample D20-1 was performed every 0.3 mm, totalizing 106 microanalyses. The Co contents acquired by EPMA were also used to calculate the growth rates of the microlayers using equation 1.

5.4 Results

5.4.1 Structure of deep-water FeMn crusts from RGR and surrounding seamounts

The FeMn crusts are 6 to 60 mm thick and predominantly black (Figure 2). Under the microscope, some samples show shades of brown marking the patchy accumulation of detrital grains or following the entire extent of a layer (Figure 2A and C). Other samples are fractured with a submetallic luster (Figure 2D). Pervasive impregnation by CFA occurs in the lower part of crust D28-32(C) as whitish haze (Figure 2E) and in D31-9. The substrate of the deep-water FeMn crusts is predominantly altered volcanic rock, in some samples very fractured and altered with the presence of a pale brown loose material that was incorporated by the overlying crusts, probably a product of alteration of the volcanic rock. Phosphorite also occurs as substrate rock for crusts and some samples were collected without their substrate rock. The surface of all samples is abraded to different degrees, but ablation is more intense in samples from shallower depths (Supplementary Material SM1). Sample D3-11 has no information on thickness, substrate rock, surface texture, and cross section aspects because it was already broken into small fragments when taken from the OSU repository.

5.4.2 Mineralogy

Three groups of Mn oxides were identified in the FeMn crusts by XRD:

(1) No basal reflection and diagnostic reflections at 2.45Å and 1.42Å, corresponding to the disordered phyllomanganate vernadite (Lee et al., 2019), as known as □-MnO2;

(2) Basal reflections around 10Å and 5Å, corresponding to 10Å phyllomanganates, can be disordered 10Å vernadite, ordered buserite or asbolane, or a mixture of those (Kuhn et al., 2017; Manceau et al., 1992). This identification is supported by the collapse of the 10Å reflection after thermal treatment of the sample at 300°C (Novikov and Bogdanova, 2007; Wegorzewski et al., 2015);

(3) Reflections at 10Å and 5Å that do not collapse after thermal treatment at 300°C, corresponding to the tectomanganate todorokite (Kuhn et al., 2017; Novikov and Bogdanova, 2007; Wegorzewski et al., 2015).

Vernadite is the main Mn phase in the FeMn crusts studied and, together with goethite, compose most of the sample content (Table 1). Five samples show a small reflection at 10Å, three of which (samples D21-8, D24-1, D28-32B) collapsed after the thermal treatment and therefore is a 10Å phyllomanganate (Figure 3). However, the 10Å reflection did not collapse after the thermal treatment of samples D1-1 and D28-32C and is therefore todorokite (Figure 3). The 10Å phyllomanganates and todorokite are accessory minerals in the samples mentioned, i.e., present in a minor amount. Other accessory minerals include quartz, feldspars (e.g., albite, anorthite, labradorite), calcite, and possibly clay minerals. Samples D7-25, D12-31A, D21-8, and D22-31 have substantially more aluminosilicates (quartz and feldspars).

The impregnation by phosphate of sample D28-32C was confirmed by its predominant CFA composition and calcite by XRD, with todorokite and magnetite as accessory minerals and no aluminosilicate minerals. Thus, samples D28-32C resembles a phosphorite rock, similar to the first generation of crusts from the summit of RGR.

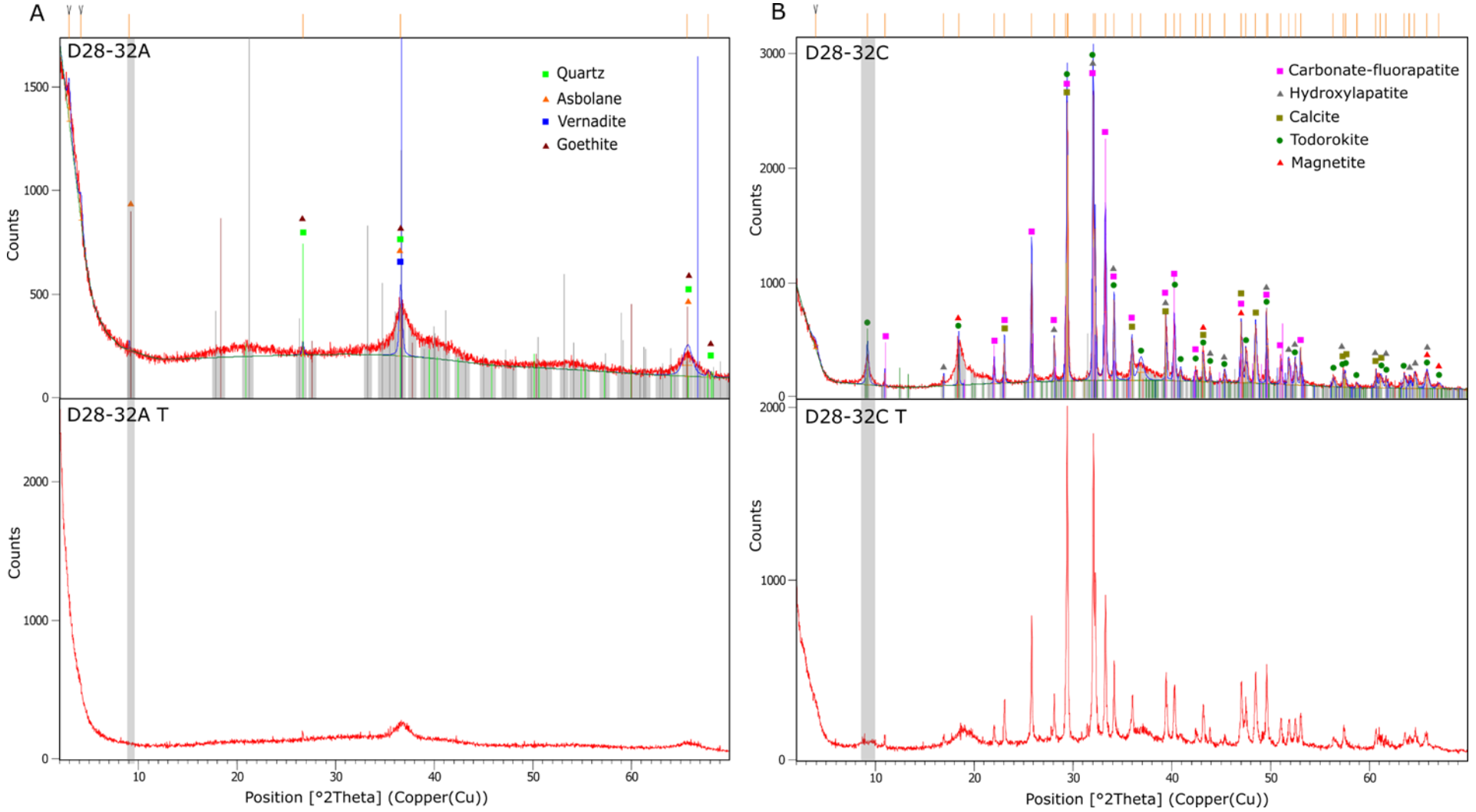

Figure 3: XRD scans of samples 28-32A and 28-32C before and after heating (T) to 300°C. Note that the peak at the 10 Å region completely collapses in sample 28-32A but not in sample 28-32C.

5.4.3 Chemical composition

5.4.3.1 Major elements

The complete chemical composition dataset is given in the Supplementary Materials (SM2). The phosphatized sample D28-32C is discussed separately because its composition is different from the other 26 samples. The 11 bulk and 15 layers of FeMn crusts are composed by subequal Fe and Mn contents, varying from 12.8 to 24.4% (mean 18.6%) and 13.1 to 25.8% (mean 21%), respectively (Table 2). The Fe/Mn ratios are between 0.64 and 1.51 and average 0.93, typical of hydrogenetic FeMn precipitation. Aluminosilicate-related elements are highly variable, ranging from 1.46 - 11.8% Si (mean 4.28%), 0.57 - 4.64% Al (mean 1.86%), 1.29 – 1.92% Na (mean 1.55%), and 0.35 – 1.19% K (mean 0.50%). Samples D7-25, D12-31A, D21-8, and D22-31 have the highest concentrations of Si and Al, reflecting the abundant quartz and feldspars. Samples D7-25, D9-7A, D9-7B, D18-6, and D21-8 have the highest Na and high contents of Si and Al, reflecting the presence of Na-rich feldspars (albite to labradorite). The P content varies from 0.34 to 0.71% (mean 0.47%), typical of non-phosphatized FeMn crusts. The Ca content of 1.91 – 3.30% (mean 2.54%) reflects the presence of calcite and feldspars as minor phases in some samples.

The phosphatized sample D28-32C has considerably more Ca (25.3%) and P (6.11%) and less Fe (4.73%) and Mn (9.27%), including only 2.2% sorbed water versus 19.8% on average in the other crusts; this is consistent with a significant CFA and minor calcite content of a phosphorite rock.

5.4.3.2 Trace metals

The trace metals of greatest economic importance in FeMn crusts are Co, Ni, and Cu: Co varies from 2112 to 9978 ppm (mean 6411 ppm); Ni from 1600 to 3996 ppm (mean 2390 ppm Ni); and Cu from 274 to 1239 ppm (mean 591 ppm). The sum of REE+Y is equally highly variable from 1941 to 3193 ppm (mean 2670 ppm). Other trace metals of economic interest include mean 953 ppm V (545 – 1164 ppm), 525 ppm Mo (120 – 749 ppm), 355 ppm As (135 – 465 ppm), 51 ppm Sb (28 – 68 ppm), 3.8 ppm Cd (2.7-5.5 ppm). Other metals with high concentration are 143 ppm Tl (16 – 242 ppm) and 58 ppm Th (28 – 103 ppm). Sample D30-34 has the highest Co content and the lowest Cu content, while being the shallowest sample studied. On the other hand, the lowest Co content is the deepest water sample studied, D21-8, which also has the lowest contents of As, Sb, Tl, and U, and highest contents of Li, Cu and Cd. Thus, a relationship with water depth is apparent for these elements.

The phosphatized sample D28-32C has extremely low contents of most trace metals (Be, V, Co, As, Mo, Ag, Sb, Th, all REE), but extremely high contents of Li, Y, and the percentage of heavy REE out of total REE (%HREY) compared to the other 26 samples.

Table 2: Summary statistics of chemical composition of FeMn crusts from Table S1 (2008 m to 5218 m), RGR and surrounding seamounts. Phosphatized sample D28-32C is presented separately.

	N	min	max	mean	St dev.	Relative St. Dev.	range	D28-32C
Si (%)	26	1.46	11.8	4.36	3.10	71.2%	10.3	2.24
Al	26	0.57	4.64	1.86	1.12	60.1%	4.07	1.31
Fe	26	12.8	24.4	18.6	2.48	13.3%	11.7	4.73
Ca	26	1.91	3.30	2.54	0.36	14.3%	1.38	25.3
Ti	26	0.91	1.54	1.21	0.15	12.2%	0.63	0.15
Mn	26	13.1	25.8	21.0	3.79	18.1%	12.7	9.27
K	26	0.35	1.19	0.50	0.20	40.3%	0.84	0.43
Mg	26	1.21	1.65	1.36	0.10	7.39%	0.45	1.68
P	26	0.34	0.71	0.47	0.08	17.7%	0.38	6.11
Na	26	1.29	1.92	1.55	0.18	11.6%	0.63	0.77
H2O[1]	26	14.1	23.3	19.8	2.52	12.7%	9.12	2.24
LOI[2]	26	26.3	38.4	34.6	3.44	9.94%	12.1	20.0
Fe/Mn	26	0.64	1.51	0.93	0.25	27.3%	0.87	0.51
Si/Al	26	1.66	2.90	2.28	0.36	15.9%	1.24	1.71
Be (ug/g)	26	4.79	9.99	7.46	1.45	19.5%	5.20	1.52
Li	26	17.0	52.8	19.4	7.4	38.2%	35.8	98.9
V	26	545	1164	953	181	19.0%	619	269
Co	26	2112	9978	6411	2164	33.7%	7867	1476
Ni	26	1600	3996	2390	493	20.6%	2396	3575
Cr	26	5.67	33.1	15.0	6.69	44.5%	27.4	12.1
Cu	26	274	1239	591	262	44.3%	965	564
Zn	26	463	783	628	80.1	12.7%	320	485
As	26	135	465	355	86.1	24.2%	330	76.9
Mo	26	219	749	525	179	34.1%	530	120
Ag	26	0.08	0.16	0.10	0.02	18.2%	0.08	0.02
Cd	26	2.66	5.49	3.81	0.66	17.3%	2.83	4.83
Sb	26	28.2	68.4	50.9	10.3	20.2%	40.2	16.2
Tl	26	16.1	242	143	54.6	38.2%	226	69.1
Th	26	28.0	103	57.6	20.7	35.8%	74.6	3.38
U	26	5.86	16.5	12.8	2.50	19.5%	10.7	6.06
Y	26	101	199	155	24.5	15.8%	97.7	288
La	26	164	358	275	50.0	18.2%	193	139
Ce	26	1264	2183	1696	284	16.7%	920	109
Pr	26	39.4	72.2	56.5	8.89	15.7%	32.8	19.8
Nd	26	169	312	243	39.3	16.2%	143	93.8
Sm	26	38.3	63.9	52.1	7.70	14.8%	25.6	18.7
Eu	26	8.75	14.7	12.0	1.78	14.9%	5.94	4.62
Gd	26	41.1	70.0	56.3	8.29	14.7%	28.9	26.4
Tb	26	5.92	10.2	8.27	1.19	14.4%	4.28	3.80
Dy	26	32.9	58.6	46.9	6.84	14.6%	25.7	25.6
Ho	26	6.63	11.89	9.33	1.40	15.0%	5.26	6.40
Er	26	19.8	34.9	27.6	4.08	14.8%	15.1	21.3
Tm	26	2.85	4.88	3.96	0.56	14.1%	2.03	2.96
Yb	26	17.8	30.8	25.2	3.52	14.0%	13.0	18.7
Lu	26	2.60	4.50	3.69	0.52	14.1%	1.91	2.97
∑REY[3]	26	1941	3193	2670	322	12.1%	1251	782

HREY[4]	26	8%	17%	13%	2%	16.8%	8.90%	51.3%

[1]Sorbed water

[2]Loss on Ignition

[3]Summation of the rare earth elements plus Y

[4]Percentage of the heavy rare earth elements out of total REY

5.4.4 Microstructure and high-resolution chemical composition

The FeMn crusts present laminated, columnar, botryoidal, dendritic, and mottled textures. In general, the black FeMn crusts have a columnar texture (Figure 4A). However, areas with detrital material (pale brown) have a dendritic-mottled texture (Figure 4B). Erosional surfaces occur between some layers. Within the area with accumulation of detrital material, erosion of individual botryoids also occurs (Figure 4C). The botryoids are usually hydrogenetic (Figure 4D and G, points 4 and 7) with Fe/Mn from 0.76 to 1.60, surrounded by aluminosilicates (Figure 4D and G point 5) and other detrital minerals, e.g., Ti oxide (probably rutile or anatase from volcanic rock) (Figure 4E and G point 10). However, extremely bright Fe-rich lamina are found on the contours of the botryoids in contact with the detrital material (Figure 4D and G points 3 and 9), with strong fractionation between Fe (mean 40%) and Mn (< 1%, but as low as 0.17%). Thus, some process at the contact between hydrogenetic botryoids and detrital material favors the nearly sole enrichment of Fe oxides.

The phosphatized portion of D31-9 has alternating laminated and botryoidal textures, while the top non-phosphatized section is mottled. Chemical mapping of a structure in the phosphatized section (Figure 4H and I) shows Mn and Ni-rich lamina with no Fe, indicating the precipitation of diagenetic Mn oxide. Likewise, Mn-rich Fe-poor lamina (39% Mn and 1% Fe) with Fe/Mn of 0.02 also occurs within vesicles of the volcanic rock substrate of D09-54 (Figure 4F and G, points 12 and 13).

The EPMA transect along the growth axis of sample D20-1 (Figure 5) reveals that Fe/Mn ratios remained between 0.40 and 1.36, meaning a hydrogenetic origin for its entire history. The Fe/Mn ratio was higher at the base of the crust because Fe content was higher rather than Mn being lower, accompanied by higher P and Si but lower Ni. Mn, Co, and Mo decrease in the uppermost 7.5 mm of the crust, while Al shows a significant enrichment towards the top accompanied by a slight increase of Si. Thus, environmental conditions must have changed during the formation of the uppermost 7.5 mm of the crust.

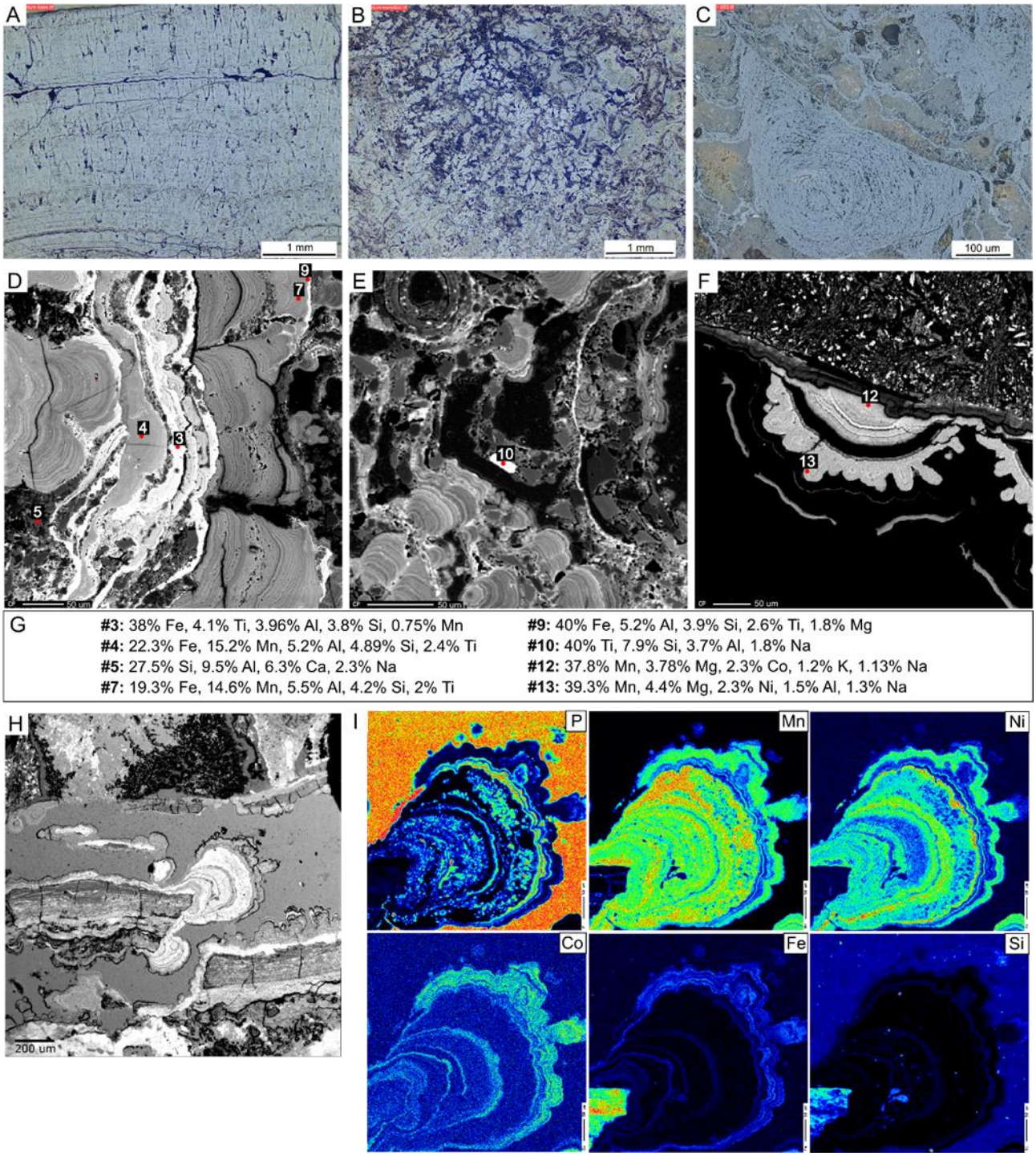

Figure 4: Optical microscope images of (A) laminae with columnar texture; (B) transition from columnar (lower left lamina) to dendritic or acicular central lamina to mottled texture (upper right lamina); and (C) individual botryoid or nodule surrounded by detritus and fracture fill stringers; the central nodule was truncated by a fracture or erosion. EPMA images of (D) hydrogenetic Fe-rich (bright, points 3, 9) and Mn-rich (gray with finer laminations, points 4, 7) surrounded by detrital material (point 5); (E) a Ti mineral (rutile or anatase) among detrital material; and (F) Mn-oxide lamina (points 12 and 13) within basalt substrate. (G) EPMA chemical composition of the points 3 through 13 displayed in previous images. (H) EPMA image and (i) chemical mapping of a diagenetic structure of Mn oxide within the phosphatized portion of sample D31-9, showing several episodes of overgrowths cemented by CFA.

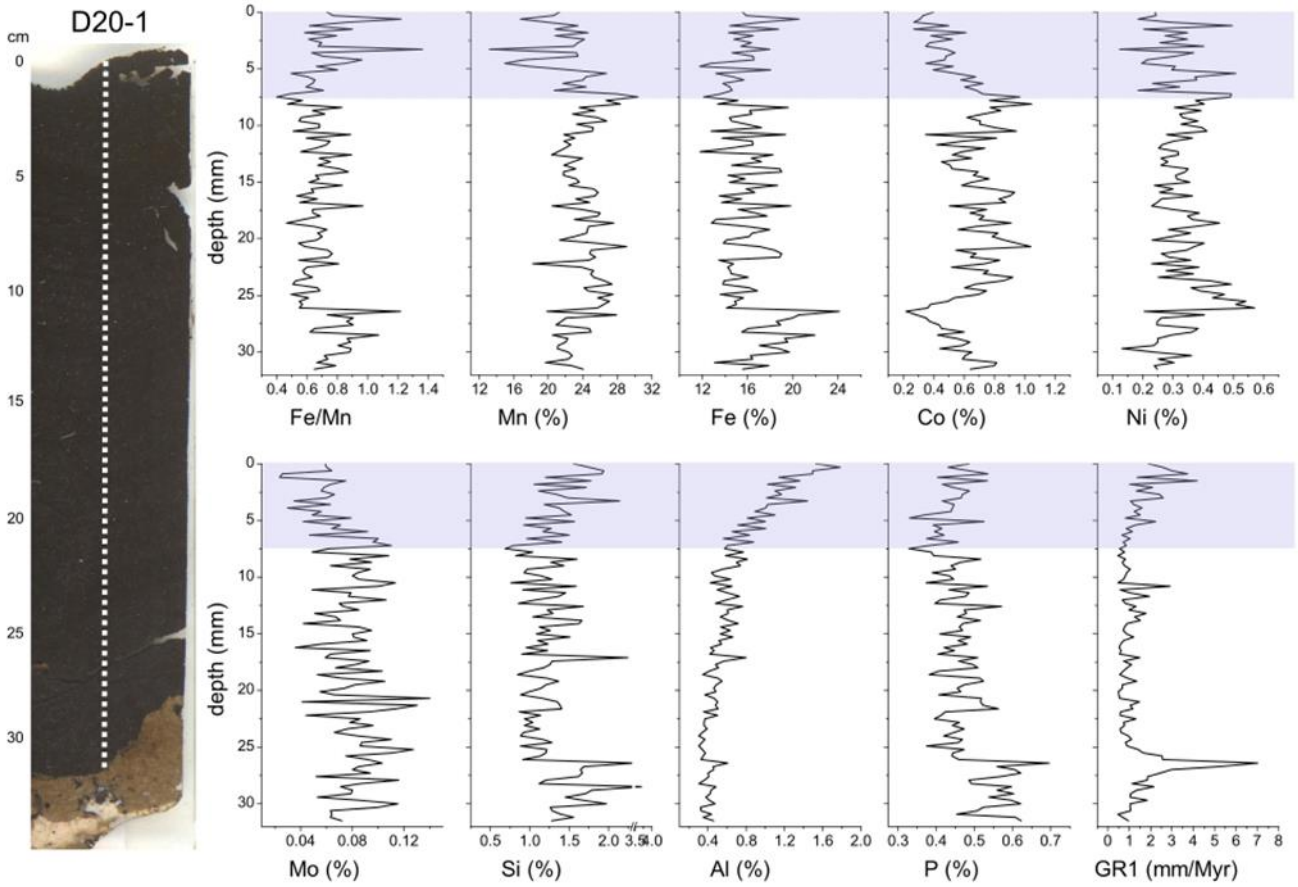

Figure 5: EPMA transect along the growth axis of sample D20-1. GR1 = growth rate as calculated from the Co-chronometer equation of Manheim and Lane-Bostwick (1988). The two shaded bars represent the uppermost 7.5 cm with Mn, Co, Ni, and Mo decrease and Fe, Si, Al, and growth rates increase towards the top.

5.4.5 Growth rates and calculated ages

The growth rates calculated from equation 1 (see Methods section) for bulk and layers of the FeMn crusts vary from 0.79 to 4.65 mm/Myr, mean 1.77 mm/Myr (Table 1). The growth rates calculated from Co content data from the EPMA transect of sample D20-1 vary from 0.46 to 7.02 mm/Myr (mean 1.31 mm/Myr).

Considering the stratigraphic layers of subsampled FeMn crusts, the growth rates decrease with time in samples D9-7, D12-31, D13-25, D14-1, D20-6, D28-32 (C to B), and D30-34, although some of them are similar and probably within error. The growth rate increases with time only for D28-32B to D28-32A, but that also may be within error. The EPMA transect for D20-1 shows an increasing growth rate towards the top only in the uppermost 7.5 mm, coinciding with decreasing Co.

Growth rates and thicknesses of samples were used to estimate the ages of initiation of FeMn crust growth. The oldest FeMn crust is D13-25 yielding an age of 47.6 Ma. The

initiation age of the non-phosphatized layer D28-32B is 20.1 Ma, indicating the minimum age of phosphatization of the underlying layer D28-32C.

5.4.6 Correlation matrix, scatter plots, and Q-mode factors

The correlation matrix is in the Supplementary Material (SM3) and all correlation coefficients reported in the next lines are significant at the 99% confidence level (CL) which is > 0.48 for n=26. The phosphatized sample D28-32C was excluded from the correlation matrix calculation because of its singular composition. The only significant correlation coefficient between chemical elements and latitude is with Fe, which is rather weak (r = 0.53), suggesting that Fe content of FeMn crusts may increase to the north. No significant correlation was found between longitude and chemical elements. Si, Al, K, Cu, and Th are strongly correlated with water depth (r > 0.74), while Ca, Mn, P, V, As, Mo, Tl, and U (r < -0.74), and Co, Ni, Zn, Sb, (r < -0.74 to -0.57) show negative correlations with water depth. Positive correlations exist between aluminosilicate elements (Si, Al, K, Na) and the trace elements Cu, Th, and Cd, while they all show negative correlation with Ca, Mn, P, V, Co, Zn, As, Mo, Tl, U, and La (r < -0.70). Mn correlates well with Mo (r = 0.96), Ca, V, Co, Ni, As, Tl, U, La (r > 0.70), P and Zn (r > 0.60); Mn shows negative correlations with the aluminosilicate elements, Cu, and Th. No significant correlation occurs between Fe and other elements except for Be (r = 0.51). The correlations of Si, Al, Cu, Th, Mn, Co, V, As, Ni, Mo, P, and growth rates with water depth is better visualized in the scatter plots with linear regression (Figure 6).

The Q-mode factor analysis based on all 27 samples and 4 factors accounts for 99.1% of the variance (Table 3). The first factor corresponds to 53.2% of the variance and is composed of Mo, As, Co, Tl, V, Mn, U, Be, Sb, Ti, Zn, and the REE except Ce; we interpret this factor to represent the hydrogenetic Mn-oxide phases. The second factor accounts for 33.9% of the variance and is composed of Si, Al, Th, Cu, K, Na, Ag, Cd, Fe, Cr, Ce, Ti, Eu, and Sm; we interpret this factor to represent the aluminosilicate and associated elements. The third factor accounts for 11.2% of the variance and is composed of P, Ca, Y, Ni, Mg, Cd, Zn, Lu, Er, Tm, and Yb; we interpret this factor to represent calcite and carbonate fluorapatite and its presence is dominant in the phosphatized sample D28-32C. The fourth factor accounts for 0.8% of the variance and is composed of Tl, Cr, Sb, Cd, Ni, Ce, V, Zn, Mn, and Mg; we interpret this factor to represent the minor amounts of 10Å manganates identified by XRD.

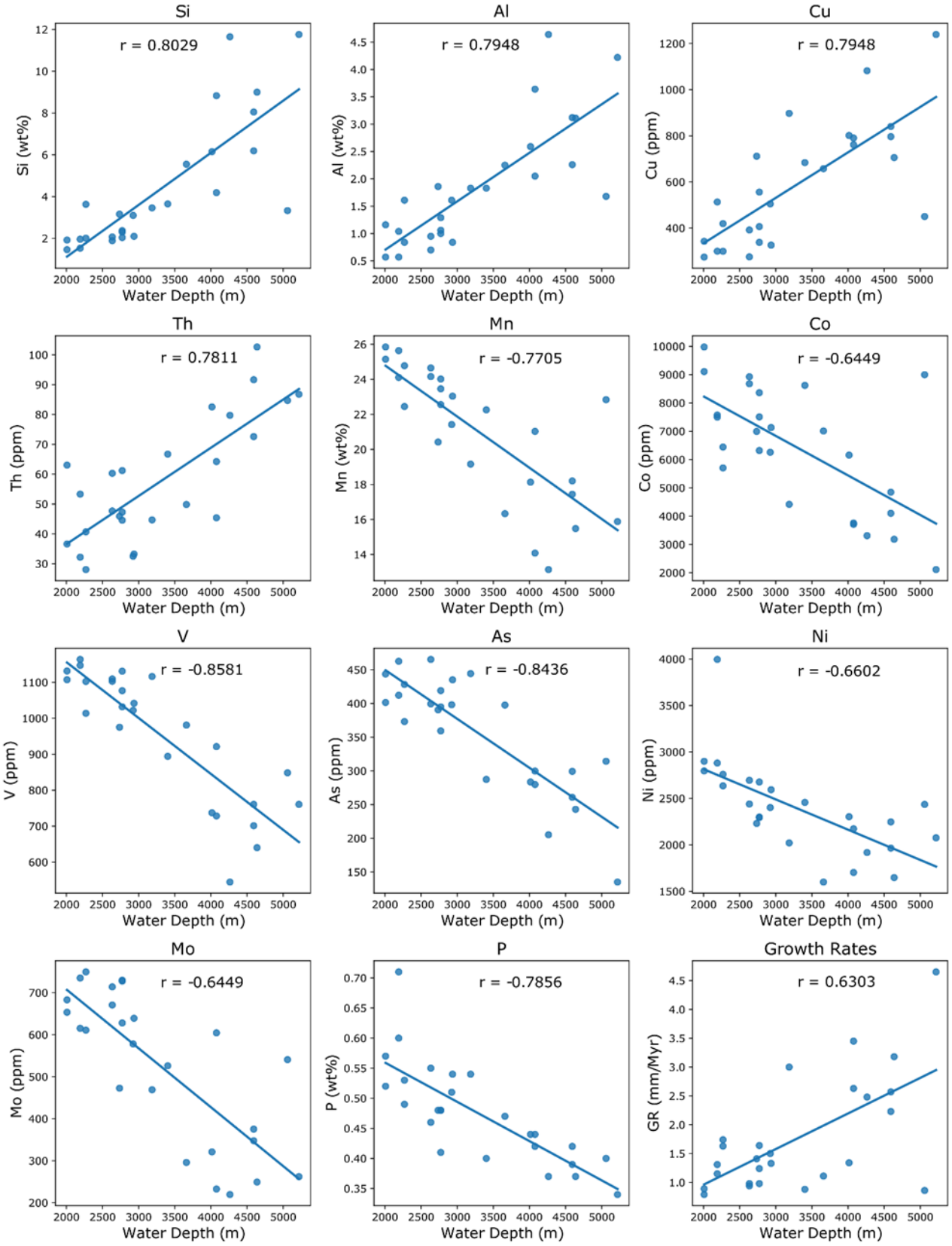

Figure 6: Scatter plots of elements in the FeMn crusts versus water depth with linear regressions and r values (N = 26).

Table 3: Rotated VARIMAX factor scores for elements included in the Q-mode factor analysis of samples from Rio Grande Rise (n=27). The four factors explain 99.07% of the variance. Elements are listed from highest to

lowest score for each factor and the 4 factors are interpreted to be: (1) hydrogenetic Mn-oxide phases, (2) aluminosilicate and associated elements, (3) calcite and carbonate fluorapatite, and (4) minor amounts of 10Å manganates. Bolded scores represent the major mineral phase.

Factor 1		**Factor 2**		**Factor 3**		**Factor 4**	
53%		**34%**		**11%**		**0.78%**	
Mo	0.294	**Si**	**0.398**	**P.**	**0.439**	Tl	0.304
As	0.263	**Al**	**0.365**	**Ca**	**0.434**	Cr	0.262
Co	0.255	Th	0.328	Y.	0.368	Sb	0.258
Tl	0.237	Cu	0.308	Ni	0.311	Cd	0.242
V.	0.234	K.	0.266	Mg	0.305	Ni	0.238
Mn	**0.220**	Na	0.223	Cd	0.271	Ce	0.220
U.	0.219	Ag	0.174	Lu	0.164	V.	0.185
La	0.198	Cd	0.168	Er	0.146	Zn	0.165
Be	0.174	Fe	0.164	Tm	0.141	**Mn**	**0.154**
Nd	0.171	Cr	0.164	Yb	0.139	Mg	0.143
Pr	0.170	Ce	0.154	Zn	0.136		
Sb	0.168	Ti	0.149			Y.	-0.131
Ce	0.157	Eu	0.136	Th	-0.143	Pr	-0.136
Sm	0.153	Sm	0.135	Ce	-0.146	Lu	-0.151
Ti	0.153					Nd	-0.152
Eu	0.150					Tm	-0.159
Gd	0.148					Yb	-0.160
Se	0.143					Sm	-0.166
Tb	0.141					Er	-0.171
Dy	0.138					Eu	-0.180
Ho	0.134					Ho	-0.182
Zn	0.131					Gd	-0.184
						Tb	-0.189
Cu	-0.141					Dy	-0.190
Al	-0.178					Se	-0.192
Si	-0.195						

5.5 Discussion

The results of mineralogy, chemical composition, and petrography reveal that the FeMn crusts from 1500 to >5000 m water depth along RGR and surrounding seamounts differ significantly from previously studied crusts from the summit of the RGR. We discuss these differences, the controls on the composition, and the formation and evolution of these crusts in the context of the evolution of the RGR.

5.5.1 Genetic type and mineral association

The FeMn crusts from 1500 to more than 5000 m water depths along the RGR are typical hydrogenetic crusts, i.e., with the predominance of columnar and layered/laminated textures (Baturin et al., 2012; Benites et al., 2018; Lusty and Murton, 2018; Yeo et al., 2018; Marino et al, 2017), mineral phases dominated by vernadite and Fe-oxyhydroxide (x-ray amorphous, goethite), and high contents of REYs and trace metals Co, Ni, Cu, V, Tl, Te, and

others. These crusts fall in the hydrogenetic field of the discrimination diagram of Bonatti et al. (1972) based on Fe, Mn, and Co+Ni+Cu contents (Figure 7A). The REY_{SN} (SN = shale normalized) patterns of these crusts have a strong positive Ce_{SN} anomaly, negative Y_{SN} anomaly (Figure 7B), and no Eu anomaly, all fingerprints of hydrogenetic FeMn crusts (Bau et al., 2014). These crusts also plot in the hydrogenetic field of the two REE diagrams of Bau et al. (2014), Ce_{SN} anomalies (Ce_{SN}/Ce_{SN}*) versus Y_{SN}/Ho_{SN}, and versus Nd contents (Figure 7C and D). The only exception to these observations is the phosphatized sample D28-32C that plots out of the hydrogenetic field and has a negative Ce_{SN} anomaly and positive Y_{SN} anomaly, which commonly occur with phosphorites and phosphatized FeMn crusts (Hein et al., 2016b), similar to the old generation of FeMn crusts from the summit of the RGR (Benites et al., 2021).

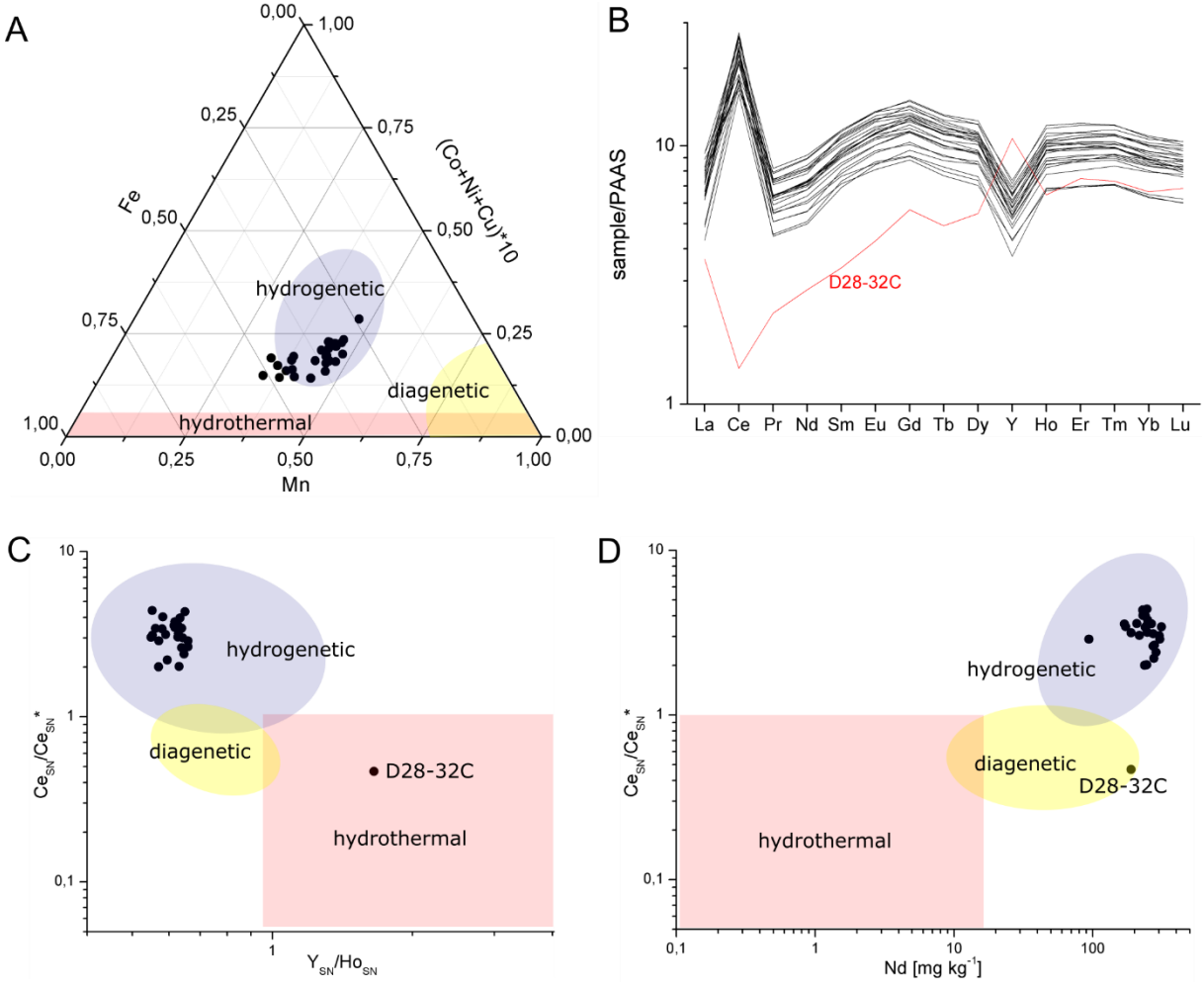

Figure 7: Various genetic discrimination plots (A) Ternary diagram of Bonatti et al. (1982); (B) REY_{SN} (SN = shale normalized) patterns of all samples consistent with hydrogenetic formation, except for D28-32C; Discrimination diagrams (C) Ce anomalies (Ce_{SN}/Ce_{SN}*) vs. Y_{SN}/Ho_{SN} and (D) vs. Nd contents from Bau et al. (2014).

The mineral association observed from the factor analyses (Table 3) can be explained by the classical adsorption model of hydrogenetic precipitation as cations in seawater such as Co, Ni, Zn, and Tl(I and III) bind preferentially onto the negatively charged surface of Mn

oxides, while neutral and negatively charged species such as As, V, Mo, U, Be, Ti, and Sb, bind to the slightly positively charged Fe-oxyhydroxide surfaces (Koschinsky and Hein, 2003; Manceau et al., 2022). A strong association of Co, and in part Tl, to MnO_2 occurs due to surface oxidation (Koschinsky and Hein, 2003). Fe does not appear in factor 1, but it must be noted that correlations of Fe can be problematic due its ubiquitous nature in crusts, occurring in the Mn, Fe, detrital, and easily soluble phases (Koschinsky and Hein, 2003). The accumulation of detrital material is relevant in some samples (D7-25, D12-31A, D21-8, and D22-31) especially from water depths below 4000 m and comprises the components of aluminosilicate minerals (Si, Al, K, and Na) and minor elements incorporated in these minerals, e.g., Th, Cu, Ag, Cd, Fe, Cr, Ce, Ti, Eu, and Sm, which have also been found as associated with the aluminosilicate minerals in the Gulf of Cadiz (González et al., 2008). The entrained detrital material causes dendritic to mottled textures, similar to crust and nodules with abundant detrital minerals at other locations (e.g., Gulf of Cadiz, Canary Islands).

Phosphatization, a diagenetic component, is restricted to the phosphatized generation of two samples (D28-32C and D31-9). For samples D28-32C, CFA dominates and explains the enrichment in Y, Ni, Mg, Cd, Zn, and the heavy REE by replacement in the CFA structure (e.g., Y, and probably Cd, replacing Ca; Hein et al., 2016b; Jiang et al., 2020) or inherited from precursor carbonate bioclasts (e.g., Mg and Ni from foraminifera and coccoliths; Koschinsky et al., 1995; Marino et al., 2019; Wang et al., 2011). Furthermore, a minor component of diagenetic Mn phases occurs as 10Å manganates associated with the enrichment of Ni. Ni is known to be preferentially adsorbed in the tunnel structure of todorokite as an important charge balancing element for its stability (Burns and Burns, 1978; Dymond et al., 1984; Koschinsky et al., 1997) and in the interlayers of asbolane and buserite (Kuhn et al., 2017; Post, 1999; Wegorzewski and Kuhn, 2014), which are all 10Å phyllomanganates. Mn-rich lamina with high Mn/Fe ratios and Ni contents like those found in phosphatized sample D28-32C and within the substrate of D9-54 are typical of suboxic diagenetic growth in manganese nodules (Benites et al., 2018; Halbach et al., 1981; Wegorzewski et al., 2015; Wegorzewski and Kuhn, 2014) and in FeMn crusts from the CISP (Marino et al., 2019). It has been demonstrated that the transformation of vernadite to todorokite occurs under suboxic conditions and that it involves incorporation of Ni (Bodeï et al., 2007). Todorokite has been identified in the phosphatized sample D28-32C, therefore this transformation could have occurred during phosphatization. Todorokite and 10Å phyllomanganates present in non-phosphatized samples probably formed in suboxic microenvironments within the sample, for instance in Mn oxides in pore spaces in the substrate rock (Fig. 4F).

5.5.2 Comparison with FeMn crusts from the summit of the RGR and elsewhere

The FeMn crusts from water depths greater than 1500 m on RGR contrast with those from the summit (625 – 1300 m) especially by the lack of the dual structure comprising a phosphatized generation and younger non-phosphatized crust, with two exceptions (D28-32 and D31-9). Moreover, the non-phosphatized generation of D28-32 is much thicker (25 mm), contrasting with the few mm thick non-phosphatized generation of FeMn crusts from the summit. This may be due to: (1) the non-phosphatized generation grew at a slower rate in summit crusts, (2) it was initially thicker but was eroded in part, or (3) the summit crusts initiated growing more recently. The first hypothesis agrees with the fact that growth rates are greater at greater water depths (Figure 6). The second is supported by the observation of pristine and better-preserved surface textures of FeMn crust from below 4000 m (dredges D7, D12, D22, D26), but very abraded surfaces with furrows at 2190 m (D28) and 2008 m (D30), suggesting that samples from shallower water on RGR underwent erosion by bottom currents. This is also seen from the erosive discontinuities in the internal structure mentioned above. Moreover, rocks with a FeMn patina showing a polished surface by bottom currents occur along the summit (Benites et al., 2020). The third hypothesis agrees with the age of the non-phosphatized generation of crusts from the summit of RGR (<14.7 Myr; Benites et al., 2020) being younger than the age of the non-phosphatized generation of sample D28-32 (20.1 Ma). Another important difference between FeMn crusts from the summit and from greater water depths is the abundance of entrained foraminifera tests, and consequently elevated calcite content in the summit crusts (Benites et al., 2020), which is not the case for crusts below 2008 m. On the other hand, these deeper water crusts have more entrained aluminosilicates, reflected in their higher contents of Si and Al than crusts from the summit. Further, bulk FeMn crusts from the summit of RGR have relatively less Fe, Mn, and more hydrogenetic metals such as As, Be, Co, Cu, Mo, Sb, Ti, Th, Tl, U, Zn, and REE due to dilution by CFA, while crusts from 2008 to 5218 m have higher contents of these elements (Figure 8). However, bulk crusts from the summit of RGR are significantly more enriched in Ca, P, Li, Mg, Cd, Ni, and %HREY, which are associated predominantly with the CFA.

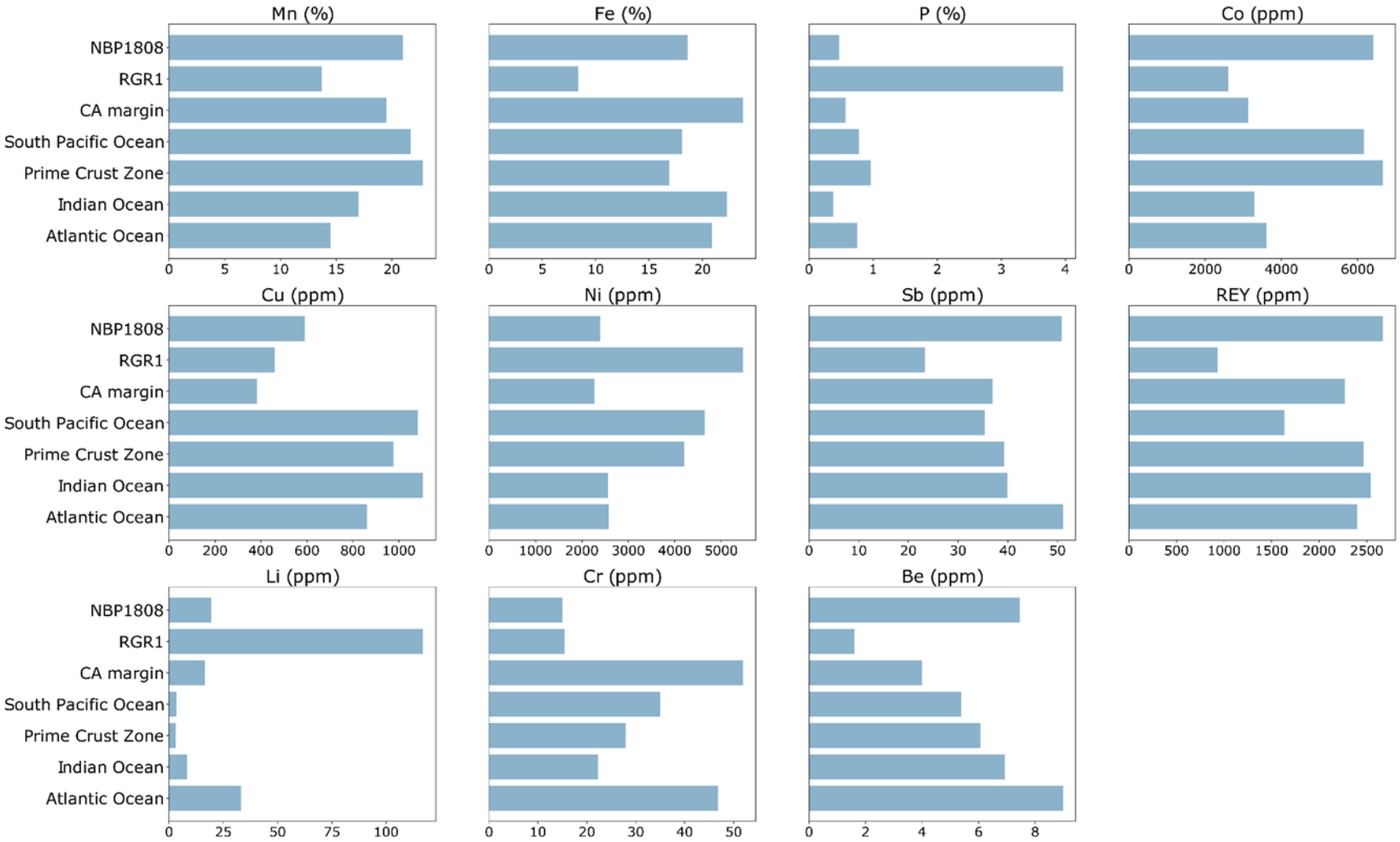

Figure 8: Comparison of element contents in FeMn crusts from 2008 to 5218 m water depths along RGR (NBP1808), the crest of RGR (600 – 800 m, RGR1, from Benites et al., 2020), and from elsewhere in the global ocean (data from Conrad et al., 2017 and references therein).

In comparison to the average of Atlantic Ocean crusts, FeMn crusts from 2008 to 5218 m on RGR have more Mn and Co, less Fe and Si, and significantly less Cr and Cu. It must be noted that the Atlantic Ocean crust dataset consists mostly of NE Atlantic samples, which receive a significant input of atmospheric dust from the Sahara (Koschinsky et al., 1995; Marino et al., 2017). Both the accumulation of sinking dust particles and a higher availability of dissolved Fe contribute to the prevalence of Fe-oxyhydroxide over Mn oxide in crusts from the NE Atlantic (Marino et al., 2017), which is not the case for the RGR. The content of Sb in RGR deep-water crusts is consistent with the average for Atlantic Ocean crusts, which is the highest among other ocean averages, suggesting that this is a common and unique feature for the Atlantic Ocean. The content of Li in the RGR deep-water crusts is significantly lower compared to the crusts from the summit, and lower than the average Atlantic Ocean crusts, but higher than the average Pacific and Indian Ocean crusts. This suggests that crusts from the Atlantic are overall more enriched in Li. In the samples studied here, the majority has Li < 17 ppm (detection limit of the method), but Li contents are higher in D28-32-C (99 ppm), D21-8 (53 ppm), and D7-25 (28 ppm). Li in D28-32C is probably associated to the CFA and calcite phases similarly to the Li-rich phosphatized crusts from the summit (Benites et al., 2020). Samples D7-25 and D21-8 have high input of detrital material and Li can be associated to these mineral phases, as it is in Arctic Ocean crusts (Hein et al., 2017), where Li can also be associated to residual biogenic and the Mn phase (Konstantinova et al., 2018). In addition, Li enrichment in crusts has been linked to hydrothermal input (Hein et al., 2005), but hydrothermal fields have not been identified in the RGR region. Deep-water RGR crusts are still more enriched in V, Be, Mo, and slightly more in REY than the average North Pacific Prime Crust Zone and South Pacific crusts, the most prominent regions for resource consideration (Conrad et al., 2017 and references therein).

5.5.3 Chemical composition variation with water depth

The chemical composition of each sample reflects the average concentration during the entire period of the crust growth, since we analyzed mostly bulk crusts. Thus, contemporary oceanographic conditions must be combined to paleoceanographic information of the region to discuss chemical variations.

As shown by the correlation matrix (Supplementary Material SM3) and scatter plots (Figure 6), V, U, As, Ca, Tl, P, Mo, Mn, Ni, Co, Sb, and Zn contents decrease with water depth in FeMn crusts from 2008 to 5218 m along the RGR, with negative correlation coefficient at the 99% confidence level (CL).

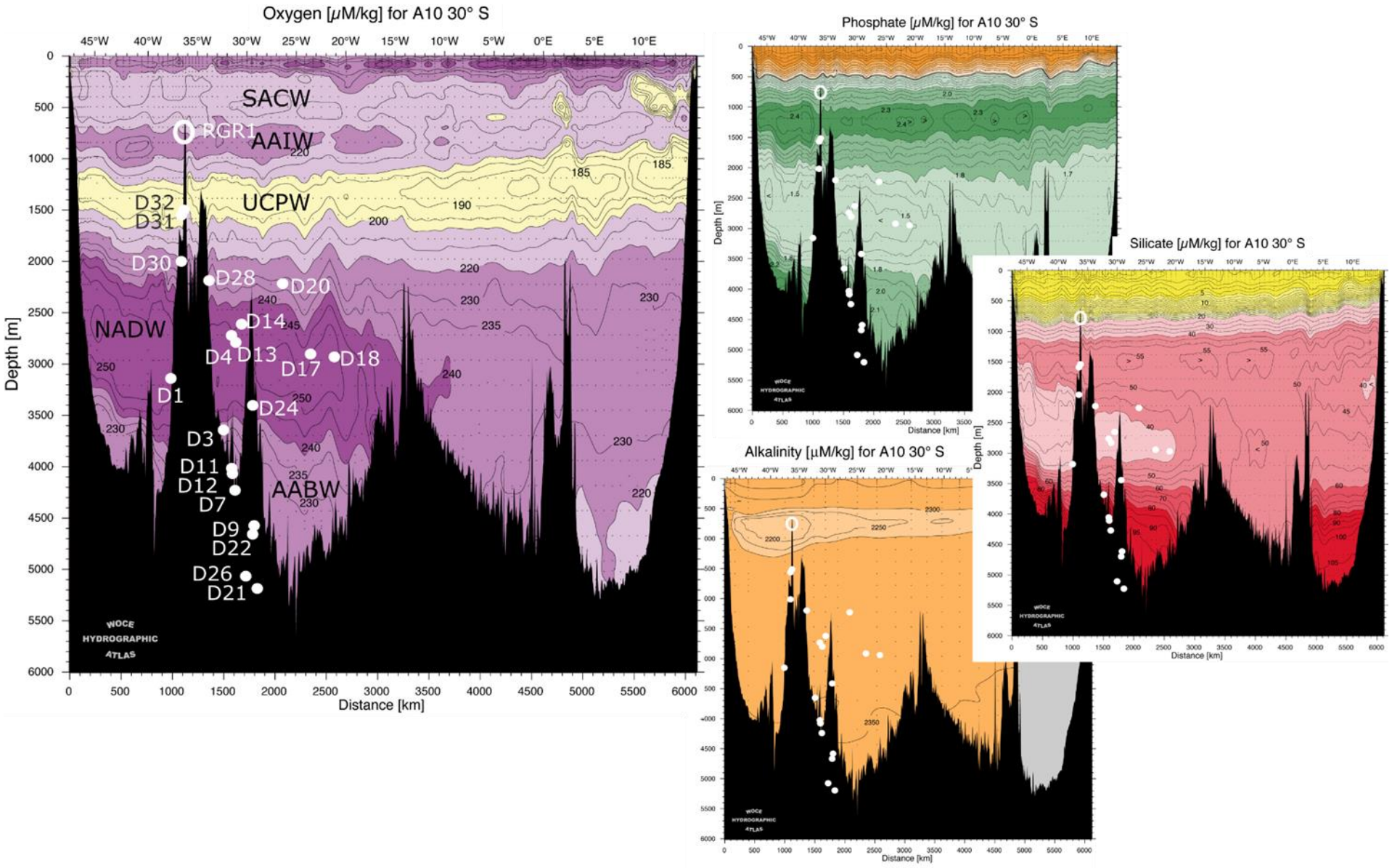
Oxygen [μM/kg] for A10 30° S
SACW
AAIW
UCPW
NADW
AABW
RGR1
D32
D31
D30
D28
D20
D14
D4
D13
D17
D18
D1
D24
D3
D11
D12
D7
D9
D22
D26
D21
Depth [m]
Distance [km]
Phosphate [μM/kg] for A10 30° S
Silicate [μM/kg] for A10 30° S
Alkalinity [μM/kg] for A10 30° S
WOCE HYDROGRAPHIC ATLAS

Figure 9: Seawater dissolved oxygen, phosphate, silicate, and alkalinity profiles along the WOCE A10 transect (World Ocean Circulation Experiment) at 30°S latitude, modified from Koltermann et al. (2011). SACW = South Atlantic Central Water; AAIW = Antarctic Intermediate Water; UCPW = Upper Circumpolar Water; NADW = North Atlantic Deep Water; AABW = Antarctic Bottom Water.

The content of Mn in FeMn crusts is dominantly controlled by seawater oxygenation and reach greater enrichments with proximity to the OMZ (Glasby et al., 2010; Hein et al., 2000; Mizell et al., 2020; Marino et al., 2016, Usui et al., 2017). The OMZ supports a large reservoir of dissolved divalent Mn (dMn) which is transported to depths above and below by advection and turbulent mixing (Halbach and Puteanus, 1984). However, in the absence of deep-water dMn sources (e.g., hydrothermal fluids, remineralization of organic matter in the sediments, and transport from water masses), dMn tends to decrease. On RGR, the UCPW comprises the oxygen minimum of ~4.2 mL/L O_2 and nutrient maximum between 1100 – 1600 m (Figure 9). Below it, the NADW provides an oxygen maximum of ~5.6 mL/L at around 3000 m (Figure 9) (Koltermann et al., 2011; Reid et al., 1977). Considering this oxygen profile on the water depth interval of our samples (2008 m – 5218 m), Mn-oxide precipitation was probably more intense at 2000 m but slowed with depth (Figure 6). A slight decrease in the oxygen occurs below 3600 m into the AABW (Figure 9) (Koltermann et al., 2011; Reid et al., 1977), unaccompanied by increases in Mn in the crusts (Figure 6). This can be explained by insufficient dMn due to distance from the OMZ and the lack of deep-water sources of dMn.

Co, Ni, Mo, and Zn concentrations in FeMn crusts also show strong negative correlation with seawater oxygen concentrations in the Pacific Ocean (Mizell et al., 2020). After Mn, Co is the most abundant redox-sensitive dissolved element derived from seawater that occurs in crusts (Usui et al., 2017). Besides, these four trace elements are generally associated with the Mn phase in crusts and naturally their content is influenced by the amount of Mn oxide (Kashiwabara et al., 2009; Koschinsky and Hein, 2003). Moreover, Co has a scavenged-type vertical distribution in the North Atlantic with surface enrichment and depletion with depth due to particle scavenging (Martin et al., 1993), thus dCo supply may also control the decrease in crusts Co content with water depth. Dissolved Ni and Zn have a nutrient-type vertical profile although they are almost constant below 2000 m under present conditions (Bruland, 1980). Sb contents in crusts decrease with depth, which may reflect the scavenged-type vertical seawater dSb profile in the Southwest Atlantic (Cutter et al., 2001).

The Fe content of crusts show no trend with water depth between 2008 and 5218 m in the RGR area. In other regions, Fe contents of crusts increase with water depth (Mizell et al., 2020; Usui et al., 2017) due to multiple reasons: (1) lesser Mn content resulting in proportionally more Fe; (2) advection of nutrient- and oxygen-rich deep water masses; (3)

dissolution of carbonates in deeper waters, leading to higher seawater pH and enhanced Fe oxyhydroxide precipitation (Halbach and Puteanus, 1984; Hein et al., 2016a; Mizell et al., 2020; Usui et al., 2017); (4) increased detrital material entrained in the crusts, as Fe is present in most aluminosilicates and detrital magnetite-titanomagnetite; (5) hydrothermal flux of Fe; and (6) Fe flux from the sediments. However, unlike the crust regions in the Indian and Pacific Oceans mentioned above, the dO of the bottom water (AABW) is lower than the overlying water mass (NADW) in the RGR area. Besides, the alkalinity profile does not show a pH level (Figure 9) that would favor the oxidation of Fe(II) (King, 1998) and decrease the solubility of Fe(III) in seawater (Liu and Millero, 2002). These two factors combined probably mediated Fe oxyhydroxide contribution to crusts below ~3500 m. However, compensation by other factors, e.g., entrained detrital material in crusts and Fe flux from sediments, may produce a zero correlation between Fe content of crusts and water depth instead of a negative correlation. A moderated Fe-oxyhydroxide contribution to the crusts below ~3500 m explains why the growth rates do not consistently increase with water depth as observed in the Indian Ocean (Ninetyeast Ridge; Hein et al., 2016a) and Pacific Ocean (Halbach, 1983; Mizell et al., 2020), where the increased oxidation potential and supply of Fe lead to faster crust growth. In the RGR area, the growth rates are slower for the group of crusts from 2000 to 3500 m, but growth rates for the crusts from > 3500 m nearly completely overlaps with the first group. Nevertheless, faster growth rates occur at places and are likely related to local conditions.

V, U, and As crusts contents have the strongest negative correlation coefficients with water depth. Dissolved U has a conservative vertical profile in seawater (Chen et al., 1986) and, although V and As have a nutrient-type vertical profile, their concentrations are almost uniform below 2000 m under present conditions (Andreae, 1979; Cutter et al., 2001; Collier, 1984); the same can be said for Tl (Flegal and Patterson, 1983). The average concentration of dissolved inorganic As is nearly identical when moving from the NADW (2200-3200 m: 21.2 ±1.7 nmol/l) into the AABW domain (3950 – 4460 m: 20.4 ±0.4 nmol/l) in the Argentine and Brazil Basins, not far from the RGR (Cutter et al., 2001). Thus, the present supply of dissolved V, U, As, and Tl is unlikely a major cause for the decrease of their contents in crusts between 2008 and 5218 m. Enrichment of Tl in Fe-vernadite in hydrogenetic crusts is known to occur due to oxidative scavenging and sorption (Manceau et al., 2022). Thus, the Tl content of crusts seems to follow the pattern of its host Mn oxide. For V, U, and As, their dominant phase associations are Fe-oxyhydroxide phases based on sequential leaching studies (Konstantinova et al., 2018; Koschinsky and Hein, 2003; Marino et al., 2018), although V and U are typically also distributed among the easily leachable carbonate and Mn-oxide phases. Thus, their distribution

in crusts with depth may be influenced by the lower Fe oxyhydroxide contents in crusts below ~3500 m. In addition, V, U, and As correlate positively with Mn at the 99% CL, suggesting that they are partially associated with the Mn phase. A strong correlation of As with Mn occurs in crusts from parts of the Pacific Ocean (Mizell et al., 2020), which can be explained by co-precipitation of As(V) arsenates with Mn oxides (Kashiwabara et al., 2008) or adsorption on Mn(IV) vacancy sites in Mn oxides (Foster et al., 2003), which would explain the As decrease with water depth following the pattern of Mn. As(V) arsenate is the main As form in seawater (Byrne, 2002) as well as the oxidation state of As in crusts (Kashiwabara et al., 2008).

Phosphorus contents of crusts decrease with depth, which is opposite to the present day seawater dissolved phosphate concentration from 2008 to 5218 m, which increases from the nutrient-poor NADW to the underlying nutrient-rich AABW (Figure 9) (Koltermann et al., 2011; Reid et al., 1977). This decoupling has been observed in crusts from the Pacific Ocean (Hein et al., 2000; Mizell et al., 2020), but is still unaccounted for. Since Fe-oxyhydroxide particles are known to scavenge high amounts of P (Filippelli & Delaney, 1996), the lower Fe-oxyhydroxide content in crusts below ~3500 m in the RGR proposed above could be the cause for the decrease of P content of crusts with depth.

The amount of entrained carbonate shells in crusts from 2008 m to 5218 m is small, so carbonate is an unlikely source of Ca in crusts. The carbonate compensation depth in the RGR area is at 4500 m (Dutkiewicz and Müller, 2021), so we would expect a positive correlation of Ca contents in crusts with depth as more dissolved Ca would be available, which is not the case. In fact, alkalinity seawater profiles at RGR show little variation below 2000 m (Figure 9) (Koltermann et al., 2011), indicating that a pH-related contribution due to carbonate dissolution is not important. However, it is known from leaching experiments that Ca can sorb to the negatively charged Mn-oxide surface in crusts (Koschinsky and Hein, 2003). Therefore, crusts Ca content could follow the same vertical distribution as Mn contents in crusts between 2008 to 5218 m in the RGR.

Apart from the contemporary oceanographic conditions, the RGR underwent episodes of increased paleoproductivity (23.9 - 22.9 Ma; Florindo et al., 2015) and phosphatization of rocks on its summit due to expansion/intensification of the OMZ and vertical mixing in the Miocene (Benites et al., 2021). These facts give a hint on why most elements that correlate negatively with water depth are nutrients and important to biological activity (V, As, Ca, Tl, P, Mo, Mn, Ni, Co, and Zn). The increased biological productivity and expanded/intensified OMZ likely enhanced the availability of dissolved Mn, Ni, Co, Zn, V, As, Tl, and P within and in proximity to the OMZ. In this scenario, the present-day oxygen minima, and nutrient maximum

between 1100 – 1600 m, would reach deeper-water or be intensified, with metals being transported to depths above and below by advection and turbulent mixing. Either way, more of these elements would have been available, especially for shallower crusts from the water depths of 2008 to 5218 m than it is today.

Si, Al, Th, Cu, and K contents increase with water depth. Si has a slow regeneration rate in the water column with a maximum availability of dSi in deeper abyssal waters, which is the case for RGR (Figure 9) (Koltermann et al., 2011; Reid et al., 1977). In addition, Si and Al contents in crusts increase with detrital input, which tend to increase in FeMn crusts from greater water depth, as observed in samples from >4000 m studied here. Thus, the correlation of other metals linked to aluminosilicates, such as K, Th and Cr, follow this trend with water depth. In the case of Cu, the increased content in crusts with depth is probably due to the dissolved Cu (dCu) seawater profile increasing almost linearly with depth because it undergoes intermediate and deep-water scavenging and bottom water input from the sediments (Bruland et al., 1980; 1983; Heggie et al., 1986).

From the data presented here and in Benites et al. (2020) and Sousa et al. (2021), the presence of a phosphatized old FeMn crust generation is common to almost all samples collected between 600 to 1300 m water depths but rare in sample between 1300 and 2190 m and absent below 2190 m water depth. This agrees with the observation that phosphatization of FeMn crusts was stronger above 2500 m in the Pacific Ocean crusts (Koschinsky et al., 1997). However, the phosphatized generation of crust D28-32 resembles those from the RGR summit, with the same P content as the pervasively phosphatized sample RGR1-D11-003 (>6%) but from a location 1439 m deeper while sample D30-34 from 2008 m is not phosphatized. Considering this and the location of dredge D28 on the rift wall (Figure 1), we suspect that the phosphatized generation of D28-32 was formed along the summit margin and was displaced down the rift wall to its current water depth. If true, phosphatization would have mineralized crusts from a narrower water depth range than otherwise indicated.

As observed in the chemical transect through crust D20-1, an environmental change probably occurred during the formation of the top 7.5 mm of the sample. The decrease of Mn, Co, and Mo contents towards the top of this section suggests a transition to more oxidizing conditions at 2269 m, since these elements are anticorrelated with oxygenation of seawater as discussed above. There are two hypotheses for this: the onset of a more oxidizing water mass encompassing 2269 m, or the deepening of the sample from shallower water depths to its current 2269 m due to thermal subsidence of the seamount. If the first was true, we would expect a more abrupt change instead of the subtle and continuous trend observed, which is better

explained by the continuous subsidence through time. In fact, subsidence of the RGR was discussed by Barker (1983), who showed that the paleodepth of DSDP Site 516 on the WRGR deepened from 600 m to its current position at 1313 m in the middle Eocene (47.8 - 38 Ma). The summit of RGR subsided below sea level about 30 Myr ago and continued to subside to its current depth of about 500 m (Thiede, 1977). Then, the transition to more oxidizing conditions towards the top of sample D20-1 reflects the subsidence of the seafloor into a more oxygenated water mass.

5.5.4 Detrital material accumulation

Accumulation of detrital material is not a common feature to all the FeMn crusts studied here but is restricted to some dredge hauls below 4000 m and to specific crust layers. Thus, the input of detrital material is more likely a local feature rather than regional (entire RGR). The mean Si/Al of 2.28 is very similar to Si/Al of FeMn crusts from the CISP and NE Atlantic in general (e.g., Marino et al., 2017). Along the Indian Ocean NER, a Si/Al <2.90 in samples with a large detrital component suggests that aluminosilicate originated from weathering of local basalts, while FeMn crusts with abundant detrital material from river discharge into the NE Indian Ocean have Si/Al as high as 5.2 (Hein et al., 2016a). Thus, the detrital material in FeMn crusts studied here is most likely from weathering of local volcanic rocks. Yet, transport of detrital material from volcanic rocks from other locations by deep currents and especially minor atmospheric input cannot be excluded.

As observed from EPMA, Fe-rich (40%) lamina depleted in Mn (<2%) with high Ti is often in contact with detrital material accumulation. Similar laminae were observed in FeMn crusts from the CISP area in direct contact with altered basaltic substrate and have been linked to eolian input of Sahara dust and/or local volcanic events promoting enrichment of dissolved Fe in seawater (Marino et al., 2019). However, in the absence of Sahara dust and volcanic activity along RGR after the initiation of crust growth, the existence of this Fe-Ti-rich lamina may be due to the precipitation of Fe oxides catalyzed by the Fe-oxide surface alteration of basalts, halmyrolysis of the volcanic substrate (Dubinin et al., 2018; Konstantinova et al., 2018; Marino et al., 2019; Templeton et al., 2009).

5.5.5 Estimated ages of FeMn crusts and phosphatization events

The growth rates calculated using the Co chronometer (equation 1) of 0.86 to 4.65 mm/Myr agree with the $^{230}Th_{excess}/^{232}Th$ ratios modeled accretion rates of 0.5 to 2.5 mm/Myr for a crust from the summit of RGR (Benites et al., 2020) and with Os isotopes age dating of a

crust from 2871 m water depth in the vicinity of RGR with values of 0.5 to 3 mm/Myr (Goto et al., 2017). However, since we lack a cross-validation with an independent age proxy for the samples studied here, the possibility of higher growth rates cannot be excluded, especially when related to input of detrital material and diagenetic events (Hein et al., 2017).

The estimated age of the oldest sample (D13-25; 2772 m water depth) is 47.6 Ma and, if true, implies that the crust began to grow during or right after the last volcanic event on RGR when the summit was subaerially exposed. Favorable conditions for FeMn crust formation were already established to have existed for the past ~30 Myr in the vicinity of RGR at 2871 m (Goto et al., 2017).

The age of the non-phosphatized generation of sample D28-32 is estimated to be 20.1 Ma, which implies that the underlying phosphatized layer D28-32C was impregnated with phosphate prior to that age. This agrees with the major Cenozoic phosphatization event at the transition between late Oligocene-early Miocene identified in phosphorites and phosphatized FeMn crusts in the Pacific Ocean which occurred due to changes from glacial to warm global climate (Hein et al., 1993). This phosphatization event was found to have occurred during the same time interval in the equatorial Atlantic Ocean (González et al., 2016; Jones et al., 2002), and at the summit of RGR (Benites et al., 2021). The non-phosphatized layer of D28-32 is older than the non-phosphatized generation of crusts from the summit of RGR studied so far (<14.7 Ma; Benites et al., 2020). A possible explanation can be gleaned from the study of Nishi et al. (2017) where the maximum age of the non-phosphatized generation of FeMn crusts from northwest and central Pacific seamounts varies with water depth, which are 10 Ma old between 991-1575 m but 17 Ma old at 2262 m. For RGR, the time gap can be due to subsidence of RGR, as deeper-water crusts subsided to water depths where phosphatization did not occur before those from shallower locations, which were still under the influence of the environmental conditions conducive for phosphatization.

5.6 Conclusion

We analyzed for the first time a suite of FeMn crusts from deep water in the RGR (1505 to 5060 m) area, southwest Atlantic Ocean and compared the results with crusts from the summit of RGR (625 – 850 m). In contrast to the dual structure of FeMn crusts from the summit of RGR, the deep-water crusts are typically single-layered dark-brown hydrogenetic crusts. They are composed of vernadite and goethite containing high amounts of hydrogenetic metals (e.g., As, Be, Co, Cu, Mo, Sb, Ti, Th, Tl, U, Zn, REE). High contents of detrital minerals (quartz, feldspars) occur in some samples collected from below 4000 m water depths. In these samples,

Fe-Ti-rich lamina in contact with the detritus occurs, likely due to precipitation of Fe oxides catalyzed by the Fe-oxide surface alteration of basalts. Minor diagenetic 10Å manganates occur in some samples, which may reflect formation within suboxic microenvironments. The initiation age of formation of the oldest deep-water crusts along RGR is about 47 Ma.

Increasing oxygenation due to presence of the NADW between 2000 and 3500 m is an important control on the decreasing contents of Mn, Co, Ni, and Mo with depth. The contents of Zn, Tl, and Ca in RGR area FeMn crusts are interpreted to follow the behavior of Mn as Mn oxide is their host phase. A subtle drop in oxygenation from the NADW to the AABW (below 3500 m) may limit the Fe oxyhydroxide component in crusts and, therefore influence the distribution of dominantly Fe-phase associated elements with water depth (V, As, U, P). Besides, past episodes of increased biological productivity and expanded/intensified OMZ likely provided more metals related to biological activity (Mn, Co, Ni, V, As, Tl, P) especially in the shallower crusts at water depths from 2000 to 5218 m. Si, Al, K, Cu, and Th contents in crusts increase with water depth due to greater accumulation of detrital material in crusts below 4000 m, the linear pattern of Cu increase with depth due to intermediate and deep-water scavenging and regeneration at greater depths, and the flow of the silicate-rich AABW. Growth rates of crusts correlate with water depth within the NADW due to more oxidizing environmental conditions. However, growth rates correlation with water depth below 3500 m in the AABW is less clear, which may be due to a drop in dissolved oxygen.

From our suite of samples, the dual structure crusts containing an old, phosphatized generation are restricted to the upper 2190 m around RGR, but potentially that maximum depth is shallower, as we suspect that sample D28-32 collected at this water depth was formed at the summit of RGR and was displaced down the rift wall through gravity processes. In this case, the phosphatization of crusts might be restricted to water depths above 1523 m. The non-phosphatized crust generation from the summit crusts is much thinner compared to phosphatized sample D28-32 collected at 2190 m because summit crusts represent a younger and narrower time span, grew at a slower rate, and were potentially eroded.

Decrease in the contents of Mn, Co, Mo, and the growth rate across the top 7.5 mm of crust D20-1 indicates transition to more oxidizing oceanic conditions, most likely related to the subsidence of the RGR. Subsidence is also possibly responsible for the age difference between the non-phosphatized crust generation from 2190 m (20.1 Ma) and summit crusts (<14.7 Ma). Further chronological and isotopic analyses along the FeMn crusts growth axis are necessary to cross validate the Co-chronometer ages and better constrain the evolution of the FeMn crusts studied here.

The target area for FeMn crust exploration along RGR focused on the summit, however we show that deeper-water crusts were not affected by phosphatization and, therefore, contain relatively higher amounts of hydrogenetic metals typically considered of economic interest (e.g., Co, V, As, Mo, Tl, U, Zn, Sb, Cu). On the other hand, the FeMn crusts from the summit are a potential target for phosphate, Ni, Li, and Y.

References

Andreae, M.O., 1979. Arsenic speciation in seawater and interstitial waters: the influence of biological-chemical interactions on the chemistry of a trace element. Limnol. Oceanogr. 24, 440–452. https://doi.org/10.4319/lo.1979.24.3.0440

Barker, P.F., 1983. Tectonic evolution and subsidence history of the Rio Grande Rise. Initial reports DSDP, Leg 72, Santos, Brazil 953–976. https://doi.org/10.2973/dsdp.proc.72.151.1983

Baturin, G.N., Dubinchuk, V.T., Rashidov, V.A., 2012. Ferromanganese Crusts from the Sea of Okhotsk. Oceanology 52, 88–100. https://doi.org/10.1134/S0001437012010031

Bau, M., Schmidt, K., Koschinsky, A., Hein, J., Kuhn, T., Usui, A., 2014. Discriminating between different genetic types of marine ferro-manganese crusts and nodules based on rare earth elements and yttrium. Chem. Geol. 381, 1–9. https://doi.org/10.1016/j.chemgeo.2014.05.004

Benites, M., Hein, J.R., Mizell, K., Blackburn, T., Jovane, L., 2020. Genesis and evolution of ferromanganese crusts from the summit of Rio Grande Rise, Southwest Atlantic Ocean. Minerals 10, 349. https://doi.org/10.3390/min10040349

Benites, M., Hein, J.R., Mizell, K., Jovane, L., 2021. Miocene Phosphatization of Rocks From the Summit of Rio Grande Rise, Southwest Atlantic Ocean. Paleoceanogr. Paleoclimatology 36, 1–24. https://doi.org/10.1029/2020PA004197

Benites, M., Millo, C., Hein, J., Nath, B.N., Murton, B., Galante, D., Jovane, L., 2018. Integrated geochemical and morphological data provide insights into the genesis of ferromanganese nodules. Minerals 8, 1–16. https://doi.org/10.3390/min8110488

Bergo, N.M., Bendia, A.G., Ferreira, J.C.N., Murton, B., Brandini, F.P., Pellizari, D.V.H., 2021. Microbial diversity of deep-sea ferromanganese crust field in the rio grande rise, southwestern Atlantic Ocean. Microb. Ecol. https://doi.org/10.1007/s00248-020-01670-y

Bodeï, S., Manceau, A., Geoffroy, N., Baronnet, A., Buatier, M., 2007. Formation of todorokite from vernadite in Ni-rich hemipelagic sediments. Geochim. Cosmochim. Acta 71, 5698–5716. https://doi.org/10.1016/j.gca.2007.07.020

Bonatti, E., Kraemer, T., Rydell, H., 1972. Classification and genesis of submarine iron-manganese deposits, in: Horn, D.R. (Ed.), Ferromanganese Deposits on the Ocean Floor. NSF, Alexandria, VA, USA, pp. 149–166.

Bruland, K.W., Middag, R., Lohan, M.C., 2013. Controls of Trace Metals in Seawater, in: Mottl, M.J., Elderfield, H. (Eds.), Treatise on Geochemistry: Second Edition. Elsevier Ltd., Philadelphia, PA, USA, pp. 19–51. https://doi.org/10.1016/B978-0-08-095975-7.00602-1

Burns, V.M., Burns, R.G., 1978. Post-depositional metal enrichment processes inside manganese nodules from the north equatorial Pacific. Earth Planet. Sci. Lett. 39, 341–348. https://doi.org/10.1016/0012-821X(78)90020-1

Byrne, R.H., 2002. Inorganic speciation of dissolved elements in seawater: The influence of pH on concentration ratios. Geochem. Trans. 3, 11–16. https://doi.org/10.1039/b109732f

Camboa, L.A.P., Rabinowitz, P.D., 1984. The evolution of the Rio Grande Rise in the Southwest Atlantic Ocean. Mar. Geol. 58, 35–58. https://doi.org/10.1016/0025-3227(84)90115-4

Collier, R.W., 1984. Particulate and dissolved vanadium in the North Pacific Ocean. Nature 309, 441–444. https://doi.org/10.1038/309441a0

Conrad, T., Hein, J.R., Paytan, A., Clague, D.A., 2017. Formation of Fe-Mn crusts within a continental margin environment. Ore Geol. Rev. https://doi.org/10.1016/j.oregeorev.2016.09.010

Corrêa, P.V.F., Jovane, L., Murton, B.J., Sumida, P.Y.G., 2022. Benthic megafauna habitats, community structure and environmental drivers at Rio Grande Rise (SW Atlantic). Deep. Res. Part I Oceanogr. Res. Pap. 186. https://doi.org/10.1016/j.dsr.2022.103811

Cutter, G.A., Cutter, L.S., Featherstone, A.M., Lohrenz, S.E., 2001. Antimony and arsenic biogeochemistry in the western Atlantic Ocean. Deep. Res. Part II Top. Stud. Oceanogr. 48, 2895–2915. https://doi.org/10.1016/S0967-0645(01)00023-6

da Silveira, I.C.A., Napolitano, D.C., Farias, I.U., 2020. Water Masses and Oceanic Circulation of the Brazilian Continental Margin and Adjacent Abyssal Plain 7–36. https://doi.org/10.1007/978-3-030-53222-2_2

Dubinin, A. V., Rimskaya-Korsakova, M.N., Berezhnaya, E.D., Uspenskaya, T.Y., Dara, O.M., 2018. Ferromanganese Crusts in the South Atlantic Ocean: Compositional Evolution and Specific Features of Ore Formation. Geochemistry Int. 56, 1093–1108. https://doi.org/10.1134/s0016702918110034

Dutkiewicz, A., Müller, R.D., 2021. The carbonate compensation depth in the South Atlantic Ocean since the Late Cretaceous. Geology 49, 873–878. https://doi.org/10.1130/G48404.1

Dymond, J., Lyle, M., Finney, B., Piper, D.Z., Murphy, K., Conard, R., Pisias, N., 1984. Ferromanganese nodules from MANOP Sites H, S, and R - control of mineralogical and chemical composition by multiple accretionary processes. Geochim. Cosmochim. Acta 48, 931–949. https://doi.org/10.1016/0016-7037(84)90186-8

Flegal, A.R., Patterson, C.C., 1983. Vertical concentration profiles of lead in the Central Pacific at 15°N and 20°S. Earth Planet. Sci. Lett. 64, 19–32. https://doi.org/10.1016/0012-821X(83)90049-3

Florindo, F., Gennari, R., Persico, D., Turco, E., Villa, G., Lurcock, P.C., Roberts, A.P., Winkler, A., Carter, L., Pekar, S.F., 2015. New magnetobiostratigraphic chronology and paleoceanographic changes across the Oligocene-Miocene boundary at DSDP Site 516 (Rio Grande Rise, SW Atlantic). Paleoceanography 30, 659–681. https://doi.org/10.1002/2014PA002734

Frank, M., O'Nions, R.K., Hein, J.R., Banakar, V.K., 1999. 60 Myr records of major elements and Pb-Nd isotopes from hydrogenous ferromanganese crusts: Reconstruction of seawater paleochemistry. Geochim. Cosmochim. Acta 63, 1689–1708. https://doi.org/10.1016/S0016-7037(99)00079-4

Glasby, G.P., Mountain, B., Vineesh, T.C., Banakar, V., Rajani, R., Ren, X., 2010. Role of hydrology in the formation of Co-rich Mn crusts from the equatorial N pacific, equatorial S Indian ocean and the NE Atlantic ocean. Resour. Geol. 60, 165–177. https://doi.org/10.1111/j.1751-3928.2010.00123.x

González, F.J., Medialdea, T., Schiellerup, H., Zananiri, I., Ferreira, P., Somoza, L., Monteys, X., Alcorn, T., Marino, E., Lobato, A.B., Zalba-balda, Í., Kuhn, T., Nyberg, J., Malyuk, B., Magalhães, V., Hein, J.R., Cherkashov, G., 2022. MINDeSEA – Exploring Seabed Mineral Deposits in European Seas, Metallogeny and Geological Potential for Stategic and Critical Raw Materials. Geol. Soc. London, Spec. Publ. 526. https://doi.org/10.1144/SP526-2022-150

González, F.J., Somoza, L., Hein, J.R., Medialdea, T., León, R., Urgorri, V., Reyes, J., Martín-Rubí, J.A., 2016. Phosphorites, Co-rich Mn nodules, and Fe-Mn crusts from Galicia Bank, NE Atlantic: reflections of cenozoic tectonics and paleoceanography. Geochemistry, Geophys. Geosystems 17, 346–374. https://doi.org/10.1002/2015GC00586 1

González, F.J., Somoza, L., Medialdea, T., Léon, R., Vázquez, J.T., Marino, E., Bellido, E., Reyes, J., 2014. Volcanism and Ferromanganese Deposits on Seamounts and New Volcanoes From the Canary Archipelago, in: IV Congress of Marine Sciences. Las Palmas de Gran Canaria, Spain, p. 186. https://doi.org/10.13140/2.1.3205.2168

Goto, K.T., Nozaki, T., Toyofuku, T., Augustin, A.H., Shimoda, G., Chang, Q., Kimura, J.I., Kameo, K., Kitazato, H., Suzuki, K., 2017. Paleoceanographic conditions on the São Paulo Ridge, SW Atlantic Ocean, for the past 30 million years inferred from Os and Pb isotopes of a hydrogenous ferromanganese crust. Deep. Res. Part II Top. Stud. Oceanogr. 146, 82–92. https://doi.org/10.1016/j.dsr2.2016.10.010

Graça, M.C., Kusznir, N., Stanton, N.S.G., 2019. Crustal thickness mapping of the central South Atlantic and the geodynamic development of the Rio Grande Rise and Walvis Ridge. Mar. Pet. Geol. 101, 230–242. https://doi.org/10.1016/j.marpetgeo.2018.12.011

Halbach, P., 1983. The polymetallic deposits of the deep-sea bottom within the Pacific ocean. Monogr. Ser. Miner. Depos. 22, 123.

Halbach, P., Puteanus, D., 1984. The influence of the carbonate dissolution rate on the growth and composition of Co-rich ferromanganese crusts from Central Pacific seamount areas. Earth Planet. Sci. Lett. 68, 73–87. https://doi.org/10.1016/0012-821X(84)90141-9

Halbach, P., Sattler, C.D., Teichmann, F., Wahsner, M., 1989. Cobalt-rich and platinum bearing manganese crust deposits on seamounts: nature, formation, and metal potential. Mar. Min. 8, 23–39.

Halbach, P., Scherhag, C., Hebisch, U., Marchig, V., 1981. Geochemical and mineralogical control of different genetic types of deep-sea nodules from the Pacific Ocean. Miner. Depos. 16, 59–84. https://doi.org/10.1007/BF00206455

Heggie, D., Kahn, D., Fischer, K., 1986. Trace metals in metalliferous sediments, MANOP Site M: interfacial pore water profiles. Earth Planet. Sci. Lett. 80, 106–116. https://doi.org/10.1016/0012-821X(86)90023-3

Hein, J., Conrad, T., Mizell, K., Banakar, V.K., Frey, F.A., Sager, W.W., 2016a. Controls on ferromanganese crust composition and reconnaissance resource potential, Ninetyeast Ridge, Indian Ocean. Deep. Res. Part I 110, 1–19. https://doi.org/10.1016/j.dsr.2015.11.006

Hein, J., Gunn, H., Sliter, V., Benninger, M., 1993. Two major Cenozoic episodes of phosphogenesis recorded in Equatorial Pacific seamounts deposits. Paleoceanography 8, 293–311. https://doi.org/10.1029/93PA00320

Hein, J., Koschinsky, A., Mikesell, M., Mizell, K., Glenn, C., Wood, R., 2016b. Marine phosphorites as potential resources for heavy rare earth elements and yttrium. Minerals 6, 88. https://doi.org/10.3390/min6030088

Hein, J.R., Konstantinova, N., Mikesell, M., Mizell, K., Fitzsimmons, J.N., Lam, P.J., Jensen, L.T., Xiang, Y., Gartman, A., Cherkashov, G., Hutchinson, D.R., Till, C.P., 2017. Arctic Deep Water Ferromanganese-Oxide Deposits Reflect the Unique Characteristics of the Arctic Ocean. Geochemistry, Geophys. Geosystems 18, 3771–3800. https://doi.org/10.1002/2017GC007186

Hein, J.R., Koschinsky, A., 2014. Deep-Ocean Ferromanganese Crusts and Nodules, in: Scott, S. (Ed.), Treatise on Geochemistry. Elsevier, Amsterdam, Netherlands, pp. 273–291. https://doi.org/10.1016/B978-0-08-095975-7.01111-6

Hein, J.R., Koschinsky, A., Bau, M., Manheim, F.T., Kang, J., Roberts, L., 2000. Cobalt-rich ferromanganese crusts in the Pacific, in: Cronan, D.S. (Ed.), Handbook of Marine Mineral Deposits. CRC Marine Science Series. CRC Press, Boca Raton, Florida, pp. 239–279.

Hein, J.R., Mizell, K., Koschinsky, A., Conrad, T.A., 2013. Deep-ocean mineral deposits as a source of critical metals for high- and green-technology applications: Comparison with land-based resources. Ore Geol. Rev. 51, 1–14. https://doi.org/10.1016/j.oregeorev.2012.12.001

Hein, J.R., Schulz, M.S., Kang, J.-K., 1990. Insular and submarine ferromanganese mineralization of the Tonga-Lau region. Mar. Min. 9, 305–354.

Hoyer, P.A., Haase, K.M., Regelous, M., O'Connor, J.M., Homrighausen, S., Geissler, W.H., Jokat, W., 2022. Mantle plume and rift-related volcanism during the evolution of the Rio Grande Rise. Commun. Earth Environ. 3. https://doi.org/10.1038/s43247-022-00349-1

Hyeong, K., Kim, J., Yoo, C.M., Moon, J.W., Seo, I., 2013. Cenozoic history of phosphogenesis recorded in the ferromanganese crusts of central and western Pacific seamounts: Implications for deepwater circulation and phosphorus budgets. Palaeogeogr. Palaeoclimatol. Palaeoecol. 392, 293–301. https://doi.org/10.1016/j.palaeo.2013.09.012

Jiang, X.-D., Sun, X.-M., Chou, Y.-M., Hein, J.R., He, G.-W., Fu, Y., Li, D., Liao, J.-L., Ren, J.-B., 2020. Mineralogy and geochemistry of carbonate fluorapatite in seamount Fe Mn crusts from the Pacific Ocean. Mar. Geol. 423, 106135. https://doi.org/10.1016/j.margeo.2020.106135

Josso, P., Lusty, P., Chenery, S., Murton, B., 2021. Controls on metal enrichment in ferromanganese crusts: Temporal changes in oceanic metal flux or phosphatisation? Geochim. Cosmochim. Acta 308, 60–74. https://doi.org/10.1016/j.gca.2021.06.002

Josso, P., Parkinson, I., Horstwood, M., Lusty, P., Chenery, S., Murton, B., 2019. Improving confidence in ferromanganese crust age models: A composite geochemical approach. Chem. Geol. 513, 108–119. https://doi.org/10.1016/j.chemgeo.2019.03.003

Josso, P., Rushton, J., Lusty, P., Matthews, A., Chenery, S., Holwell, D., Kemp, S.J., Murton, B., 2020. Late cretaceous and Cenozoic paleoceanography from north-East Atlantic ferromanganese crust microstratigraphy. Mar. Geol. 422, 106122. https://doi.org/10.1016/j.margeo.2020.106122

Jovane, L., Hein, J.R., Yeo, I.A., Benites, M., Bergo, N.M., Corrêa, P.V.F., Couto, D.M., Guimarães, A.D., Howarth, S.A., Miguel, H.R., Mizell, K.L., Moura, D.S., Vicentini Neto, F.L., Pompeu, M., Rodrigues, I.M.M., Santana, F.R., Serrao, P.F., Silva, T.E., Tura, P.M., Viscarra, C.L., Chuqui, M.G., Pellizari, V.H., Signori, C.N., Da Silveira, I.C.A., Sumida, P.Y.G., Murton, B.J., Brandini, F.P., 2019. Multidisciplinary scientific cruise to the Rio Grande Rise. Front. Mar. Sci. 6, 1–7. https://doi.org/10.3389/fmars.2019.00252

Kashiwabara, T., Mitsunobu, A.S., Das, A., Itai, T., Tanimizu, M., Takahashi, Y., 2008. Oxidation states of antimony and arsenic in marine ferromanganese oxides related to their fractionation in oxic marine environment. Chem. Lett. 37, 756–757. https://doi.org/10.1246/cl.2008.756

Kashiwabara, T., Takahashi, Y., Tanimizu, M., 2009. A XAFS study on the mechanism of isotopic fractionation of molybdenum during its adsorption on ferromanganese oxides. Geochem. J. 43, 31–36. https://doi.org/10.2343/geochemj.1.0060

Kfouri, L.O., Millo, C., Estela de Lima, A., Silveira, C.S., Sant'Anna, L.G., Marino, E., González, F.J., Sayeg, I.J., Hein, J.R., Jovane, L., Bernardini, S., Lusty, P.A.J., Murton, B.J., 2021. Growth of ferromanganese crusts on bioturbated soft substrate, Tropic Seamount, northeast Atlantic ocean. Deep. Res. Part I Oceanogr. Res. Pap. 175. https://doi.org/10.1016/j.dsr.2021.103586

King, D.W., 1998. Role of carbonate speciation on the oxidation rate of Fe(II) in aquatic systems. Environ. Sci. Technol. 32, 2997–3003. https://doi.org/10.1021/es980206o

Klovan, J.E., Imbrie, J., 1971. An algorithm and Fortran-iv program for large-scale Q-mode factor analysis and calculation of factor scores. J. Int. Assoc. Math. Geol. 3, 61–77. https://doi.org/10.1007/BF02047433

Koltermann, K.P., Gouretski, V.V., Jancke, K., 2011. Hydrographic Atlas of the World Ocean Circulation Experiment (WOCE). Volume 3: Atlantic Ocean. International WOCE Project Office, Southampton, UK. https://doi.org/10.21976/C6RP4Z

Konstantinova, N., Hein, J.R., Gartman, A., Mizell, K., Barrulas, P., Cherkashov, G., Mikhailik, P., Khanchuk, A., 2018. Mineral phase-element associations based on sequential leaching of ferromanganese crusts, Amerasia Basin Arctic ocean. Minerals 8, 1–21. https://doi.org/10.3390/min8100460

Koschinsky, A., Halbach, P., Hein, J.R., Mangini, A., 1996. Ferromanganese crusts as indicators for paleoceanographic events in the NE Atlantic. Geol. Rundschau 85, 567–576. https://doi.org/10.1007/BF02369011

Koschinsky, A., Hein, J.R., 2003. Uptake of elements from seawater by ferromanganese crusts: solid-phase associations and seawater speciation. Mar. Geol. 198, 331–351. https://doi.org/10.1016/S0025-3227(03)00122-1

Koschinsky, A., Stascheit, I.A., Bau, M., Halbach, P., 1997. Effects of phosphatization on the geochemical and mineralogical composition of marine ferromanganese crusts. Geochim. Cosmochim. Acta 6, 4079–4094. https://doi.org/10.1016/S0016-7037(97)00231-7

Koschinsky, A., Van Gerven, M., Halbach, P., 1995. First investigations of massive ferromanganese crusts in the NE Atlantic in comparison with hydrogenetic pacific occurrences. Mar. Georesources Geotechnol. 13, 375–391. https://doi.org/10.1080/10641199509388294

Kuhn, T., Wegorzewski, A., Rühlemann, C., Vink, A., 2017. Composition, formation, and occurrence of polymetallic nodules, in: Sharma, R. (Ed.), Deep-Sea Mining. Springer International Publishing, Basel, Switzerland, pp. 23–63. https://doi.org/10.1007/978-3-319-52557-0_2

Lee, S., Xu, H., Xu, W., Sun, X., 2019. The structure and crystal chemistry of vernadite in ferromanganese crusts research papers. Acta Crystallogr. B75, 591–598. https://doi.org/10.1107/S2052520619006528

Liu, X., Millero, F.J., 2002. The solubility of iron in seawater. Mar. Chem. 77, 43–54. https://doi.org/10.1016/S0304-4203(01)00074-3

Lusty, P.A.J., Murton, B.J., 2018. Deep-ocean mineral deposits: Metal resources and windows into earth processes. Elements 14, 301–306. https://doi.org/10.2138/gselements.14.5.301

Manceau, A., Gorshkov, A.I., Drits, V.A., 1992. Structural chemistry of Mn, Fe, Co, and Ni in manganese hydrous oxides: Part II. Information from EXAFS spectroscopy and electron and X-ray diffraction. Am. Mineral. 77, 1144–1157.

Manceau, A., Simionovici, A., Findling, N., Glatzel, P., Detlefs, B., Wegorzewski, A. V., Mizell, K., Hein, J.R., Koschinsky, A., 2022. Crystal Chemistry of Thallium in Marine

Ferromanganese Deposits. ACS Earth Sp. Chem. 6, 1269–1285. https://doi.org/10.1021/acsearthspacechem.1c00447

Manheim, F.T., Lane-Bostwick, C.M., 1988. Cobalt in ferromanganese crusts as a monitor of hydrothermal discharge on the Pacific sea floor. Nature 335, 59–62.

Marino, E., González, F.J., Kuhn, T., Madureira, P., Wegorzewski, A. V., Mirao, J., Medialdea, T., Oeser, M., Miguel, C., Reyes, J., Somoza, L., Lunar, R., 2019. Hydrogenetic, diagenetic and hydrothermal processes forming ferromanganese crusts in the Canary Island seamounts and their influence in the metal recovery rate with hydrometallurgical methods. Minerals 9. https://doi.org/10.3390/min9070439

Marino, E., González, F.J., Lunar, R., Reyes, J., Medialdea, T., Castillo-Carrión, M., Bellido, E., Somoza, L., 2018. High-resolution analysis of critical minerals and elements in Fe–Mn crusts from the canary island seamount province (Atlantic ocean). Minerals 8, 1–36. https://doi.org/10.3390/min8070285

Marino, E., González, F.J., Somoza, L., Lunar, R., Ortega, L., Vázquez, J.T., Reyes, J., Bellido, E., 2017. Strategic and rare elements in Cretaceous-Cenozoic cobalt-rich ferromanganese crusts from seamounts in the Canary Island Seamount Province (northeastern tropical Atlantic). Ore Geol. Rev. 87, 41–61. https://doi.org/10.1016/j.oregeorev.2016.10.005

Martin, J.H., Fitzwater, S.E., Michael Gordon, R., Hunter, C.N., Tanner, S.J., 1993. Iron, primary production and carbon-nitrogen flux studies during the JGOFS North Atlantic bloom experiment. Deep. Res. Part II 40, 115–134. https://doi.org/10.1016/0967-0645(93)90009-C

Mizell, K., Hein, J.R., 2018. Ferromanganese crusts and nodules: Rocks that grow, Encyclopedia of Earth Sciences Series. https://doi.org/10.1007/978-3-319-39312-4_101

Mizell, K., Hein, J.R., Au, M., Gartman, A., 2022. Estimates of Metals Contained in Abyssal Manganese Nodules and Ferromanganese Crusts in the Global Ocean Based on Regional Variations and Genetic Types of Nodules. Perspect. Deep. Min. 53–80. https://doi.org/10.1007/978-3-030-87982-2_3

Mizell, K., Hein, J.R., Lam, P.J., Koppers, A.A.P., Staudigel, H., 2020. Geographic and oceanographic influences on ferromanganese crust composition along a pacific ocean meridional transect, 14 N to 14S. Geochemistry, Geophys. Geosystems 21, 1–19. https://doi.org/10.1029/2019GC008716

Montserrat, F., Guilhon, M., Vinicius, P., Corrêa, F., Menezes, N., Negrão, C., Marone, P., Santos, M.D.L., Moura, D., Jovane, L., Pellizari, V., Yukio, P., Sumida, G., Pereira, F., Turra, A., 2019. Deep-sea mining on the Rio Grande Rise (Southwestern Atlantic): A review

on environmental baseline, ecosystem services and potential impacts. Deep. Res. Part I 145, 31–58. https://doi.org/10.1016/j.dsr.2018.12.007

Muiños, S.B., Frank, M., Maden, C., Hein, J.R., van de Flierdt, T., Lebreiro, S.M., Gaspar, L., Monteiro, J.H., Halliday, a. N., 2008. New constraints on the Pb and Nd isotopic evolution of NE Atlantic water masses. Geochemistry, Geophys. Geosystems 9, n/a-n/a. https://doi.org/10.1029/2007GC001766

Muiños, S.B., Hein, J.R., Frank, M., Monteiro, J.H., Gaspar, L., Conrad, T., Pereira, H.G., Abrantes, F., 2013. Deep-sea Fe-Mn Crusts from the Northeast Atlantic Ocean: Composition and Resource Considerations. Mar. Georesources Geotechnol. 31, 40–70. https://doi.org/10.1080/1064119X.2012.661215

Nishi, K., Usui, A., Nakasato, Y., Yasuda, H., 2017. Formation age of the dual structure and environmental change recorded in hydrogenetic ferromanganese crusts from Northwest and Central Pacific seamounts. Ore Geol. Rev. 87, 62–70. https://doi.org/10.1016/j.oregeorev.2016.09.004

Novikov, G. V., Bogdanova, O.Y., 2007. Transformations of ore minerals in genetically different oceanic ferromanganese rocks. Lithol. Miner. Resour. 42, 303–317. https://doi.org/10.1134/S0024490207040013

Pisias, N.G., Murray, R.W., Scudder, R.P., 2013. Multivariate statistical analysis and partitioning of sedimentary geochemical data sets: General principles and specific MATLAB scripts. Geochemistry, Geophys. Geosystems 14, 4015–4020. https://doi.org/10.1002/ggge.20247

Post, J.E., 1999. Manganese oxide minerals: Crystal structures and economic and environmental significance. Proc. Natl. Acad. Sci. U. S. A. 96, 3447–3454. https://doi.org/10.1073/pnas.96.7.3447

Reid, J.L., Nowlin Jr, W.D., Patzert, W.C., 1977. On the characteristics and circulation of the Southwestern Atlantic Ocean. J. Phys. Oceanogr. 7, 62–91. https://doi.org/10.1175/1520-0485(1977)007<0062:OTCACO>2.0.CO;2

Rohde, J.K., van den Bogaard, P., Hoernle, K., Hauff, F., Werner, R., 2013. Evidence for an age progression along the Tristan-Gough volcanic track from new 40Ar/39Ar ages on phenocryst phases. Tectonophysics 604, 60–71. https://doi.org/10.1016/j.tecto.2012.08.026

Sergipe, P.P., Louro, V., Marangoni, Y.R., Moura, D.S. De, Jovane, L., 2023. A study of volcanic rocks and ferromanganese crusts through marine geophysical methods integration in the north portion of Cruzeiro do Sul Rift in the Rio Grande Rise. Front. Mar. Sci. 1–13. https://doi.org/10.3389/fmars.2023.1093108

Sousa, I.M.C., Santos, R. V., Koschinsky, A., Bau, M., Wegorzewski, A. V., Cavalcanti, J.A.D., Dantas, E.L., 2021. Mineralogy and chemical composition of ferromanganese crusts from the Cruzeiro do Sul Lineament - Rio Grande Rise, South Atlantic. J. South Am. Earth Sci. 108, 103207. https://doi.org/10.1016/j.jsames.2021.103207

Stramma, L., England, M., 1999. On the water masses and mean circulation of the South Atlantic Ocean. J. Geophys. Res. Ocean. 104, 20863–20883. https://doi.org/10.1029/1999JC900139

Templeton, A.S., Knowles, E.J., Eldridge, D.L., Arey, B.W., Dohnalkova, A.C., Webb, S.M., Bailey, B.E., Tebo, B.M., Staudigel, H., 2009. A seafloor microbial biome hosted within incipient ferromanganese crusts. Nat. Geosci. 2, 872–876. https://doi.org/10.1038/ngeo696

Ussami, N., Chaves, C.A.M., Marques, L.S., Ernesto, M., 2012. Origin of the Rio Grande Rise-Walvis Ridge reviewed integrating palaeogeographic reconstruction, isotope geochemistry and flexural modelling, in: Mohriak, W.U., Danforth, A., Post, P.J., Brown, D.E., Tari, G.C., Nemcok, M., Sinha, S.T. (Eds.), Conjugate Divergent Margins. Geological Society Special Publication, London, p. 369. https://doi.org/10.1144/SP369.10

Usui, A., Nishi, K., Sato, H., Nakasato, Y., Thornton, B., Kashiwabara, T., Tokumaru, A., Sakaguchi, A., Yamaoka, K., Kato, S., Nitahara, S., Suzuki, K., Iijima, K., Urabe, T., 2017. Continuous growth of hydrogenetic ferromanganese crusts since 17 Myr ago on Takuyo-Daigo Seamount, NW Pacific, at water depths of 800–5500 m. Ore Geol. Rev. 87, 71–87. https://doi.org/10.1016/j.oregeorev.2016.09.032

Wang, X., Peine, F., Schmidt, A., Schröder, H.C., Wiens, M., Schloßmacher, U., Müller, W.E.G., 2011. Concept of biogenic ferromanganese crust formation: Coccoliths as bio-seeds in crusts from Central Atlantic Ocean (Senghor Seamount/Cape Verde). Nat. Prod. Commun. 6, 679–688. https://doi.org/10.1177/1934578x1100600522

Wegorzewski, A. V., Kuhn, T., 2014. The influence of suboxic diagenesis on the formation of manganese nodules in the Clarion Clipperton nodule belt of the Pacific Ocean. Mar. Geol. 357, 123–138. https://doi.org/10.1016/j.margeo.2014.07.004

Wegorzewski, A. V., Kuhn, T., Dohrmann, R., Wirth, R., Grangeon, S., 2015. Mineralogical characterization of individual growth structures of Mn-nodules with different Ni+Cu content from the central Pacific Ocean. Am. Mineral. 100, 2497–2508. https://doi.org/10.2138/am-2015-5122

Yeo, I.A., Dobson, K., Josso, P., Pearce, R.B., Howarth, S.A., Lusty, P.A.J., Bas, T.P. Le, Murton, B.J., 2018. Assessment of the Mineral Resource Potential of Atlantic

Ferromanganese Crusts Based on Their Growth History, Microstructure, and Texture. Minerals 8, 327. https://doi.org/10.3390/min8080327

Yi, L., Medina-Elizalde, M., Kletetschka, G., Yao, H., Simon, Q., Paterson, G.A., Bourlès, D.L., Deng, X., Du, J., Qin, H., Chen, Y., Xie, Q., Xiao, J., Wang, Y., Andreucci, C., Keddadouche, K., Aumaître, G., Liu, Y., Wang, H., Shen, Z., Gu, X., Smith, T., Dang, H., Jian, Z., Song, T., He, H., Deng, C., Zhu, R., 2020. The Potential of Marine Ferromanganese Nodules From Eastern Pacific as Recorders of Earth's Magnetic Field Changes During the Past 4.7 Myr: A Geochronological Study by Magnetic Scanning and Authigenic 10Be/9Be Dating. J. Geophys. Res. Solid Earth 125, 1–15. https://doi.org/10.1029/2019JB018639

Supplementary Material

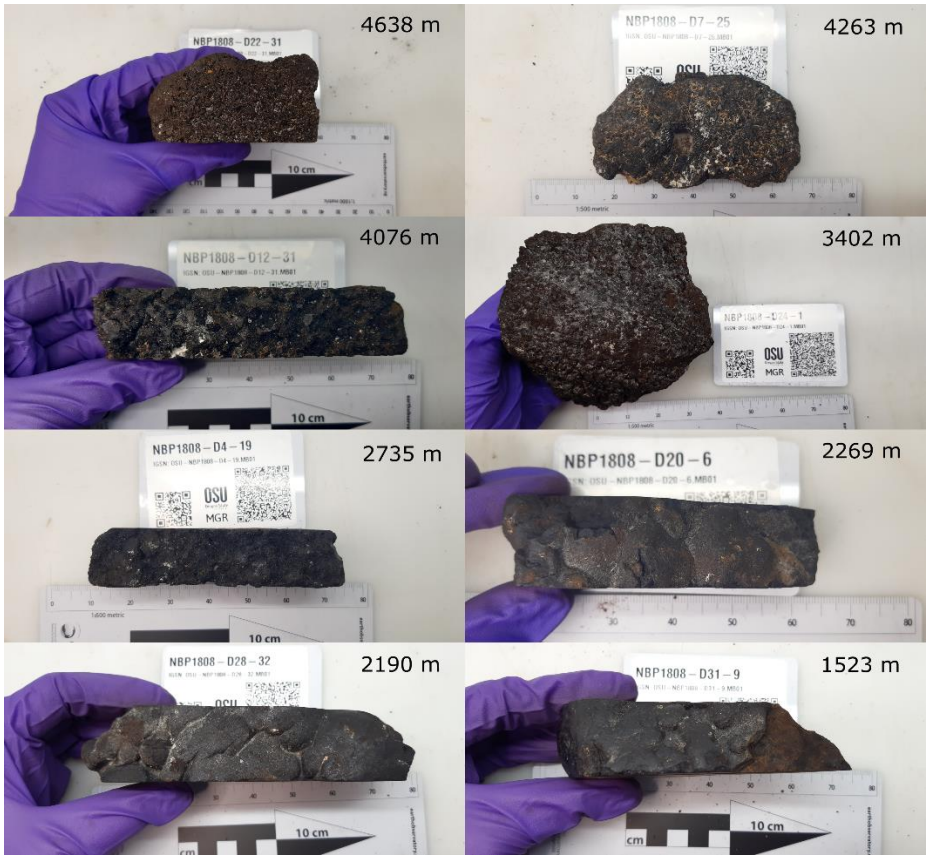

SM1: Surfaces of ferromanganese crust samples D22-31, D7-25, D12-31, D24-1, D4-19, D20-6, D28-32, and D31-9. Note how the surface of samples tend to be more abraded with shallower water deths.

SM2: Chemical composition of individual ferromanganese crust samples and layers.

	D1-1	D3-11	D4-19	D7-25	D9-7A	D9-7B	D11-2	D12-31A	D12-31B	D13-25A	D13-25B	D13-25C	D14-1A	D14-1B	D17-5	D18-6	D20-6A	D20-6A	D21-8	D22-31	D24-1	D26-4	D28-32A	D28-32B	D28-32C	D30-34A	D30-34B
Depth (m)	3185	3660	2735	4263	4592	4592	4014	4076	4076	2772	2772	2772	2634	2634	2923	2935	2269	2269	5218	4638	3402	5060	2190	2190	2190	2008	2008
Si (%)	3.46	5.55	3.16	11.6	6.19	8.05	6.15	8.83	4.19	2.04	2.37	2.30	1.89	2.07	3.10	2.10	2.01	3.63	11.8	9.00	3.65	3.33	1.53	1.96	2.24	1.46	1.92
Al	1.83	2.25	1.86	4.64	2.26	3.12	2.59	3.64	2.05	1.00	1.06	1.29	0.70	0.95	1.61	0.84	0.84	1.61	4.22	3.11	1.83	1.68	0.57	1.04	1.31	0.57	1.16
Fe	24.4	22.9	23.1	17.1	21.7	19.5	20.1	21.2	19.6	18.7	18.6	18.4	18.5	17.3	19.0	18.0	17.8	17.8	12.8	17.0	17.0	17.1	16.9	17.1	4.73	16.5	16.6
Ca	2.17	2.60	2.41	2.17	2.17	2.00	2.33	1.97	2.24	2.69	2.70	2.97	2.82	2.74	2.77	2.76	2.80	2.52	1.91	2.18	2.50	2.39	2.96	3.30	25.30	3.01	2.86
Ti	1.18	1.54	1.43	0.95	1.24	1.00	1.33	1.27	1.11	1.15	1.28	1.06	1.28	1.25	1.16	1.07	1.07	1.16	0.91	1.31	1.34	1.33	1.18	1.27	0.15	1.35	1.29
Mn	19.2	16.3	20.4	13.1	18.2	17.4	18.1	14.1	21.0	22.6	23.5	24.0	24.2	24.6	21.4	23.0	24.8	22.4	15.9	15.5	22.3	22.8	25.6	24.1	9.3	25.8	25.2
K	0.38	0.44	0.39	0.95	0.53	0.74	0.56	0.62	0.43	0.38	0.48	0.43	0.35	0.41	0.37	0.35	0.36	0.44	1.19	0.78	0.46	0.50	0.37	0.45	0.43	0.36	0.37
Mg	1.53	1.65	1.40	1.40	1.21	1.34	1.38	1.23	1.29	1.34	1.26	1.32	1.32	1.41	1.41	1.36	1.29	1.31	1.47	1.23	1.40	1.35	1.33	1.54	1.68	1.33	1.39
P	0.54	0.47	0.48	0.37	0.42	0.39	0.44	0.44	0.42	0.48	0.41	0.48	0.55	0.46	0.51	0.54	0.53	0.49	0.34	0.37	0.40	0.40	0.60	0.71	6.11	0.57	0.52
Na	1.57	1.59	1.69	1.92	1.77	1.80	1.70	1.42	1.30	1.36	1.41	1.40	1.53	1.55	1.44	1.92	1.42	1.43	1.87	1.49	1.48	1.48	1.53	1.46	0.77	1.57	1.29
H2O[1]	18.8	16.5	19.6	15.7	19.1	18.7	17.1	15.3	18.3	21.0	21.7	20.7	21.1	22.4	19.4	23.0	21.5	19.6	14.1	18.9	22.1	22.7	23.3	20.7	2.2	22.7	21.8
LOI[2]	33.2	30.7	34.8	28.1	33.2	32.0	31.9	28.4	33.5	38.3	37.0	36.3	37.2	37.7	35.0	38.4	36.9	34.7	26.3	31.7	36.5	37.1	38.3	36.0	20.0	38.0	37.2
Fe/Mn	1.3	1.4	1.1	1.3	1.2	1.1	1.1	1.5	0.9	0.8	0.8	0.8	0.8	0.7	0.9	0.8	0.7	0.8	0.8	1.1	0.8	0.8	0.7	0.7	0.5	0.6	0.7
Si/Al	1.9	2.5	1.7	2.5	2.7	2.6	2.4	2.4	2.0	2.0	2.2	1.8	2.7	2.2	1.9	2.5	2.4	2.3	2.8	2.9	2.0	2.0	2.7	1.9	1.7	2.6	1.7
K/Al	0.2	0.2	0.2	0.2	0.2	0.2	0.2	0.2	0.2	0.4	0.4	0.3	0.5	0.4	0.2	0.4	0.4	0.3	0.3	0.3	0.3	0.3	0.7	0.4	0.3	0.6	0.3
Be (µg/g)	9.12	7.94	9.78	5.75	5.99	6.37	6.36	7.73	9.25	8.57	9.19	9.99	7.70	8.12	8.51	7.64	7.70	8.21	4.79	5.07	8.04	7.38	5.69	6.81	1.52	5.64	6.62
Li	23.93	<17	<17	28.36	<17	<17	<17	<17	<17	<17	<17	<17	<17	<17	<17	<17	<17	<17	52.78	<17	<17	<17	<17	25.15	98.93	<17	<17
V	1116	981	975	545	761	701	737	728	921	1032	1131	1077	1109	1103	1022	1042	1102	1014	761	640	894	848	1164	1147	269	1107	1132
Co	4416	7008	6993	3309	4846	4100	6156	3709	3757	8362	7507	6318	8926	8678	6257	7130	6442	5704	2112	3183	8620	8998	7498	7573	1476	9978	9108
Ni	2021	1600	2230	1918	1965	2247	2303	1703	2173	2300	2294	2677	2440	2695	2402	2594	2759	2636	2076	1648	2457	2436	2881	3996	3575	2796	2900
Cr	12.6	22.8	18.9	25.3	10.0	15.3	16.5	25.3	9.6	9.2	8.9	9.0	5.7	12.2	33.1	13.5	10.7	12.8	16.2	15.8	13.1	10.4	8.6	16.4	12.1	12.3	26.7
Cu	897	658	711	1082	796	840	801	762	790	338	406	556	275	392	505	326	300	419	1239	706	684	450	300	513	564	274	343
Zn	725	597	682	463	553	498	584	571	721	571	717	783	640	710	657	660	645	651	523	528	711	594	592	700	485	589	670
As	444	398	391	205	299	261	284	280	300	419	395	359	465	399	398	435	428	373	135	243	287	314	463	412	77	444	401
Se	32.6	37.6	37.2	29.8	39.5	38.6	35.1	28.6	30.7	44.3	39.7	36.8	43.0	37.6	37.5	42.2	37.1	30.6	25.3	35.0	33.0	37.8	31.3	24.7	16.6	33.9	26.0

Mo	469	296	473	219	348	375	321	233	604	628	730	728	671	714	578	639	749	611	262	249	526	541	735	615	120	683	653
Ag	0.10	0.10	0.12	0.09	0.11	0.09	0.11	0.11	0.09	0.09	0.12	0.11	0.09	0.10	0.10	0.16	0.08	0.11	0.10	0.11	0.09	0.10	0.08	0.08	0.02	0.08	0.08
Cd	3.95	3.22	3.17	4.58	3.73	3.72	3.90	5.19	4.51	2.92	2.66	3.33	3.20	3.25	4.15	3.27	3.59	3.92	5.49	3.43	4.13	4.04	3.75	4.40	4.83	3.66	3.78
Sb	44.3	60.3	67.8	40.3	44.8	39.1	43.2	68.4	50.8	48.1	64.0	59.6	49.8	62.5	45.3	44.8	47.7	52.9	28.2	36.4	49.9	45.3	52.3	66.4	16.2	52.0	60.6
Tl	120	103	152	72	92	88	142	88	89	171	174	188	157	218	108	155	172	195	16	73	174	164	164	242	69	169	233
Th	44.7	49.8	45.9	79.7	72.6	91.6	82.5	64.2	45.4	44.6	61.2	47.3	47.7	60.3	32.5	33.3	28.0	40.7	86.8	102.6	66.7	84.7	32.2	53.3	3.4	36.6	63.0
U	12.9	12.9	13.7	8.5	11.3	9.6	11.3	11.0	12.1	13.3	12.8	13.1	15.7	14.0	15.1	14.9	15.4	14.3	5.9	10.1	11.5	12.3	16.5	14.6	6.1	16.3	14.4
Y	155	177	174	129	163	143	162	140	146	172	156	146	193	143	187	199	184	141	116	150	133	156	167	117	288	176	101
La	244	276	292	185	273	256	253	189	270	338	357	316	358	317	288	339	300	245	164	236	276	308	288	237	139	305	245
Ce	1438	1646	1787	1376	1802	1709	1860	1485	1904	1338	2008	2130	1509	1871	1440	1305	1361	1778	1264	1685	2183	2106	1420	1945	109	1648	2092
Pr	49.6	56.4	57.0	45.0	63.6	62.5	56.5	39.4	55.9	69.9	72.2	64.6	69.0	63.8	55.3	65.2	56.5	48.1	40.2	54.3	56.7	65.7	52.1	44.9	19.8	56.3	48.7
Nd	217	247	244	189	272	264	240	169	236	304	312	276	302	272	244	286	249	208	172	229	239	278	229	189	94	246	203
Sm	46.5	53.2	51.1	44.6	61.3	60.6	53.9	38.3	49.9	63.8	63.9	57.4	63.0	56.2	51.7	59.1	51.7	43.3	40.5	52.7	50.5	59.8	47.7	39.6	18.7	50.6	42.3
Eu	10.9	12.6	12.1	10.3	14.1	13.8	12.4	9.1	11.5	14.7	14.6	13.4	14.6	12.8	12.2	13.5	12.0	10.1	9.4	12.0	11.6	13.7	10.9	8.75	4.62	11.6	9.21
Gd	53.2	61.0	58.7	47.1	64.4	61.6	57.7	44.9	52.7	69.3	66.1	60.8	70.0	59.1	59.9	66.8	58.5	48.1	42.6	54.4	53.1	62.6	52.5	41.1	26.4	56.3	42.3
Tb	7.73	9.03	8.56	7.12	9.60	9.20	8.64	6.79	7.74	10.13	9.41	8.78	10.21	8.63	8.84	9.74	8.60	7.03	6.41	8.13	7.79	9.20	7.58	5.92	3.80	8.12	6.18
Dy	44.4	52.0	49.6	39.7	52.9	49.9	48.4	39.7	43.7	56.6	52.3	48.9	58.6	48.3	51.8	56.9	50.6	40.7	35.5	44.9	43.2	51.1	44.0	32.9	25.6	47.3	34.4
Ho	8.87	10.37	10.17	7.69	10.15	9.47	9.48	8.15	8.69	11.09	10.03	9.57	11.89	9.56	10.77	11.57	10.43	8.36	6.79	8.65	8.42	9.91	9.29	6.63	6.40	9.80	6.71
Er	26.2	30.5	30.7	22.9	29.3	27.4	28.1	24.9	25.9	32.0	28.9	28.1	34.9	28.0	32.2	34.3	31.4	25.1	19.8	25.3	24.8	29.0	28.1	19.8	21.3	29.5	19.9
Tm	3.73	4.42	4.45	3.38	4.19	3.96	4.10	3.74	3.77	4.49	3.97	4.00	4.88	3.97	4.68	4.86	4.49	3.67	2.87	3.61	3.57	4.13	4.00	2.85	2.96	4.20	2.88
Yb	23.9	28.3	29.0	22.3	26.8	25.5	26.8	24.9	24.2	28.0	24.5	25.1	30.4	24.9	29.9	30.8	28.4	23.6	18.3	23.4	22.6	26.4	25.0	17.8	18.7	25.9	17.9
Lu	3.61	4.14	4.32	3.36	3.92	3.64	3.99	3.77	3.58	3.99	3.41	3.54	4.36	3.50	4.50	4.49	4.22	3.48	2.69	3.48	3.28	3.78	3.75	2.61	2.97	3.83	2.60
[3]	2332	2667	2813	2133	2851	2699	2825	2227	2843	2516	3181	3193	2733	2921	2481	2486	2410	2633	1941	2591	3117	3183	2390	2711	782	2678	2875
HREY [4] (%)	14.5	14.6	13.6	13.7	13.3	12.9	12.8	13.8	11.5	16.0	11.6	10.9	15.8	11.7	16.2	17.4	16.3	11.8	13.4	12.9	10.0	11.5	14.7	9.4	51.3	13.9	8.5

[1]Sorbed w ater

[2]Loss on Ignition

[3]Summation of the rare earth elements plus Y

[4]Percentage of the heavy rare earth elements out of total REY

SM3: Pearson correlation coefficient matrix of chemical composition of ferromanganese crust samples. Sample D28-32C is not included because of its different chemical composition. Highlighted coefficients are significant at the 99% confidence level.

	lat	lon	WD*	Si	Al	Fe	Ca	Ti	Mn	K	Mg	P	Na	Be	V	Co	Ni	Cr	Cu	Zn	As	Se	Mo
lat	1.00																						
lon	**-0.54**	1.00																					
WD*	-0.17	-0.02	1.00																				
Si	-0.26	0.00	**0.80**	1.00																			
Al	-0.30	0.05	**0.79**	**0.98**	1.00																		
Fe	**-0.53**	0.31	0.03	-0.08	0.01	1.00																	
Ca	0.28	-0.10	**-0.84**	**-0.82**	**-0.84**	-0.23	1.00																
Ti	-0.11	0.34	-0.19	-0.33	-0.30	0.40	0.23	1.00															
Mn	0.38	-0.07	**-0.77**	**-0.92**	**-0.94**	-0.27	**0.83**	0.13	1.00														
K	-0.10	-0.03	**0.74**	**0.92**	**0.88**	-0.37	**-0.67**	-0.46	**-0.74**	1.00													
Mg	0.00	0.18	-0.09	-0.02	0.04	0.14	0.16	0.18	-0.08	0.01	1.00												
P	0.21	0.01	**-0.79**	**-0.70**	**-0.70**	0.07	**0.79**	0.19	**0.63**	**-0.66**	0.27	1.00											
Na	-0.28	-0.24	0.44	**0.53**	0.48	0.00	-0.41	-0.31	-0.48	**0.53**	0.19	-0.27	1.00										
Be	-0.05	0.02	-0.35	**-0.51**	-0.39	**0.51**	0.20	0.16	0.30	**-0.58**	0.07	0.13	-0.45	1.00									
V	0.28	0.07	**-0.86**	**-0.90**	**-0.90**	0.01	**0.81**	0.21	**0.86**	**-0.78**	0.21	**0.76**	-0.49	0.46	1.00								
Co	0.14	0.09	**-0.64**	**-0.82**	**-0.81**	-0.12	**0.76**	**0.53**	**0.80**	**-0.72**	0.11	**0.51**	-0.36	0.22	**0.68**	1.00							
Ni	0.38	-0.13	**-0.66**	**-0.64**	**-0.64**	-0.41	**0.79**	-0.05	**0.77**	-0.42	0.14	**0.74**	-0.27	0.02	**0.63**	**0.56**	1.00						
Cr	-0.15	-0.05	0.10	0.38	0.45	0.10	-0.17	0.07	-0.45	0.23	0.33	-0.08	0.09	-0.13	-0.30	-0.23	-0.20	1.00					
Cu	-0.31	0.18	**0.75**	**0.85**	**0.90**	0.15	**-0.80**	-0.31	**-0.84**	**0.79**	0.21	**-0.61**	**0.51**	-0.24	**-0.74**	**-0.81**	**-0.55**	0.30	1.00				
Zn	0.24	0.06	**-0.57**	**-0.71**	**-0.63**	0.18	**0.51**	0.21	**0.62**	**-0.66**	0.13	0.41	**-0.54**	**0.77**	**0.72**	0.40	0.44	-0.24	-0.39	1.00			
As	0.11	0.05	**-0.84**	**-0.89**	**-0.90**	0.26	**0.77**	0.35	**0.75**	**-0.89**	0.13	**0.81**	-0.39	0.43	**0.89**	**0.70**	0.49	-0.24	**-0.82**	**0.54**	1.00		
Se	-0.15	-0.27	-0.04	-0.33	-0.37	0.31	0.11	0.14	0.19	-0.38	-0.24	-0.08	0.09	0.34	0.13	0.33	-0.23	-0.38	-0.39	0.03	0.36	1.00	
Mo	0.35	-0.12	**-0.78**	**-0.90**	**-0.91**	-0.23	**0.80**	-0.01	**0.96**	**-0.73**	-0.14	**0.58**	**-0.51**	0.43	**0.87**	**0.69**	**0.70**	-0.47	**-0.82**	**0.67**	**0.75**	0.24	1.00
Ag	0.01	-0.43	0.18	0.08	0.08	0.25	-0.21	0.01	-0.20	0.01	-0.16	-0.22	0.38	0.26	-0.14	-0.18	-0.31	0.00	0.07	0.12	-0.06	0.38	-0.15
Cd	0.17	-0.01	0.45	**0.59**	**0.63**	-0.26	-0.46	-0.37	-0.46	**0.58**	0.11	-0.20	0.15	-0.37	-0.46	**-0.55**	-0.07	0.39	**0.62**	-0.29	**-0.62**	**-0.76**	-0.49
Sb	-0.18	0.26	**-0.58**	**-0.50**	-0.43	0.31	0.48	**0.53**	0.37	**-0.56**	0.07	0.44	-0.49	**0.54**	**0.52**	0.46	0.33	0.08	-0.43	**0.57**	**0.50**	-0.07	0.38
Tl	0.21	0.07	**-0.79**	**-0.83**	**-0.79**	-0.12	**0.80**	0.32	**0.83**	**-0.71**	0.06	**0.63**	-0.49	0.34	**0.73**	**0.81**	**0.78**	-0.24	**-0.76**	**0.61**	**0.68**	0.06	**0.77**
Th	-0.21	0.18	**0.78**	**0.72**	**0.70**	-0.19	**-0.63**	-0.04	**-0.61**	**0.75**	-0.11	**-0.70**	0.32	**-0.51**	**-0.78**	-0.42	-0.40	0.12	**0.59**	**-0.54**	**-0.81**	-0.17	**-0.68**
U	0.23	-0.08	**-0.86**	**-0.90**	**-0.91**	0.12	**0.82**	0.36	**0.81**	**-0.91**	-0.01	**0.81**	-0.45	0.34	**0.83**	**0.73**	**0.58**	-0.19	**-0.89**	**0.52**	**0.94**	0.27	**0.79**
Y	0.04	-0.37	-0.20	-0.38	-0.43	0.37	0.22	0.20	0.20	-0.49	-0.13	0.23	0.11	0.25	0.25	0.27	-0.16	-0.23	-0.43	0.03	**0.53**	**0.78**	0.24
La	0.07	-0.16	-0.47	**-0.78**	**-0.81**	0.11	**0.58**	0.27	**0.70**	**-0.72**	-0.20	0.29	-0.26	0.49	**0.61**	**0.71**	0.25	**-0.53**	**-0.76**	0.46	**0.69**	**0.80**	**0.73**
Ce	-0.07	0.28	-0.04	-0.28	-0.20	0.00	0.19	0.43	0.29	-0.23	-0.07	-0.10	-0.41	0.27	0.09	0.36	0.27	-0.14	-0.12	0.48	-0.05	-0.10	0.21
Pr	-0.12	-0.13	-0.11	-0.49	**-0.53**	0.14	0.27	0.16	0.43	-0.44	-0.28	-0.06	-0.08	0.38	0.27	0.49	0.00	**-0.55**	-0.49	0.24	0.37	**0.90**	0.46
Nd	-0.10	-0.16	-0.15	**-0.52**	**-0.56**	0.15	0.30	0.16	0.44	-0.47	-0.27	-0.01	-0.08	0.38	0.32	**0.50**	0.00	**-0.55**	**-0.52**	0.24	0.43	**0.92**	0.48
Sm	-0.19	-0.15	0.07	-0.30	-0.35	0.17	0.10	0.10	0.24	-0.29	-0.30	-0.18	0.06	0.25	0.09	0.33	-0.15	**-0.51**	-0.34	0.04	0.23	**0.93**	0.27
Eu	-0.21	-0.17	0.08	-0.28	-0.33	0.23	0.07	0.11	0.19	-0.29	-0.29	-0.20	0.08	0.30	0.07	0.31	-0.21	-0.49	-0.31	0.04	0.23	**0.95**	0.24

Gd	-0.16	-0.22	-0.02	-0.36	-0.41	0.30	0.14	0.15	0.23	-0.40	-0.24	-0.07	0.07	0.35	0.17	0.35	-0.20	-0.44	-0.39	0.08	0.37	**0.99**	0.28
Tb	-0.19	-0.23	0.05	-0.29	-0.33	0.32	0.07	0.13	0.15	-0.34	-0.24	-0.13	0.12	0.30	0.08	0.29	-0.26	-0.40	-0.33	0.00	0.30	**0.99**	0.20
Dy	-0.15	-0.28	-0.03	-0.34	-0.38	0.35	0.12	0.15	0.19	-0.41	-0.22	-0.04	0.10	0.34	0.15	0.32	-0.24	-0.37	-0.39	0.04	0.39	**0.98**	0.24
Ho	-0.07	-0.32	-0.16	-0.42	-0.46	0.35	0.21	0.18	0.26	**-0.51**	-0.20	0.10	0.06	0.36	0.25	0.36	-0.17	-0.33	-0.47	0.09	**0.50**	**0.94**	0.31
Er	-0.05	-0.34	-0.20	-0.44	-0.48	0.37	0.23	0.19	0.27	**-0.54**	-0.20	0.14	0.05	0.37	0.27	0.37	-0.15	-0.29	-0.49	0.10	**0.53**	**0.90**	0.33
Tm	-0.07	-0.36	-0.17	-0.39	-0.42	0.40	0.18	0.19	0.22	**-0.52**	-0.19	0.13	0.07	0.37	0.22	0.32	-0.19	-0.22	-0.45	0.07	0.49	**0.87**	0.27
Yb	-0.11	-0.37	-0.09	-0.30	-0.31	0.46	0.08	0.19	0.10	-0.46	-0.20	0.06	0.12	0.36	0.11	0.23	-0.27	-0.15	-0.36	0.01	0.41	**0.84**	0.16
Lu	-0.09	-0.37	-0.08	-0.24	-0.25	0.49	0.04	0.19	0.04	-0.44	-0.17	0.09	0.14	0.32	0.07	0.16	-0.30	-0.07	-0.30	-0.03	0.39	**0.76**	0.09
REY**	-0.08	0.15	-0.15	**-0.51**	-0.46	0.10	0.33	0.48	0.47	-0.47	-0.17	-0.03	-0.40	0.42	0.26	**0.55**	0.24	-0.35	-0.38	**0.54**	0.21	0.33	0.42

(continued)

	Ag	Cd	Sb	Tl	Th	U	Y	La	Ce	Pr	Nd	Sm	Eu	Gd	Tb	Dy	Ho	Er	Tm	Yb	Lu	REY**
Ag	1.00																					
Cd	-0.23	1.00																				
Sb	0.00	-0.28	1.00																			
Tl	-0.15	-0.46	**0.61**	1.00																		
Th	0.02	0.28	-0.40	-0.43	1.00																	
U	-0.11	**-0.52**	**0.50**	**0.72**	**-0.81**	1.00																
Y	0.33	**-0.54**	-0.06	-0.04	**-0.51**	**0.51**	1.00															
La	0.19	**-0.83**	0.27	**0.52**	-0.48	**0.66**	**0.66**	1.00														
Ce	-0.06	-0.17	0.43	0.48	0.26	0.04	-0.41	0.17	1.00													
Pr	0.26	**-0.80**	0.04	0.28	-0.11	0.31	**0.56**	**0.90**	0.23	1.00												
Nd	0.27	**-0.82**	0.04	0.27	-0.18	0.35	**0.62**	**0.92**	0.16	**0.99**	1.00											
Sm	0.28	**-0.74**	-0.12	0.08	0.02	0.15	**0.59**	**0.80**	0.12	**0.97**	**0.97**	1.00										
Eu	0.31	**-0.73**	-0.11	0.04	-0.01	0.15	**0.64**	**0.79**	0.08	**0.96**	**0.96**	**0.99**	1.00									
Gd	0.35	**-0.75**	-0.07	0.06	-0.18	0.28	**0.78**	**0.83**	-0.05	**0.93**	**0.95**	**0.96**	**0.98**	1.00								
Tb	0.35	**-0.71**	-0.12	-0.02	-0.12	0.21	**0.77**	**0.78**	-0.08	**0.90**	**0.92**	**0.95**	**0.97**	**0.99**	1.00							
Dy	0.37	**-0.70**	-0.08	0.00	-0.25	0.31	**0.86**	**0.79**	-0.16	**0.86**	**0.89**	**0.90**	**0.93**	**0.98**	**0.99**	1.00						
Ho	0.35	**-0.68**	-0.02	0.05	-0.40	0.45	**0.93**	**0.80**	-0.24	**0.79**	**0.83**	**0.81**	**0.85**	**0.94**	**0.93**	**0.98**	1.00					
Er	0.34	**-0.65**	0.01	0.06	-0.46	**0.50**	**0.96**	**0.79**	-0.27	**0.73**	**0.78**	**0.75**	**0.79**	**0.90**	**0.89**	**0.95**	**0.99**	1.00				
Tm	0.35	**-0.59**	0.01	0.02	-0.46	0.47	**0.96**	**0.73**	-0.29	**0.67**	**0.73**	**0.70**	**0.75**	**0.86**	**0.86**	**0.93**	**0.98**	**0.99**	1.00			
Yb	0.39	**-0.53**	-0.01	-0.06	-0.40	0.40	**0.94**	**0.64**	-0.31	**0.61**	**0.66**	**0.65**	**0.71**	**0.83**	**0.84**	**0.91**	**0.95**	**0.97**	**0.99**	1.00		
Lu	0.37	-0.43	-0.03	-0.13	-0.42	0.39	**0.94**	**0.54**	-0.38	0.48	**0.54**	**0.53**	**0.60**	**0.73**	**0.75**	**0.83**	**0.90**	**0.93**	**0.96**	**0.99**	1.00	
REY**	0.08	**-0.52**	0.41	**0.55**	0.06	0.26	0.00	**0.58**	**0.89**	**0.63**	**0.58**	**0.52**	0.48	0.39	0.35	0.28	0.21	0.18	0.14	0.09	-0.01	1.00

*Water Depth

**Summation of the rare earth elements plus Y

6 THESIS CONCLUSION

Mineral deposits in the RGR comprise mainly hydrogenetic ferromanganese crusts, found from the summit at 600 m to abyssal depths at more than 5000 m. FeMn crusts from the summit present a dual structure comprising an old phosphatized and younger non-phosphatized crust generation. These dual structures differ significantly in mineralogy, chemical composition, and petrography, but since the phosphatized crust generation makes most of the crusts volume, bulk crusts from the summit of RGR have a diagenetic signature and are depleted in critical metals typically considered of economic interest (Co, REE, Mo, Zr), but are the most enriched in Ni, Li, and Y. However, deep-water crusts are entirely hydrogenetic and enriched in, e.g., As, Be, Co, Cu, Mo, Sb, Se, Ti, Th, Tl, U, Zn, and rare earth elements.

Phosphatization affected mainly FeMn crusts shallower than 1500 m, but also produced phosphorites, phosphatized limestones, ironstones, and carbonate algal concretions in the summit. This likely occurred due dissolution of foraminifera and nannofossil tests, and through the precipitation of CFA in pore space, including foraminifera chambers. Conditions suitable for these processes occurred throughout the Miocene and accompanied major paleoceanpgraphic changes in the South Atlantic Ocean, which likely resulted in phosphorus upwelling and increased productivity in surface waters. FeMn crusts from the summit were more proximal to the OMZ, a reservoir for reactive phosphorus. Despite not being phosphatized, deep-water crusts from the RGR also reflect these paleoceanographic events in their decreasing contents of biologically related metals (Mn, Co, V, As, Mo, Tl, U, Zn, Li, and Y). Besides, modern water masses in the RGR are an important control on the chemical composition of FeMn crusts. Increased oxygenation provided by the NADW and AABW favors the enrichment of the hydrogenetic metals mentioned above in crusts below 2000 m.

The presence of ironstones in the RGR summit is still puzzling, but it is possible to hypothesize that iron precipitation occurred from a fluid other than seawater, e.g., a low-temperature fluid ascending from deep faults along the RGR rift.

This thesis produced a plethora of high-quality and high-resolution geochemical data of ferromanganese crusts, phosphate rocks, and ironstones from the RGR which are important baseline information for future mining activities in the region. Besides, the ideas discussed here contribute to the understanding of mineral deposits formation and evolution at oceanic elevations globally.